NUMERICAL SIMULATION
OF A
SINGLE SCREW PLASTICATING EXTRUDER

BY

© ENNO ERIC AGUR, B.A.Sc., M.Eng.

A Thesis
Submitted to the School of Graduate Studies
in Partial Fulfilment of the Requirements
for the Degree

Doctor of Philosophy

McMaster University
June 1982

Library

NUMERICAL SIMULATION

OF A

SINGLE SCREW PLASTICATING EXTRUDER

To my dear and loving wife,

ANNE

ERRATUM

Thesis complete - page 6-214 material not missing

Page misnumbering

DOCTOR OF PHILOSOPHY (1982)
(Chemical Engineering)

McMaster University
Hamilton, Ontario.

TITLE: Numerical Simulation of a Single Screw Plasticating Extruder

AUTHOR: Enno Eric Agur,
B.A. Sc. (University of Waterloo)
M.Eng. (McMaster University)

SUPERVISOR: Dr. J. Vlachopoulos

NUMBER OF PAGES: xxii, 399

ABSTRACT

A fully-predictive steady-state computer model has been developed for a single screw plasticating extruder. Included in the model are:

(i) a model for the flow of polymer solids in the feed hopper,

(ii) a variation of the Darnell and Mol model for solids flow in the extruder screw channel,

(iii) a modification of the Tadmor melting model for the melting zone in the screw channel,

(iv) an implicit finite difference solution of the conservation of mass, momentum and energy equations for the flow of the polymer melt in the screw channel and die, and

(v) a predictive correlation for the extrudate swell at the die exit.

A temperature and shear rate dependent viscosity relation is used to describe the melt flow behaviour in the model. The parameters in the viscosity relation are obtained by applying regression analysis to Instron capillary rheometer data. Extrudate swell theories developed for capillary rheometers have been utilized in the development of the correlation for the prediction of the extrudate swell at the extruder die exit. The parameters in the correlation are obtained by applying regression analysis to Instron extrudate swell data.

Given the material and rheological properties of the polymer, the screw geometry and dimensions, and the extruder operating conditions (i.e. screw speed, barrel temperature profile, etc.), the following are

predicted:

(i) mass flow rate of the polymer,

(ii) pressure and temperature profiles along the extruder screw channel and in the die, and

(iii) extrudate swell at the die exit.

The overall extruder model predictions have been confirmed with experimental results from a 1 1/2 inch (38 mm) diameter, 24:1 L/D single screw extruder with a 3/16 inch (4.76 mm) diameter cylindrical rod die. High- and low-density polyethylene resins were used.

ACKNOWLEDGEMENTS

It is with pleasure that I express my thanks to all fo those who contributed to this work.

I am particularly indebted to my research supervisor, Dr. J. Vlachopoulos, for his enthusiasm, interest and guidance throughout the course of this study.

To Dr. P.A. Taylor and Dr. C.M. Crowe, I am grateful for their interest in my work and for their many helpful suggestions.

The technical support provided by Messrs. R. Dunn, J. Newton, L. Suggett and H. Behman of the Chemical Engineering Department is very much appreciated. I would also like to thank Mrs. A. Stott for the typing of this thesis.

To my fellow graduate students I would like to express my thanks for a most memorable and enriching experience.

Finally and most importantly I am most appreciative of my family and my wife, Anne, for their confidence and patience during the years of this work. They provided encouragement and support when it was most needed.

Acknowledgement is also made to the Natural Sciences and Engineering Research Council of Canada and McMaster University for financial support, and to Union Carbide Canada Ltd. and DuPont Canada Inc. for donations of polymer used in this work.

CONTENTS

TABLE OF CONTENTS (cont'd)

TABLE OF CONTENTS (cont'd)

FIGURES

FIGURES (cont'd)

FIGURES (cont'd)

FIGURES (cont'd)

FIGURES (cont'd)

FIGURES (cont'd)

FIGURES (cont'd)

TABLES

NOTATION

Dimensions and units

The absolute system of dimensions (mass-length-time-temperature) is used, and the units are in SI (Système International d'Unités):

m	mass, kg (kilogram)
L	length, m (metre)
t	time, s (second)
T	temperature, ^{o}C (Celsius) or K (Kelvin)
E	energy, J(joule)
F	force, N (Newton)

Variables

A	=	area, m^2
A	=	degree of taper, dimensionless
Cp	=	heat capacity, J/(kg·K)
d/D	=	extrudate swell ratio, dimensionless
D_b	=	inside barrel diameter, m
D_s	=	diameter of the root of the screw, m
e	=	width of the screw flights (perpendicular to the flights), m
f_b	=	dynamic coefficient of friction at barrel surface, dimensionless
f_s	=	dynamic coefficient of friction at screw surface, dimensionless
f'_w	=	static coefficient of friction at feed hopper wall, dimensionless
F	=	force, N

NOTATION (cont'd)

F_d	=	shape factor for drag flow, dimensionless
F_p	=	shape factor for pressure flow, dimensionless
g	=	gravitational acceleration, m/s^2
g_c	=	gravitational constant = 1.0 $(kg \cdot m)/(N \cdot s^2)$
G	=	mass flow rate, kg/s
$\acute{G}$	=	elastic modulus, dimensionless
H	=	screw channel depth, m
H	=	height of the vertical feed hopper, m
H_A	=	depth of adapter flow channel, m
H_{ex}	=	screw channel depth in metering section, m
H_o, h_o	=	heights in the convergent feed hopper, m
H_o	=	screw channel depth in feed section, m
H^*	=	height of solid bed, m
I_2	=	second invariant of the rate of deformation tensor, s^{-2}
k	=	thermal conductivity, $W/(m \cdot K)$
ℓ	=	axial distance, m
L	=	screw lead, m
M	=	number of grid divisions perpendicular to the direction of flow (y- or r-direction) in the finite difference grid
n	=	power-law index
N	=	frequency of screw rotation, revolution/min
N_B	=	number of breaker plate channels
N_{delay}	=	length of delay zone, screw turns
N_1	=	first normal stress difference, Pa
p	=	pressure, Pa

NOTATION (cont'd)

P	=	dimensionless pressure
q	=	heat flux, W/m^2
Q	=	volumetric flow rate, m^3/s
Q_d	=	volumetric drag flow rate, m^3/s
Q_p	=	volumetric pressure flow rate, m^3/s
r	=	radial distance in cylindrical coordinates, m
R	=	internal radius of a tube, m
R	=	dimensionless radial distance
R_B	=	radius of breaker plate flow channel
R_D	=	radius of die flow channel
t	=	time, s
S_R	=	recoverable shear, dimensionless
T	=	temperature, ^oC or K
T_A	=	adapter temperature, ^oC
T_b	=	barrel surface temperature, ^oC
T_{bulk}	=	flow-average (bulk) temperature, ^oC
T_D	=	die temperature, ^oC
T_{melt}	=	melting temperature of polymer, ^oC
T_s	=	solid bed temperature, ^oC
T_{sc}	=	screw surface temperature, ^oC
v	=	velocity, m/s
v_x	=	cross channel velocity, m/s
v_z	=	down channel velocity, m/s
V_b	=	tangential barrel velocity, m/s
V_j	=	velocity of barrel with respect to solid bed, m/s

NOTATION (cont'd)

V_{sy} = velocity of solid bed moving into solid-melt interface, m/s

V_{sz} = downchannel velocity of solid bed, m/s

Vx = dimensionless cross channel velocity

$Vx_{m,n}$ = dimensionless cross channel velocity at node (m,n) on finite difference grid

Vz = dimensionless downchannel velocity

$Vz_{m,n}$ = dimensionless downchannel velocity at node (m,n) on finite difference grid

W = width of the screw channel (perpendicular to the flights), m

W = width of the vertical feed hopper, m

x = cross channel distance in rectangular coordinates, m

X = dimensionless cross channel distance

X = width of the solid bed

X/W = solid bed profile

y = distance perpendicular to x- and z- directions in rectangular coordinates, m

Y = dimensionless y-distance

z = downchannel distance in rectangular coordinates, m

z_b = downchannel distance at the barrel surface, m

Z = dimensionless down channel distance

Greek letters

$\dot{\gamma}$ = shear rate, s^{-1}

δ = effective angle of friction, deg

δ = thickness of melt film between barrel and solid bed, m

δ_f = flight clearance, m

NOTATION (cont'd)

$\overline{\overline{\Delta}}$	=	rate of deformation tensor, s^{-1}
η	=	non-Newtonian viscosity, Pa·s
θ	=	helix angle, deg
θ	=	dimensionless temperature
$\theta_{m,n}$	=	dimensionless temperature at node (m,n) in finite difference grid
λ	=	heat of fusion, J/kg
μ	=	Newtonian viscosity, Pa·s
ρ	=	density, kg/m^3
$\overline{\overline{\tau}}$	=	deviatoric stress tensor, Pa
τ_{yx}, τ_{yz}	=	shear stress in rectangular coordinates, Pa
ϕ	=	angle between the direction of the flow of the solid plug relative to the barrel, deg
ω	=	rate of melting per unit down channel distance, kg/(m·s)

Subscripts

b	refers to barrel surface
c	refers to compression section
f	refers to feed section
m	refers to polymer melt, or metering section
m,n	refers to location on finite difference grid
o	refers to the entrance to a flow channel
s	refers to polymer solid or screw surface
sc	refers to screw surface (T_{sc})

Overscripts

$-$	refers to a vector, or the midpoint between the barrel and screw root

NOTATION (cont'd)

$=$	refers to a tensor

Mathematical conventions

$\frac{D}{Dt}$	=	substantial derivative; $\frac{DT}{Dt} = \frac{\partial T}{\partial t} + v_x \frac{\partial T}{\partial x} + v_y \frac{\partial T}{\partial y} + v_z \frac{\partial T}{\partial z}$
∇	=	vector differential operator

CHAPTER 1

INTRODUCTION

1.1 The Extrusion Process

The screw extruder[1] is a key component of the polymer processing industry which is concerned with the conversion of polymers in raw material form (ie. solid polymer pellets, granules or powder) into finished products. Operating on the principle of an Archimedean screw rotating in a heated barrel, an extruder is used to convert the solid polymer granules into melt and pump the highly viscous[2] melt through a die at high pressure to give it a shape, for example a rod or tube. After being extruded, the polymer melt is cooled in order that its shape may be retained. As opposed to cyclic processes such as blow moulding or injection moulding, screw extruders operate at steady state and produce items that are "infinite" in one direction, for example wire and cable coatings, filaments, rods, pipes, films, sheets and various

---

[1] The word "extrude" is derived from the Latin words "ex" and "trudere" meaning, respectively, "out" and "to thrust, push". Webster's New Collegiate Dictionary defines "extrude" as "to force, press or push out; to shape (as metal, plastic, etc.) by forcing through a die". Perhaps a more straightforward way of illustrating the extrusion process is to think of toothpaste being squeezed from a tube (49).

[2] Typical values in the extrusion of low-density polyethylene are: viscosity = 1000 Pa·s, die head pressure = 10,000 kPa.

contoured profiles.

Extruders used today in the polymer processing industry date back to the middle 1800s in Great Britain when ram extruders were invented to coat telegraph wires with gutta percha, a naturally occuring thermoplastic for insulation purposes. This extrusion process however was intermittent in nature, and was not well suited for the production of mile upon mile of cable. Thus arose the need for a continuous extrusion process, and in time the screw extruder was invented. Screw extruders were also developed in the U.S.A. and Germany at this time. For a more detailed historical account of the extruder, one is referred to any of several textbooks on polymer processing (99a, 112a, 114a). Kaufman (49), in particular, has presented an in-depth review of the history of the screw extruder before 1945, and has provided us with many details of its earlier developments. Since 1945 the polymer industry as a whole has experienced phenomenal growth, and as a consequence the screw extruder has undergone numerous improvements and developments resulting in the sophisticated polymer processing machine as we know it today.

A schematic cross-section of a single screw plasticating extruder is shown in Fig. 1.1. Although some extruders are melt fed, the plasticating extruder is supplied with polymer in solid form. The solid polymer, usually in the shape of pellets, granules or powder, is gravity fed through the feed hopper onto the screw, and then is compressed and driven forward by the rotating screw. As the polymer moves forward it is gradually melted. The heat required for melting is supplied from two

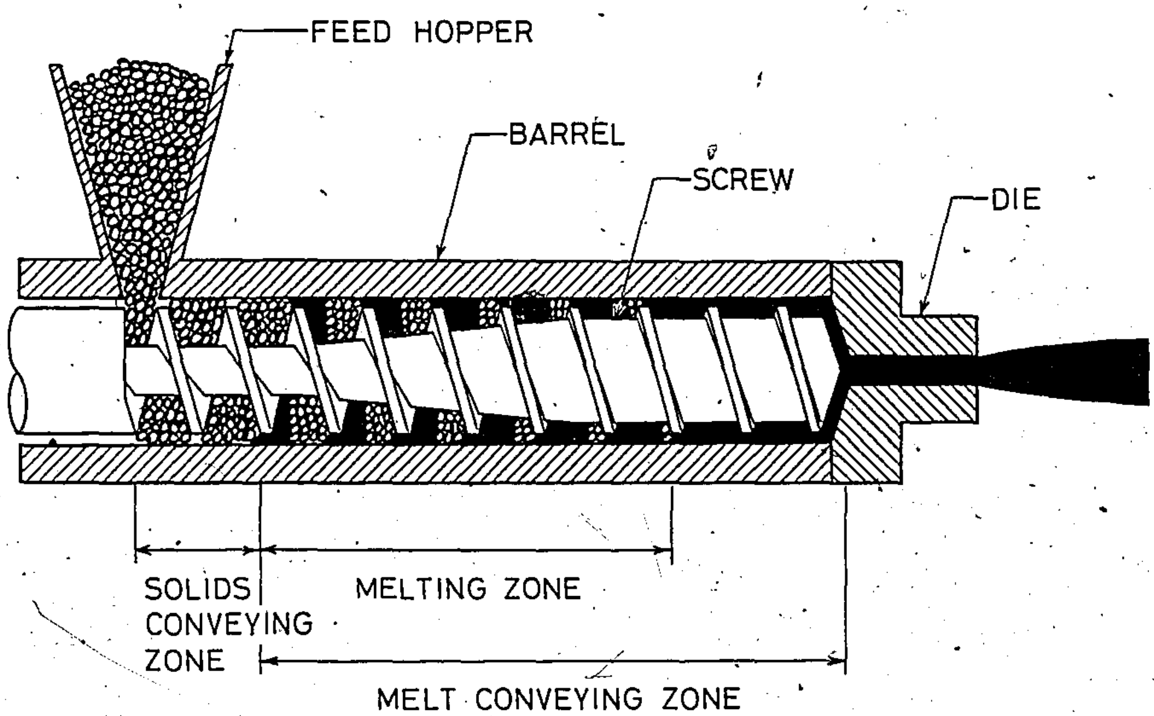

Fig. 1.1 Schematic cross-section of a single screw plasticating extruder.

sources: frictional heat developed through the shearing action of the screw and barrel on the polymer, and heat conducted from the barrel wall. Once melted, the polymer is homogenized and pumped through the die. Upon exiting from the die, the melt exhibits an increase in cross-sectional area provided there is no subsequent draw down effect. This phenomenon is called extrudate swell and is due to the viscoelastic behaviour of the polymer melt. Depending on the extrusion conditions, rheological properties of the polymer, and the die geometry and dimensions, the increase in diameter (in the case of a circular die) may range from 1.5 to 4 times the die diameter.

In the extruder screw channel the polymer flow may be analyzed as three distinct operations: solids conveying, melting and melt conveying, as shown in Fig. 1.1. The relative lengths of these functional zones depend on the extruder operating conditions, the material properties of the polymer and the screw geometry. Each of these zones as well as the feed hopper, die flow and extrudate swell sections will be individually dealt with in much greater detail in Chap. 2.

1.2 Mathematical Modelling

The development of mathematical models for single screw plasticating extruders has been covered extensively in the literature. By far, the majority of these studies have concentrated on melt flow in extruders and dies, the primary reason being that the analysis and modelling of melt flow is far simpler than that of solids conveying or melting of the polymer. Applications for melt fed extruders can be found in the polymer processing industry, for example in the homogenization and pelletization of the polymer immediately after polymerization. Most extruders used in the plastics industry, however, are plasticating extruders.

Modelling of a plasticating extruder should include the analysis of (112b):

(i) gravitational flow behaviour of particulate solids in hoppers, in particular pressure distribution, arching and bridging,

(ii) stress and temperature distribution in the solids conveying zone,

(iii) rate of melting, mean width profile of the solid bed (solid bed profile) and mean temperature of the melt flow into the melt pool in the melting zone,

(iv) drag induced pressurization and laminar mixing of the melt in both the melt conveying zone and the melt pool in the melting zone,

(v) power consumption in the solids conveying, melting and melt conveying zones,

(vi) pressure flow in the die,

(vii) surging conditions, and

(viii) extrudate swelling at the die exit.

In more general terms, one should be able to obtain velocity, temperature and stress profiles in both the solid and melt phases, from which all the other variables of interest could then be calculated.

1.3 Objectives

The objective of this thesis is to describe the development of a fully-predictive computer model of a single screw plasticating extruder, and to present results of simulations and experimental runs for a 1 1/2 inch (38 mm) diameter, 24:1 L/D single screw extruder. The extruder model is divided into six distinct but interdependent sections (or submodels): solids flow in the feed hopper, solids flow, melting and melt pumping in the extruder screw channel, melt flow in the die and swelling of the extrudate at the die exit. Models for each of these sections are developed and described in detail in this thesis. Given the material and rheological properties of the polymer, the screw geometry and dimensions, and the extruder operating conditions (screw speed and barrel temperature profile), the overall model is used to predict:

(i) flow rate of the polymer,

(ii) pressure and temperature profiles along the extruder flow channel and in the die, and

(iii) extrudate swell at the die exit.

1.4 Outline of Thesis

Chapter 2: Background information is presented for the screw geometry and for each of the six submodels in the overall extruder model. Included are descriptions of the mechanisms for solids flow in the feed hopper and screw channel, melting in the screw channel, melt flow in the screw channel and in the die and swelling of the extrudate at the die exit. In the case of melt flow, the equations of conservation of mass, momentum and energy are introduced and simplified using the assumptions which are given in the chapter. Constitutive equations and the method of solution are also discussed.

Chapter 3: A model developed by Walker for solids flow in vertical and converging hoppers is described. Results from this model are presented for a typical feed hopper containing solid polymer granules.

Chapter 4: This chapter concerns the flow of solids in the extruder screw channel. A literature survey of solids conveying models is presented. A variation of the model developed by Darnell and Mol for the prediction of the pressure profile in the solids conveying zone is described. Typical predictions of pressure profiles from the model are also given.

Chapter 5: A literature survey of melting models is presented. The Tadmor Newtonian melting model is described in detail followed by a description of a modified version which was developed for the present overall extruder model. A new method of solution is also described. Typical solid bed profile results are presented for both the Tadmor Newtonian melting model and the present modified version.

Chapter 6: The development of melt flow models for extruder screw channels is discussed. A literature survey is presented which covers the simplest Newtonian isothermal flow models to the very complex non-Newtonian nonisothermal developing flow models. Starting with a Newtonian isothermal model, a step-by-step development of the present non-Newtonian nonisothermal developing flow model is described. Typical results of down channel pressure and bulk temperature profiles are given at the various stages of model development.

Chapter 7: The non-Newtonian nonisothermal developing flow model for the extruder screw channel is extended to melt flow the die section. Included in the model are melt flow in the breaker plate, adapter and cylindrical rod die. Typical down channel pressure and bulk temperature profiles for this section are also presented.

Chapter 8: A correlation for predicting extrudate swell at the extruder die exit is developed in this chapter based on Tanner's elastic recovery theory and measurements of extrudate swell performed on an Instron capillary rheometer.

Chapter 9: The overall extruder model is described including a summary of the six individual submodels. This chapter summarizes the most important contribution of this thesis, that is, a fully-predictive computer model which includes all the extrusion steps from solids flow in the feed hopper to swelling of the extrudate at the die exit.

Chapter 10: Brief discriptions of the 1 1/2 inch (38 mm) diameter screw extruder including the adapter and die, and of the Instron capillary rheometer are presented. Experimental procedures for the experimental runs on the extruder and for the measurements of melt viscosity and extrudate swell using the Instron capillary rheometer are outlined.

Chapter 11: The material and rheological properties of the polymers and the extruder operating conditions which are utilized in the present extruder model are presented.

Chapter 12: A comparison of the simulation and experimental results as well as a general critique of the overall extruder model are included in this chapter.. First the extruder model predictions and experimental results for the polymers studied are presented and compared. Results of a sensitivity study performed on each of the polymer properties utilized in the extruder model are also discussed. Finally a critical discussion of the overall model is presented. Each of the individual submodels is examined for possible improvements.

Chapter 13: The results of this thesis are summarized and conclusions and recommendations are presented.

CHAPTER 2

BACKGROUND INFORMATION

2.1 Extruder Screw Geometry

Most extruders in the plastics industry have a single screw rotating in a heated, tightly fitted barrel. A popular and common screw design is the "general-purpose" or metering screw, as shown in Fig. 2.1. It consists of three geometrical sections: a deep feed section, a tapered compression section, and a relatively shallow metering section. Since the effective density of the solids feed is lower than that of the melt, the feed section should be deeper than the metering section in order that the polymer can be conveyed at the same rate in the entire extruder. A typical compression ratio, that is the ratio of the feed section channel depth to the metering section channel depth, for a polyethylene metering screw is 3:1.

To define the screw geometry, an enlarged and exaggerated section of the screw is shown in Fig. 2.2. D_b is the inside diameter of the barrel, H the channel depth (the distance between the root of the screw and the inner suface of the barrel), δ_f the radial clearance between the crest of the screw flights and the inner barrel surface, L the screw pitch or lead (the axial distance of one full turn), W(r) and e the channel and flight widths respectively normal to the flights, and $\theta(r)$ the helix angle (the angle formed between the flight and the plane normal to the screw axis. The screw rotates at N revolutions per unit

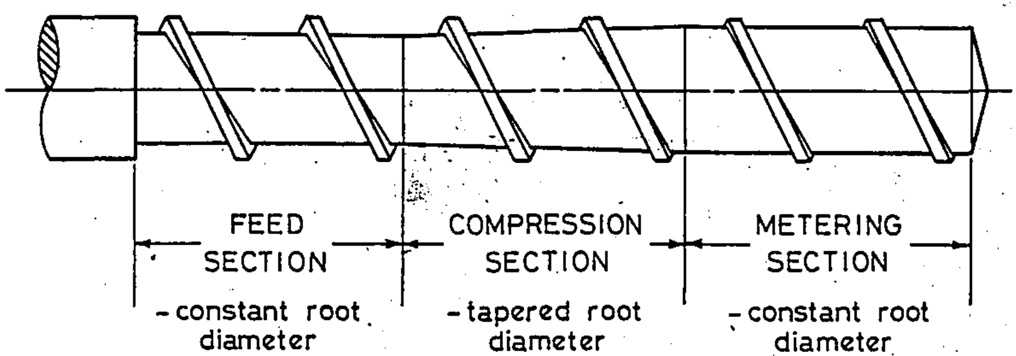

Fig. 2.1 Schematic illustration of a metering screw.

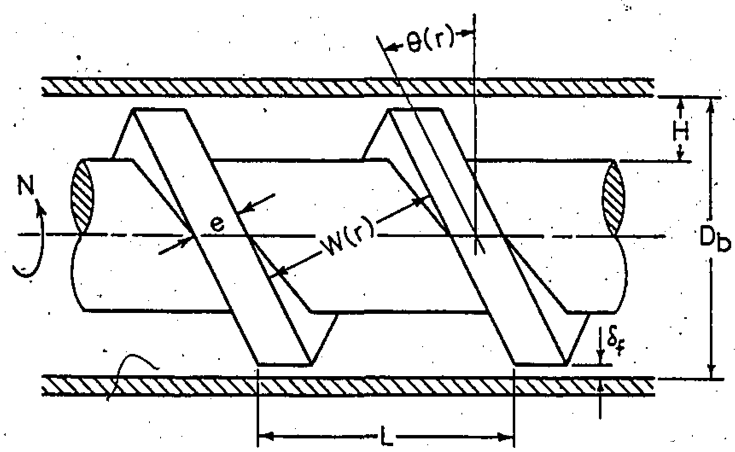

Fig. 2.2 Geometry of extruder screw showing characteristic dimensions.

time.

An important point to note here is that W, $\dot{\theta}$ and z, the down channel distance, are not the same at different radial positions. To illustrate this, consider the two sets of traces shown in Fig. 2.3. One set may be obtained by painting the flight crests of a screw with ink and rotating one full turn on a sheet of paper; the other set may be obtained by the same procedure but with the flights filed down to the screw root surface (114b). Thus, it is important that each time W, θ or z is cited, the radial position in the screw channel should also be stated. For example, θ_b, θ_s and $\bar{\theta}$ denote, respectively, the helix angle at the inside barrel surface, screw surface, and midpoint between the barrel and screw surfaces.

The helix angle can be expressed as:

$$\tan \theta(r) = \frac{L}{2\pi r} \tag{2.1}$$

The width of the channel perpendicular to the flights is:

$$W(r) = L \cos \theta(r) - e \tag{2.2}$$

Finally, the down channel (or helical distance) at a given radius is given by:

$$z(r) = \frac{\ell}{\sin \theta(r)} \tag{2.3}$$

where ℓ is the corresponding axial distance. In the remainder of this thesis, z will imply $\bar{z}$, the average down channel distance as traced out on the cylindrical plane half way between the barrel and screw surfaces.

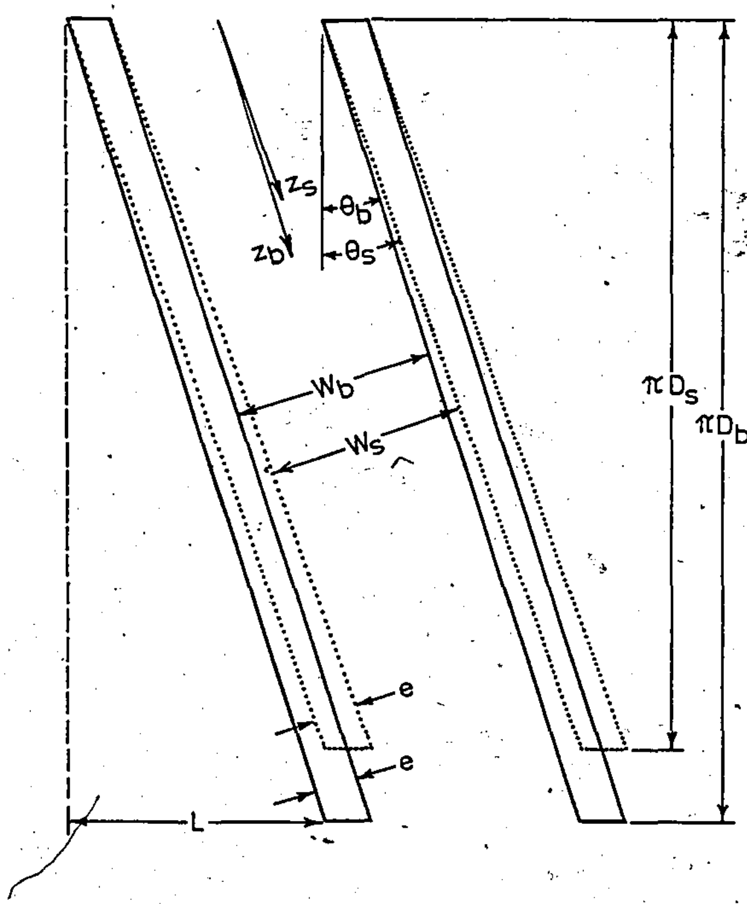

Fig. 2.3 Traces imprinted by the tips of the screw flight placed on a plane surface and rotated one full turn. Solid lines - screw with flights; dotted lines - screw with flights filed down to screw root (114b).

For the analysis of melt flow in the screw channel, the following geometric assumptions are made:

(i) the sides of the screw flights are radial to the screw axis, and

(ii) the depth H of the screw channel is constant across its width.

It is convenient to choose a coordinate system that is relative to the screw. Also, one may treat the barrel as rotating about a stationary screw, a valid procedure[1] since:

(iii) body forces (such as gravity) and centrifugal inertia forces in polymer melt flow are negligible in comparison with viscous and pressure forces.

The most natural coordinate system to choose is the helical one. However, it is very difficult to obtain solutions for melt flow using this system (see Sec. 2.4). A standard simplifying assumption is:

(iv) consider the helical screw channel as "unwound" and rectilinear, thus allowing the use of Cartesian coordinates.

This is a valid assumption because in most single screw extruders the screw channel is relatively shallow in the melt flow regions, typically

---

[1]The two flow situations, stationary barrel/rotating screw and rotating barrel/stationary screw have identical tangential velocity profiles but different radial pressure distributions. The radial pressure distribution originates from the centrifugal forces present in the flow channel which are different in the two cases. However, these forces are negligible due to the slow flow of the highly viscous polymer melt, and consequently the assumption of rotating barrel/stationary screw is valid (114c).

$H/D_b = 0.05$. An enlarged view of the channel cross-section for a screw with $H/D_b = 0.05$ is shown in Fig. 2.4. The "unwound" rectangular channel is illustrated in Fig. 2.5. As stated earlier in this section, the plane of unwinding should be the one located half way between the screw and barrel surfaces.

2.2 Solids Flow in the Hopper and Extruder Screw Channel

The analysis of solids flow in the feed hopper and extruder screw channel is based on the dynamics of particulate solids systems. Solid polymer pellets are fed into the screw channel through the hopper. Flow in the hopper is usually by gravity, although force feeding is required in certain circumstances. The latter will not be considered in this discussion. By assuming stress equilibrium in the solids, the pressure distribution in the hopper may be calculated. The relevant equations for the pressure distribution are presented in Chap. 4. Once the polymer pellets are in the extruder screw channel, they are compacted to form a solid bed or plug which is then conveyed downstream by a drag induced mechanism, that is, flow due to the frictional drag of the barrel and screw surfaces on the polymer pellets.

The solids conveying mechanism may be explained most easily, following Tadmor and Klein (114d), by considering the frictional forces between the solid polymer plug and the barrel and screw sufaces, and by assuming that the screw is stationary and the barrel rotates. In this case the frictional force between the barrel surface and the solid plug will cause forward motion, while the frictional force between the screw

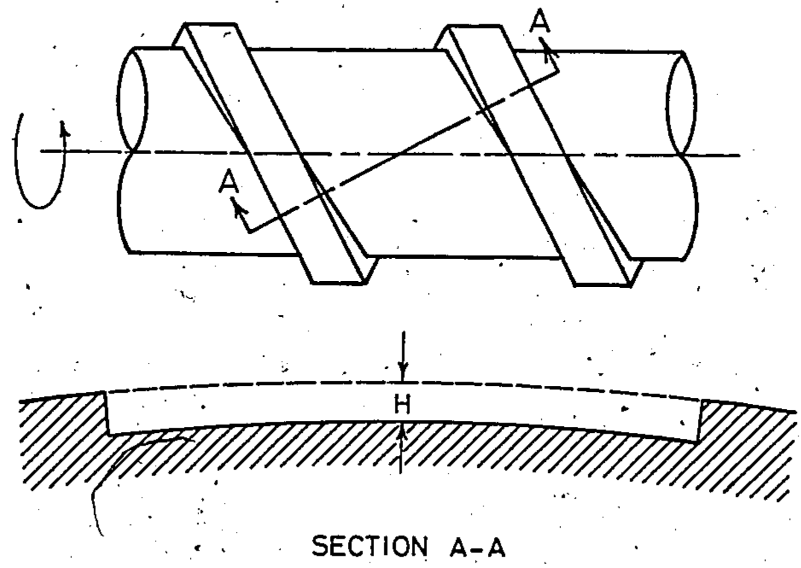

Fig. 2.4 Magnified cross-section of screw channel where $H/D_b = 0.05$, H is the channel depth and D_b the inside diameter of the barrel.

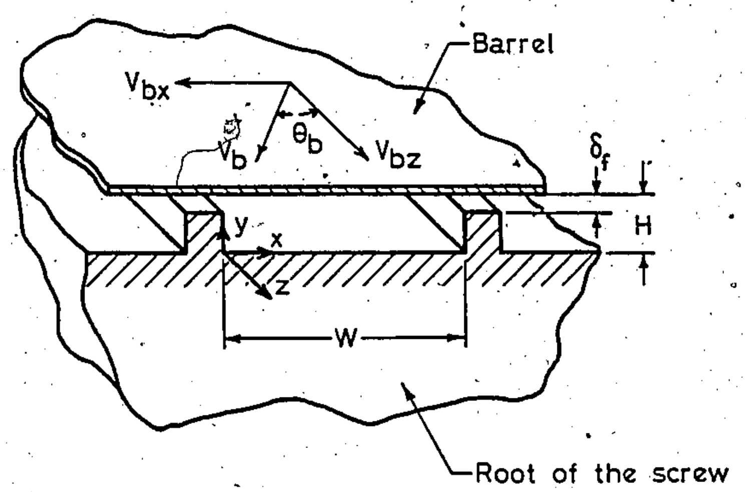

Fig. 2.5 "Unwrapped" rectangular screw channel. V_b is the tangential barrel velocity, V_{bx} and V_{bz} the x and z barrel velocity components.

surface and the plug will retard its motion. Consider the movement of a solid plug in a rectangular channel as shown in Fig. 2.6. The upper plate, representing the barrel, moves at a constant velocity V_b and at an angle θ to the down channel direction. If the solid plug has a constant velocity U in the down channel direction, then the force of the moving plate on the plug in the direction $\theta + \phi$ will be:

$$F_b = A\ f_b\ P \tag{2.4}$$

where A and f_b are, respectively, the area of contact and the dynamic coefficient of friction between the plug and the upper moving plate, P is the pressure in the solid plug, and ϕ is the angle between the relative movements of the plug and the upper moving plate as shown in Fig. 2.7. The angle ϕ is a function of the plug velocity U. The component of the force F_b in the down channel direction z is:

$$F_{bz} = A\ f_b\ P\cos(\theta + \phi) \tag{2.5}$$

The retarding force of the lower stationary surface which represents the screw (neglecting the sides) is given by:

$$F_s = A\ f_s\ P \tag{2.6}$$

where f_s is the dynamic coefficient of friction between the solid plug and the stationary surface. In a steady state condition the two forces F_{bz} and F_s are equal, thus:

$$A\ f_s\ P = A\ f_b\ P\cos(\theta + \phi) \tag{2.7}$$

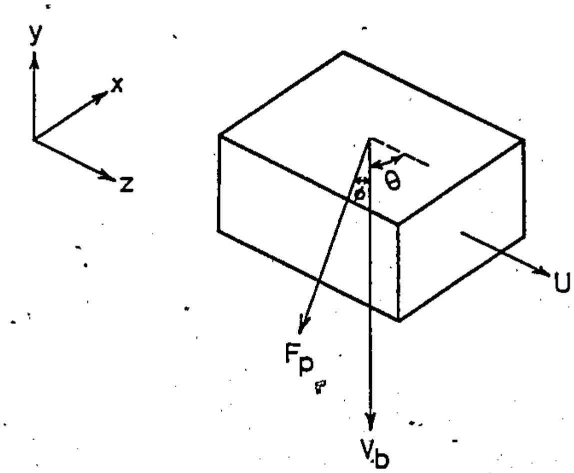

Fig. 2.6 Idealized model of the solids conveying mechanism. Upper plate (not shown, but representing barrel) moves with velocity V_b in direction . Solid plug slides along the stationary rectangular screw channel (also not shown) with velocity U.

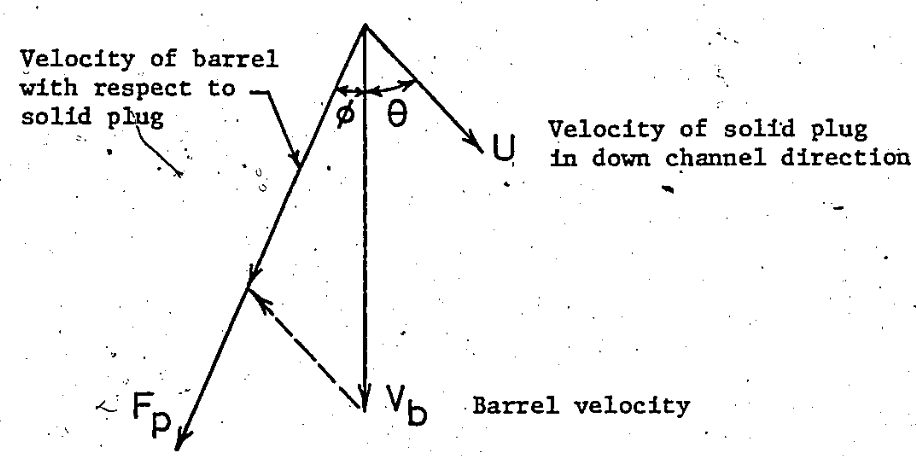

Fig. 2.7 Velocity vector diagram showing the velocity of the barrel with respect to the moving plug, and direction of the force F_p.

The objective of this discussion is not to calculate the plug velocity U or the angle ϕ, but to show their interdependence and the importance of the dynamic coefficients of friction, f_b and f_s. The equations for the flow of a solid plug in a helical channel are presented in Chap. 5 along with more detailed expressions for the plug velocity U, angle ϕ and pressure P in the solid plug.

2.3 The Melting Mechanism in Extruders

In plasticating extruders solid polymer pellets or powder are supplied through the feed hopper and the polymer melt is pumped from the screw channel into the die. Between the hopper and the die the solid polymer is melted. The melting zone is that portion of the screw channel in which the solid polymer and melt coexist.

Unlike the analyses of solids conveying and melt flow in extruders which can be developed from basic principles with little or no reference to observed behaviour, the mechanism of melting cannot easily be visualized or modelled without some experimentation based on visual analysis. A qualitative understanding of the melting process was obtained only after Maddock (63) and Street (105) reported results of their visual analyses of the melting of polyethylene in screw extruders. Their experiments were performed by first achieving steady state operating conditions, then abruptly stopping the extruder, chilling both the barrel and screw to solidify the polymer, extracting the screw from the barrel, unwinding the polymer from the screw, and finally slicing the helical strip into flat sections perpendicular to the flights.

Coloured polymer was added as a tracer to the feed to help distinguish between the solid and molten regions of the cross sections. More recently Tadmor et al. (111) reported results of cooling experiments in conjunction with a quantitative analysis of the melting process. Photographs of the cross sections included low- and high-density polyethylene, polypropylene, rigid PVC (polyvinyl chloride) and ABS (acrylonitrile-butadiene-styrene copolymer).

As stated above, solid and melt phases coexist in the melting zone. The cooling experiments showed that the two phases are clearly set apart from each other, with the solids segregated as a solid bed at the front flight and the melt phase accumulating in a melt pool at the rear flight. An idealized cross-section of the melting zone is presented in Fig. 2.8. In addition to the solid bed and melt pool there exists a thin film of melt between the barrel surface and the solid bed. Due to the intense shear in this melt film and the proximity of the heated barrel, much of the melting occurs in this region, or more precisely, at the interface between the solid bed and the melt film. The energy required for melting originates primarily from two sources: heat conducted from the heated barrel surface through the thin melt film, and viscous dissipation due to shearing of the melt in the film. The motion of the barrel relative to the solid bed drags the melt in the film into the melt pool. The width of the melt pool gradually increases in the down channel direction, and that of the solid bed decreases until the end of melting at which point the screw channel is completely filled with molten polymer. The width of the solid bed as a function of down

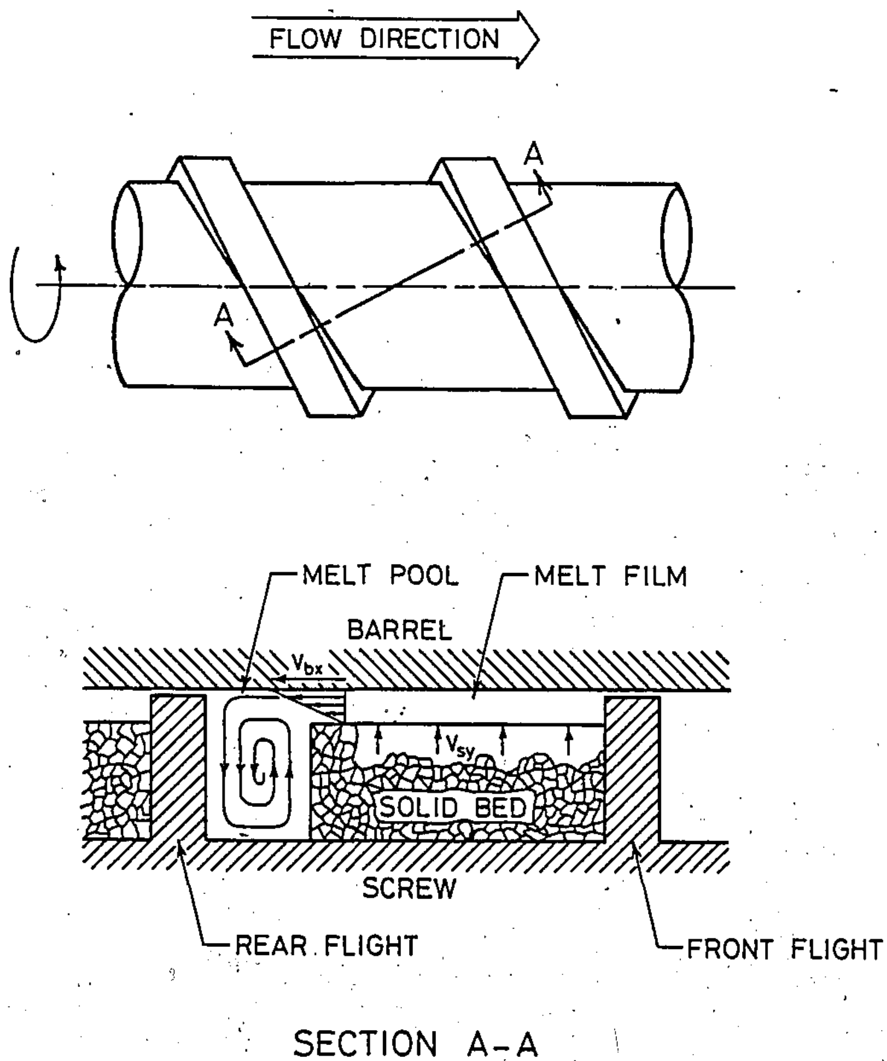

Fig. 2.8 Idealized cross-section of screw channel in the melting zone. V_{bx} is the cross channel component of the barrel velocity, and V_{sy} is the velocity of the solid bed moving into the solid-melt interface.

channel direction is called the solid bed profile. In Chap. 5 a melting model is developed for the melting zone. Equations are presented for the calculation of the solid bed profile and the rate of melting.

2.4 Melt Flow in the Extruder Screw Channel and Die

Melt flow in the extrusion process occurs in the extruder screw channel and the die. In the screw channel the melt flow section (usually referred to as the melt conveying zone) may be considered as existing in two regions. One is downstream of the melting zone and occupies the entire width of the screw channel. This is the region which conventionally has been regarded as the melt conveying zone. The other region occurs in the melt pool which extends side by side with the solid bed in the melting zone. Here the width of the melt flow region changes in the down channel direction as the solid polymer is melted. Only recently has this region been also considered as a part of the melt conveying zone in the screw channel.

The analysis and modelling of melt flow in the extrusion process is usually based on the principle of continuum mechanics which ingores the molecular nature of the materials concerned. Thus, the problem of melt flow in extruder screw channels and dies can be fully described in terms of the equations of conservation of mass, momentum and energy. To obtain solutions, we need boundary conditions at the channel walls and constitutive relations which describe the stress and temperature behaviour of the melts. Solutions of the conservation equations in general form are very complicated even for Newtonian, constant property fluids. The introduction of constitutive equations describing polymer melt behaviour renders the system of equations extremely difficult even for very simple flow geometries, not to mention flow in a helical system. The conservation equations and flow geometry must be simplified substantially to even make solution by numerical methods feasible. A simplified flow geometry for the extruder screw was already presented in Sec. 2.1, notably an "unwound" rectangular flow channel.

In this section, the conservation equations, the constitutive relation and the method of solution for melt flow in extruder screw channels and dies are presented and discussed. The principle assumptions involved are numbered consecutively as they occur in the analysis. The concepts presented here are utilized, respectively, in Chaps. 5, 6 and 7 in the development of models for the melting, melt conveying and die sections of the extruder. The relevant boundary conditions for the individual models will also be covered in these chapters.

2.4.1 Conservation Equations

In general tensorial form, the conservation equations are (7):

Mass: $$\frac{D\rho_m}{Dt} + \rho_m(\nabla \cdot \bar{v}) = 0 \tag{2.8}$$

Momentum: $$\rho_m \frac{D\bar{v}}{Dt} = - \nabla p + \nabla \cdot \bar{\bar{\tau}} + \rho_m \bar{g} \tag{2.9}$$

Energy: $$\rho_m \, Cp_m \frac{DT}{Dt} = - \nabla \cdot \bar{q} + \bar{\bar{\tau}} : \nabla \bar{v} \tag{2.10}$$

Assuming that (30):

(a) the melt is incompressible (constant density), the continuity equation for conservation of mass (2.8) reduce to:

$$\nabla \cdot \bar{v} = 0 \tag{2.11}$$

The equation of conservation of momentum involves a balance between inertia, viscous, pressure and body forces. Because polymer melt flows are very slow flows with extremely small Reynolds number[1], it may be assumed that:

(b) inertia effects are negligible in comparison with viscous and pressure forces.

Also assuming that:

(c) body forces (such as gravity) are negligible in comparison with viscous and pressure forces, and

(d) the flow is steady ($\frac{\partial}{\partial t} \equiv 0$),

---

[1]Reynolds number for polymer melt flow may be expressed as $Re_H = \rho_m V_b H/\mu$, where ρ_m is the melt density, V_b the tangential barrel velocity, H the screw channel depth, and μ the apparent melt viscosity (at shear rate $\dot{\gamma} = V_b/H$). For the flow of low-density polyethylene melt in a 1 1/2 inch (38 mm) screw extruder, $Re_H = 1.87 \times 10^{-4}$ when $\rho_m = 779$ kg/m^3, $V_b = 0.12$ m/s (screw speed = 60 rpm), H = 0.002 m, and $\mu = 1000$ Pa·s ($\dot{\gamma} = 60\ s^{-1}$).

the equation of conservation of momentum (2.9) reduces to:

$$-\nabla\cdot p + \nabla\cdot\bar{\bar{\tau}} = \bar{0} \tag{2.12}$$

Turning to the equation of conservation of energy (2.10), the following assumptions are usually made:

(e) thermal conductivity k_m is constant, and

(f) the specific heat at constant pressure Cp_m is constant.

The resulting energy equation is:

$$\rho_m\, Cp_m\, \bar{v}\cdot\nabla T = k_m\, \nabla^2 T + \bar{\bar{\tau}}:\nabla\bar{v} \tag{2.13}$$

Further simplifications to the conservation equations are usually introduced with the aid of the lubrication approximation (89a) which is applicable for flows in screw channels and dies. This involves the local replacement of the actual flow in the parallel or nearly parallel gap between smooth surfaces by uniform flow between plane parallel surfaces. Since the depth of the extruder channel is either constant or varies slowly in the downstream direction, it is reasonable to apply the lubrication approximation in the z direction to velocities and assume that (30):

(g) velocities are fully developed in the downstream direction, and

(h) normal forces are negligible (78a,122).

The fully developed velocity profiles may be written as:

$$v_x = v_x(x,y),\ v_y = v_y(x,y),\ v_z = v_z(x,y) \tag{2.14}$$

It is much less reasonable to assume a fully developed temperature profile in the downstream direction as verified in Chap. 6 where it is shown that the temperature profile changes significantly in the downstream direction of the extruder screw channel. The momentum equation (2.12) and energy equation (2.13) may be expressed as:

Momentum:
$$-\frac{\partial p}{\partial x} + \frac{\partial \tau_{yx}}{\partial y} = 0 \tag{2.15}$$

$$-\frac{\partial p}{\partial y} + \frac{\partial \tau_{xy}}{\partial x} = 0 \tag{2.16}$$

$$-\frac{\partial p}{\partial z} + \frac{\partial \tau_{xz}}{\partial x} + \frac{\partial \tau_{yz}}{\partial y} = 0 \tag{2.17}$$

Energy:
$$\rho_m\, Cp_m\, \bar{v}\cdot\nabla T = k_m\, \nabla^2 T + \tau_{yx}\left(\frac{\partial v_x}{\partial y} + \frac{\partial v_y}{\partial x}\right) + \tau_{yz}\frac{\partial v_z}{\partial x} + \tau_{yz}\frac{\partial v_z}{\partial y} \tag{2.18}$$

The next stage of simplification is to apply the lubrication approximation to velocities in the x direction. In Sec. 2.1 it was assumed that the channel depth is constant in this direction except at the flight. Therefore, for the lubrication approximation to be valid it must be assumed that:

(i) the influence of the flight is negligible, and that the flow may be treated as though the channel were infinitely wide.

Typically the aspect ratio in the metering section of a screw extruder is H/W = 0.05. The fully developed velocity profiles may be written as:

$$v_x = v_x(y),\ v_y = 0,\ v_z = v_z(y) \tag{2.19}$$

The momentum equations (2.15 to 2.18) reduce to:

$$-\frac{\partial p}{\partial x} + \frac{\partial \tau_{yx}}{\partial y} = 0 \tag{2.20}$$

$$-\frac{\partial p}{\partial y} = 0 \tag{2.21}$$

$$-\frac{\partial p}{\partial z} + \frac{\partial \tau_{yz}}{\partial z} = 0 \tag{2.22}$$

As in the case of the downstream direction, it is less reasonable to assume a fully developed temperature profile in the cross channel direction. If we assume that:

(j) heat transfer by conduction in the direction of flow (x or z) is negligible as compared to both convection in the direction of flow (x or z) and conduction perpendicular to the direction of flow (y),

the energy equation reduces to the following:

$$\rho_m Cp_m \left(v_x \frac{\partial T}{\partial x} + v_z \frac{\partial T}{\partial z}\right) = k_m \frac{\partial^2 T}{\partial y^2} + \tau_{yx} \frac{\partial v_x}{\partial y} + \tau_{yz} \frac{\partial v_z}{\partial y} \tag{2.23}$$

Assuming that:

(k) thermal convection in the x direction is neglected, or preferably, accounted for by an appropriate choice of wall temperature boundary conditions (as discussed in Chap. 6), the energy equation (2.23) may be written as:

$$\rho_m Cp_m v_z \frac{\partial T}{\partial z} = k_m \frac{\partial^2 T}{\partial y^2} + \tau_{yx} \frac{\partial v_x}{\partial y} + \tau_{yz} \frac{\partial v_z}{\partial y} \qquad (2.24)$$

Assumptions (j) and (k) are necessary simplifications in order that the momentum and energy equations can be reduced to representing two-directional flow (v_x,v_z) in two dimensions (y,z). A two-dimensional system is needed to keep the computation time requirements of the numerical solution within reasonable limits. This is dealt with in more detail in Sec. 2.4.3 where the method of numerical solution is discussed.

To summarize, the momentum and energy equations in simplified form are given by:

Momentum: $$-\frac{\partial p}{\partial x} + \frac{\partial \tau_{yx}}{\partial y} = 0 \qquad (2.25)$$

$$-\frac{\partial p}{\partial z} + \frac{\partial \tau_{yz}}{\partial y} = 0 \qquad (2.26)$$

Energy: $$\rho_m Cp_m v_z \frac{\partial T}{\partial z} = k_m \frac{\partial^2 T}{\partial y^2} + \tau_{yx} \frac{\partial v_x}{\partial y} + \tau_{yz} \frac{\partial v_z}{\partial y} \qquad (2.27)$$

For melt flow in dies, the cross channel components in Eqs. 2.25 to 2.27 are neglected since only downstream flow is relevant in this case.

2.4.2 Constitutive Equation

In order to solve the momentum and energy equations (2.25 to 2.27), a constitutive expression is required for the shear stress components, τ_{yx} and τ_{yz}. The constitutive equation describes the relationship between the state of stress and the rate of deformation of a fluid. Included in the constitutive relationship are the effects of pressure and temperature. The rheological behaviour of polymer melts is very complex. No usable constitutive equation has yet been developed that describes quantitatively all the flow phenomena involving polymer melts (112c). There are, however, constitutive equations that predict only certain aspects of polymer flow behaviour. The choice of constitutive equation depends on the problem at hand, and in this study, should be suitable for melt flow in extruder screw channels and dies.

Polymer melts are often referred to as viscoelastic fluids. Such a fluid behaves partly as an elastic solid and partly as a viscous liquid. The visoelasticity of fluids is often characterized by the dimensionless Deborah number (22, 76):

$$De = \frac{\lambda}{t} \tag{2.28}$$

where λ is the relaxation time or elastic memory effect of the fluid, and t is the residence time of the fluid in the process. A viscoelastic fluid behaves like a pure viscous liquid when the Deborah number is small and like an elastic solid when the Deborah number is large. The Deborah number for flow of polymer melts in extruders and dies is usually small[1], so it may be assumed that:

---

[1]The relaxation time for commercially important molten polymers at processing temperatures ranges from less than 10^{-2} s for polyesters to 1 to 10 s for polyethylenes. The residence time of the melt in the extruder flow channel is in the order of minutes, and several seconds for dies. Thus the Deborah number will usually be quite small (22).

(ℓ) polymer melts may be treated as inelastic viscous fluids.

A constitutive equation for an inelastic fluids relates the stress tensor $\bar{\bar{\tau}}$ to the rate of deformation tensor $\bar{\bar{\Delta}}$ which is defined as:

$$\bar{\bar{\Delta}} = \begin{bmatrix} 2\frac{\partial v_x}{\partial x} & \frac{\partial v_x}{\partial y} + \frac{\partial v_y}{\partial x} & \frac{\partial v_x}{\partial z} + \frac{\partial v_z}{\partial x} \\ \frac{\partial v_y}{\partial x} + \frac{\partial v_x}{\partial y} & 2\frac{\partial v_y}{\partial y} & \frac{\partial v_y}{\partial z} + \frac{\partial v_z}{\partial y} \\ \frac{\partial v_z}{\partial x} + \frac{\partial v_x}{\partial z} & \frac{\partial v_z}{\partial y} + \frac{\partial v_y}{\partial z} & 2\frac{\partial v_z}{\partial z} \end{bmatrix} \tag{2.29}$$

For polymer melt flow in extruder screw channels and dies, the power-law temperature dependent constitutive equation has been used extensively in the literature. One way of expressing such an equation is (30):

$$\bar{\bar{\tau}} = \eta\, \bar{\bar{\Delta}} \tag{2.30}$$

where the shear viscosity η is given by:

$$\eta = A\, e^{-B(T-T_o)} \left| \sqrt{\frac{I_2}{2}} \right|^{n-1} \tag{2.31}$$

A and B are empirical constants, n is the power-law index, and T_o is some convenient reference temperature. I_2 is the second invariant of the rate of deformation tensor $\bar{\bar{\Delta}}$, and is given by:

$$I_2 = \Delta_{ij}\,\Delta_{ij}$$

$$= 4\left[\left(\frac{\partial v_x}{\partial x}\right)^2 + \left(\frac{\partial v_y}{\partial y}\right)^2 + \left(\frac{\partial v_z}{\partial z}\right)^2\right] + 2\left[\left(\frac{\partial v_x}{\partial y} + \frac{\partial v_y}{\partial x}\right)^2 + \left(\frac{\partial v_x}{\partial z} + \frac{\partial v_z}{\partial x}\right)^2 + \left(\frac{\partial v_y}{\partial z} + \frac{\partial v_z}{\partial y}\right)^2\right] \quad (2.32)$$

Using the expressions for velocity in Eq. 2.19 and the lubrication approximation assumptions (g) and (i), Eqs. 2.30 to 2.32 reduce to the following:

$$\tau_{yx} = \eta\,\frac{\partial v_x}{\partial y} \quad (2.33)$$

$$\tau_{yz} = \eta\,\frac{\partial v_z}{\partial y} \quad (2.34)$$

$$\eta = A\,e^{-B(T-T_o)}\,\dot{\gamma}^{n-1} \quad (2.35)$$

where $\dot{\gamma} = \sqrt{\left(\frac{\partial v_x}{\partial y}\right)^2 + \left(\frac{\partial v_z}{\partial y}\right)^2}$

A typical logarithmic plot of viscosity versus shear rate for low-density polyethylene is shown in Fig. 2.9. The power-law equation (2.35) is represented by a straight line on this plot. A shortcoming of the power-law model is that at zero shear rate it predicts an infinite viscosity, whereas it can be seen in Fig. 2.9 that polymer melts tend to Newtonian behaviour at low shear rates as indicated by the decrease in slope of the viscosity curve. For flow situations where the shear rate reaches very low values or even a value of zero (as in the case of pressure flow at the centre of a tube), a certain error will be

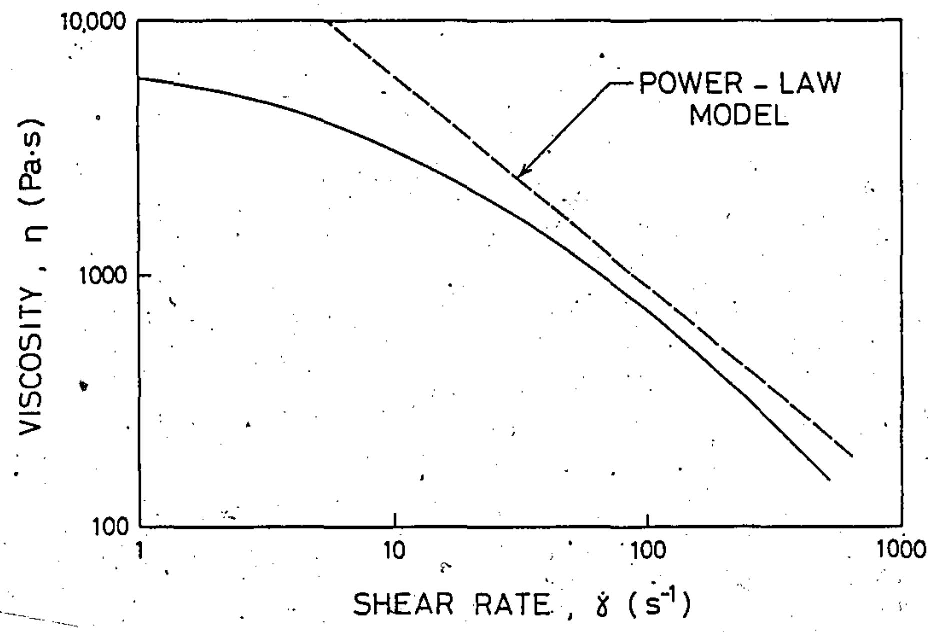

Fig. 2.9 Typical viscosity curve for low-density polyethylene as compared with the power-law model.

introduced in the flow rate calculations if the power-law equation is used. It can also be seen in Fig. 2.9 that the slope of the melt viscosity curve is not exactly constant even in the power-law region. The power-law index decreases with increasing shear rate. Thus, the power-law equation holds exactly only for limited ranges of shear rate for a given value of the power-law index n. A more general and accurate representation of the melt viscosity is given by the following shear rate and temperature dependent viscosity equation (114e):

$$\log \eta = a_0 + a_1 \log \dot{\gamma} + a_2 (\log \dot{\gamma})^2 + a_3 T + a_4 T^2 + a_5 T \log \dot{\gamma} \quad (2.36)$$

The empirical parameters a_0 to a_5 are obtained by fitting Eq. 2.36 to viscometric data covering a suitable range of shear rate and temperature using linear regression.

Finally, the shear viscosity of polymer melts is influenced somewhat by pressure. The pressure dependence of the viscosity may be given by (28a):

$$\eta = \eta_o \exp[\alpha(p-p_o)] \quad (2.37)$$

where η_o is the viscosity at reference pressure p_o, and α is the pressure coefficient of viscosity. The experimental determination of α is difficult, and as a result is rarely attempted. Semjonow (101) obtained values of α in the range 3.2 - 6.1 x 10^{-6} kPa^{-1} for polyethylenes using a rotational viscometer. For usual processing conditions ($\Delta p \approx$ 10,000 kPa), the change in viscosity will be of the order 3 to 6 per cent. Since other simplifications in the overall extruder model have a greater effect on the model predictions, it is assumed that the viscosity is independent of pressure.

2.4.3 Method of Solution

Given a suitable constitutive equation and appropriate boundary conditions for velocity, pressure and temperature, the simplified conservation equations can be solved numerically. An iterative implicit finite difference method (33a) has been used in this study to obtain velocity and temperature profiles and a pressure distribution for melt flow in the extruder screw channel and die. A brief description of the method will be given here. More detailed descriptions, including the finite difference approximations and equations, are located in Chaps. 5, 6 and 7.

A finite difference grid is superimposed on the flow field as illustrated in Fig. 2.10. Values of velocity, pressure and temperature, are calculated at the nodal points of the grid by replacing the derivatives in the conservation equations with the appropriate finite difference approximations, and then solving the resulting difference equations at each node. This can be done explicitly or implicitly. In the explicit method, the difference equations are solved one node at a time for all the nodes in the grid. In the implicit method, the equations for an entire column of nodes are solved simultaneously, and progress through the grid is made by "marching" downstream column by column.

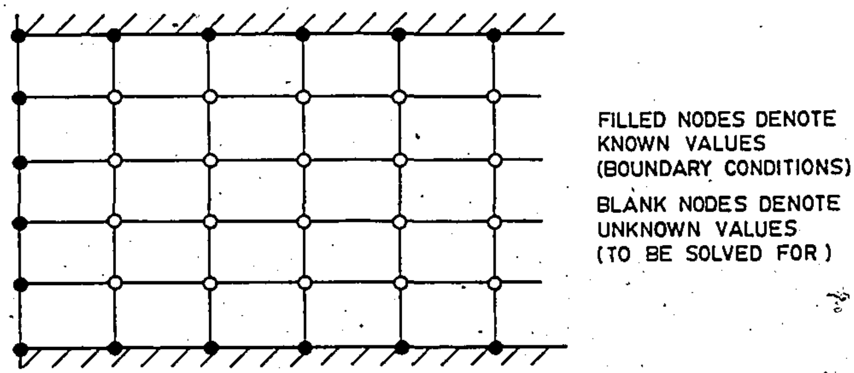

Fig. 2.10 Finite difference grid.

Examining the conservation equations (Eqs. 2.25 to 2.27) and constitutive equations (Eqs. 2.33, 2.34 and 2.36), we see that the x- and z- momentum equations each contain a viscosity term which is a function of temperature and shear rate, and that the energy equation contains a viscosity, velocity and velocity gradients in the x and z directions. As a consequence, these equations are coupled by velocity and temperature, and cannot be solved independently. It is, however, possible to iterate to a solution by repeatedly solving the equations in the order: (i) x- momentum equation, (ii) z- momentum equation and (iii) energy equation until the solution converges. For example, at a given column in the grid, the initial estimates of the velocity and temperature profiles along the column are obtained from the final profiles calculated in the preceding column. New v_x, v_z and T profiles are calculated and compared with the estimated profiles. If the changes are greater than a specified tolerance, all three profiles are recalculated. This process is repeated until the desired error tolerance is achieved. The most recently calculated profiles are always used as profile estimates in subsequent iterations, for example, to calculate viscosities, velocity gradients, etc. When the desired error tolerance has been attained, the profiles in the next column downstream are calculated. Thus the velocity and temperature profiles and the pressure distribution are calculated for the entire flow field.

In Sec. 2.4.1, it was stated that the simplified conservation equations should represent flow in two dimensions rather than three dimensions so that the computation time requirements for the numerical solution could be kept within reasonable limits. For the two-dimensional problem representing melt flow in an extruder screw channel, approximately 50,000 nodal points are utilized in a typical finite difference solution (100 in the y direction, 500 in the z direction). Due to the iterative nature of the method, this represents a substantial amount of computation on a digital computer[1]. If the conservation equations were to be solved in three dimensions (that is, if assumption (i) was eliminated), then an additional equation, the y-momentum equation, would have to be solved. The number of nodal points in the finite difference solution would increase by about 100 fold and the resulting computation time requirements would become prohibitive. For this reason, the melt flow problem is solved in only two dimensions.

2.4.4 Convergence, Stability and Step Size

Problems with convergence and stability arise from the substitution of finite difference approximations in the differential equations. By convergence, it is meant that the results of the finite difference method approach "true" or analytical (if they were to exist) values as the step sizes become infinitely small. By stability, it is meant that errors made at one stage of the calculations do not grow as the computations are continued, but instead damp out. These errors are due to round-off, the choice of a finite step size, and the use of a finite tolerance in the iteration procedure (33b).

[1]A typical program for the melt flow region in the extruder screw channel requires about 400 seconds on the CYBER 170/730 computer at McMaster University.

Convergence to the correct solution of the finite difference results can only be rigorously tested by comparison with an analytical solution. In simpler cases, stability criteria have been developed, such as for the solution of single linear partial differential equations (33b). However, in our case less rigorous techniques for testing convergence and stability have to be used since no analytical solutions have been developed, and the equations to be solved are too complex for stability criteria to be applicable.

A good indication of the convergence and stability of the finite difference results is the negligible change in results obtained when the step sizes in the finite difference grid are decreased. In selecting step sizes, it should be remembered that by using smaller step sizes, the cost of computing inceases. This increase can be significant when an iterative type of solution is used. There is also an upper limit of accuracy attainable by decreasing the step size. This occurs when computer round-off errors become larger than the errors due to finite step sizes. Such accuracy is usually not necessary in engineering design.

The above general guidelines were followed in selecting the appropriate step sizes for the finite difference programs in the present extruder model. The programs were tested by using various step sizes and step size ratios across and along the flow channel. In the present model, the results obtained are independent of step size within at least 3 significant digits.

2.5 Extrudate Swell

Polymer melts, primarily due to their viscoelastic behaviour, exhibit an increase in cross-sectional area whenever they emerge from a die, provided there is no subsequent drawdown. This phenomenon is usually called extrudate swell. Depending on the extrusion conditions, the die geometry and dimensions, and the rheological properties of the polymer, the extrudate swell ratio (ratio of extrudate diameter to die diameter in the case of a circular die) may range from 1.5 to 4.

It may be argued that four mechanisms are responsible for the phenomenon of extrudate swell from long dies: Newtonian swell, a sudden elastic recovery, an inelastic swell and finally stress relaxation. For short dies the swelling of the extrudate is also affected by the memory effect. Various models and theories have been developed for the prediction of extrudate swell, and are reviewed by Vlachopoulos (121).

Newtonian jets swell at low Reynolds numbers ($Re_D < 16$), with the maximum value being about 12%. This is due to streamline adjustments as the liquid emerges from an orifice into air and acquires a free surface. Using a finite element program, Tanner (116) solved the conservation of momentum equations for slow flow and predicted a swelling of 13%, which corresponds to earlier experimental observations. For large values of Re_D it is easy to show, by performing an overall mass and momentum balance (78b,121), that the liquid jet exhibits a 13% diameter contraction. Thus, for Newtonian jets the diameter ratio (jet diameter/die diameter) varies from 1.12 to 0.87 as shown in Fig. 2.11.

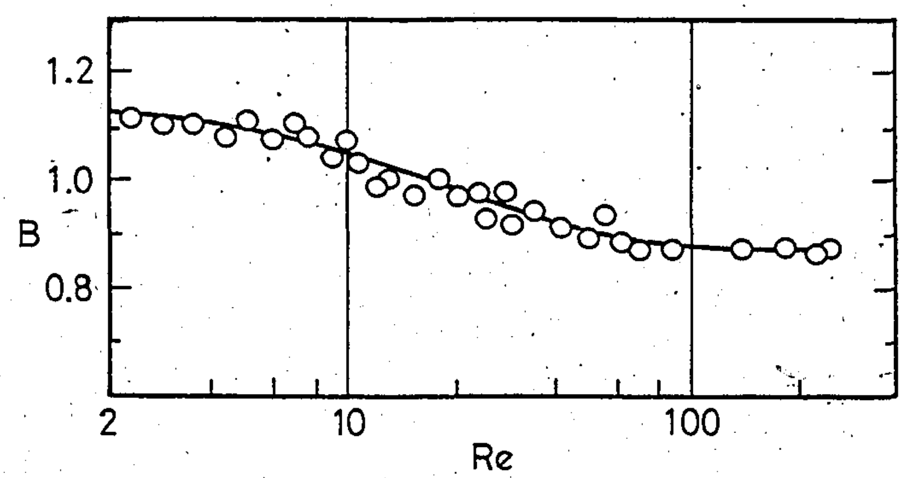

Fig. 2.11 Diameter ratio (B = d/D) for several Newtonian liquids extruded from a long capillary into air as a function of the Reynolds number (Re = $\rho VD/\mu$). (From Refs. (78b) and (79)).

In the extrusion of non-Newtonian viscoelastic fluids it is generally recognized that elasticity is the main cause of swelling. The principle parameter found in theories based on elastic recovery is the recoverable shear S_R. The recoverable shear is usually defined from Hooke's law:

$$S_R = \frac{\tau_{12}}{G} \tag{2.38}$$

where τ_{12} is the shear stress and G an elastic modulus. Experiments have shown (32) that for polymeric materials at low shear rates:

$$S_R = \frac{\tau_{11} - \tau_{22}}{2\tau_{12}} \tag{2.39}$$

where $\tau_{11} - \tau_{22}$ is the first normal stress difference.

The swelling of slow moving viscoelastic jets can be thought of as a three step process: a small Newtonian swelling, a sudden elastic recovery and further a swelling due to stress relaxation. The sequence of deformations of an imaginary fluid element as it enters the die, travels through and finally emerges from it, is shown in Fig. 2.12. In the die the fluid element is stretched out, and then upon exiting from the die it contracts and swells. It should be noted that the degree of swelling d/D depends on the die length to diameter ratio L/D. For short dies the fluid residence time is shorter than the fluid memory resulting in the tendency for the fluid to retain the shape it had in the reservoir. For sufficiently long dies the fluid memory fades completely and an asymptotic swelling ratio is reached as shown in Fig. 2.13.

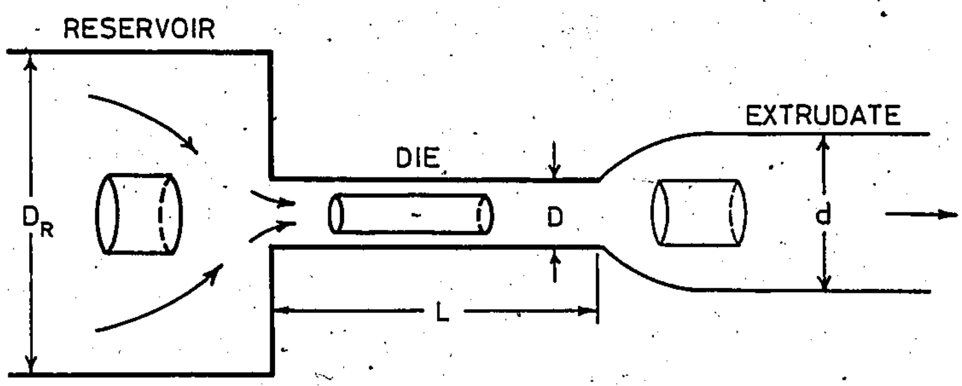

Fig. 2.12 Schematic representation of the sequence of deformations of a material element as it enters, travels through, and emerges from a die.

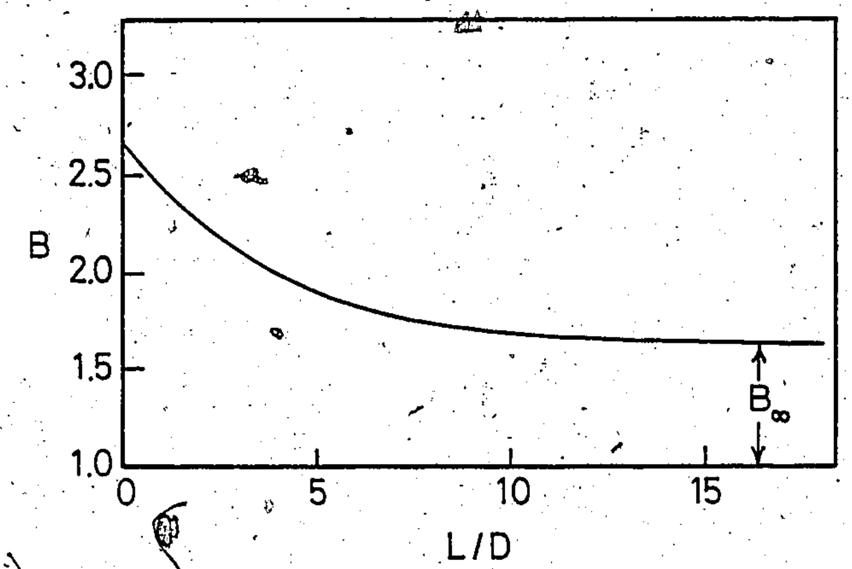

Fig. 2.13 Variation of extrudate swell (B=d/D) as a function of L/D ratio (die length/die diameter).

Although many models have been developed for the swelling of viscoelastic fluids (121), only a few will be considered for the development of a predictive model in Chap. 8.

The two remaining causes of extrudate swell are inelastic swell and stress relaxation. Tanner (92, 117) developed the inelastic theory to explain the swelling phenomenon of Newtonian fluids with temperature dependent viscosity. The extrudate was considered as consisting of two layers: the outer layer in tension and the inner core in compression. It was assumed that the swelling is caused by an increased resistance to deformation of elongated filaments near the extrudate surface. Tanner predicted the swelling for power-law, variable-viscosity Newtonian, second-order and Maxwell fluids. This inelastic theory is new, and at present there are no reliable estimates as to how much it contributes to the overall swelling.

The swelling due to stress relaxation varies significantly for different thermoplastic melts. For polystyrene melts it is small, usually of the order of a few percent. Polyethylene and polypropylene melts may exhibit a substantial swelling due to stress relaxation. Presently there is no theory to estimate this effect. However, when extrudates are rapidly frozen, as is the case in most extrusion processes, the contribution of stress relaxation to the total swelling is negligible.

In summary, extrudate swelling of polymer melts is due to (i) Newtonian swell, (ii) sudden recovery of stored elastic energy, (iii) inelastic swell, and (iv) subsequent stress relaxation. Despite the large number of investigations on extrudate swell, there is still no clear understanding of the interrelations between the molecular, rheological and geometrical parameters of polymers and their effect on extrudate swell. A fully predictive theory has not yet been developed. However, a predictive equation for extrudate swell at the extruder die exit based on theory and extrudate swell measurements on a viscometer is developed in Chap. 8.

CHAPTER 3

PARTICLE FLOW IN THE FEED HOPPER

In plasticating extruders the polymer in the form of solid pellets or powder is fed to the screw channel through the feed hopper, usually by gravity. On account of the stresses in the solid particles, there exists a pressure distribution in the feed hopper. The objective of modelling solids flow in the feed hopper is to determine the pressure distribution, and in particular, to obtain the base pressure of the hopper which is required later in the solids conveying model.

The pressure distribution in hoppers containing particulate solids was analyzed by Janssen (45) in 1895 and more recently by Walker (123). Their derivations have been summarized and presented by Tadmor and Gogos (112d) with application to extruder feed hoppers.

If the material in the feed hopper was a liquid, the base pressure would be the hydrostatic pressure p given as:

$$p = \frac{\rho g H}{g_c} \tag{3.1}$$

where ρ is the density of the liquid, g the acceleration due to gravity, g_c the gravitational constant, and H the height of the column of liquid. Such a linear relationship is, however, not valid for a column of particulate solids contained in a vertical bin. The base pressure is not proportional to the height of the column because of the friction between the solids and the wall. Janssen (45) derived an equation for the pressure profile for solids in a vertical bin. The following assumptions were made:

(1) The vertical compressive stress (pressure) is constant over any horizontal plane.

(2) The ratio of horizontal and vertical stresses is constant and independent of depth.

(3) The bulk density of the solid is constant.

(4) The particles at the wall are in incipient slip condition.

(5) The particles do not adhere to the wall.

Consider a vertical column of solids with cross-sectional area A and "wetted" perimeter C. A force balance over a differential element of thickness dh, as shown in Fig. 3.1, consists of the following components:

(1) A force in the upward direction due to pressure p at height h:

$$F_1 = pA \tag{3.2}$$

(2) A force in the downward direction due to pressure p+dp at height h+dh:

$$F_2 = (p + dp)A \tag{3.3}$$

(3) Weight of the element:

$$F_3 = A \, \rho_{bulk} \frac{g}{g_c} \, dh \tag{3.4}$$

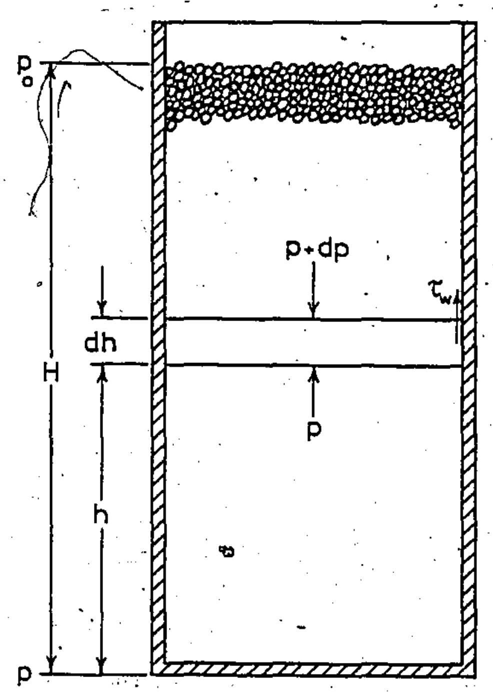

Fig. 3.1 Vertical bin filled with particulate solids.

(4) A frictional force at the side walls supporting the element in the upward direction:

$$F_4 = \tau_w \, C \, dh \tag{3.5}$$

The shear stress at the wall τ_w is defined as:

$$\tau_w = f'_w \, \sigma_w \tag{3.6}$$

where f'_w is the coefficient of friction at the wall and σ_w is the normal stress at the wall (also horizontal pressure or compressive stress in the horizontal direction). According to Janssen, σ_w is proportional but somewhat smaller than the vertical pressure p. Therefore:

$$K = \frac{\sigma_w}{p}$$

$$\simeq \frac{\sigma_{min}}{\sigma_{max}} = \frac{1 - \sin \delta}{1 + \sin \delta} \tag{3.7}$$

where K is the ratio of compressive stress in the horizontal direction to compressive stress in the vertical direction, and δ is the effective angle of friction. Thus, Eq. 3.5 may be rewritten as:

$$F_4 = f'_w \, KpC \, dh \tag{3.8}$$

Assuming that the differential slice is in equilibrium, the force balance may be written by combining Eqs. 3.2, 3.3, 3.4 and 3.8 as follows:

$$A\,\rho_{bulk}\frac{g}{g_c}\,dh + (p + dp)A = f'_w\,Kp\,C\,dh + pA \qquad (3.9)$$

Weight of element	Pressure force acting downward	Frictional force supporting the element at the side walls	Pressure force acting upward

or

$$\frac{dp}{dh} - f'_w\frac{KC}{A}\,p = -\rho_{bulk}\frac{g}{g_c} \qquad (3.10)$$

Equation 3.10 may be integrated to obtain the following expression for the base pressure:

$$p = p_o\exp\left(-f'_w\frac{CKH}{A}\right) + A\frac{\rho_{bulk}\,g}{f'_w\,CKg_c}\left[1 - \exp\left(-f'_w\frac{CKH}{A}\right)\right] \qquad (3.11)$$

where p_o is the pressure at the top of the bin and H is the height of the bin. For a square vertical hopper the base pressure is given by:

$$p = p_o\exp\left(-4\,f'_w\frac{KH}{W}\right) + \frac{\rho_{bulk}\,gW}{4\,f'_w\,Kg_c}\left[1 - \exp\left(-4\,f'_w\frac{KH}{W}\right)\right] \qquad (3.12)$$

where $K = \dfrac{1 - \sin\,\delta}{1 - \sin\,\delta}$

W = width of the hopper

A more rigorous derivation of the pressure distribution in vertical bins was presented by Walker (123) assuming stress equilibrium in the solids. The results are slightly different from those predicted by using Eq. 3.12. The base pressure again for a square hopper is given by:

$$p = p_o\exp\left(-\frac{4BD^*H}{W}\right) + \frac{\rho_{bulk}\,gW}{4BD^*g_c}\left[1 - \exp\left(-\frac{4BD^*H}{W}\right)\right] \qquad (3.13)$$

where BD* replaces $f'_w K$ in Eq. 3.12. D* is defined as a distribution factor relating the average vertical stress with the vertical stress near the wall, and can be assumed to be unity as a first approximation. B, the ratio of the shear to the normal stress at the wall, is given by:

$$B = \frac{\sin \delta \sin \kappa_o}{1 - \sin \delta \cos \kappa_o} \tag{3.14}$$

$$\text{where} \quad \kappa_o = \beta_w + \arcsin \left(\frac{\sin \beta_w}{\sin \delta}\right) \quad , \quad \arcsin > \frac{\pi}{2} \tag{3.15}$$

$$\beta_w = \arctan (f'_w) \tag{3.16}$$

The pressure distribution in convergent hoppers has also been analyzed by Walker (123). The base pressure for a convergent hopper with square cross-section as shown in Fig. 3.2, is given by:

$$p = \left(\frac{h_o}{H_o}\right)^{\psi} p_o + \frac{\rho_{bulk}\, g h_o}{(\psi-1)\, g_c} \left[1 - \left(\frac{h_o}{H_o}\right)^{\psi-1}\right] \quad , \quad \psi \neq 1 \tag{3.17}$$

$$p = \left(\frac{h_o}{H_o}\right) p_o + \frac{\rho_{bulk}\, g h_o}{g_c} \ln\left(\frac{H_o}{h_o}\right) \quad , \quad \psi = 1 \tag{3.18}$$

$$\text{where} \quad \psi = \frac{2B'D^*}{\tan \alpha} \tag{3.19}$$

2α = hopper angle

$$B' = \frac{\sin \delta \sin (2\alpha + \kappa_o)}{1 - \sin \delta \cos (2\alpha + \kappa_o)} \tag{3.20}$$

$$\kappa_o = \beta_w + \arcsin \left(\frac{\sin \beta_w}{\sin \delta}\right) \quad , \quad \arcsin < \frac{\pi}{2} \tag{3.21}$$

$$\beta_w = \arctan (f'_w) \tag{3.22}$$

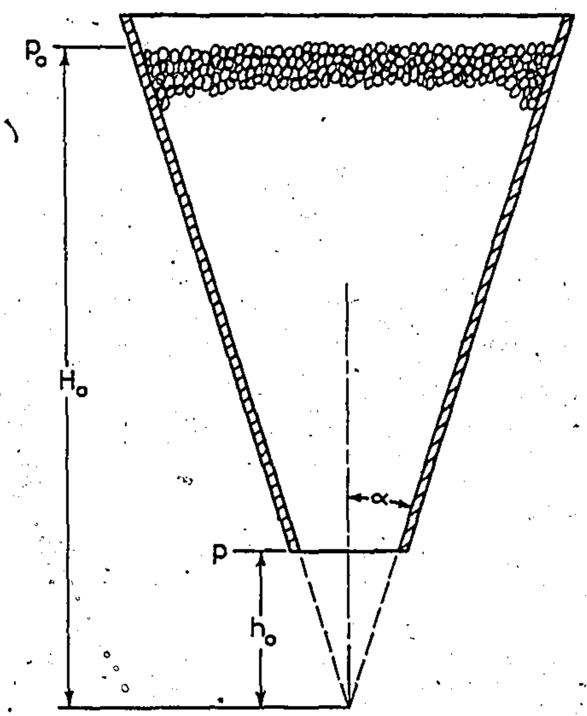

Fig. 3.2 Schematic representation of a convergent hopper.

Summary of Feed Hopper Equations

The equations for the vertical and convergent sections of a feed hopper with square cross-section are as follows:

Vertical Section:

$$p = p_o \exp(-\frac{4BD^*H}{W}) + \frac{\rho_{bulk}}{4BD^*}\frac{gW}{g_c}[1 - \exp(-\frac{4BD^*H}{W})] \qquad (3.23)$$

$$\text{where } B = \frac{\sin\delta \sin\kappa_o}{1 - \sin\delta\cos\kappa_o}$$

$$\kappa_o = \beta_w + \arcsin(\frac{\sin\beta_w}{\sin\delta}) \quad , \quad \arcsin > \frac{\pi}{2}$$

$$\beta_w = \arctan(f'_w)$$

Convergent Section:

$$p = (\frac{h_o}{H_o})^{\psi} p_o + \frac{\rho_{bulk}}{(\psi-1)}\frac{gh_o}{g_c}[1 - (\frac{h_o}{H_o})^{\psi-1}] \quad , \quad \psi \neq 1 \qquad (3.24)$$

$$p = (\frac{h_o}{H_o})p_o + \frac{\rho_{bulk}\, gh_o}{g_c}\ln(\frac{H_o}{h_o}) \quad , \quad \psi = 1 \qquad (3.25)$$

$$\text{where} \quad \psi = \frac{2B'D^*}{\tan\alpha}$$

$$B' = \frac{\sin\delta\sin(2\alpha + \kappa_o)}{1 - \sin\delta\cos(2\alpha + \kappa_o)}$$

$$\kappa_o = \beta_w + \arcsin(\frac{\sin\beta_w}{\sin\delta}) \quad , \quad \arcsin < \frac{\pi}{2}$$

$$\beta_w = \arctan(f'_w)$$

Equations 3.23 and 3.24 or 3.25 may be used in combination when calculating the base pressure in a feed hopper as shown in Fig. 3.3. A typical pressure at the base of such a hopper filled with low- or high-density polyethylene pellets is 1 kPa which indicates that virtually all of the weight of the polymer solids is supported by the hopper walls.

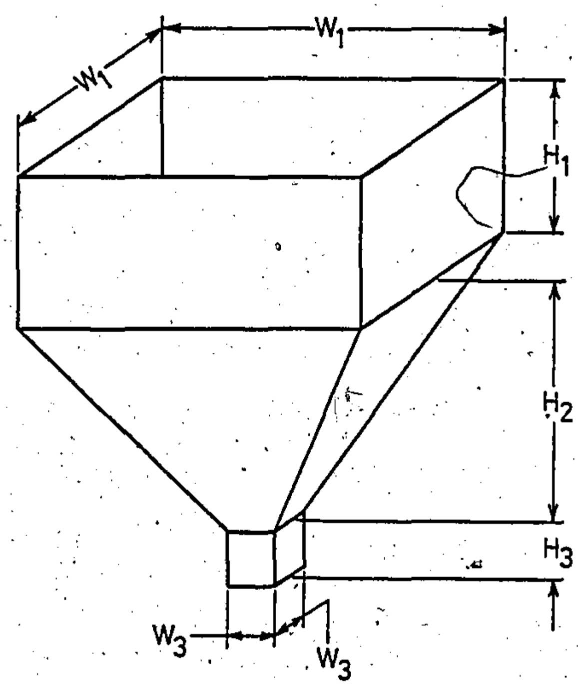

Fig. 3.3 Schematic diagram of a feed hopper with square cross-section. Hopper dimensions are given in App. G.1.

CHAPTER 4

SOLIDS FLOW IN THE EXTRUDER SCREW CHANNEL

The first of three functional zones in the screw extruder is the solids conveying zone. In this zone the solid polymer granules are conveyed down the screw channel by a drag induced mechanism, that is flow due to the frictional drag of the barrel and screw surfaces on the solid granules. The solids conveying zone occupies only a few turns of the screw channel, extending from the feed hopper to a down channel position where a significant amount of melting at the barrel surface has occurred. The objective of modelling solids flow is to calculate the down channel pressure profile in the solids conveying zone.

4.1 Literature Survey of Solids Conveying Models

In comparison with the large number of studies reported in the literature on melting and melt flow in screw extruders, relatively little attention has been given to the solids conveying zone. The development of theoretical models for the solids conveying zone has been reviewed and analyzed by Tadmor and Klein (114f), Tadmor and Gogos (112e), and Fenner (30). Most of the published analyses for this region consider the solids as a continuum, and thus ignore the particulate nature of the polymer feed. Even in this case solutions are difficult to obtain. Consequently many analyses contain further simplifications such as treating the material movement as plug flow in the screw channel temperature profile in the solids conveying zone together with a strongly interacting pressure profile. A subsequent model was developed by Kacir and Tadmor (47) to predict the pressure profile in the delay zone, i.e. the region where the melt exists at the barrel surface after the termination of the solids conveying but before the start of the steady state melting mechanism. Finally, Chung (18) presented a modification of the Darnell and Mol model in which the solid plug is entirely surrounded by a melt film. In this case the solids conveying mechanism is due to viscous drag.

All solids conveying models require an estimate of the inlet pressure. In most cases, this pressure is assumed to be equal to the base pressure of the feed hopper. This approach neglects the transition between the gravitational flow in the hopper and the drag induced flow of the solid polymer in the screw channel. It does, however, relate the hopper design and loading to the extruder performance. Another approach to this problem, proposed by Lovegrove and Williams (58,59,60), assumes that the initial pressure in the solids conveying zone is entirely the result of local gravitational and centrifugal forces. The base pressure of the feed hopper is disregarded as contributing to the initial pressure. This is a reasonable assumption since tests have shown that pressures can be generated in the solids conveying zone even with no head of material in the hopper. As of the present time, no mathematical models have been developed which relate both the head of solids in the feed hopper and the gravitational and centrifugal forces in the solid plug to the development of pressure in the solids conveying zone.

4.2 Development of a Solids Conveying Model

The mathematical model developed below for the solids conveying zone is similar to the one described by Tadmor and Klein (114f). It is a slight variation of the model developed by Darnell and Mol (20). The following assumptions are made:

(1) The solid polymer in the screw channel behaves as a continuum.

(2) The solid contacts all sides of the channel, i.e. the barrel surface, root of the screw, and screw flights.

(3) The channel depth is constant.

(4) The flight clearance is neglected.

(5) The polymer flows with constant velocity as a solid plug (plug flow).

(6) The pressure p is a function of down channel direction only.

(7) The dynamic coefficients of friction f_b and f_s between the solid polymer and the barrel and screw surfaces are independent of pressure and temperature.

(8) The gravitational and centrifugal forces are neglected.

(9) The density changes in the solid plug are neglected.

Flow Rate

The mass flow rate of the solid plug is given by:

$$G = V_{p\ell} \, \rho_{bulk} \int_{R_s}^{R_b} \left(2\pi r - \frac{e}{\sin\theta}\right) dr \qquad (4.1)$$

where $V_{p\ell}$ is the unknown velocity component of the plug in the axial direction (see Fig. 4.1). Integrating Eq. 4.1 and assuming an average helix angle $\bar{\theta}$, we obtain:

$$G = V_{p\ell}\,\rho_{bulk}\left[\frac{\pi}{4}(D_b^2 - D_s^2) - \frac{eH}{\sin\bar{\theta}}\right] \qquad (4.2)$$

or

$$V_{p\ell} = \frac{G/\rho_{bulk}}{\frac{\pi}{4}(D_b^2 - D_s^2) - \frac{eH}{\sin\bar{\theta}}} \qquad (4.3)$$

The value of $V_{p\ell}$ is needed to calculate the angle ϕ between the velocities of the solid plug and barrel surface (see Fig. 4.2). The angle ϕ, required in the force and torque balance on the solid plug described later in this section, is given by:

$$\tan\phi = \frac{V_{p\ell}}{V_b - V_{p\ell}/\tan\theta_b} \qquad (4.4)$$

Rearranging Eq. 4.4 and substituting for the tangential velocity of the barrel ($V_b = \pi D_b N$), we obtain:

$$V_{p\ell} = \pi D_b N \frac{\tan\phi\tan\theta_b}{\tan\phi + \tan\theta_b} \qquad (4.5)$$

Substituting Eq. 4.5 into Eq. 4.3, substituting for $D_b^2 - D_s^2 = 4H(D_b - H)$, writing in terms of the average channel width, $\bar{W} = \pi(D_b - H)\sin\bar{\theta} - e$ and rearranging, we obtain:

$$\tan\phi = \frac{\tan\theta_b}{\frac{\pi^2 N}{G}\rho_{bulk} H D_b (D_b - H)\tan\theta_b\left(\frac{\bar{W}}{\bar{W}+e}\right) - 1} \qquad (4.6)$$

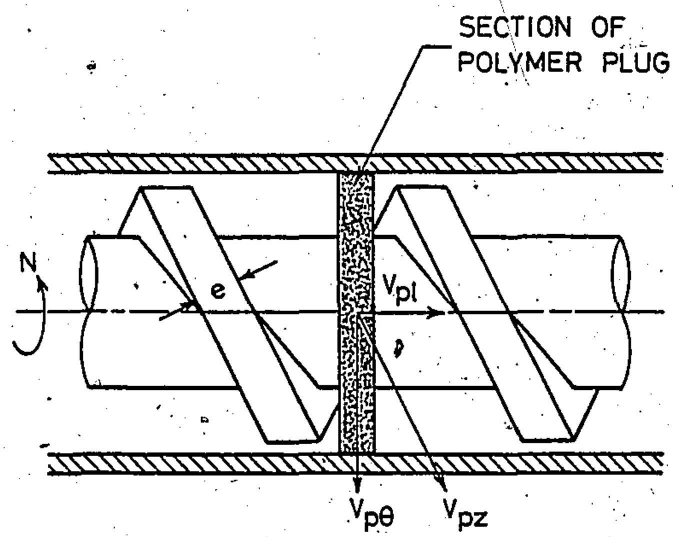

Fig. 4.1 Differential element of solid plug. Velocities are measured relative to the screw. $V_{p\theta}$ and V_{pz} are measured at the barrel surface. $V_{p\ell}$ is independent of channel depth.

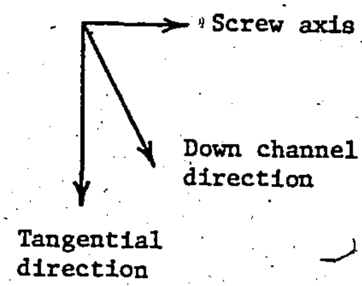

$$\tan\phi = \frac{V_{pl}}{V_b - V_{pl}/\tan\theta_b}$$

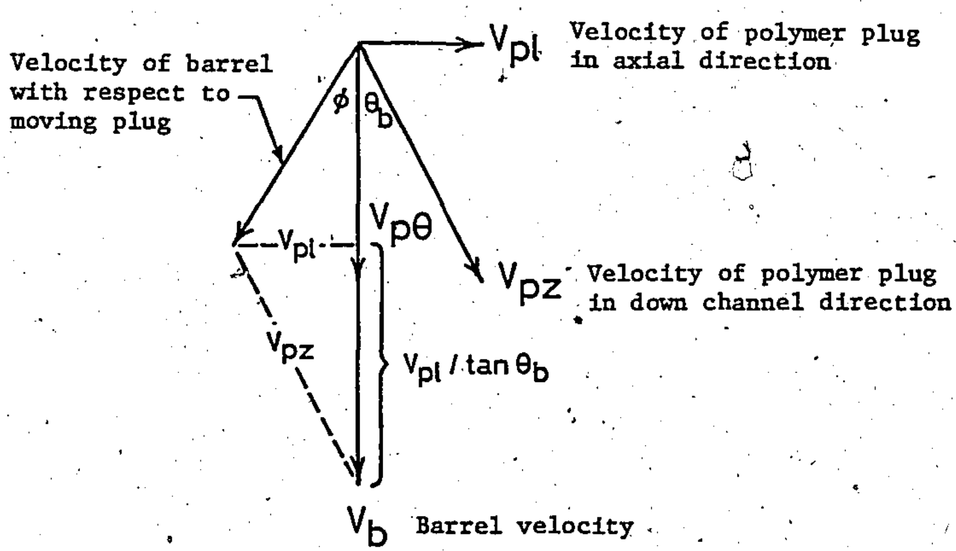

Fig. 4.2 Velocity vector diagram for calculating angle ϕ, the angle between the velocities of the solid plug and the barrel.

Thus, the angle ϕ is expressed as a function of the mass flow rate G, screw speed N and the dimensions of the screw channel.

Force and Torque Balance

The pressure profile in the down channel direction may be determined by performing a force and torque balance on the solid plug. Fig. 4.3 shows the forces acting on the plug when the screw is stationary and the barrel is rotating. F_1 is the frictional force between the barrel surface and the plug. The force F_1, proportional to the pressure p in the plug and in the direction of angle ϕ, is given by:

$$F_1 = f_b \, p \, W_b \, dz_b \tag{4.7}$$

Since it is assumed that the pressure gradient is only a function of down channel distance, the net force $F_6 - F_2$ due to pressure drop is:

$$F_6 - F_2 = H\overline{W} \, dp \tag{4.8}$$

F_7 and F_8 are the forces that the flights exert on the plug, and they are normal to the flights. F_8 is due to the pressure p and equals:

$$F_8 = p \, H \, d\bar{z} \tag{4.9}$$

F_7 is composed of two terms: one equal to F_8 and the other, an additional normal force F^* on the pushing flight, to balance the other forces. The magnitude of F^* is unknown.

$$F_7 = p \, H \, d\bar{z} + F^* \tag{4.10}$$

$$F_7 - F_8 = F^* \tag{4.11}$$

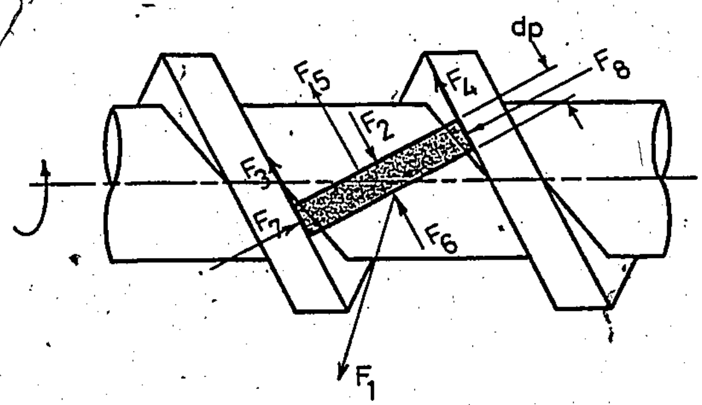

Fig. 4.3 Forces acting on the solid plug.

F_3, F_4 and F_5 are the frictional forces between the two flights and the root of the screw and the solid plug:

$$F_3 = f_s\, F_7 = (p\, H\, d\bar{z} + F^*)\, f_s \tag{4.12}$$

$$F_4 = f_s\, F_8 = p\, H\, d\bar{z}\, f_s \tag{4.13}$$

$$F_5 = p\, W_s\, dz_s\, f_s \tag{4.14}$$

Since the solid plug has a constant axial velocity component $V_{p\ell}$, the sum of all the forces in the axial direction should be zero:

$$F_{1\ell} + (F_6 - F_2)_\ell - (F_7 - F_8)_\ell + F_{3\ell} + F_{4\ell} + F_{5\ell} = 0 \tag{4.15}$$

where $F_{1\ell} = f_b\, p\, W_b\, dz_b \sin\phi$

$$(F_6 - F_2)_\ell = H\bar{W}\, dp \sin\bar{\theta}$$

$$(F_7 - F_8)_\ell = F^* \cos\bar{\theta}$$

$$F_{3\ell} = (p\, H\, d\bar{z} + F^*)\, f_s \sin\bar{\theta}$$

$$F_{4\ell} = p\, H\, d\bar{z}\, f_s \sin\bar{\theta}$$

$$F_{5\ell} = p\, W_s\, dz_s\, f_s \sin\theta_s$$

The following relationships can be obtained given that $d\ell = dz_b \sin\theta_b = d\bar{z}\sin\bar{\theta} = dz_s \sin\theta_s$ (refer to Fig. 2.3):

$$\frac{d\bar{z}}{dz_b} = \frac{\sin\theta_b}{\sin\bar{\theta}} \tag{4.16}$$

$$\frac{dz_s}{dz_b} = \frac{\sin\,\theta_b}{\sin\,\theta_s} \tag{4.17}$$

Substituting Eqs. 4.16 and 4.17 into Eq. 4.15 and rearranging gives:

$$p\,dz_b\,(f_b\,W_b\,\sin\,\phi + 2H\,f_s\,\sin\,\theta_b + W_s\,f_s\,\sin\,\theta_b)$$

$$+ H\overline{W}\,\sin\,\overline{\theta}\,dp - F^*\,(\cos\,\overline{\theta} - f_s\,\sin\,\overline{\theta}) = 0 \tag{4.18}$$

Defining:

$$A_1 \equiv f_b\,W_b\,\sin\,\phi + 2H\,f_s\,\sin\,\theta_b + W_s\,f_s\,\sin\,\theta_b \tag{4.19}$$

$$A_2 \equiv H\overline{W}\,\sin\,\overline{\theta} \tag{4.20}$$

and introducing them into Eq. 4.18 gives:

$$F^* = \frac{A_1\,p\,dz_b + A_2\,dp}{\cos\,\overline{\theta} - f_s\,\sin\,\overline{\theta}} \tag{4.21}$$

A torque balance about the axis of the screw on the solid plug can be made in a similar way. Since the plug has a constant angular velocity $V_{p\theta}$ at the barrel surface, the sum of all the torques should equal zero:

$$F_{1\theta}\,\frac{D_b}{2} - (F_6 - F_2)_\theta\,\frac{\overline{D}}{2} - (F_7 - F_8)_\theta\,\frac{\overline{D}}{2}$$

$$- F_{3\theta}\,\frac{\overline{D}}{2} - F_{4\theta}\,\frac{\overline{D}}{2} - F_{5\theta}\,\frac{D_s}{2} = 0 \tag{4.22}$$

where

$$F_{1\theta} = f_b\, p\, W_b\, dz_b \cos\phi$$

$$(F_6 - F_2)_\theta = H\overline{W}\, dp \cos\overline{\theta}$$

$$(F_7 - F_8)_\theta = F^* \sin\overline{\theta}$$

$$F_{3\theta} = (pH\, d\overline{z} + F^*)\, f_s \cos\overline{\theta}$$

$$F_{4\theta} = pH\, d\overline{z}\, f_s \cos\overline{\theta}$$

$$F_{5\theta} = p\, W_s\, dz_s\, f_s \cos\theta_s$$

Once again, introducing Eqs. 4.16 and 4.17 into Eq. 4.22 and rearranging gives:

$$pD_b dz_b\left(f_b W_b \cos\phi - 2Hf_s \frac{\overline{D}}{D_b} \sin\theta_b \operatorname{cotan}\overline{\theta} - W_s f_s \frac{D_s}{D_b} \sin\theta_b \operatorname{cotan}\theta_s\right)$$

$$- H\overline{W}\overline{D} \cos\overline{\theta}\, dp - F^*\, \overline{D}\, (\sin\overline{\theta} + f_s \cos\overline{\theta}) = 0 \qquad (4.23)$$

Defining:

$$B_1 \equiv f_b W_b \cos\phi - 2Hf_s \frac{\overline{D}}{D_b} \sin\theta_b \operatorname{cotan}\overline{\theta} - W_s f_s \frac{D_s}{D_b} \sin\theta_b \operatorname{cotan}\theta_s \qquad (4.24)$$

$$B_2 \equiv H\overline{W} \frac{\overline{D}}{D_b} \cos\overline{\theta} \qquad (4.25)$$

and substituting into Eq. 4.23 gives:

$$F^* = \frac{B_1\, p\, dz_b - B_2\, dp}{\frac{\overline{D}}{D_b}(\sin\overline{\theta} + f_s \cos\overline{\theta})} \qquad (4.26)$$

Combining Eqs. 4.21 and 4.26, F* from the force and torque balances is eliminated:

$$\frac{A_1\ p\ dz_b + A_2\ dp}{\cos\overline{\theta} - f_s \sin\overline{\theta}} = \frac{B_1\ p\ dz_b - B_2\ dp}{\frac{\overline{D}}{D_b}(\sin\overline{\theta} + f_s \cos\overline{\theta})} \qquad (4.27)$$

Defining:

$$K \equiv \frac{\overline{D}}{D_b}\ \frac{\sin\overline{\theta} + f_s \cos\overline{\theta}}{\cos\overline{\theta} - f_s \sin\overline{\theta}} \qquad (4.28)$$

and substituting it into Eq. 4.27 gives:

$$A_1\ K\ p\ dz_b + A_2\ K\ dp = B_1\ p\ dz_b - B_2\ dp \qquad (4.29)$$

or

$$\frac{dp}{dz_b} = \frac{(A_1\ K - B_1)\ p}{-(A_2\ K + B_2)} \qquad (4.30)$$

Integrating Eq. 4.30 from $z_b = 0$ where $p = p_o$ to a down channel distance z_b, the pressure p at z_b is given by:

$$\ln\frac{p}{p_o} = -\frac{(A_1\ K - B_1)}{(A_2\ K + B_2)}\ z_b \qquad (4.31)$$

or

$$p = p_o\ e^{-\lambda z_b} \qquad (4.32)$$

where $$\lambda = \frac{A_1\ K - B_1}{A_2\ K + B_2}$$

λ is a function of the screw dimensions, screw speed N, mass flow rate G, bulk density ρ_{bulk} and the dynamic coefficients of friction f_b and f_s

between the polymer solid and the barrel and screw surfaces. Equation 4.32 indicates an exponential rise of pressure along the solids conveying zone. If z_b is taken to be the length of the solids conveying zone in the down channel direction, then p is the pressure at the end of this zone given that p_o is the pressure at the base of the feed hopper. It should be noted that the pressure at the end of the solids conveying zone is usually of the order 1000 - 3000 kPa as compared to a maximum pressure of 10,000 - 20,000 kPa further down the screw channel.

4.3 Length of the Solids Conveying Zone - The Delay Zone

To calculate the pressure at the end of the solids conveying zone using Eq. 4.32, a down channel length of this section is needed. However, there is no sharp transition point in the screw channel at which the solids conveying zone ends and the melting and melt conveying zones begin. In Sec. 4.1, it was stated that there exists a transition or "delay" zone between the two zones. In the present model, it is assumed that the solids conveying zone extends to the end of the delay zone.

The delay zone starts at the down channel location where a film of polymer melt is first formed at the barrel surface (either due to barrel heating or frictional heat generation) and ends at the point where a melt pool first appears at the rear flight (for more details on the melting mechanism, see Sec. 2.3). The conveying mechanism in the delay zone is considered to be one of viscous drag at the barrel surface and frictional drag at the screw root and flight surfaces. There is no reliable mathematical model available to predict the length of the delay zone, but Tadmor and Klein (114g) have presented an empirical correlation, shown in Fig. 4.4, which is based on limited experimental data. The delay in melting based on this correlation is given by:

$$N_{delay} = \frac{0.008}{\psi} \tag{4.33}$$

where N is the number of turns of the screw and ψ is related to the melting rate at the beginning of the melting zone. For a non-Newtonian fluid, the dimensionless parameter ψ is given by (see Sec. 5.2.2, Eq. 5.74):

$$\psi = \frac{V_{bx}\ \rho_m\ \delta\ H_o}{2G} \tag{4.34}$$

where V_{bx} is the cross channel component of the barrel velocity, ρ_m the polymer melt density, δ the thickness of the melt film adjacent to the barrel at the beginning of the melting zone, H_o the channel depth at the beginning of the melting zone and G the mass flow rate of the polymer in the screw channel. For a 1 1/2 inch diameter screw extruder, the delay zone occupies approximately 1 screw turn as compared to a total screw length of 24 turns.

Since the solids flow is assumed to be isothermal in the present model, there is no direct way of predicting the down channel distance at which the polymer adjacent to the barrel reaches its melting point (which coincides with the start of the delay zone). Therefore, it is

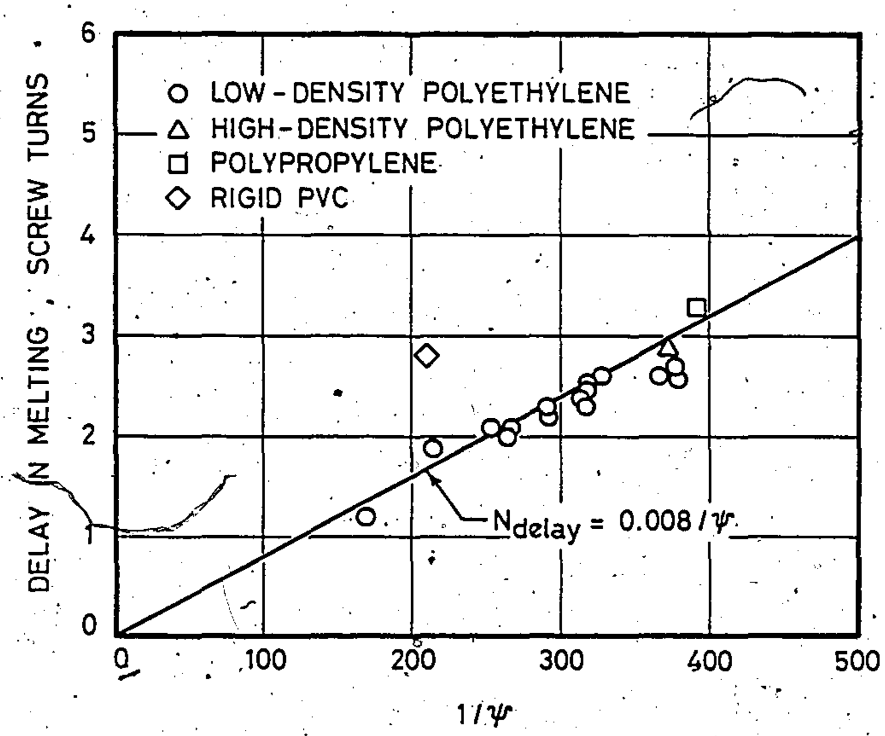

Fig. 4.4 Delay in melting expressed in screw turns versus dimensionless group $1/\psi$. (From Ref. (114g))

assumed that the beginning of the delay zone corresponds to the location of the first heater band on the extruder barrel (regardless of the extruder operating conditions or type of polymer used). Another assumption considered is that no differentiation is made between the solids conveying mechanism in the solids conveying and delay zones, that is, it is assumed that the frictional drag mechanism at the barrel surface continues to the end of the delay zone. This is the basis for allowing the delay zone to be included in the solids conveying zone, as was stated above. Thus, the length of the solids conveying zone $z_{b,t}$ may be calculated as follows:

$$N_t = N_o + N_{delay} \tag{4.35}$$

$$z_{b,t} = N_t \left(\frac{L}{\sin \theta_b}\right) \tag{4.36}$$

where N_o is the number of screw turns between the feed hopper opening and the first barrel heater band, and L is the screw lead.

4.4 Summary of the Solids Flow Equations

For the present solids conveying model, we assume that the solid polymer is isothermal and travels as a solid plug with a constant velocity. The stress distribution is assumed to be isotropic, that is the pressure varies only in the down channel direction. At the end of the solids conveying zone (including the delay zone), the pressure is given by:

$$p = p_o \, e^{-\lambda z_{b,t}} \tag{4.37}$$

where $\lambda = \dfrac{A_1 K - B_1}{A_2 K + B_1}$

$$A_1 = f_b W_b \sin\phi + 2H f_s \sin\theta_b + W_s f_s \sin\theta_b$$

$$A_2 = H\overline{W} \sin\overline{\theta}$$

$$B_1 = f_b W_b \cos\phi - 2H f_s \frac{\overline{D}}{D_b} \sin\theta_b \operatorname{cotan}\overline{\theta} - W_s f_s \frac{D_s}{D_b} \sin\theta_b \operatorname{cotan}\theta_s$$

$$B_2 = H\overline{W} \frac{\overline{D}}{D_b} \cos\overline{\theta}$$

$$K = \frac{\overline{D}}{D_b} \frac{\sin\overline{\theta} + f_s \cos\overline{\theta}}{\cos\overline{\theta} - f_s \sin\overline{\theta}}$$

$$\tan\phi = \frac{\tan\theta_b}{\frac{\pi^2 N}{G} \rho_{bulk} H D_b (D_b - H) \tan\theta_b \left(\frac{\overline{W}}{\overline{W}+e}\right) - 1}$$

and where p_o is the base pressure in the feed hopper and $z_{b,t}$ is the length of the solids conveying zone in the down channel direction. $z_{b,t}$ may be written as:

$$z_{b,t} = (N_o + N_{delay}) \frac{L}{\sin\theta_b} \tag{4.38}$$

where $N_{delay} = \dfrac{0.008}{\psi}$

$$\psi = \frac{V_{bx}\, \rho_m\, \delta\, H_o}{2G}$$

and where N_o is the distance between the feed hopper opening and the first barrel heater band in screw turns. Typical pressure profiles in the solids conveying zone of a 1 1/2 inch (38 mm) diameter screw extruder are shown in Fig. 4.5 and 4.6 (see App. G.2 for polymer properties and processing conditions). In Fig. 4.5, pressure profiles are presented for three frequencies of screw rotation: 40, 60 and 80 rpm. Although the pressure at a given down channel position does not vary significantly with screw speed, it can be seen that the length of the solids conveying zone increases appreciably with increasing screw speed. This is due to a longer delay zone at higher screw speeds. Thus, for increasing screw speeds the length of the solids conveying zone increases and the pressure at the end of the solids conveying zone is correspondingly higher. Pressure profiles at a given screw speed are shown in Fig. 4.6 for three values of f_b, the dynamic coefficient of friction between the polymer solid and the barrel surface. It can be seen that the pressure profiles are very sensitive to the choice of f_b (and likewise, f_s). The sensitivity of the overall extruder performance to changes in f_b and f_s is discussed in more detail in Sec. 12.2.

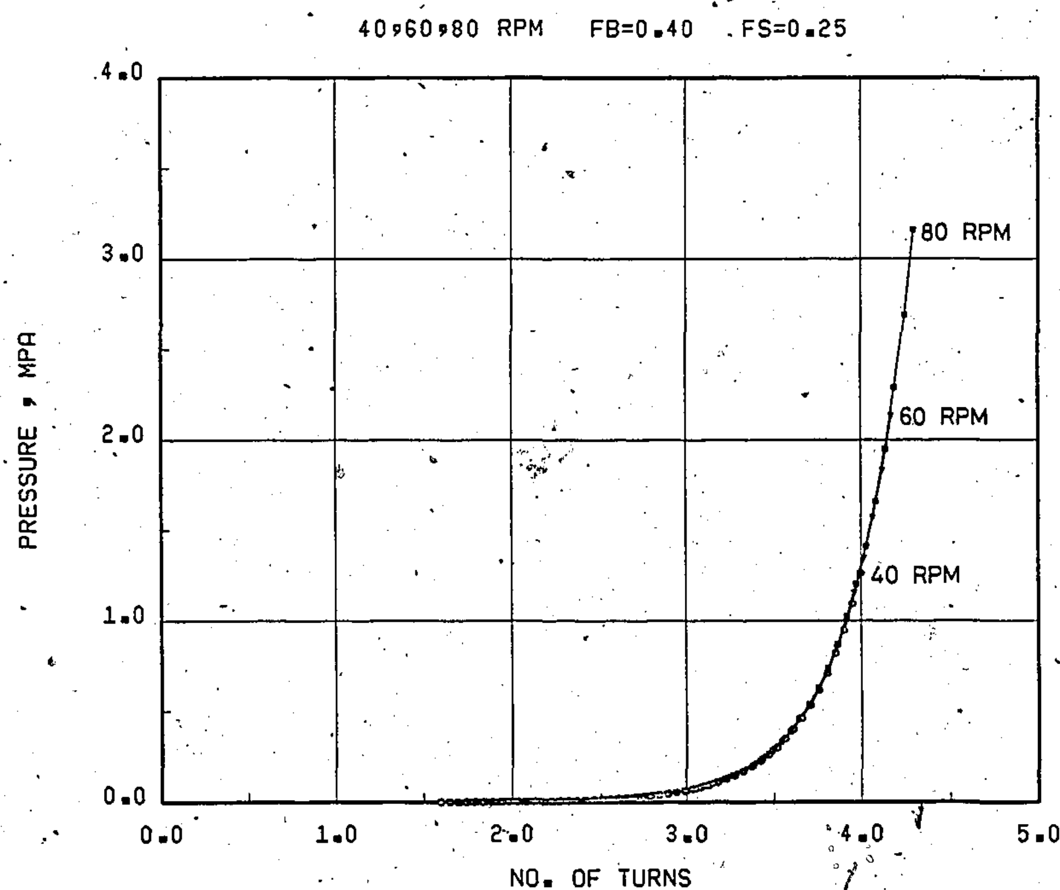

Fig. 4.5 Development of down channel pressure profiles in the solids conveying zone (including the delay zone). Data for the polymer properties, screw channel dimensions and extruder operating conditions are given in App. G.2.

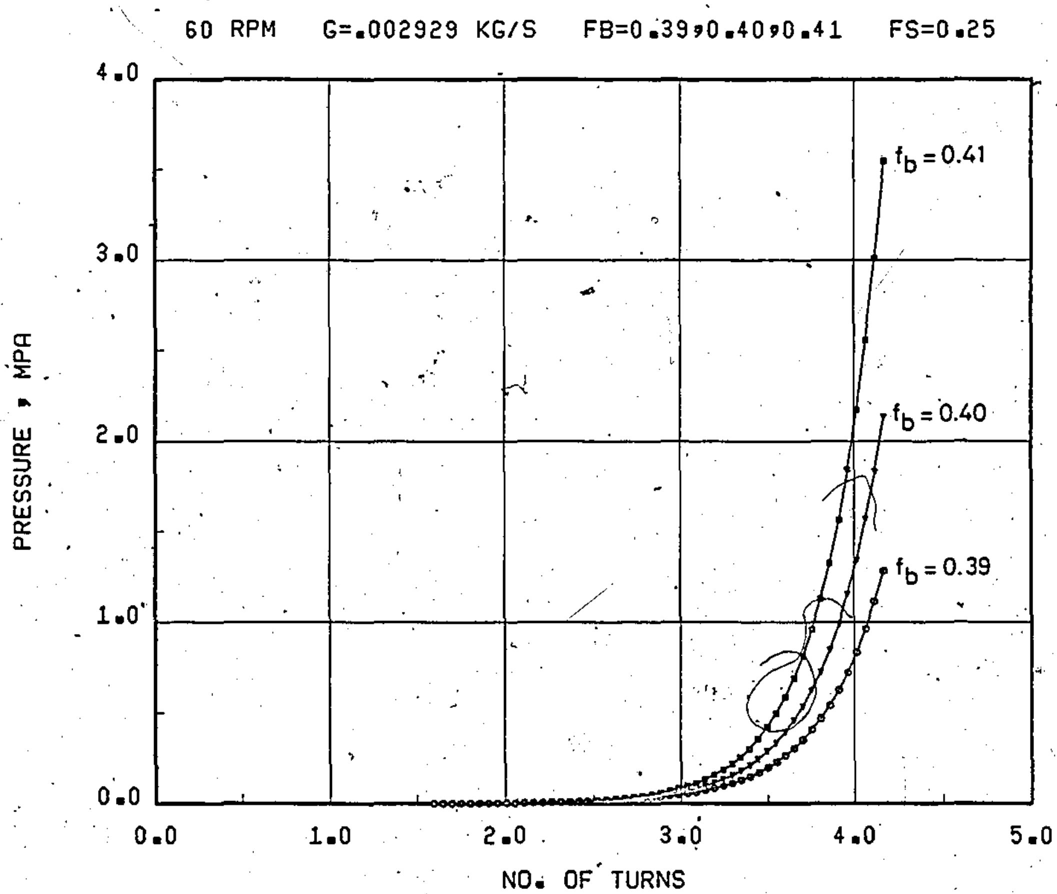

Fig. 4.6 Development of down channel pressure profiles in the solids conveying zone (including the delay zone). Data for the polymer properties, screw channel dimensions and extruder operating conditions are given in App. G.2.

CHAPTER 5

MELTING IN THE EXTRUDER SCREW CHANNEL

In plasticating extruders, the polymer solids are melted before being pumped through the die. The energy for melting originates primarily from two sources: heat conducted from the heated barrel and viscous dissipation due to shearing in a thin film of melt between the barrel surface and solid bed. The objective of modelling the melting process is to predict the rate of melting and to obtain the solid bed profile in the screw channel, that is the width profile of the solid bed as a function of the down channel direction.

5.1 Literature Survey of Melting Models

A model to describe the melting mechanism in plasticating extruders was first developed by Tadmor (107) on the basis of visual analyses (see Sec. 2.3 for description of melting experiments). This model, known as the Tadmor melting model, forms the basis for many of the more recent melting models reported in the literature. An idealized cross-section of the screw channel in the melting zone is shown in Fig. 5.1 (and in less detail, Fig. 5.2(a)). It is assumed that the down channel bed velocity is constant and that the thickness of the upper melt film between the solid bed and barrel surface is constant over the width of the solid bed at a given down channel position. The flow in the upper melt film is treated as fully-developed isothermal Newtonian

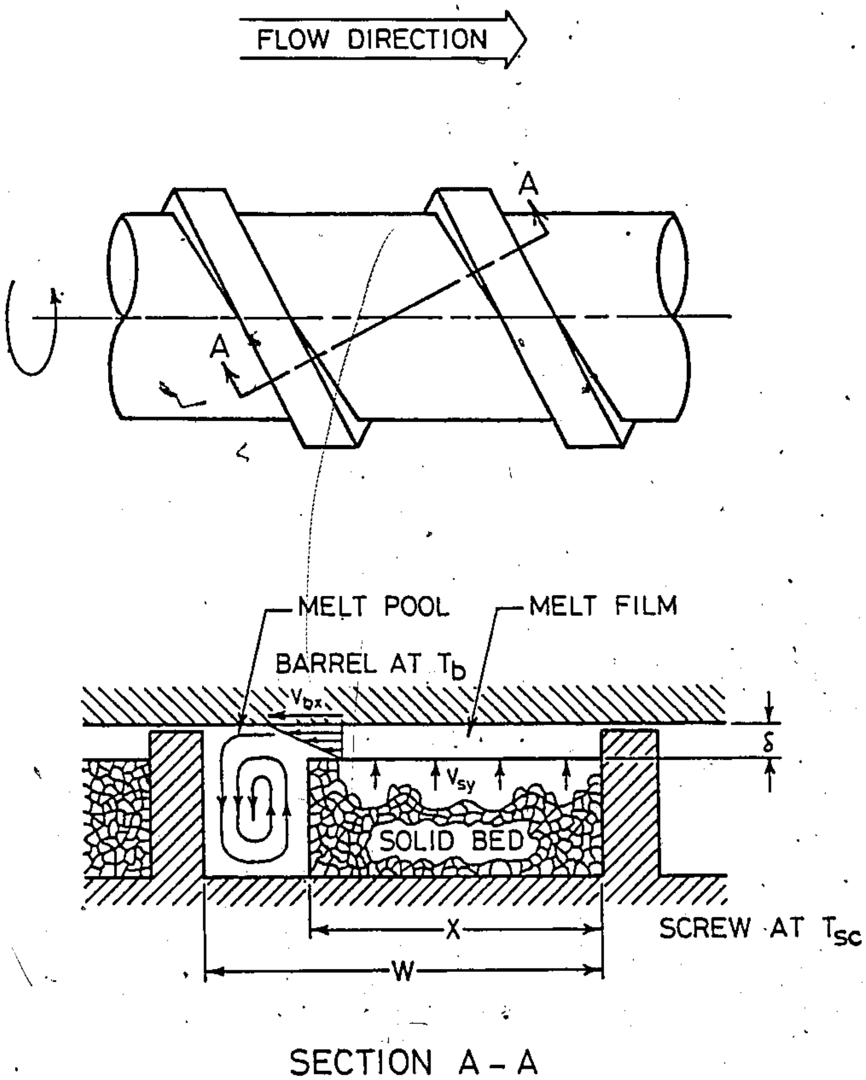

Fig. 5.1 Idealized cross-section of the extruder screw channel in the melting zone (Tadmor melting model). V_{bx} is the cross channel component of the barrel velocity, and V_{sy} is the velocity of the solid bed moving into the solid-melt interface.

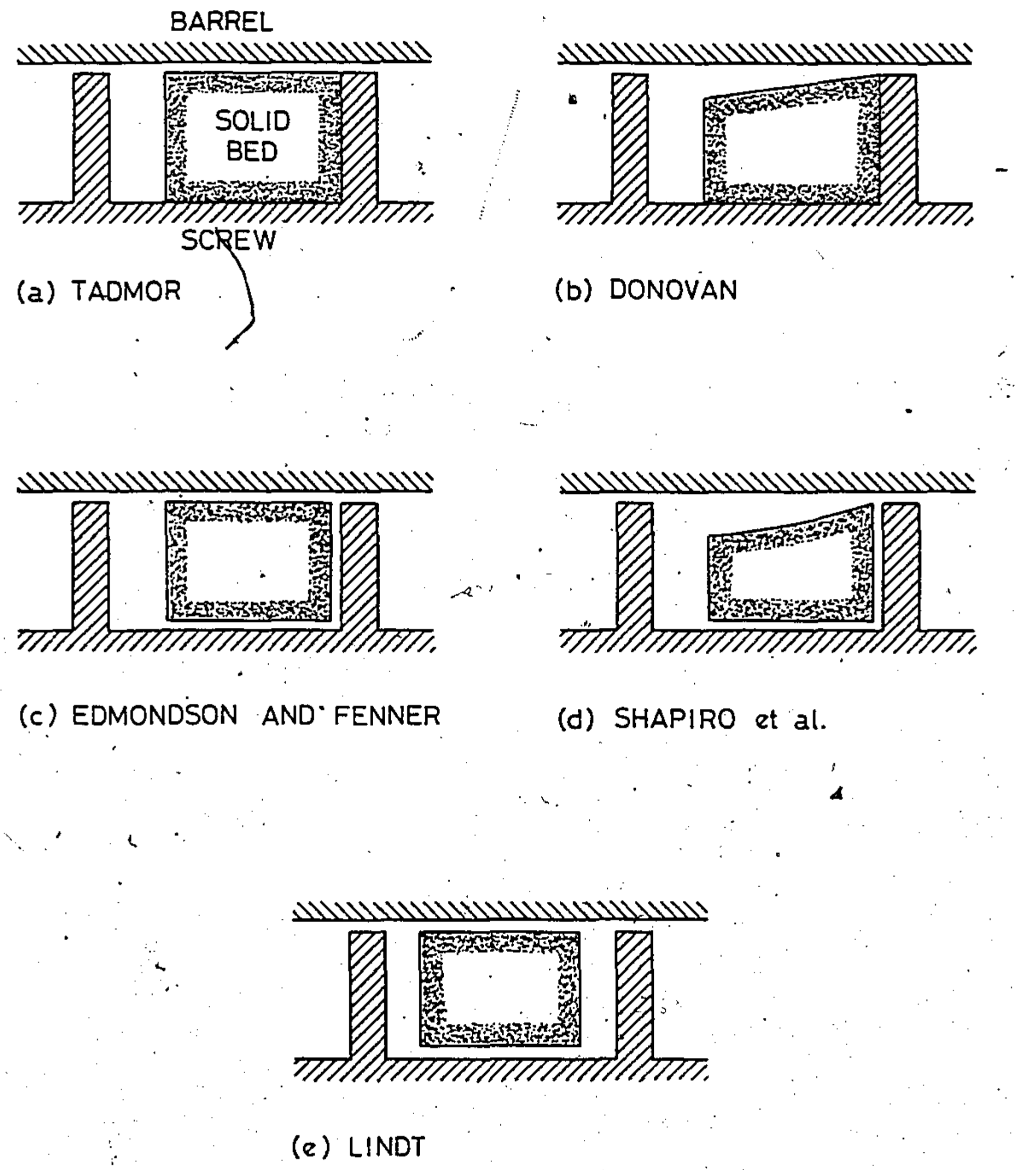

Fig. 5.2 Schematic cross-sections of the extruder screw channel for various melting models.

drag flow. In subsequent treatments Tadmor et al. (111) replaced the isothermal Newtonian flow in the melt film by nonisothermal non-Newtonian flow. It is assumed that melting occurs only at the upper melt film - solid bed interface. Mass and energy balances on the melt film and solid bed are involved in obtaining relationships for the rate of melting and the solid bed profile. The Tadmor melting model is described in more detail in Sec. 5.2.1 in conjunction with the development of the present melting model used in this study.

In the span of five years, several publications by Tadmor et al. appeared that dealt with the development and utilization of the Tadmor melting model. Tadmor's original paper (107) describes an isothermal, Newtonian melting model together with a limited amount of experimental verification. In companion papers, Marshall and Klein (67) presented results of further melting experiments, and Klein and Marshall (51) discussed the development of a computer program for a plasticating screw extruder which incorporated the Tadmor melting model. A subsequent paper by Tadmor, Duvdevani and Klein (111) introduces a modified melting model representing nonisothermal, non-Newtonian flow in the melt film, and compares the theoretical results and experimental data in detail. In a book by Klein and Marshall (52) on computer programs for plastics engineers, an algorithm for the extruder program is described utilizing the modified melting model. Correction factors for channel curvature and an allowance for flow in the flight clearance are presented as additional modifications in the book by Tadmor and Klein (114h). Finally, Tadmor and Klein (113,114i) used the latest version of their melting model to examine the effects of various design and operating parameter changes in the extruder, including flow rate, screw speed, barrel temperature, channel dimensions, helix angle and flight clearance.

Various refinements have been added to the Tadmor melting model by other researchers. Chung (17) treated the solid bed as being of finite thickness and the screw surface as being thermally insulated for the purpose of analyzing the temperature profile in the bed. The solid bed in Tadmor's model was assumed to be semi-infinite in thickness, thus avoiding the need to specify temperature boundary conditions at the screw. Hinrichs and Lilleleht (41) derived correction factors for screw channel curvature, allowed for flow in the flight clearance, and used a more sophisticated method for calculating the solid bed velocity. Vermeulen et al. (120) developed a model in which the thickness of the upper melt film is allowed to vary with cross channel position, x. This is a good assumption because, as polymer entrains in the film and flows toward the melt pool, it is expected to grow in thickness. The model is similar to Tadmor's in all other aspects, except that the viscous dissipation term is omitted from the energy equation used for the upper melt film.

Much more significant changes to Tadmor's model were introduced by Donavan (23). An idealized cross-section of his version of the melting model is shown in Fig. 5.2(b). Flow of the solid bed is represented by a solid bed acceleration parameter which permits bed acceleration in the tapered section of the screw channel. Also down channel thermal convection in the solid bed is included. This allows for gradual heating of the bulk of the bed. The thickness of the melt film was assumed to vary linearly across the width of the bed, as shown in Fig. 5.2(b), to allow for entrainment of the melt in the film. Finally an exact solution was obtained analytically for the coupled momentum and energy equations given a temperature and shear rate dependent power-law constitutive relation. The theoretical results were compared to new experimental data for low-density polyethylene, PVC, ABS and polypropylene.

Edmondson and Fenner (26,27) and Shapiro et al. (37,102,103) developed melting models in which the down channel bed velocity is treated as an unknown function of down channel distance, z (in previous models, this velocity is considered as a prescribed function of z, and in most cases as a constant). The solid bed experiences a substantial amount of deformation as its width is decreased, while at the same time most of the melting occurs at the upper melt film interface. There may also be elongation in the z direction. Consequently a stress analysis was performed on the solid bed by both Edmondson and Fenner, and Shapiro et al. Idealized cross-sections are shown in Figs. 5.2(c) and 5.2(d) for their melting models. It should be noted that in both cases a thin film of melt was included between the screw and flight surfaces and the solid bed. The primary difference between the two models is that Edmondson and Fenner chose to assume the upper melt film thickness to vary in the down channel direction while Shapiro et al. took the other alternative and chose it to vary in the cross channel direction. In both models, flow in the melt film is treated as being fully developed and obeying the temperature and shear rate dependent power-law constitutive relation. Flow in the melt pool is treated as being isothermal and Newtonian. Edmondson and Fenner compared their theoretical results with experimental data for low-density polyethylene granules and powder, plasticized PVC and polypropylene. No experimental comparisons were made by Shapiro et al.

Finally, a dynamic melting model was developed by Lindt (56) for extruders operating at autogenous[1] conditions. This model differs from all others in that a significant accumulation of melt in the films surrounding the solid bed is considered. As shown in Fig. 5.2(e), the thickness of the melt film is substantially greater than in the other models. Again fully developed flow in the melt film is assumed using a temperature and shear rate dependent power-law constitutive relation. The velocity of the solid bed is, however, treated as constant. Experimental data are obtained for polypropylene processed in a 90 mm diameter extruder.

5.2 Development of a Melting Model

Tadmor's melting model has been used as the basis for the development of the present melting model in this thesis. To describe

---

[1] An autogenous extruder is one which operates without barrel heating during steady state operation. Naturally, barrel heating is required at start up. Much larger pressure gradients are present in the melting zone of autogeneous extruders than in conventional extruders.

the present model, Tadmor's melting model will be treated first in detail.

5.2.1 The Tadmor Newtonian Melting Model

The basic assumptions in the Tadmor Newtonian melting model are (114j):

(1) The melting process is a steady state mechanism.

(2) The melting region consists of three distinct regions: a melt pool, a film of molten polymer, and a solid bed with sharp boundaries at each interface (see Fig. 5.1).

(3) Conceptually the screw channel is unwound and is described by a Cartesian coordinate system.

(4) The solid bed is a homogeneous, isotropic continuum with a constant down channel velocity V_{sz}.

(5) Significant melting only occurs at the solid bed - melt film interface near the barrel surface.

(6) To maintain steady state melting, the solid bed moves at a constant velocity V_{sy} into the interface.

(7) For heat transfer analysis the solid bed is assumed to have an infinite depth (y direction).

(8) The thickness of the melt film δ is constant across the cross section of the bed, but varies in the down channel direction z.

(9) For momentum and heat transfer analysis in the melt film, it is assumed that the film is confined between two infinite parallel plates.

(10) Flow in the melt film is assumed to be pure drag flow of a Newtonian fluid (later to be replaced by the power-law constitutive relation).

(11) The polymer has a sharp melting temperature T_{melt} and an associated latent heat of fusion λ.

(12) The polymer solid and melt have constant physical properties: heat capacities Cp_s and Cp_m, densities ρ_s and ρ_m, and thermal conductivities k_s and k_m.

Assuming a stationary screw and a rotating barrel, the barrel surface moves at a tangential velocity V_b which can also be expressed as:

$$V_b = \pi N D_b \tag{5.1}$$

where N is the frequency of screw rotation and D_b is the diameter of the barrel. The velocity may be broken up into two components: V_{bx} in the cross channel direction perpendicular to the flights, and V_{bz} in the down channel direction. These components are:

$$V_{bx} = V_b \sin \theta_b \tag{5.2}$$

$$V_{bz} = V_b \cos \theta_b \tag{5.3}$$

where θ_b is the helix angle at the barrel surface. The temperature of the barrel T_b is constant at a particular location in the extruder, but can be a specified function of the down channel direction. The temperature at the solid bed - melt film interface is T_{melt}, and the temperature of the solid bed far away from the interface is T_s (not to be confused with the screw temperature, T_{sc}). If the solid is not preheated, then T_s will be at room temperature. The width of the screw channel is designated as $\overline{W}$ (corresponding to W as discussed in Sec. 2.1) and that of the solid bed as X. At the beginning of melting X=W, and upon its completion X=0. The function X/W(z) represents the solid bed profile and is dependent upon the rate of melting of the polymer at incremental points in the down channel direction.

To obtain relationships for the rate of melting and the solid bed profile, mass and energy balances must be performed on the melt film and solid bed. For this analysis, consider an incremental element of the solid bed and melt film having length Δz, and width X as shown in Fig. 5.3. First an energy balance is conducted across the melt film - solid bed interface. For heat transfer analysis in the melt film, consider the melt flowing between two infinitely wide parallel plates, with the lower being stationary at T_{melt}, and the upper plate at T_b and moving at a velocity V_j. Define the barrel velocity relative to the solid bed as (see Fig. 5.3(a)):

$$\overline{V}_j = \overline{V}_b - \overline{V}_{sz} \tag{5.4}$$

where

$$|V_j|^2 = |V_b|^2 + |V_{sz}|^2 - 2|V_b||V_{sz}| \cos \theta_b$$

The velocity of the melt relative to the solid bed (for pure drag flow) is given by:

$$v_j(y) = V_j \frac{y}{\delta} \tag{5.5}$$

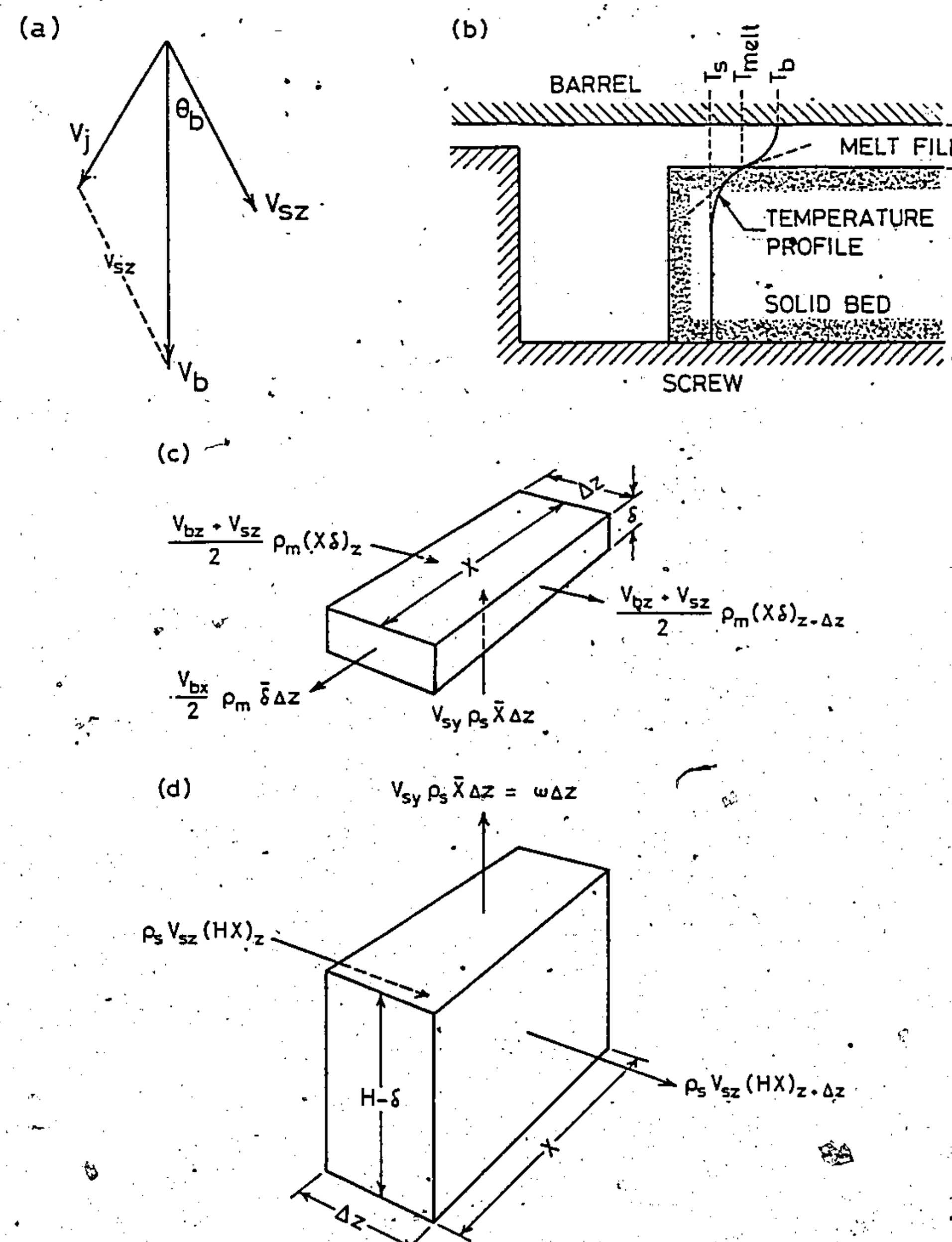

Fig. 5.3 Various aspects of the Tadmor melting model. (a) Barrel velocity with respect to down channel solid bed velocity. (b) Heat balance at solid-melt interface. (c) Mass balance on melt film. (d) Mass balance on solid bed.

The energy equation for the melt film, neglecting convection, can be written as:

$$k_m \frac{d^2T}{dy^2} + \mu\left(\frac{dv_j}{dy}\right)^2 = 0 \tag{5.6}$$

where
$$T = T_{melt} \text{ at } y = 0$$
$$T = T_b \quad \text{ at } y = \delta$$

After substituting for v_j from Eq. 5.5, integrating Eq. 5.6 twice and including the boundary conditions, the following fully developed temperature profile in the melt film is obtained:

$$T = \mu \frac{V_j^2}{2k_m}\left(\frac{y}{\delta} - \frac{y^2}{\delta^2}\right) + (T_b - T_{melt})\left(\frac{y}{\delta}\right) + T_{melt} \tag{5.7}$$

The heat flux at the interface is given by:

$$(q_y)_1 = - k_m \left(\frac{dT}{dy}\right)_{y=0}$$
$$= \frac{-[\mu \frac{V_j^2}{2} + k_m (T_b - T_{melt})]}{\delta} \tag{5.8}$$

Next, the temperature profile in the solid bed is determined. The energy equation is given by:

$$\rho_s \, Cp_s \, V_{sy} \frac{dT}{dy} = k_s \frac{d^2T}{dy^2} \tag{5.9}$$

where $T = T_{melt}$ at $y = 0$

$T = T_s$ at $y = -\infty$

Integrating Eq. 5.9 and including the boundary conditions gives the following temperature profile in the solid bed:

$$T = (T_{melt} - T_s) \exp\left[\frac{V_{sy}\, \rho_s\, Cp_s\, y}{k_s}\right] + T_s \tag{5.10}$$

Heat flux at the interface for the solid side is given by:

$$(q_y)_2 = -k_s\left(\frac{dT}{dy}\right)_{y=0}$$

$$= -\rho_s\, Cp_s\, (T_{melt} - T_s)\, V_{sy} \tag{5.11}$$

The rate of melting per unit interface area is obtained from the following heat balance at the interface (see Fig. 5.3(b)):

$$\begin{bmatrix}\text{Rate of accumulation}\\ \text{or}\\ \text{Rate of melting per}\\ \text{unit area times heat}\\ \text{of fusion}\end{bmatrix} = \begin{bmatrix}\text{Heat flux}\\ \text{into}\\ \text{interface}\end{bmatrix} - \begin{bmatrix}\text{Heat flux}\\ \text{out of}\\ \text{interface}\end{bmatrix}$$

$$= (q_y)_2 - (q_y)_1 \tag{5.12}$$

Substituting Eqs. 5.8 and 5.12 into the above balance and defining the rate of melting as $V_{sy}\, \rho_s$, gives:

$$V_{sy}\, \rho_s\, \lambda = -\rho_s\, Cp_s\, (T_{melt} - T_s)\, V_{sy} + \frac{[\mu \frac{V_j^2}{2} + k_m\, (T_b - T_{melt})]}{\delta} \tag{5.13}$$

or
$$V_{sy} = \frac{[\mu \frac{V_j^2}{2} + k_m (T_b - T_{melt})]}{[\rho_s Cp_s (T_{melt} - T_s) + \rho_s \lambda]\delta} \tag{5.14}$$

where λ is the heat of fusion of the polymer. Eq. 5.14 contains two unknowns, V_{sy} and δ.

A second relationship between V_{sy} and δ may be obtained by performing a mass balance over the melt film for a down channel increment Δz (see Fig. 5.3(c)). The various contributions to the mass balance are:

$$\begin{bmatrix}\text{Mass flow rate}\\ \text{into increment}\end{bmatrix} = \frac{(V_{bz} + V_{sz})}{2} \rho_m (X\delta)\Big|_z \tag{5.15}$$

$$\begin{bmatrix}\text{Mass flow rate}\\ \text{out of increment}\end{bmatrix} = \frac{(V_{bz} + V_{sz})}{2} \rho_m (X\delta)\Big|_{z+\Delta z} \tag{5.16}$$

$$\begin{bmatrix}\text{Mass flow rate}\\ \text{entering through}\\ \text{interface by}\\ \text{melting}\end{bmatrix} = V_{sy} \rho_s (\bar{X} \Delta z) \tag{5.17}$$

$$\begin{bmatrix}\text{Mass flow rate}\\ \text{exiting to melt}\\ \text{pool}\end{bmatrix} = \frac{V_{bx}}{2} \rho_m (\bar{\delta} \Delta z) \tag{5.18}$$

where $\bar{X}$ is the average solid bed width, and $\bar{\delta}$ is the average film thickness in the increment. Combining Eqs. 5.15 to 5.18, the mass balance is given by:

$$\left(\frac{V_{bz} + V_{sz}}{2}\right) \rho_m [(X\delta)_z - (X\delta)_{z+\Delta z}] + V_{sy} \rho_s \bar{X} \Delta z - \frac{V_{bx}}{2} \rho_m \bar{\delta} \Delta z = 0 \tag{5.19}$$

Dividing Eq. 5.19 by Δz and taking the limit as $\Delta z \to 0$, we obtain:

$$\left(\frac{V_{bz} + V_{sz}}{2}\right) \rho_m \frac{d(X\delta)}{dz} + V_{sy} \rho_s X - \frac{V_{bx}}{2} \rho_m \delta = 0 \tag{5.20}$$

Since

$$\left(\frac{V_{bz} + V_{sz}}{2}\right) \rho_m \frac{d(X\delta)}{dz} \ll V_{sy} \rho_s X - \frac{V_{bx}}{2} \rho_m \delta \tag{5.21}$$

then Eq. 5.20 may written as:

$$V_{sy} \rho_s X - \frac{V_{bx}}{2} \rho_m \delta = 0 \tag{5.22}$$

or

$$\omega \equiv V_{sy} \rho_s X = \frac{V_{bx}}{2} \rho_m \delta \tag{5.23}$$

where ω is defined as the rate of melting per unit down channel distance. Equation 5.22 may be also written as follows:

$$\delta = \frac{2 V_{sy} \rho_s X}{V_{bx} \rho_m} \tag{5.24}$$

Substituting Eq. 5.14 into Eq. 5.24 above gives:

$$\delta = \left[\frac{[2k_m (T_b - T_{melt}) + \mu V_j^2] X}{V_{bx} \rho_m [Cp_s (T_{melt} - T_s) + \lambda]}\right]^{0.5} \tag{5.25}$$

and substituting Eq. 5.25 into Eq. 5.23 gives the following expression for ω:

$$\omega = \left[\frac{V_{bx} \rho_m [k_m (T_b - T_{melt}) + \frac{\mu}{2} V_j^2] X}{2[Cp_s (T_{melt} - T_s) + \lambda]}\right]^{0.5}$$

$$= \phi X^{0.5} \tag{5.26}$$

where $$\Phi = \left[\frac{V_{bx} \rho_m [k_m (T_b - T_{melt}) + \frac{\mu}{2} V_j^2]}{2[Cp_s (T_{melt} - T_s) + \lambda]} \right]^{0.5}$$

Tadmor et al. (111,114k) introduced a modification to the heat balance at the interface by replacing the heat of fusion with an effective heat of fusion λ^*. This effective heat of fusion is defined as the amount of heat required to melt the polymer and heat it to the average temperature of the film, T_{avg}. λ^* is given by:

$$\lambda^* = \lambda + Cp_m (T_{avg} - T_{melt}) \tag{5.27}$$

where $$T_{avg} = \frac{\int_0^{\delta} v_j(y)\, T(y)\, dy}{\int_0^{\delta} v_j(y)\, dy}$$

$$= \frac{2\, T_b + T_{melt}}{3} + \frac{\mu V_j^2}{12\, k_m} \tag{5.28}$$

Thus, Eq. 5.26 with the effective heat of fusion may be written as:

$$\omega = \Phi X^{0.5} \tag{5.29}$$

where $$\Phi = \left[\frac{V_{bx} \rho_m [k_m (T_b - T_{melt}) + \frac{\mu}{2} V_j^2}{2[Cp_s (T_{melt} - T_s) + \lambda + Cp_m (T_{avg} - T_{melt})} \right]^{0.5}$$

In Eq. 5.29, the rate of melting ω is a function of the unknown solid bed profile X. A second relationship between ω and X can be obtained by a mass balance over the solid bed for a down channel increment ΔZ (see Fig. 5.3(d)). The various contributions to the mass balance are:

$$\begin{bmatrix}\text{Mass flow rate}\\ \text{into increment}\end{bmatrix} = \rho_s V_{sz} (H^*X)\Big|_z \tag{5.30}$$

$$\begin{bmatrix}\text{Mass flow rate}\\ \text{out of increment}\end{bmatrix} = \rho_s V_{sz} (H^*X)\Big|_{z+\Delta z} \tag{5.31}$$

$$\begin{bmatrix}\text{Mass flow rate}\\ \text{exiting through}\\ \text{interface by melting}\end{bmatrix} = V_{sy} \rho_s (X \ \Delta z) = \omega \ \Delta z \tag{5.32}$$

where H* is the height of the solid bed and equals the channel depth H minus the film thickness δ. Since the film thickness is small relative to the bed height and since it varies only slowly with z, then H* can be taken to equal the channel depth minus a constant value. A reasonable choice for this constant value is the flight clearance δ_f, and thus:

$$H^* = H - \delta_f \tag{5.33}$$

Combining Eqs. 5.30 to 5.32 in the mass balance, we obtain:

$$\rho_s V_{sz}[(H^*X)_z - (H^*X)_{z+\Delta z}] - \omega \ \Delta z = 0 \tag{5.34}$$

Again dividing Eq. 5.34 by Δz and taking the limit as $\Delta z \rightarrow 0$ gives:

$$\frac{d(H^*X)}{dz} = \frac{-\omega}{\rho_s V_{sz}} \tag{5.35}$$

For a constant depth channel, Eq. 5.35 can be written as:

$$\frac{dX}{dz} = \frac{-\omega}{\rho_s V_{sz} H^*} = \frac{-\Phi X^{0.5}}{\rho_s V_{sz} H^*} \tag{5.36}$$

The solution for this first order differential equation is given by:

$$\frac{X}{W} = \frac{X_1}{W}\left[1 - \frac{\phi\,(z - z_1)}{2\rho_s\, V_{sz}\, H^*\, X_1^{0.5}}\right]^2 \tag{5.37}$$

and when $z_1 = 0$ and $X_1 = W$, Eq. 5.37 becomes:

$$\frac{X}{W} = \left[1 - \frac{\phi}{2\rho_s\, V_{sz}\, H^*\, W^{0.5}}\, z\right]^2 \tag{5.38}$$

The down channel velocity of the solid bed V_{sz} has been assumed to be constant throughout the extruder and may be obtained from the mass flow rate G in the solids conveying zone:

$$G = V_{sz}\, H_o\, W\, \rho_s \tag{5.39}$$

where H_o is the channel depth in the feed zone. Substituting Eq. 5.39 into Eq. 5.38 gives:

$$\frac{X}{W} = \left[1 - \frac{\phi\, W^{0.5}\, H_o}{2\, G\, H^*}\, z\right]^2 \tag{5.40}$$

Define the dimensionless group ψ:

$$\psi = \frac{\phi}{V_{sz}\, \rho_s\, W^{0.5}} = \frac{\phi\, W^{0.5}\, H_o}{G} \tag{5.41}$$

ψ is the ratio of the rate of melting per unit down channel distance to the mass flow rate of solids per unit channel depth. Substituting Eq. 5.41 into Eq. 5.40 gives:

$$\frac{X}{W} = \left[1 - \frac{\psi}{2H^*}\, z\right]^2 \tag{5.42}$$

Eq. 5.42 is used to calculate the solid bed profile for the feed and metering sections of the extruder.

For the <u>compression section</u> which usually has a constant taper, the channel depth can be expressed as:

$$H = H_1 - Az \tag{5.43}$$

where H_1 is the channel depth at the beginning of the taper (at z=0), and A is the degree of tapering. Substituting Eq. 5.43 into Eq. 5.35 and replacing ω by $\Phi\, X^{0.5}$ gives:

$$(H_1^* - Az)\,\frac{dX}{dz} - XA = -\frac{\Phi\, X^{0.5}}{V_{sz}\,\rho_s} \tag{5.44}$$

The solution for this first order differential equation is given by:

$$\frac{X}{W} = \frac{X_1}{W}\left[\frac{\psi}{A} - \left(\frac{\psi}{A} - 1\right)\left(\frac{H_1^*}{H_1^*-Az}\right)^{0.5}\right]^2 \tag{5.45}$$

and when $X_1 = W$ at $z = 0$, Eq. 5.45 becomes:

$$\frac{X}{W} = \left[\frac{\psi}{A} - \left(\frac{\psi}{A} - 1\right)\left(\frac{H_1^*}{H_1^*-Az}\right)^{0.5}\right]^2 \tag{5.46}$$

where ψ is defined in Eq. 5.41 and $H_1^* = H_1 - \delta_f$.

As stated in Sec. 5.1, Tadmor et al. (111, 114ℓ) modified the Newtonian melting model to account for non-Newtonian flow in the melt film and to correct for curvature in the screw channel. To account for the non-Newtonian behaviour of the melt, a temperature and shear rate dependent power-law constitutive relation was utilized. Instead of treating the momentum and energy equations as coupled equations to be solved simultaneously, a particular methematical form for the temperature profile was assumed based on Newtonian flow results. With the introduction of the above modifications, the resulting equations for the solid bed profile still had to be solved numerically.

Summary of the Tadmor Newtonian Melting Model Equations

The following equations are obtained by performing heat and mass balances across the upper melt film - solid bed interface where all the melting is assumed to take place:

Heat balance over interface:

$$V_{sy}\,\rho_s\,(\lambda + Cp_m\,(T_{avg} - T_{melt}) = -\,\rho_s\,Cp_s\,(T_{melt} - T_s)\,V_{sy} + \frac{[\frac{\mu}{2}\,V_j^{\,2} + k_m\,(T_b - T_{melt})]}{\delta} \qquad (5.47)$$

Mass balance over interface:

$$V_{sy}\,\rho_s\,X - \frac{V_{bx}}{2}\,\rho_m\,\delta = 0 \qquad (5.48)$$

or

$$\omega \equiv V_{sy}\,\rho_s\,X = \frac{V_{bx}}{2}\,\rho_m\,\delta \qquad (5.49)$$

Rate of melting, ω:

$$\omega = \Phi\,X^{0.5} \qquad (5.50)$$

where $$\Phi = \left[\frac{V_{bx}\ \rho_m\ [k_m\ (T_b - T_{melt}) + \frac{\mu}{2} V_j^2}{2[Cp_s\ (T_{melt} - T_s) + \lambda + Cp_m\ (T_{avg} - T_{melt})} \right]^{0.5}$$

Mass balance over solid bed:

A mass balance is performed over the solid bed to determine the solid bed profile, X/W.

$$\frac{d(H^*X)}{dz} = \frac{-\omega}{\rho_s\ V_{sz}} = \frac{-\Phi X^{0.5}}{\rho_s\ V_{sz}} \tag{5.51}$$

where $H^* = H - \delta_f$

Solid bed profile - constant depth channel:

$$\frac{X}{W} = \left[1 - \frac{\psi}{2H^*} z\right]^2 \tag{5.52}$$

where $$\psi = \frac{\Phi\ W^{0.5}\ H_o}{G}$$

Solid bed profile - tapered channel:

$$\frac{X}{W} = \left[\frac{\psi}{A} - \left(\frac{\psi}{A} - 1\right)\left(\frac{H_1^*}{H_1^* - Az}\right)^{0.5}\right]^2 \tag{5.53}$$

where A = degree of taper

Typical solid bed profiles obtained by using the Tadmor Newtonian melting model are presented in Figs. 5.4 and 5.5 for a constant depth

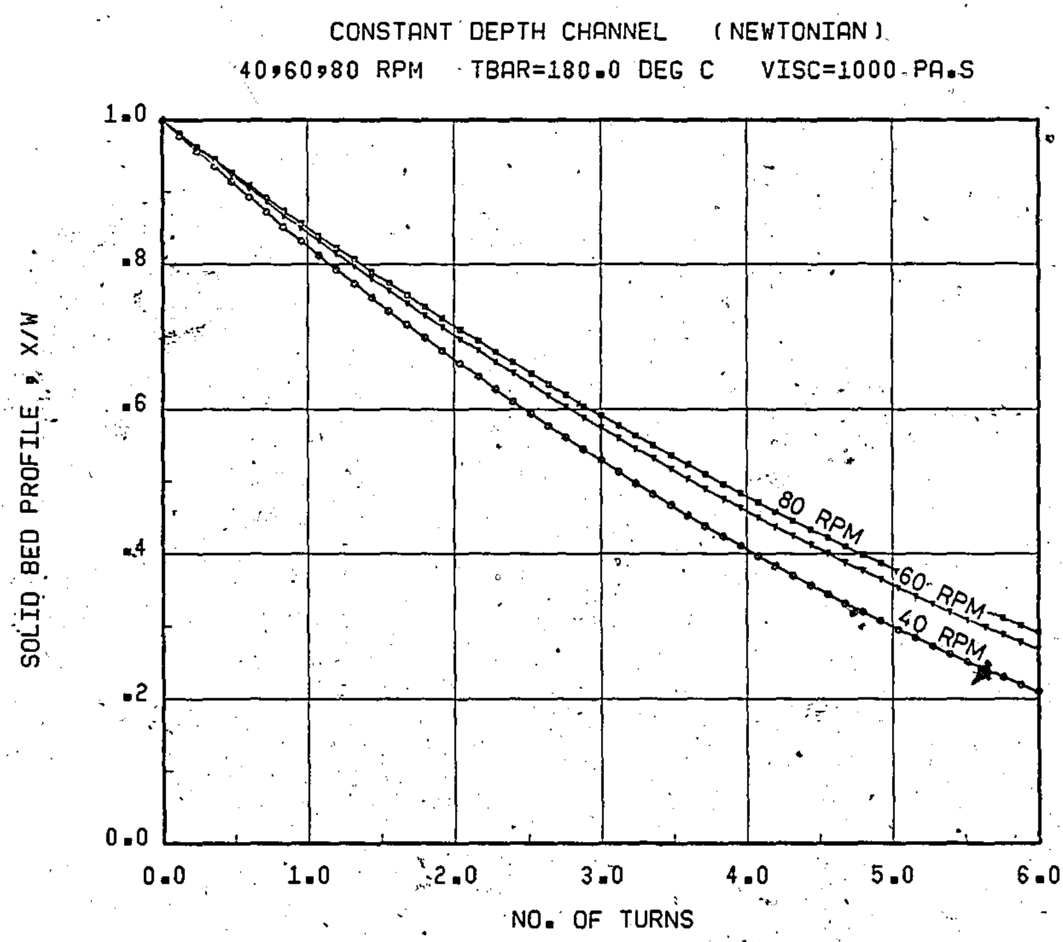

Fig. 5.4 Solid bed profiles (Tadmor Newtonian melting model) for a constant depth extruder screw channel. Data for the polymer properties, screw channel dimensions and extruder operating conditions are given in App. G.3.

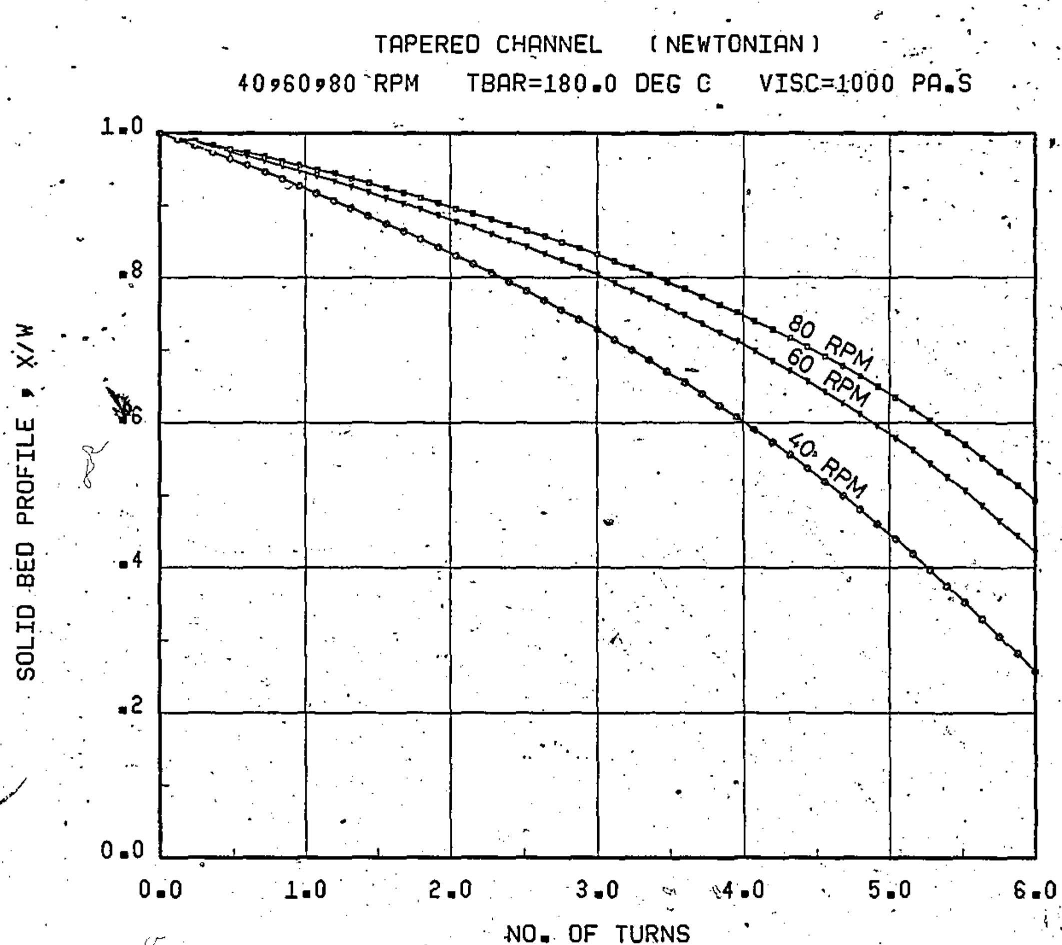

Fig. 5.5 Solid bed profiles (Tadmor Newtonian melting model) for a tapered screw channel. Data for the polymer properties, screw channel dimensions and extruder operating conditions are given in App. G.3.

and tapered screw channel respectively. Material properties and processing conditions used to obtain the results are given in App. G.3. In each case, solid bed profiles are shown for three frequencies of screw rotation: 40, 60 and 80 rpm. Although the rate of melting increases with increasing screw speed, it can be seen that the solid bed extends further down the screw channel at increased screw speeds due to the higher solid bed velocity.

5.2.2 Present Modification of the Tadmor Melting Model

In developing a modified Tadmor melting model, each of the assumptions given in Section 5.2.1 is utilized with the exception of Assumption (10). Here, a non-Newtonian fluid described by the following temperature and shear rate dependent constitutive relation is used (see also Eq. 2.36):

$$\tau_{yj} = \eta \frac{dv_j}{dy} = \eta \dot{\gamma} \tag{5.54}$$

$$\log \eta = a_o + a_1 \log \dot{\gamma} + a_2 (\log \dot{\gamma})^2 + a_3 T + a_4 T^2 + a_5 T \log \dot{\gamma} \tag{5.55}$$

Analysis of the heat transfer in the melt film is treated by solving the coupled momentum and energy equations simultaneously using the finite difference method.

To analyze the flow in the melt film, the simplified conservation equations can be written as:

$$\text{Mass:} \qquad \int_o^{\delta} v_j(y)\, dy = Q \tag{5.56}$$

Momentum: $$-\frac{dp}{dx_j} + \eta \frac{d^2 v_j}{dy^2} + \frac{d\eta}{dy}\frac{dv_j}{dy} = 0 \qquad (5.57)$$

Energy: $$k_m \frac{d^2 T}{dy^2} + \eta \left(\frac{dv_j}{dy}\right)^2 = 0 \qquad (5.58)$$

where $v_j = 0$, $T = T_{melt}$ at $y = 0$

$v_j = V_j$, $T = T_b$ at $y = \delta$

Q in Eq. 5.56 is defined as the flow rate per unit width. In Eq. 5.57, dp/dx_j is a temperature-induced pressure gradient (127). If the temperatures at the interface and barrel surface were identical, then this term would disappear. Equations 5.56 to 5.58 with the accompanying boundary conditions can be solved numerically (using the finite difference method) to obtain a velocity and temperature profile. The heat flux at the interface for the melt side is given by:

$$(q_y)_1 = -k_m \left(\frac{dT}{dy}\right)_{y=0} \qquad (5.59)$$

where the temperature gradient at y = 0 may be approximated by the following third-order finite difference equation for derivatives:

$$\left(\frac{dT}{dy}\right)_{y=0} \approx \frac{-11T_o + 18T_1 - 9T_2 + 2T_3}{6\ \Delta y} \qquad (5.60)$$

The heat flux at the interface for the solid bed side is still (see Eq. 5.11):

$$(q_y)_2 = - \rho_s \, Cp_s \, (T_{melt} - T_s) \, V_{sy} \tag{5.61}$$

Using Eqs. 5.59 and 5.61, the heat balance at the interface may be expressed as (see Eq. 5.12):

$$V_{sy} \, \rho_s \, \lambda = - \rho_s \, Cp_s \, (T_{melt} - T_s) \, V_{sy} + k_m \left(\frac{dT}{dy}\right)_{y=0} \tag{5.62}$$

or

$$V_{sy} = \frac{k_m \left(\frac{dT}{dy}\right)_{y=0}}{\rho_s \, Cp_s \, (T_{melt} - T_s) + \rho_s \, \lambda} \tag{5.63}$$

Replacing λ by the effective heat of fusion λ^* (see Eq. 5.27), Eq. 5.63 becomes:

$$V_{sy} = \frac{k_m \left(\frac{dT}{dy}\right)_{y=0}}{\rho_s \, Cp_s \, (T_{melt} - T_s) + \rho_s \, [\lambda + Cp_m(T_{avg} - T_{melt})]} \tag{5.64}$$

It should be noted that $\left(\frac{dT}{dy}\right)_{y=0}$ is a function of δ, and consequently Eq. 5.64 still contains the two unknowns, V_{sy} and δ.

The mass balance over the melt film is identical to that obtained in the last section and is represented by the following equation (see Eq. 5.23):

$$\omega = V_{sy} \, \rho_s \, X = \frac{V_{bx}}{2} \, \rho_m \, \delta \tag{5.65}$$

Equations 5.64 and 5.65 cannot be combined as in the previous section (see Eqs. 5.23 to 5.26) because δ does not appear explicitly in Eq. 5.64. Instead, Eq. 5.64 is substituted into the left-hand side of Eq.

5.65 to give:

$$\omega = \frac{k_m \left(\frac{dT}{dy}\right)_{y=0} \rho_s X}{\rho_s Cp_s (T_{melt} - T_s) + \rho_s [\lambda + Cp_m (T_{avg} - T_{melt})]}$$

$$= \frac{k_m}{Cp_s (T_{melt} - T_s) + \lambda + Cp_m (T_{avg} - T_{melt})} \left(\frac{dT}{dy}\right)_{y=0} X \qquad (5.66)$$

or

$$\omega = \Psi \left(\frac{dT}{dy}\right)_{y=0} X \qquad (5.67)$$

where $\Psi = \dfrac{k_m}{Cp_s (T_{melt} - T_s) + \lambda + Cp_m (T_{avg} - T_{melt})}$

Since Eq. 5.67 is implicitly a function of δ (through $\left(\frac{dT}{dy}\right)_{y=0}$), the rate of melting ω can be calculated only when δ has been specified. The procedure for determining δ is discussed later in this section.

As in the previous section, the mass balance over the solid bed can be represented by the following ordinary differential equation (see Eq. 5.35):

$$\frac{d(H^*X)}{dz} = \frac{-\omega}{\rho_s V_{sz}} \qquad (5.68)$$

For a <u>constant depth channel</u>, Eq. 5.68 becomes:

$$\frac{dX}{dz} = \frac{-\omega}{\rho_s V_{sz} H^*}$$

$$= \frac{-\Psi}{\rho_s V_{sz} H^*} \left(\frac{dT}{dy}\right)_{y=0} X \qquad (5.69)$$

For a tapered channel, Eq. 5.68 may be written as:

$$(H_1{}^* - Az)\frac{dX}{dz} - XA = \frac{-\omega}{\rho_s V_{sz}}$$

$$= -\frac{\Psi}{\rho_s V_{sz}}\left(\frac{dT}{dy}\right)_{y=0} X \qquad (5.70)$$

Equations 5.69 and 5.70 are non-linear ordinary differential equations and as a result must be solved numerically (for example, using the fourth-order Runge-Kutta method). An additional complication in Eqs. 5.69 and 5.70 is that there is an implicit dependence on δ (through $\left(\frac{dT}{dy}\right)_{y=0}$) which cannot be determined independently. Therefore, δ must be calculated iteratively at each down channel increment in the melting zone as described in the following algorithm:

1. Assume a value of $\delta^{(k)}$ and $X^{(k)}$, where initially $k = 0$.
2. Solve the mass, momentum and energy equations (Eqs. 5.56 to 5.58) and calculate $\left(\frac{dT}{dy}\right)_{y=0}$ using Eq. 5.60.
3. Solve either Eq. 5.69 or 5.70 using the fourth-order Runge-Kutta method to obtain a new value of X, denoted by $X^{(k+1)}$.
4. Calculate V_{sy} from Eq. 5.64, and then in Eq. 5.65 by also using $X^{(k+1)}$, calculate a new value of δ which is denoted by $\delta^{(k+1)}$.
5. Compare $\delta^{(k)}$ and $\delta^{(k+1)}$. If $\left|(\delta^{(k+1)} - \delta^{(k)})/\delta^{(k+1)}\right| < \varepsilon$, then δ and X have converged, and we may proceed to the next increment in the down channel direction.
6. If the relative change in δ is greater than ε, then we must repeat the iteration. Set $\delta^{(k+1)} = (\delta^{(k+1)} + \delta^{(k)})/2$ (to avoid divergence of δ), set $X^{(k+1)} = X^{(k)}$, and return to step 2.

(k) and (k+1) refer to iteration numbers at a given increment. At the beginning of the melting zone, $\delta^{(o)} = \delta_f$ and $X^{(o)} = W$. At subsequent down channel increments, $\delta^{(o)}$ and $X^{(o)}$ assume the final values calculated at the previous increment.

The Delay Zone

A value of ψ at the beginning of the melting zone is needed to calculate the length of the delay zone as described in Sec. 4.2. The dimensionless parameter ψ is defined as (see Eq. 5.41):

$$\psi = \frac{\Phi\, W^{0.5}\, H_o}{G} \tag{5.71}$$

Substituting Eq. 5.26 into the above equation, we obtain:

$$\psi = \frac{\omega\, W^{0.5}\, H_o}{X^{0.5}\, G} \tag{5.72}$$

But X = W at the beginning of the melting zone, therefore Eq. 5.72 may be written as:

$$\psi = \frac{\omega\, H_o}{G} \tag{5.73}$$

Since $\omega = V_{bx}\, \rho_m\, \delta/2$, ψ may be written as:

$$\psi = \frac{V_{bx}\, \rho_m\, \delta\, H_o}{2G} \tag{5.74}$$

δ at the beginning of the melting zone can be determined by solving Eqs. 5.64 and 5.65 iteratively until δ converges.

Summary of the Modified Non-Newtonian Melting Model Equations

In the present melting model, the following equations are obtained as a result of performing heat and mass balances over the upper melt film-solid bed interface:

Heat balance over interface:

$$V_{sy}\ \rho_s\ [\lambda + Cp_m\ (T_{avg} - T_{melt})] = - \rho_s\ Cp_s\ (T_{melt} - T_s)\ V_{sy} + k_m \left(\frac{dT}{dy}\right)_{y=0} \tag{5.75}$$

Mass balance over interface:

$$V_{sy}\ \rho_s\ X - \frac{V_{bx}}{2}\ \rho_m\ \delta = 0 \tag{5.76}$$

or

$$\omega = V_{sy}\ \rho_s\ X = \frac{V_{bx}}{2}\ \rho_m\ \delta \tag{5.77}$$

Rate of melting, ω:

$$\omega = \Psi \left(\frac{dT}{dy}\right)_{y=0} X \tag{5.78}$$

where $\Psi = \dfrac{k_m}{Cp_s\ (T_{melt} - T_s) + \lambda + Cp_m\ (T_{avg} - T_{melt})}$

and where $\left(\frac{dT}{dy}\right)_{y=0}$ is a function of δ implicitly and is obtained by solving the mass, momentum and energy equations (5.56 to 5.58) numerically.

A mass balance over the solid bed is performed to determine the solid bed profile.

Mass balance over solid bed:

$$\frac{d(H^*X)}{dz} = \frac{-\omega}{\rho_S V_{SZ}} \tag{5.79}$$

Solid bed profile – constant depth channel:

$$\frac{dX}{dz} = \frac{-\Psi}{\rho_S V_{SZ} H^*} \left(\frac{dT}{dy}\right)_{y=0} X \tag{5.80}$$

Solid bed profile – tapered channel:

$$(H_1^* - Az) \frac{dX}{dz} - XA = \frac{-\Psi}{\rho_S V_{SZ}} \left(\frac{dT}{dy}\right)_{y=0} X \tag{5.81}$$

Equations 5.77 and 5.80 or 5.81 are solved iteratively and numerically to obtain the solid bed profile either in a constant depth or tapered screw channel.

The modified non-Newtonian version of Tadmor's melting model as described in this section is used in the present overall extruder model. Typical solid bed profiles obtained by using the non-Newtonian model are presented in Figs. 5.6 and 5.7 for a constant depth and tapered screw channel respectively (compare with solid bed profiles from the Newtonian model in Figs. 5.4 and 5.5). The polymer melt flow behaviour in the upper melt film is described by a temperature and shear rate dependent constitutive relation (Eqs. 5.54 and 5.55). No corrections, however, are performed for channel curvature.

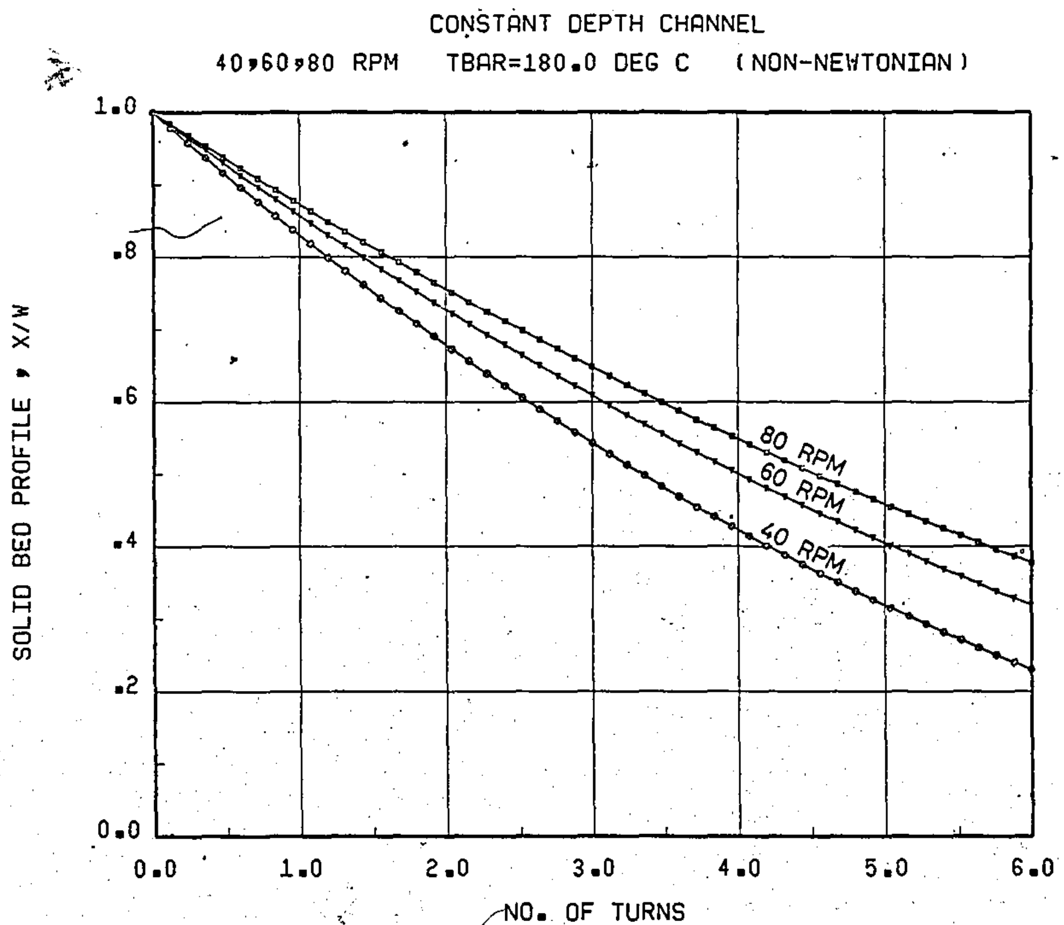

Fig. 5.6 Solid bed profiles (modified non-Newtonian melting model) for a constant depth extruder screw channel. Data for polymer properties, screw channel dimensions and extruder operating conditions are given in App. G.3.

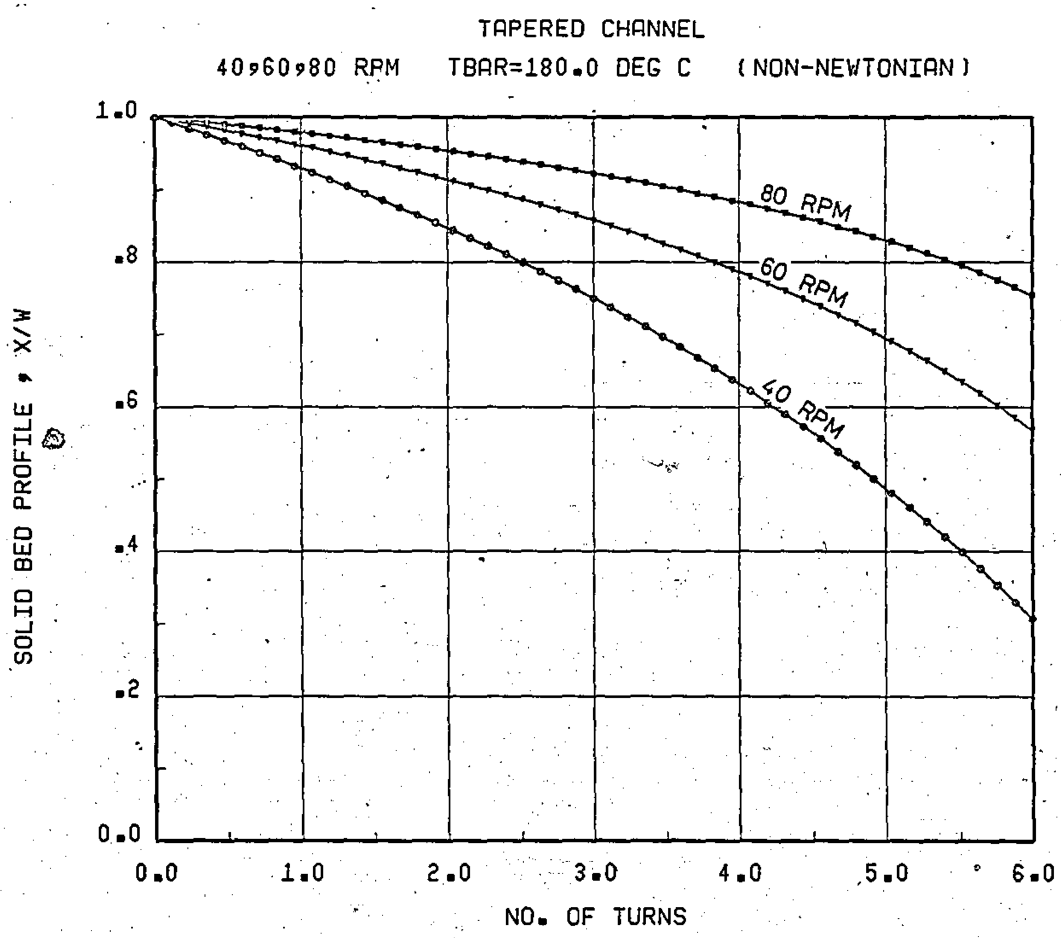

Fig. 5.7 Solid bed profiles (modified non-Newtonian melting model) for a tapered screw channel. Data for polymer properties screw channel dimensions and extruder operating conditions are given in App. G.3.

CHAPTER 6

MELT PUMPING IN THE EXTRUDER

The third of three functional zones in the extruder screw channel is the melt conveying zone. It is in this region where the pressure is developed to pump the melt through the die. As stated in Sec. 2.4 melt flow in the extruder screw channel occurs in two regions. One is downstream of the melting zone and occupies the entire width of the screw channel. The other region occurs in the melt pool and extends side by side with the solid bed. Only recently has melt flow in this region been considered as a part of the melt conveying zone.

The objectives of modelling the melt conveying zone are to predict the velocity, temperature and pressure profiles in the screw channel given the following: (i) extruder screw geometry and dimensions, (ii) extruder operating conditions, (iii) physical and rheological properties of the polymer melt, and (iv) the rate of melting of the polymer in the melting zone. In this chapter, extruder melt flow models reported in the literature are discussed, and the development of the present melt flow model is presented.

6.1 Literature Survey of Melt Conveying Models

Of all the sections in the extrusion process, melt flow in the screw channel and die has received the most attention in the literature. There are many reasons for this. Early attempts to analyze extruder performance concentrated on melt flow because it was thought that the melt flow characteristics in the metering section primarily controlled the output of the extruder. Perhaps an even better reason is that theoretical analysis of fluid flow is far simpler than that of solids conveying or melting. Also, temperatures and pressures are more easily measured in the melt flow regions of the extruder using melt thermocouples and pressure transducers than are parameters in the solids conveying and melting zones. For example, the cooling experiment (for the analysis of melting) as described in Sec 2.3 requires considerably more effort than do measurements of pressure and temperature. As a consequence, models describing melt flow in extruders are more sophisticated than those describing either solids conveying or melting.

Many textbooks on polymer extrusion have been written in the last two decades which deal with the theoretical analysis and modelling of melt flow in the screw channel. Included are books by Bernhardt (6), McKelvey (73), Schenkel (99), Klein and Marshall (52), Pearson (89), Tadmor and Klein (114), Fenner (28), Middleman (78) and Tadmor and Gogos (112). Several review articles have also appeared in the literature. The most recent one by Fenner (30) was already referred to in the solids conveying and melting sections. The purpose of this section is not to review all studies reported in the literature in detail, but to highlight the key works and contributions in this area.

6.1.1 Newtonian Flow Solutions

Nearly all of the early attempts to analyze melt flow in screw extruders assumed Newtonian melt behaviour and isothermal flow. In most cases, only down channel flow was considered (i.e. transverse flow was neglected). Two of the early contributions are noteworthy and should be pointed out here. The first isothermal analysis of screw viscosity pumps handling Newtonian fluids was published anonymously (97) in 1922 in a paper which is often attributed to Rowell and Finlayson who later extended the work. The second and perhaps more important contribution was by the team of Carley, Strub, Mallouk, McKelvey and Jepson who developed the flow theories and applied them to the extrusion of polymers. Their work was published as a series of papers in a symposium on the theory of plastics extrusion in 1953 (11,12,13,14,46,65,71), and formed the basis of polymer extrusion theory for several years to come.

The basic theory for isothermal screw extrusion was presented in two forms in the early years: (i) the two-dimensional or so-called "exact" theory in which the edge effects of the flight faces are taken into account, and (ii) the one-dimensional or so-called "simplified" theory in which edge effects are neglected and which is therefore limited in its application to screws of relatively shallow channel depth.

The differential equation which describes the two-dimensional combined drag and pressure flow in a rectangular flat channel as shown in Fig. 6.1 where the edge effects are considered is:

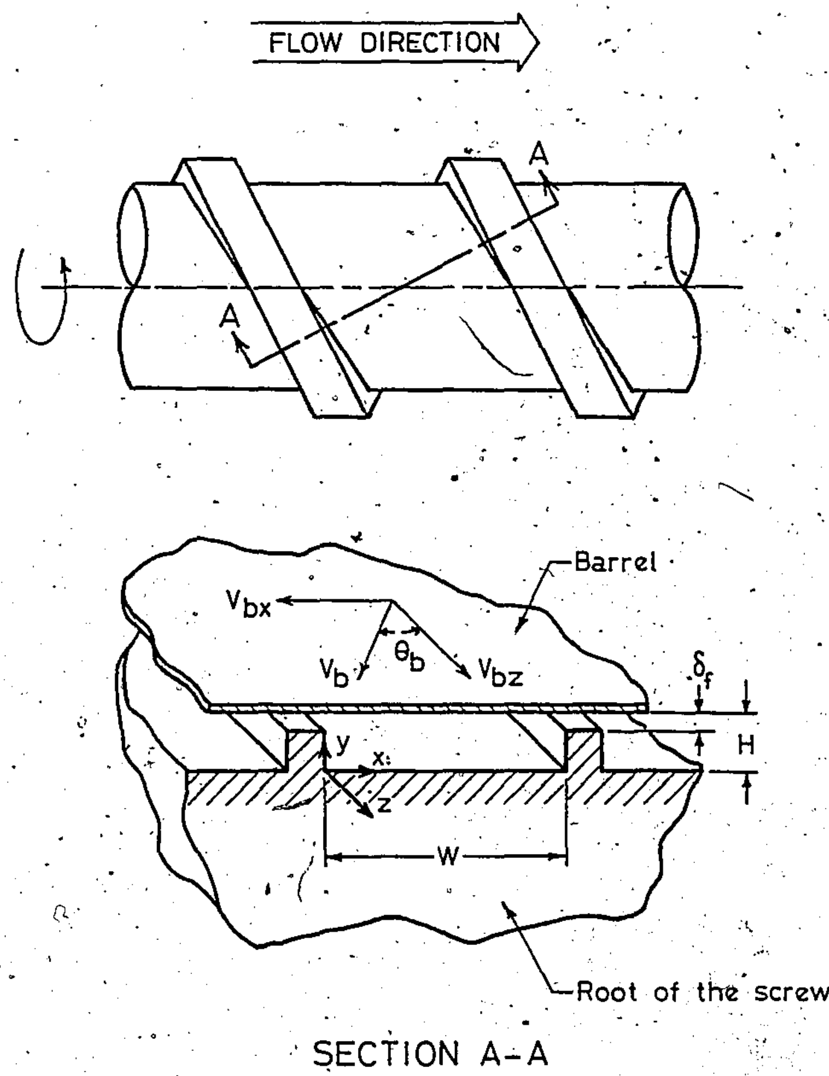

SECTION A-A

Fig. 6.1 Schematic diagram of the extruder screw channel. V_b is the tangential barrel velocity, and V_{bx} and V_{bz} are the x and z barrel velocity components.

$$-\frac{dp}{dz} + \mu\left(\frac{\partial^2 v_z}{\partial x^2} + \frac{\partial^2 v_z}{\partial y^2}\right) = 0 \tag{6.1}$$

The solution to Eq. 6.1 satisfying the boundary conditions found in screw pumps was presented in various forms by Boussinesq (9), Maillefer (64), Rowell and Finlayson (97), Strub (106), Pigott (93), and Carley and Strub (13). The form in which the solution was presented was quite different in each case, and it was only in 1955 that Meskat (75) critically reviewed the results of these works and demonstrated that their solutions were all equivalent. The solution to Eq. 6.1, presented in most conveniently in the form of the flow rate, is as follows (104):

$$Q = \frac{V_{bz}WH}{2}\left[\frac{16W}{\pi^3 H}\sum_{n=1,3,\dots}^{\infty}\frac{1}{n^3}\tanh\left(\frac{n\pi H}{2W}\right)\right]$$

$$-\frac{WH^3}{12\mu}\left(\frac{dp}{dz}\right)\left[1-\frac{192H}{\pi^5 W}\sum_{n=1,3,\dots}^{\infty}\frac{1}{n^5}\tanh\left(\frac{n\pi W}{2H}\right)\right] \tag{6.2}$$

It should be noted here that the drag flow and pressure flow components in Eq. 6.2 can be treated independently because the Newtonian viscosity μ is a constant. This enables an analytical solution to be obtained.

In the one-dimensional theory where the edge effects of the flights are ignored, the differential equation describing the flow is:

$$-\frac{dp}{dz} + \mu\frac{d^2 v_z}{dy^2} = 0 \tag{6.3}$$

The solution to Eq. 6.2 was presented and discussed by Gore (35), Carley et al. (11), and Bernhardt (5), and again is given in terms of flow rates:

$$Q = Q_d + Q_p$$
$$= \frac{V_{bz}WH}{2} - \frac{WH^3}{12\mu}\left(\frac{dp}{dz}\right) \tag{6.4}$$

The first term on the right-hand side of Eq. 6.4 represents drag flow, and the second term, pressure flow. The validity of the one-dimensional theory for predicting and evaluating the performance of relatively shallow flighted screws in extruders was verified by several workers including Maddock (61,62), Sackett (98) and McKelvey (71).

Squires (104) compared the solutions of the one-and-two-dimensional flow theories and showed that Eq. 6.2 may be written as:

$$Q = Q_d\ F_d + Q_p\ F_p$$
$$= \frac{V_{bz}WH}{2} F_d - \frac{WH^3}{12\mu}\left(\frac{dp}{dz}\right) F_p \tag{6.5}$$

where F_d and F_p are shape factors given by the expressions inside the square brackets in Eq. 6.2, and account for the effect of the flights on the flow rate. Subsequent references to "simplified" flow theory in the literature implied the solution as given in Eq. 6.5 with the choice of either retaining or neglecting the shape factors, and not exclusively the solution in Eq. 6.4.

In Newtonian flow in extruder screw channels, transverse flow does not affect the down channel velocity profiles and output, but it does contribute to the screw power dissipation and affects heat transfer and mixing characteristics in the screw channel. The first detailed study on transverse flow was published in connection with mixing by Mohr et al. (81). Assuming an infinitely wide screw channel and no net flow in the cross channel direction, the differential equation for transverse flow may be written as:

$$- \frac{dp}{dx} + \mu \frac{d^2 v_x}{dy^2} = 0 \qquad (6.6)$$

and the solution is given as:

$$v_x = V_{bx} \left[3 \left(\frac{y}{H}\right)^2 - 2 \left(\frac{y}{H}\right)\right] \qquad (6.7)$$

Numerous papers have appeared which apply various corrections and refinements to the simplified extrusion theory. Squires (104) developed a channel curvature correction factor for drag flow based on a zero helix angle and a zero aspect ratio (H/W) in the screw channel. Booy (8) derived channel curvature factors for both drag and pressure flow. These factors are functions of helix angle and aspect ratio and are combined with the respective channel shape factors by multiplication. Based on unpublished work by Squires and Galt, Bernhardt (6a) described a correction factor which accounts for the non-uniform viscosity due to temperature variations across the channel depth. A linear variation in viscosity was used to develop the correction factor. Thermal effects were also introduced by McKelvey and Bernhardt (72, 74) who used a simple energy balance and assumed adiabatic operating conditions in the extruder.

In addition to the experimental work by Maddock (61,62), Sackett (98) and McKelvey (71) which confirmed the validity of the simplified extrusion theory with respect to extruder performance (i.e. pressure profiles, flow rates), several detailed studies were conducted to experimentally verify the velocity profiles predicted by the simplified theory. Eccher and Valentinotti (25) were the first to publish direct and quantitative results of local velocity profiles inside the screw channel. Using an extruder with a rotating and transparent barrel, they extruded a mixture of polyisobutylene and paraffin oil containing small aluminum particles which were followed by a microscope. By focusing to different channel depths and measuring the displacements of the aluminum particles with a micrometer, they were able to obtain both down channel and cross channel velocity profiles. Mohr et al. (82) conducted similar experiments with a transparent barrel extruder using corn syrup, but injected a black fluid into the screw channel through probes attached to the screw. Velocity profiles were obtained by photographing the streams injected at different levels in the screw channel. It was noted by Mohr et al. that although the flow pattern in the screw channel was quite accurately described as a "helix within a helix", it was incorrect to assume that there existed a backward flow across a cross section perpendicular to the screw axis as devised by Carley and Strub (13) in a diagram of fluid motion in the extruder channel. The term "backflow" in extruders is often misinterpreted as meaning backflow in the axial direction, whereas it really means backflow in the down channel direction. Mohr et al. showed in their experiments that under no conditions did there exist a backflow in the axial direction. In a second paper, Mohr et al. (80) conducted similar experiments with a non-Newtonian fluid (hydroxyethylcellulose in water solution) which has a similar viscosity - shear rate curve as polyethylene.

The experiments by Eccher and Valentinotti, and Mohr et al. demonstrated that the simplified extrussion theory did provide a useful qualitative description of some aspects of screw extruder performance, and that it was the right approach to treating extruder flow problems. However, it did not provide accurate quantitative descriptions of practical processing operations. If flow behaviour of polymer melts was to be predicted realistically, then it would be necessary to include both the shear rate and temperature dependence of melt viscosity and the influence of thermal convection in the screw channel.

6.1.2 Isothermal Non-Newtonian Flow Solutions

The constant viscosity assumption was the first of the simplifications inherent in isothermal Newtonian solutions to be rejected. Early attempts to account for non-Newtonian flow behaviour retained the framework of the Newtonian theory, but replaced the Newtonian viscosity in the flow rate equation by some apparent viscostiy to account for the non-Newtonian effects. McKelvey (71) and Sackett (98) calculated average apparent viscosities from the Newtonian flow rate equation by using experimentally measured flow rates. Maddock (62) found that for polyethylene, viscosity data from rheological measurements could be used, provided that the apparent viscosity was taken at the drag flow shear rate in the screw channel, that is:

$$\dot{\gamma} = \frac{V_b}{H} = \frac{\pi N D_b}{H} \tag{6.8}$$

In the simplified extrusion theory based on isothermal Newtonian flow, the solution of the flow equations consists of two independent terms - one for drag flow and the other for pressure flow (see Eq. 6.5). The superposition, i.e. the linear addition of drag and pressure flows is a useful concept for Newtonian fluids. However, it is not valid for non-Newtonian fluids because the drag and pressure flow terms are no longer independent. Jacobi (44) used the superpositon principle by first calculating the drag and pressure flow terms using the power-law model, and then adding the two terms assuming that the error was not significant. Glyde and Holmes-Walker (34) and later Kroesser and Middleman (54) showed that this error could be very significant.

Several publications deal with the isothermal non-Newtonian extrusion of polymer melts in infinitely wide flow channels. In a very brief paper, Mori and Matsumoto (83) presented a flow rate equation based on the power-law fluid model. Unfortunately, their description of the method of solution is very sketchy and some of the variables in their flow equation are not defined.

DeHaven (21) chose a special case of the Ellis model, the Rabinowitsch equation as given in Eq. 6.9, to represent pseudoplastic melt flow behaviour:

$$-\frac{dv_z}{dy} = \frac{\tau}{\mu_o}(1 + c\,\tau^2) \tag{6.9}$$

A velocity profile for flow between parallel plates was derived and experiments with polymer solutions were carried out. However, the fit of experiments to theory was poor, primarily due to inaccurate experiments.

Weeks and Allen (124) obtained a solution for combined pressure and drag flow of an isothermal power-law fluid beteween infinite parallel plates. However, for practical design purposes they derived a simpler method in which an apparent viscosity is used in the Newtonian flow equation. Experiments were conducted with low-density polyethylene on a 2 inch (51 mm) diameter extruder. The theoretical results of output versus die head pressure were within 25% of the experimental values.

Exact solutions for the flow equations using the power-law fluid and infinite parallel plate model were presented by Glyde and Holmes-Walker (34) and by Kroesser and Middleman (54). Their results were given in the form of screw characteristics, that is, plots of reduced flow rate-versus-dimensionless pressure gradient. These screw characteristics were determined for several values of the power-law index.

Narkis and Ram (84) presented a general solution for the output rate of parallel (constant depth) screws for melts obeying the general Ellis model:

$$\frac{1}{\eta} = \frac{1}{\eta_o} + K\,\tau^{m-1} \qquad (6.10)$$

An approximate solution for the flow rates of power-law fluids in linear compression screws was given and checked experimentally on a 20 mm diameter extruder using low-density polyethylene.

Finally, Poon (94) proposed a numerical procedure for the solution of the two-dimensional (y, z axes) and two-directional (v_x, v_z) power-law flow equations for an infinitely wide channel. Transverse flow was included. The results were used to construct a complete model of the isothermal operation of a single screw melt extruder. Results were presented as screw characteristics, and compared with the experimental data of Week and Allen (124).

Several papers have been published which deal with the effect of finite channel width in isothermal non-Newtonian flow. In Newtonian flow, this effect was dealt with by the use of drag and pressure flow shape factors. Middleman (77) solved the equations governing (i) pressure flow, (ii) drag flow, and (iii) combined pressure and drag flow of an isothermal power-law fluid in channels of rectangular cross-section using the finite difference method. Results were presented in the form of shape factors for pure pressure and drag flows, and screw characteristics for combined pressure and drag flow. Fenner (28b) followed the same procedure but obtained slightly different results for the combined pressure and drag flows. Palit and Fenner (87) solved the above problem using the finite element method. Results were presented in the form of screw characteristics and compared with results obtained using the finite difference method. In a subsequent paper, Palit and Fenner (88) applied the finite element method to isothermal two-dimensional flows of power-law fluids. Examples included recirculating (transverse) flow in a rectangular channel which was independent of downstream flow.

The effect of channel curvature on isothermal non-Newtonian flows was examined by McKelvey (73a) and Tadmor (108,114m). McKelvey calculated the flow rate for pure drag flow of a power-law fluid in a "helical" channel with zero helix angle and zero aspect ratio (H/W). By comparing this to the flow rate between two parallel plates, a curvature correction factor was obtained for non-Newtonian fluids. Tadmor (108) obtained detailed solutions for velocity profiles and flow rates for combined drag and pressure flow in a similar "zero-helix angle" channel (i.e., for tangential flow between two infinitely long concentric cylinders, with the outer cylinder rotating and with a constant angular pressure gradient). In addition to the flow rate equations, two correction factors were derived: a curvature correction factor for pressure flow, and a correction factor for superimposing drag and pressure flows for non-Newtonian fluids. By having these correction factors available, the flow rate in extruders could be accurately calculated by: (i) using the simple expressions of drag and pressure flows developed for parallel plate theories, (ii) correcting the equations for curvature and shape, (iii) superimposing them, and (iv) multiplying the result with the superposition correction factor (114m).

A helical coordinate frame was presented by Tung and Laurence (119) for representing flow in helical channels. Although no solutions were presented, the helical coordinate frame was illustrated for the analysis of flow in a static mixer. Choo et al (15) presented a finite element method solution for the fully developed, isothermal, power-law flow in a deep, highly-curved, helical screw channel. Results were presented as screw characteristics and were compared with experimental data from a 19 mm diameter screw extruder using a high molecular weight hydroxyethyl cellulose in aqueous glucose solution. A similar finite element solution was given earlier by Hami and Pittman (38) for isothermal Newtonian fluids, based on an analysis in helical coordinates set up by Nebrensky et al. (85). Velocity profiles were reported by Choo et al. (16) for glucose syrup (Newtonian) extruded in a 1.5 inch (38 mm) diameter screw extruder to confirm the isothermal Newtonian solution.

6.1.3 Fully Developed Nonisothermal Non-Newtonian Flow Solutions

Initial attempts to allow for the effects of temperature variations on velocity profiles and flow rates treated the temperature profiles as being fully developed in both the down channel and transverse directions. Colwell and Nickolls (19) obtained solutions for fully developed downstream flow using the power-law fluid model. Transverse flow was not included. The results were obtained using both graphical and numerical integration, and were presented in the form of screw characteristics (i.e., reduced flow rates plotted against dimensionless pressure gradients). Experimental screw characteristics were obtained for a 1.5 inch (38 mm) diameter screw extruder using polystyrene.

Solutions for fully developed two-dimensional (y, z directions) and two-directional (v_x,v_z) flow using the power-law model were first obtained by Griffith (36). The effects of finite channel width, channel curvature effects and leakage across the flights were ignored. Numerical solutions for various values of power-law index were obtained and presented in the form of screw characteristics. Experimental results were obtained by extruding corn syrup (Newtonian) and a 1% carboxy vinyl polymer-in-water solution in a 2 inch (51 mm) screw extruder. It should be noted that in Griffith's solution the screw surface temperature was assumed to be equal to the barrel surface temperature. The justification for this assumption is that for very large Peclet number[1] flow, the temperature remains constant along a streamline. If there is no leakage over the flight tip, the screw and barrel surface boundaries form a single continuous streamline (30,36). More recent studies by Martin et al. (70) and Pearson (90) showed that this assumption provides a realistic and useful way of allowing for the thermal convection associated with recirculating transverse flow in two-dimensional and two-directional developing flow solutions. It is shown in the next section that in nonisothermal developing flow solutions, thermal convection is considered only in the down channel direction.

Zamodits (129,130) used almost identical methods as Griffith to solve the flow problem of a power-law fluid in the metering section of a

---

[1] Peclet number = $\dfrac{\text{(Characteristic velocity)(Characteristic length for heat conduction)}}{\text{(Thermal conductivity)/(Density)(Specific heat)}}$ and represents the ratio between convective and conductive heat transfer.

screw extruder. The equations of motion and energy were solved numerically taking into account the effect of transverse flow in the channel and the effect of a superimposed fully developed temperature profile. Results for various values of the power-law index were presented as screw characteristics. Experiments were performed on a 2.5 inch (63.5 mm) diameter screw extruder using rubber ($n = 0.26$) and polyethylene ($n = 0.31$).

Detailed comparisons of one-and two-directional flow solutions (both isothermal and fully developed nonisothermal solutions) were made by Fenner (28c,31) using the power-law model. Metering screw experiments were performed on a 1.5 inch (38 mm) diameter extruder using a dimethyl silicone polymer. The experimental pressure profiles and screw characteristics were compared with (i) isothermal Newtonian solutions, (ii) isothermal one-and two-directional power-law solutions, and (iii) nonisothermal one-and two-directional power-law solutions. The effect of leakage across the screw flights was also shown.

Martin (68,69) obtained a numerical solution for fully developed flow which allowed for the finite width of the screw channel. In this case the flow problem could be described as fully developed, three-dimensional (x,y,z directions) and three-directional (v_x,v_y,v_z). The four simultaneous coupled second-order non-linear partial differential equations (3 momentum, 1 energy) were solved using the finite difference method. Martin's work showed the dominant effect of thermal convection in the transverse direction, thus confirming that for high values of Peclet number encountered in practice the isotherms tend to take up shapes which lie along streamlines. Also it was shown that for typical screws having relatively small aspect ratio (H/W) it is reasonable to apply the lubrication approximation in the transverse direction, provided the correct screw temperature boundary condition is employed which accounts for thermal convection in the recirculating transverse flow as already discussed. Dyer (24) attempted essentially the same problem and presented a very limited number of results, but his computer program contains a number of faults according to Fenner (28d).

6.1.4 Non-Newtonian Nonisothermal Developing Flow Solutions

Few attempts have been made to include the development of temperature profiles in the down channel direction. It was already stated in the last section that thermal convection in the transverse direction may be accounted for by a suitable choice of screw temperature boundary condition (i.e. $T_{sc} = T_b$). Yates (128) used the finite difference method to solve the following momentum and energy equations for a power-law fluid:

Momentum:
$$-\frac{\partial p}{\partial x} + \frac{\partial \tau_{yx}}{\partial y} = 0 \tag{6.11}$$

$$-\frac{\partial p}{\partial z} + \frac{\partial \tau_{yz}}{\partial y} = 0 \tag{6.12}$$

Energy:
$$\rho_m C p_m \, v_z \frac{\partial T}{\partial z} = k_m \frac{\partial^2 T}{\partial y^2} + \tau_{yx} \frac{\partial v_x}{\partial y} + \tau_{yz} \frac{\partial v_z}{\partial y} \tag{6.13}$$

where
$$z = 0 \qquad T = T_o$$

$$y = 0 \qquad v_x = v_z = 0 \qquad \frac{\partial T}{\partial y} = 0$$

$$y = H \qquad v_x = V_{bx} \qquad v_z = V_{bz} \qquad T = T_b$$

The power-law constitutive relation used (see also Sec. 2.4.2, Eqs. 2.33 to 2.34) is given by:

$$\tau_{yx} = \eta \frac{\partial v_x}{\partial y} \tag{6.14}$$

$$\tau_{yz} = \eta \frac{\partial v_z}{\partial y} \tag{6.15}$$

$$\eta = Ae^{-B(T-T_o)} \dot{\gamma}^{n-1} \tag{6.16}$$

$$\dot{\gamma} = \sqrt{\left(\frac{dv_x}{dy}\right)^2 + \left(\frac{dv_z}{dy}\right)^2} \tag{6.17}$$

Fenner (29) used the same mathematical model to study the design of large melt extruders. Instead of the adiabatic screw boundary condition, the revised screw temperature boundary condition ($T_{sc} = T_b$) was utilized. To demonstrate the importance of developing flow effects, a typical bulk mean temperature profile along the down channel direction of a 300 mm diameter screw extruder was presented. It was shown that the flow was far from being fully developed even at the delivery end of the machine. Kaiser and Smith (48) presented a much less rigorous analysis which allowed for downstream thermal convection. Instead of the local temperature, an average temperature was used in the convective term of the energy equation. An apparent viscosity calculated from the average temperature was also utilized. Results were given in the form of pressure profiles and average temperature rises. Experimental data were obtained on a 3.5 inch (89 mm) diameter extruder using polystyrene resin.

In summary, solutions have been obtained for polymer melt flows in extruder screw channels, and they may be divided into four general categories:

(i) isothermal Newtonian flow,

(ii) isothermal non-Newtonian flow,

(iii) fully developed nonisothermal non-Newtonian flow, and

(iv) developing nonisothermal non-Newtonian flow.

The solutions to the flow problems in the first three categories are usually presented in the form of screw characteristics (i.e., reduced flow rates plotted against dimensionless pressure gradient). However, results for developing flow problems are more difficult to present in such a concise form. Screw characteristics, for example, are no longer relevant in this case. Results are usually given in the form of bulk mean temperature and pressure profiles along the extruder screw channel. In fact, for design purposes the most useful result is the computer program itself (30). Such a program has been developed in this study and is described in the next section.

6.2 Development of a Melt Conveying Model

The development of a melt conveying model for an extruder screw channel is presented in this section. First a simple model for combined drag and pressure flow of an isothermal Newtonian fluid between infinitely wide parallel and converging plates is described. This model is then modified step by step to its final form (i.e., a model for developing nonisothermal non-Newtonian flow in a channel having rectangular cross-section as was shown in Fig. 6.1). The effects of channel curvature are not considered.

The equations of conservation of mass, momentum and energy were presented in simplified form in Sec. 2.4.1 (see Eqs. 2.11, and 2.25 to 2.27). These equations represent polymer melt flow between infinitely wide channels, and are utilized in the melt conveying models developed in this section. Initially, solutions are obtained by assuming that the melt flow occurs between infinitely wide parallel or converging plates. Then, to account for the finite channel width, correction factors (called shape factors) are used to modify the solutions obtained for infinitely wide channels. These shape factors are also used to correct the solutions for flow in the melt pool (i.e., where the solid bed and melt exist side by side). Thus, the finite difference solutions presented in this section are always for infinitely wide channels. The shape factors are subsequently used to correct these solutions for finite channel width.

6.2.1 Isothermal Newtonian Flow in Infinitely Wide Parallel and Converging Channels

The first step in the development of a melt conveying model is to obtain solutions for unidirectional (down channel) flow of an isothermal Newtonian fluid between both infinitely wide parallel and converging plates. The difference between the parallel and converging plate models is significant enough to warrant separate treatments. Initially, transverse flow is not considered, as it does not affect down channel flow rates and velocity profiles for isothermal Newtonian flow. The effects of transverse flow become important only when thermal effects and non-Newtonian flow behaviour are added to the model. The analytical solution for combined drag and pressure flow between infinitely wide parallel plates was already given in Eq. 6.4 (see Sec. 6.1.1) and so it may seem redundant to repeat the derivation here. However, since the finite difference method is used to solve the developing nonisothermal non-Newtonian flow problem, it is used here to solve the Newtonian flow problem for illustrative purposes. If a finite difference program can be written for Newtonian flow, then with some modifications the program can be converted to solve the non-Newtonian problem.

Flow Equations

The physical systems for combined drag and pressure flow between infinitely wide parallel plates and converging plates are shown respectively in Figs. 6.2(a) and 6.2(b). The simplified conservation equations for isothermal Newtonian flow are:

Continuity equation (integral form) in z-direction:

$$\int_o^H v_z \, dy = \frac{Q}{W} \tag{6.18}$$

Momentum equation in z-direction:

$$-\frac{dp}{dz} + \mu \frac{d^2 v_z}{dy^2} = 0 \tag{6.19}$$

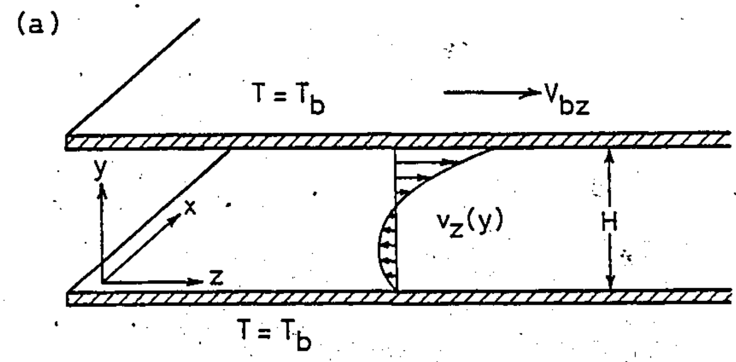

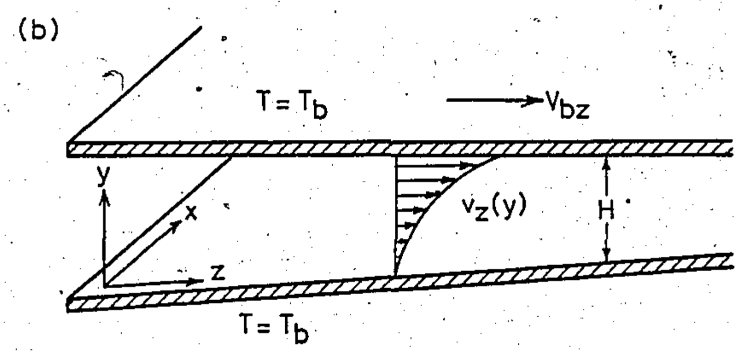

Fig. 6.2 Combined drag and pressure flow in the down channel direction between (a) infinitely wide parallel plates, and (b) infinitely wide converging plates. V_{bz} is the down channel component of the barrel velocity, and $v_z(y)$ is the down channel velocity profile of the polymer melt.

The boundary conditions for the above equations are:

$$
\begin{aligned}
z &= 0 \qquad p = p_o \\
y &= 0 \qquad v_z = 0 \\
y &= H \qquad v_z = V_{bz}
\end{aligned}
\tag{6.20}
$$

To represent Eqs. 6.18 to 6.20 in dimensionless form, let:

$$
\begin{aligned}
Vz &= \frac{v_z}{V_b} \\
P &= \frac{p}{\rho_m V_b^2} \\
Y &= \frac{y}{H} \\
Z &= \frac{k_m z}{\rho_m Cp_m V_b H_o^2}
\end{aligned}
\tag{6.21}
$$

where H is the local channel depth, and H_o the channel depth in the feed section of the extruder. Substituting the above into Eqs. 6.18 to 6.20, we obtain in terms of dimensionless parameters:

Continuity equation (integral form) in Z-direction:

$$\int_o^1 Vz\, dY = \frac{Q}{WH\, V_b} \tag{6.22}$$

Momentum equation in Z-direction:

$$\frac{-k_m}{\mu\, Cp_m\, H_o^2} \frac{dP}{dZ} + \frac{1}{H^2} \frac{d^2Vz}{dY^2} = 0 \tag{6.23}$$

Boundary conditions:

$$Z = 0 \qquad P = \frac{p_o}{\rho_m V_b^2}$$

$$Y = 0 \qquad Vz = 0 \tag{6.24}$$

$$Y = 1 \qquad Vz = \frac{V_{bz}}{V_b}$$

Finite Difference Solution - Parallel Plates

An implicit finite difference method is used to solve Eqs. 6.22 and 6.23 with the acompanying boundary conditions. The finite difference grid is illustrated in Fig. 6.3. Simpson's rule is used to represent the continuity equation (6.22) in finite difference form, and is given as follows for column n in the finite difference grid:

$$\int_o^1 Vz\, dY \approx \frac{\Delta Y}{3} [Vz_{1,n} + 4\, Vz_{2,n} + 2\, Vz_{3,n} + \ldots + 4\, Vz_{M,n} + Vz_{M+1,n}] \tag{6.25}$$

Substituting the above into Eq. 6.22, we obtain:

$$Vz_{1,n} + 4\, Vz_{2,n} + 2\, Vz_{3,n} + \ldots + 4\, Vz_{M,n} + Vz_{M+1,n} = \frac{3}{\Delta Y} \frac{Q}{WHV_b}$$

$$= 3M \frac{Q}{WHV_b} \tag{6.26}$$

For the momentum equation (6.22) the following finite difference approximation is used:

$$\frac{d^2 Vz}{dY^2} \approx \frac{Vz_{m+1,n} - 2Vz_{m,n} + Vz_{m-1,n}}{(\Delta Y)^2} \tag{6.27}$$

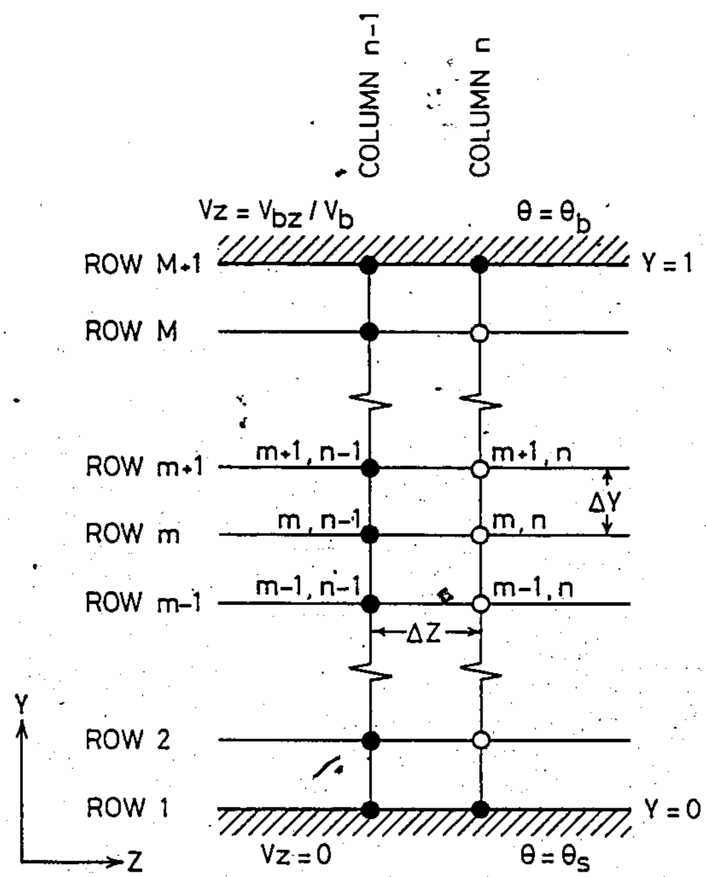

Fig. 6.3 Finite difference grid for down channel flow in a parallel channel. Dark nodes denote known values (either calculated or boundary values) and blank nodes denote values to be calculated.

Substituting the above into Eq. 6.22, we obtain for column n:

$$Vz_{m-1,n} - 2\,Vz_{m,n} + Vz_{m+1,n} - \alpha \left(\frac{dP}{dz}\right)_n = 0 \qquad (6.28)$$

where $m = 2, 3, \ldots, M$

$$\alpha = \frac{k_m}{\mu\, Cp_m} \left(\frac{H_n}{H_o}\right)^2 (\Delta Y)^2$$

Combining Eqs. 6.26 and 6.28, we have a modified tridiagonal system of M algebraic equations and M unknowns ($Vz_{2,n}$ to $Vz_{M,n}$ and $(dP/dZ)_n$). The equations may be written as follows:

$$\cancelto{0}{Vz_{1,n}} - 2\,Vz_{2,n} + Vz_{3,n} - \alpha \left(\frac{dP}{dz}\right)_n = 0$$

$$\vdots$$

$$Vz_{m-1,n} - 2\,Vz_{m,n} + Vz_{m+1,n} - \alpha \left(\frac{dP}{dZ}\right)_n = 0 \qquad (6.29)$$

$$\vdots$$

$$Vz_{M-1,n} - 2\,Vz_{M,n} + \cancelto{V_{bz}/V_b}{Vz_{M+1,n}} - \alpha \left(\frac{dP}{dZ}\right)_n = 0$$

$$\cancelto{0}{Vz_{1,n}} + 4\,Vz_{2,n} + 2\,Vz_{3,n} + \ldots + 4\,Vz_{M,n} + \cancelto{V_{bz}/V_b}{Vz_{M+1,n}} = 3M \frac{Q}{WH_n V_b}$$

or in matrix form:

$$
\begin{bmatrix}
-2 & 1 & & & & & & -\alpha \\
1 & -2 & 1 & & & & & -\alpha \\
 & & \cdot & & & & & \cdot \\
 & & & \cdot & & & & \cdot \\
 & & & & \cdot & & & \cdot \\
 & & 1 & -2 & 1 & & & -\alpha \\
 & & & & \cdot & & & \cdot \\
 & & & & & \cdot & & \cdot \\
 & & & & & & \cdot & \cdot \\
 & & & & & 1 & -2 & -\alpha \\
4 & 2 & 4 & \cdot\ \cdot\ \cdot & & 2 & -2 & 0
\end{bmatrix}
\begin{bmatrix}
Vz_{2,n} \\ Vz_{3,n} \\ \cdot \\ \cdot \\ \cdot \\ Vz_{m,n} \\ \cdot \\ \cdot \\ \cdot \\ Vz_{M,n} \\ \left(\frac{dP}{dZ}\right)_n
\end{bmatrix}
=
\begin{bmatrix}
0 \\ 0 \\ \cdot \\ \cdot \\ \cdot \\ 0 \\ \\ \\ 0 \\ -V_{bz}/V_b \\ 3M \frac{Q}{WH_n V_b} - \frac{V_{bz}}{V_b}
\end{bmatrix}
\qquad (6.30)
$$

Using Gaussian elimination this sytem of equations is solved for the down channel velocity profile and pressure gradient at column n in the finite difference grid. The algorithm used for solving the above modified tridiagonal system is described in Ref. (1). The pressure at column n may be calculated as follows:

$$P_n = P_{n-1} + \left(\frac{dP}{dZ}\right)_n \Delta Z \qquad (6.31)$$

Finally, the velocity profile and pressure gradient obtained by solving Eq. 6.30 should correspond to the analytical values given by the following expressions:

$$Vz(y) = \frac{6Q}{WH_n V_b} (Y - Y^2) + \frac{V_{bz}}{V_b} (3Y^2 - 2Y) \qquad (6.32)$$

$$\frac{dp}{dz} = 6\mu \left[\frac{V_{bz}}{H_n^2} - \frac{2Q}{WH_n^3}\right] \tag{6.33}$$

$$\frac{dP}{dZ} = \frac{Cp_m H_o^2}{k_m V_b} \frac{dp}{dz}$$

$$= \frac{6 \mu Cp_m}{k_m} \left(\frac{H_o}{H_n}\right)^2 \left[\frac{V_{bz}}{V_b} - \frac{2Q}{WH_n V_b}\right] \tag{6.34}$$

Finite Difference Solution - Converging Plates

For isothermal Newtonian flow between parallel plates, it makes no difference in Eq. 6.31 where the pressure gradient in the finite difference grid is calculated, be it at column n, column n-1 or at the midpoint between columns n and n-1, because the velocity profile and pressure gradient do not change in the down channel direction. This is, however, not the case for flow between converging plates. As the channel depth decreases in the downstream direction, the velocity profile and pressure gradient change significantly. A more accurate pressure profile is obtained by calculating the pressure gradient at the midpoint between columns n and n-1, denoted by n*, rather than at column n.

Again, an implicit finite difference method is used to solve the continuity and momentum equations (6.22 and 6.23) along with the boundary conditions (6.24). The finite difference grid is shown in Fig. 6.4. It should be noted that the dimensionless step size ΔY in the finite difference grid is always constant even though the channel depth H decreases with downstream distance Z (the number of nodal points in

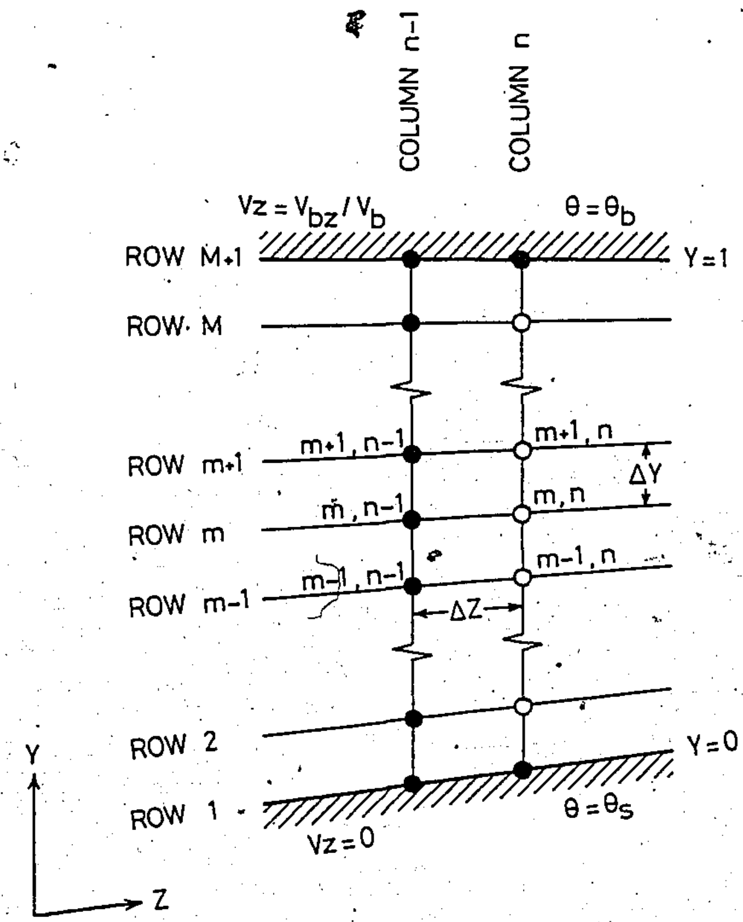

Fig. 6.4 Finite difference grid for down channel flow in a converging channel. Dark nodes denote known values (either calculated or boundary values) and blank nodes denote values to be calculated.

the Y-direction always remains the same). This is due to the definition of dimensionless distance Y (see Eq. 6.21) which is a function of local channel depth.

The continuity equation in finite difference form for converging plates is the same as for parallel plates (see Eq. 6.26):

$$Vz_{1,n} + 4Vz_{2,n} + 2Vz_{3,n} + \ldots + 4Vz_{M,n} + Vz_{M+1,n} = 3M \frac{Q}{WH_n V_b} \quad (6.35)$$

For the momentum equation (6.23) the following finite difference approximation is used:

$$\frac{1}{H^2} \frac{d^2Vz}{dY^2} = \frac{1}{2H_n^2} \left[\frac{Vz_{m+1,n} - 2Vz_{m,n} + Vz_{m-1,n}}{(\Delta Y)^2}\right] +$$

$$\frac{1}{2H_{n-1}^2} \left[\frac{Vz_{m+1,n-1} - 2Vz_{m,n-1} + Vz_{m-1,n-1}}{(\Delta Y)^2}\right] \quad (6.36)$$

Substituting the above into Eq. 6.23, we obtain:

$$Vz_{m-1,n} - 2Vz_{m,n} + Vz_{m+1,n} - \alpha \left(\frac{dP}{dz}\right)_{n*}$$

$$= -\left(\frac{H_n}{H_{n-1}}\right)^2 [Vz_{m-1,n-1} - 2Vz_{m,n-1} + Vz_{m+1,n-1}] \quad (6.37)$$

where $m = 2, 3, \ldots, M$

n^* = midpoint between columns n and n-1

$$\alpha = 2 \frac{k_m}{\mu Cp_m} \left(\frac{H_n}{H_o}\right)^2 (\Delta Y)^2$$

H_n and H_{n-1} refer to the channel depths at columns n and n-1 respectively. Combining Eqs. 6.35 and 6.37, we again obtain a modified tridiagonal system of M algebraic equations and M unknowns ($Vz_{2,n}$ to $Vz_{M,n}$ and $(dP/dz)_{n*}$). The equations may be written as follows:

$$\overset{0}{\cancel{Vz_{1,n}}} - 2Vz_{2,n} + Vz_{3,n} - \alpha \left(\frac{dP}{dz}\right)_{n*} = A_{2,n-1}$$

$$\vdots$$

$$Vz_{m-1,n} - 2Vz_{m,n} + Vz_{m+1,n} - \alpha \left(\frac{dP}{dZ}\right)_{n*} = A_{m,n-1} \tag{6.38}$$

$$\vdots$$

$$Vz_{M-1,n} - 2Vz_{M,n} + \overset{V_{bz}/V_b}{\cancel{Vz_{M+1,n}}} - \alpha \left(\frac{dP}{dZ}\right)_{n*} = A_{M,n-1}$$

$$\overset{0}{\cancel{Vz_{1,n}}} + 4Vz_{2,n} + 2Vz_{3,n} + \ldots + 4Vz_{M,n} + \overset{V_{bz}/V_b}{\cancel{Vz_{M+1,n}}} = 3M \frac{Q}{WH_n V_b}$$

where $A_{m,n-1} = -\left(\frac{H_n}{H_{n-1}}\right)^2 [Vz_{m-1,n-1} - 2Vz_{m,n-1} + Vz_{m+1,n-1}]$

The above system of equations is solved for the down channel velocity profile at column n and the pressure gradient at n* using Gaussian elimination (see Ref. (1) for algorithm). The pressure at column n is calculated as follows:

$$P_n = P_{n-1} + \left(\frac{dP}{dZ}\right)_{n*} \Delta Z \qquad (6.39)$$

It should be noted here that when dP/dZ at $n*$ is corrected for finite channel width by the use of shape factors described in the next section, the channel dimensions at $n*$ are to be used, not at column n.

6.2.2 Isothermal Newtonian Flow with the Effect of Channel Side Walls

In the previous section, solutions were presented for down channel velocity profiles and pressure gradients for isothermal Newtonian flow in infinitely wide channels. In essence it was assumed that the channel walls have negligible effect on the velocity profiles and pressure gradient. This assumption holds for pure drag or pressure flow in screw channels where H/W is less than 0.05, as is the case in the metering section of many screw extruders. The error introduced by neglecting the screw flight effects in such circumstances is relatively small compared to the errors resulting from other simplifcations.

One of the objectives in this thesis is to describe the solution for the combined drag and pressure flow of polymer melts in regions of the screw channel where the side wall effects on flow are not negligible. This may include all three sections (feed, compression, metering) of the screw channel, but more so the melt pool in the melting zone where the solid polymer coexists with the melt. It was shown in Sec. 6.1.1 (see Eq. 6.5) that the effect of screw flights on the flow rate in a completely melt filled channel could be accounted for by the use of the shape factors, F_p and F_d as in the following equation:

$$Q = Q_d F_d + Q_p F_p$$

$$= \frac{V_{bz} WH}{2} F_d - \frac{WH^3}{12\mu} \left(\frac{dp}{dz}\right) F_p \tag{6.40}$$

where Q_d and Q_p are the contributions of drag and pressure flow, respectively, to the total flow rate. The shape factors F_d and F_p are shown in Fig. 6.5 as functions of H/W.

Equation 6.40 is used to calculate the corrected flow rate in a finite width channel given the channel dimensions and the pressure gradient. Here, instead of calculating the flow rate, we would like to calculate the corrected pressure gradient given a specified value of the flow rate. To do this, we utilize the flow rate equation for an infinitely wide channel (parallel or converging) and the corresponding equation for a finite width channel. The flow rate between infinitely wide plates is given by:

$$\frac{Q}{W} = \frac{V_{bz}H}{2} - \frac{H^3}{12\mu} \left(\frac{dp}{dz}\right)^*$$

$$= a - b \left(\frac{dp}{dz}\right)^* \tag{6.41}$$

From Eq. 6.38 the flow rate in a finite width channel is given by:

$$\frac{Q}{W} = \frac{V_{bz}H}{2} F_d - \frac{H^3}{12\mu} \left(\frac{dp}{dz}\right) F_p$$

$$= a F_d - b F_p \left(\frac{dp}{dz}\right) \tag{6.42}$$

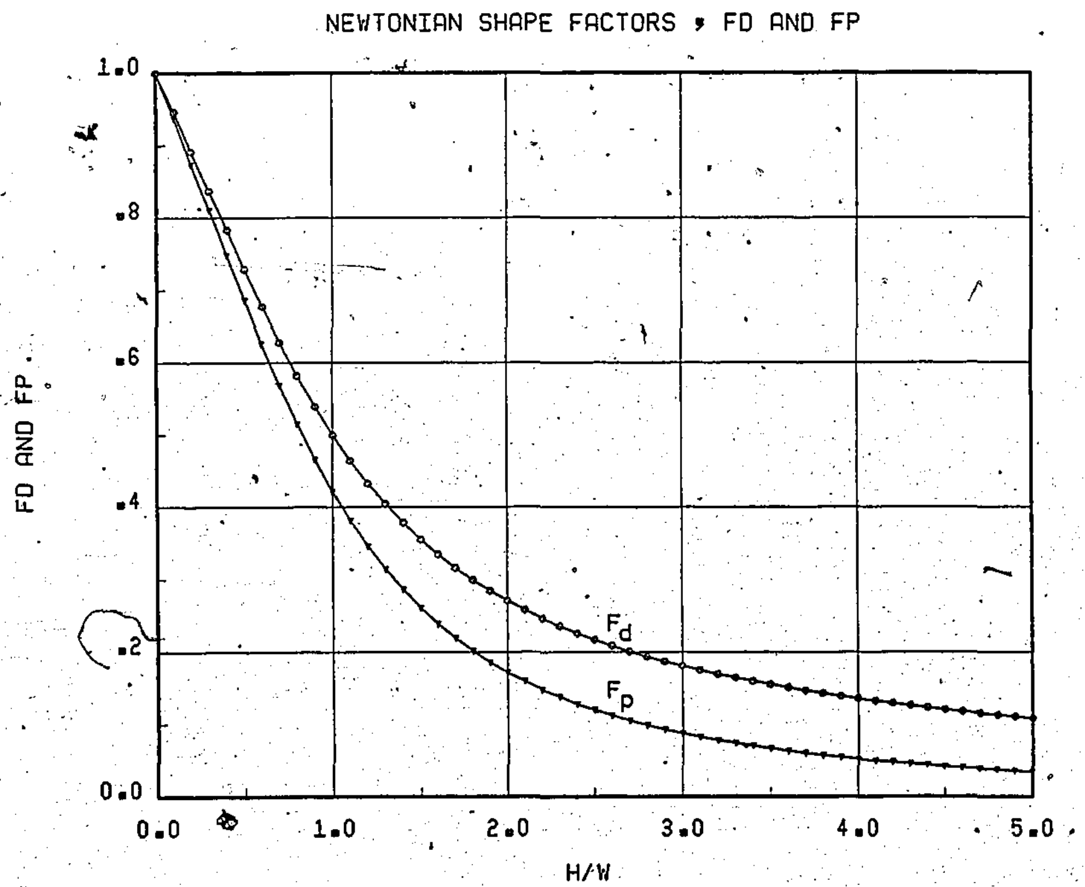

Fig. 6.5 Shape factors for drag and pressure flow.

The superscript * in Eq. 6.41 is used to indicate the pressure gradient in an infinitely wide channel as opposed to the pressure gradient in a finite width channel. Consider the case where the two flow rates are equal:

$$\frac{Q}{W} = a - b \left(\frac{dp}{dz}\right)^* = a\,F_d - b\,F_p \left(\frac{dp}{dz}\right) \qquad (6.43)$$

It can be shown upon rearrangement that:

$$\frac{dp}{dz} = \frac{1}{F_p}\left(\frac{dp}{dz}\right)^* + \frac{a(F_d - 1)}{b\,F_p}$$

$$= \frac{1}{F_p}\left(\frac{dp}{dz}\right)^* + \frac{6\,\mu\,V_{bz}}{H^2}\,\frac{(F_d - 1)}{F_p} \qquad (6.44)$$

In dimensionless terms (see Eq. 6.21),

$$\frac{dP}{dZ} = \frac{1}{F_p}\left(\frac{dP}{dZ}\right)^* + \frac{6\,\mu\,Cp_m\,V_{bz}}{k_m\,V_b}\left(\frac{H_o}{H}\right)^2\left(\frac{F_d - 1}{F_p}\right) \qquad (6.45)$$

where H_o is the channel depth in the feed section. Thus, the pressure gradient in a finite width channel can be obtained by first calculating the pressure gradient in an infinitely wide channel using the finite difference method (see Eq. 6.30 for parallel channels or Eq. 6.38 for a converging channels) and then correcting for finite channel width by using Eq. 6.45.

The effect of screw flights on pressure profiles are shown in Figs. 6.6 to 6.8 for the feed, compression and metering sections of a screw channel (completely filled with melt). In each case a solution

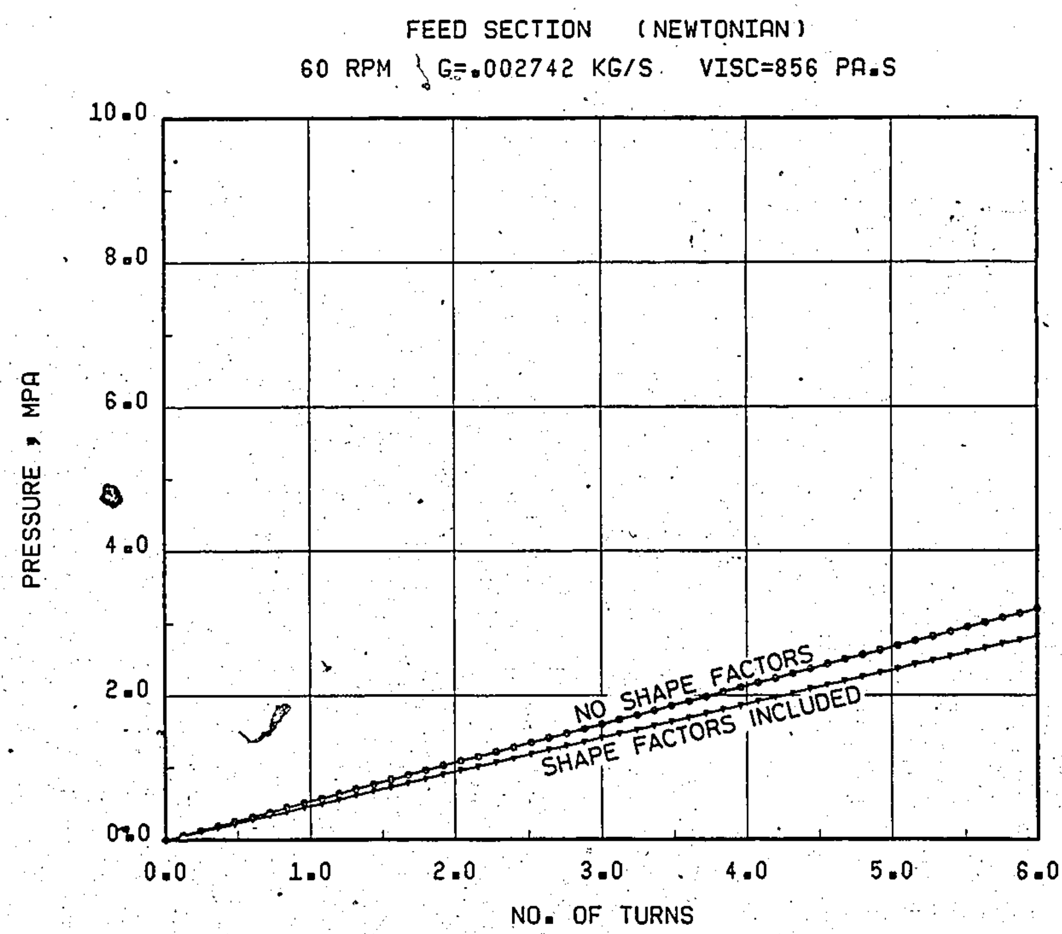

Fig. 6.6 Down channel pressure profiles in the feed section of the extruder screw channel for isothermal Newtonian flow. Data for the polymer properties, screw channel dimensions and extruder operating conditions are given in App. G.4.

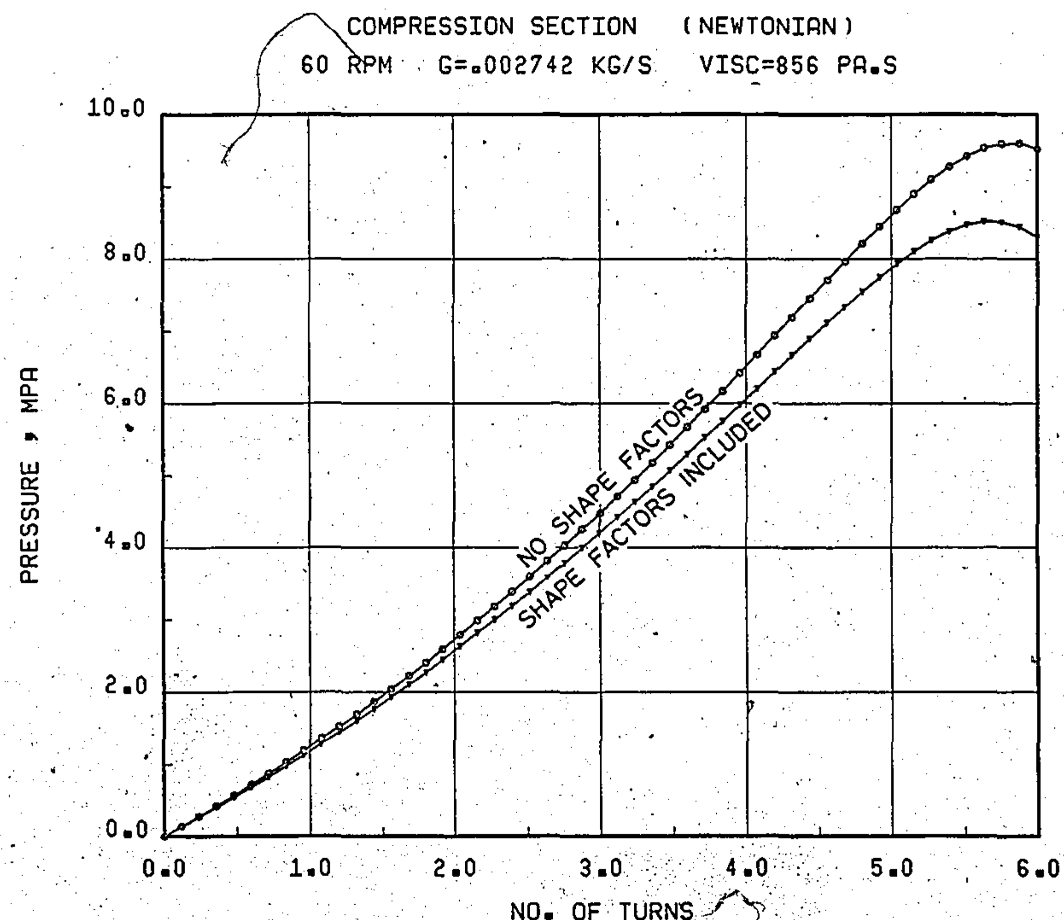

Fig. 6.7 Down channel pressure profiles in the compression section of the extruder screw channel for isothermal Newtonian flow. Data for the polymer properties, screw channel dimensions and extruder operating conditions are given in App. G.4.

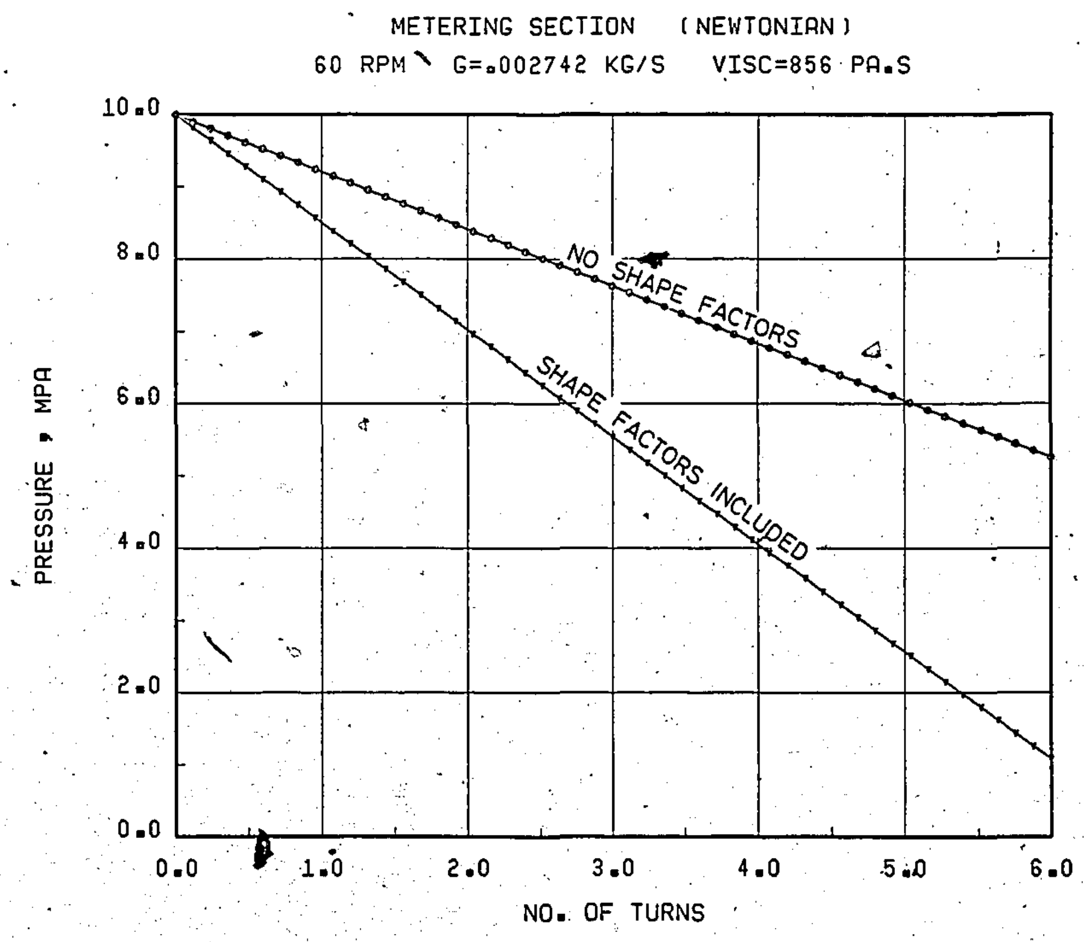

Fig. 6.8 Down channel pressure profiles in the metering section of the extruder screw channel for isothermal Newtonian flow. Data for the polymer properties, screw channel dimensions and extruder operating conditions are given in App. G.4.

for the pressure gradient was obtained for flow in an infinitely wide channel. The pressure gradient was then corrected for finite channel width using Eq. 6.45. It can be seen in Figs. 6.6 and 6.7 (where the pressures are on the rise) that the pressure gradients for flow in finite width channels are shallower than for flow in infinitely wide channels. In Fig. 6.8 the pressures are on a decline and the pressure gradient for the finite width channel is steeper than for the channel having infinite width. The effect of channel walls (for increasing pressures) is to decrease the pressure gradient whereas for decreasing pressures the pressure gradient is greater (in magnitude). For pure pressure flow, pressure gradients in finite width channels are always steeper than in channels having infinite width. Thus, for combined drag and pressure flow in finite width screw channels the effect of screw flights on pressure gradients is due to not only the channel dimensions but also the relative contributions of the drag and pressure flows to the total flow rate in the channels.

In the case of combined drag and pressure flow in the melt pool, the velocity profiles and pressure gradient are affected also by the moving solid bed. The solid bed may be thought of as a moving side wall with constant down channel velocity V_{sz} and thus contributing to drag flow in the melt pool. The flow rate in the melt pool may be expressed as:

$$Q = Q_d F_d + Q_{ds} F_{ds} + Q_p F_p$$

$$= \frac{V_{bz} WH}{2} F_d + \frac{V_{sz} WH}{2} F_{ds} - \frac{WH^3}{12\mu} \left(\frac{dp}{dz}\right) F_p \quad (6.46)$$

drag flow due to moving barrel	drag flow due to moving solid bed	pressure flow

or

$$\frac{Q}{W} = \frac{V_{bz} H}{2} F_d + \frac{V_{sz} H}{2} F_{ds} - \frac{H^3}{12\mu} \left(\frac{dp}{dz}\right) F_p$$

$$= a\ F_d + c\ F_{ds} - b\ F_p \left(\frac{dp}{dz}\right) \quad (6.47)$$

where F_{ds} is the drag flow shape factor for channel depth W and channel width H. Consider the flow rate in the melt pool equal to that in an infinitely wide channel (see Eq. 6.41):

$$\frac{Q}{W} = a - b \left(\frac{dp}{dz}\right)^* = a\ F_d + c\ F_{ds} - b\ F_p \left(\frac{dp}{dz}\right) \quad (6.48)$$

After rearrangement, the "corrected" pressure gradient is given by:

$$\frac{dp}{dz} = \frac{1}{F_p} \left(\frac{dp}{dz}\right)^* + \frac{a(F_d - 1) + c\ F_{ds}}{b\ F_p}$$

$$= \frac{1}{F_p} \left(\frac{dp}{dz}\right)^* + \frac{6\mu}{H^2} \left[\frac{V_{bz}(F_d - 1) + V_{sz} F_{ds}}{F_p}\right] \quad (6.49)$$

or in dimensionless terms:

$$\frac{dP}{dZ} = \frac{1}{F_p}\left(\frac{dP}{dZ}\right)^* + \frac{6\mu\, Cp_m}{k_m\, V_b}\left(\frac{H_o}{H}\right)^2 \left[\frac{V_{bz}\,(F_d - 1) + V_{sz}\,F_{ds}}{F_p}\right] \qquad (6.50)$$

Thus, the corrected dimensionless pressure gradients for melt filled channels and for the melt pool are given by Eqs. 6.45 and 6.50 respectively.

Calculation of Shape Factors

The shape factors, F_d and F_p, for pure drag and pressure flows respectively are given by the following analytical expressions (104):

$$F_d\left(\frac{H}{W}\right) = \frac{16W}{\pi^3 H} \sum_{n=1,3,\ldots}^{\infty} \frac{1}{n^3} \tanh\left(\frac{n\pi H}{2W}\right) \qquad (6.51)$$

$$F_p\left(\frac{H}{W}\right) = 1 - 192\,\frac{H}{\pi^5 W} \sum_{n=1,3,\ldots}^{\infty} \frac{1}{n^5} \tanh\left(\frac{n\pi W}{2H}\right) \qquad (6.52)$$

The tenth term of the summation in Eq. 6.51 is of the order 10^{-3}, and in Eq. 6.52 of the order 10^{-6}. Thus, several terms in the summation are needed in these equations, especially for F_d, in order that accurate values of shape factors may be obtained.

In the case of flow in tapered channels or in the melt pool where H/W is changing in the down channel direction, repeated calculations of F_d and F_p using Eqs. 6.51 and 6.52 can use up a significant amount of computer time. To overcome this problem, the shape factors F_d and F_p are expressed as functions of H/W by the following polynomial expressions:

$$\ln F_d \left(\frac{H}{W}\right) = a_o + a_1 \frac{H}{W} + a_2 \left(\frac{H}{W}\right)^2 + \ldots + a_N \left(\frac{H}{W}\right)^N \tag{6.53}$$

$$\ln F_p \left(\frac{H}{W}\right) = b_0 + b_1 \frac{H}{W} + b_2 \left(\frac{H}{W}\right)^2 + \ldots + b_N \left(\frac{H}{W}\right)^N \tag{6.54}$$

where a_n and b_n are parameters obtained by fitting Eqs. 6.53 and 6.54 to the analytical values of F_d and F_p using linear regression. In addition it is shown in App. A that:

$$F_d \left(\frac{H}{W}\right) = 1 - F_d \left(\frac{W}{H}\right) \tag{6.55}$$

$$F_p \left(\frac{H}{W}\right) = \left(\frac{W}{H}\right)^2 F_p \left(\frac{W}{H}\right) \tag{6.56}$$

With the identities given in Eqs. 6.55 and 6.56, it is necessary only to curve-fit F_d and F_p in the range H/W = 0 to 1 which is considerably easier than if the range were 0 to 10 or 0 to 20. If values of F_d and F_p for H/W > 1 are needed, then F_d (W/H) and F_p (W/H) for W/H < 1 are first calculated using Eqs. 6.53 and 6.54 and then are converted to F_d (H/W) and F_p (H/W) using Eqs. 6.55 and 6.56. In this study the following sixth-order polynomial equations are used to calculate F_d and F_p in the range H/W = 0 to 1:

$$\ln F_d \left(\frac{H}{W}\right) = \sum_{n=0}^{6} a_n \left(\frac{H}{W}\right)^n \tag{6.57a}$$

$$\ln F_p \left(\frac{H}{W}\right) = \sum_{n=0}^{6} b_n \left(\frac{H}{W}\right)^n \tag{6.57b}$$

where

$$a_o = -0.54184485 \qquad b_o = -0.62870425$$
$$a_1 = -0.17357760 \qquad b_1 = -0.23641853$$
$$a_2 = 0.18083463 \qquad b_2 = 0.23095889$$
$$a_3 = -0.92160908 \qquad b_3 = -1.2000440$$
$$a_4 = 1.5420764 \qquad b_4 = 1.9176489$$
$$a_5 = -1.0334506 \qquad b_5 = -1.2485500$$
$$a_6 = 0.25442251 \qquad b_6 = 0.30172093$$

6.2.3 Nonisothermal Newtonian Flow with Developing Temperature Profiles

The next step in the formulation of a melt flow model in the extruder is to include the development of temperature in the down channel direction. This entails the solution of the conservation of energy equation, which in its simplified form is given by:

$$\rho_m Cp_m v_z \frac{\partial T}{\partial z} = k_m \frac{\partial^2 T}{\partial y^2} + \mu \left[\overset{0}{\left(\frac{dv_x}{dy}\right)^2} + \left(\frac{dv_z}{dy}\right)^2 \right] \tag{6.58}$$

where

$$\begin{aligned} z &= 0 & T &= T_o \\ y &= 0 & T &= T_{sc} = T_b \\ y &= H & T &= T_b \end{aligned} \tag{6.59}$$

Equation 6.58 represents the development of temperature in an infinitely wide flow channel (parallel or convergent). The down channel velocity v_z and velocity gradient dv_z/dy may be independently obtained from the momentum equation (Eq. 6.30 or 6.38) due to the Newtonian nature of the flow. A constant temperature profile $T(y) = T_o$ has been chosen as a boundary condition at $z = 0$ (i.e. at the beginning of the melt flow region). Other profiles could have also been used. The barrel temperature boundary condition is denoted as $T = T_b$, where the barrel temperature T_b is a constant at a given down channel position but can also be a specified function of down channel distance. The latter is desirable provision since in many cases extruders operate with a specified barrel temperature profile. Finally the screw temperature boundary condition has been chosen as $T = T_{sc} = T_b$, where the screw surface temperature is assumed equal to that of the barrel as first suggested by Griffith (36) and discussed in the literature survey of melt flow models (see Sec. 6.1.3). Other screw and barrel temperature boundary conditions may be utilized, namely:

(i) $$\begin{aligned} y &= 0 \qquad T = T_{melt} \\ y &= H \qquad T = T_b \end{aligned} \tag{6.60}$$

(ii) $$\begin{aligned} y &= 0 \qquad \frac{\partial T}{\partial y} = 0 \\ y &= H \qquad T = T_b \end{aligned} \tag{6.61}$$

(iii) $$\begin{aligned} y &= 0 \qquad \frac{\partial T}{\partial y} = 0 \\ y &= H \qquad \frac{\partial T}{\partial y} = 0 \end{aligned} \tag{6.62}$$

where T_{melt} is the melting temperature of the polymer. The temperature boundary conditions in Eqs. 6.60 to 6.62 are not treated here, but may be incorporated into the flow model with minimal changes in the computer program.

Let

$$Vz = \frac{v_z}{V_b}$$

$$\theta = \frac{T}{T_{melt}}$$

$$Y = \frac{y}{H} \qquad (6.63)$$

$$Z = \frac{k_m z}{\rho_m Cp_m V_b H_o^{\,2}}$$

where H_o is the channel depth in the feed section of the screw channel. Substituting the above into the energy equation (6.58) and boundary conditions (6.59), we obtain in terms of dimensionless parameters:

Energy equation:

$$\frac{1}{H_o^{\,2}} Vz \frac{\partial \theta}{\partial Z} = \frac{1}{H^2} \frac{\partial^2 \theta}{\partial Y^2} + \frac{\mu V_b^{\,2}}{k_m T_{melt}} \left[\frac{1}{H^2} \left(\frac{dVz}{dY}\right)^2 \right] \qquad (6.64)$$

where

$$\begin{aligned} Z &= 0 & \theta &= \theta_o = T_o \\ Y &= 0 & \theta &= \theta_{sc} = T_b/T_{melt} \\ Y &= 1 & \theta &= \theta_b = T_b/T_{melt} \end{aligned} \qquad (6.65)$$

Finite Difference Solution - Parallel Channel

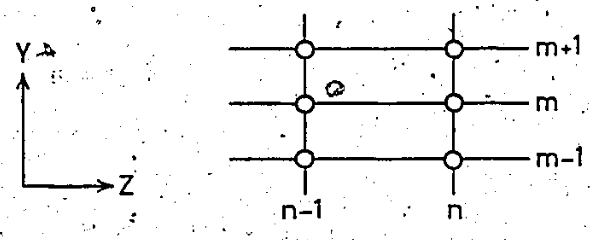

Fig. 6.9 Finite difference grid for a parallel channel.

The Crank-Nicolson implicit finite difference method is used to solve the energy equation (6.64) along with the accompanying boundary conditions (6.65). The finite difference grid used is the same as for isothermal flow (see Fig. 6.3). An abbreviated form of the finite difference grid is shown in Fig. 6.9. For the energy equation, the following finite difference approximations are used:

$$\frac{\partial\theta}{\partial Z} \simeq \frac{\theta_{m,n} - \theta_{m-1,n}}{\Delta Z} \tag{6.66}$$

$$\frac{\partial^2\theta}{\partial Y^2} \simeq \frac{1}{2}\left[\frac{\theta_{m+1,n} - 2\theta_{m,n} + \theta_{m-1,n}}{(\Delta Y)^2}\right]$$

$$+ \frac{1}{2}\left[\frac{\theta_{m+1,n-1} - 2\theta_{m,n-1} + \theta_{m-1,n-1}}{(\Delta Y)^2}\right] \tag{6.67}$$

Substituting the above into Eq. 6.64, we obtain for column n in the finite difference grid:

$$-\theta_{m-1,n} + (\beta + 2)\,\theta_{m,n} - \theta_{m+1,n} = \theta_{m-1,n-1} + (\beta - 2)\,\theta_{m,n-1} + \theta_{m+1,n-1} + \gamma_m \qquad (6.68)$$

where $\quad m = 2,3, \ldots, M$

$$\beta = 2\left(\frac{\Delta Y}{\Delta Z}\right)^2 \left(\frac{H_n}{H_o}\right)^2 Vz_{avg,n}$$

$$\gamma_m = 2(\Delta Y)^2 \frac{\mu V_b^2}{k_m T_{melt}} \left(\frac{dVz}{dY}\right)^2_{m,n}$$

H_n is the channel depth at column n, and the velocity gradient $(dVz/dY)_{m,n}$ is obtained from the velocity profile calculated earlier in Eq. 6.30. An average velocity Vz_{avg} instead of Vz is used in Eq. 6.68 because in some regions of the screw channel there may be negative down channel velocity components due to pressure backflow. Since the Crank-Nicolson method is a forward marching numerical technique, negative velocities will very quickly cause it to go unstable.

Equation 6.68 represents a tridiagonal system of M-1 equations and M-1 unknowns ($\theta_{2,n}, \theta_{3,n}, \ldots, \theta_{M,n}$), and may be written as follows:

$$-\overset{\theta_{sc}}{\cancel{\theta_{1,n}}} + (\beta + 2)\ \theta_{2,n} - \theta_{3,n} = A_{2,n-1} + \gamma_2 = B_2$$

$$\vdots$$

$$-\theta_{m-1,n} + (\beta + 2)\ \theta_{m,n} - \theta_{m+1,n} = A_{m,n-1} + \gamma_m = B_m \tag{6.69}$$

$$\vdots$$

$$-\theta_{M-1,n} + (\beta + 2)\ \theta_{M,n} - \overset{\theta_b}{\cancel{\theta_{M+1,n}}} = A_{M,n-1} + \gamma_M = B_M$$

where $A_{M,n-1} = \theta_{m-1,n-1} + (\beta - 2)\ \theta_{m,n-1} + \theta_{m+1,n-1}$

or in matrix form:

$$\begin{bmatrix} \beta+2 & -1 & & & & \\ -1 & \beta+2 & -1 & & & \\ & & \ddots & & & \\ & & -1 & \beta+2 & -1 & \\ & & & & \ddots & \\ & & & & -1 & \beta+2 \end{bmatrix} \begin{bmatrix} \theta_{2,n} \\ \theta_{3,n} \\ \vdots \\ \theta_{m,n} \\ \vdots \\ \theta_{M,n} \end{bmatrix} = \begin{bmatrix} B_2 + \theta_{sc} \\ B_3 \\ \vdots \\ B_m \\ \vdots \\ B_M + \theta_b \end{bmatrix} \tag{6.70}$$

This tridiagonal system of equations is solved for the temperature profile at column n by Gaussian elimination using Thomas' method (for details of the algorithm, see Refs. (1),(55)).

Finite Difference Solution - Converging Channel

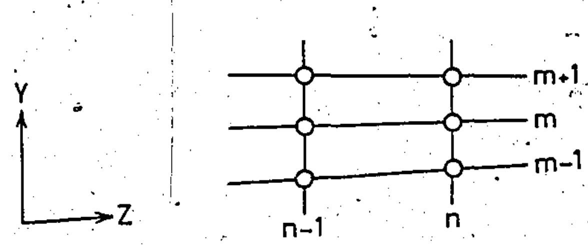

Fig. 6.10 Finite difference grid for a converging channel.

For melt flow in the compression section of the extruder screw channel, slightly different finite difference queations are used than for the parallel flow channels in the feed and metering sections. The finite difference grid used is the same as for isothermal flow in a converging channel (see Fig. 6.4). An abbreviated version of this grid is shown in Fig. 6.10. The following finite difference approximations are used for the energy equation (6.64):

$$\frac{\partial \theta}{\partial Z} = \frac{\theta_{m,n} - \theta_{m,n-1}}{\Delta Z} \tag{6.71}$$

$$\frac{1}{H^2}\frac{\partial^2 \theta}{\partial Y^2} = \frac{1}{2H_n^2}\left[\frac{\theta_{m+1,n} - 2\theta_{m,n} + \theta_{m-1,n}}{(\Delta Y)^2}\right]$$

$$+ \frac{1}{2H_{n-1}^2}\left[\frac{\theta_{m+1,n-1} - 2\theta_{m,n-1} + \theta_{m-1,n-1}}{(\Delta Y)^2}\right] \tag{6.72}$$

$$Vz = \frac{Vz_{avg,n} + Vz_{avg,n-1}}{2} \tag{6.73}$$

$$\frac{1}{H^2}\left(\frac{dVz}{dY}\right)^2 = \frac{1}{2H_n^2}\left(\frac{dVz}{dY}\right)^2_{m,n} + \frac{1}{2H_{n-1}^2}\left(\frac{dVz}{dY}\right)^2_{m,n-1}$$

where H_n and H_{n-1} are the channel depths at columns n and n-1 respectively in the finite difference grid. Substituting the above into Eq. 6.64, we obtain for column n:

$$-\theta_{m-1,n} + (\beta+2)\,\theta_{m,n} - \theta_{m+1,n}$$

$$= \delta\,\theta_{m-1,n-1} + (\beta - 2\delta)\,\theta_{m,n-1} + \delta\,\theta_{m+1,n-1} + \gamma_m \tag{6.75}$$

where $m = 2,3, \ldots, M$

$$\beta = \frac{(\Delta Y)^2}{\Delta Z}\left(\frac{H_n}{H_o}\right)^2 (Vz_{avg,n} + Vz_{avg,n-1})$$

$$\delta = \left(\frac{H_n}{H_{n-1}}\right)^2$$

$$\gamma_m = (\Delta Y)^2 \frac{\mu V_b^2}{k_m T_{melt}}\left[\left(\frac{dVz}{dY}\right)^2_{m,n} + \delta\left(\frac{dVz}{dY}\right)^2_{m,n-1}\right]$$

Again, Eq. 6.75 represents a tridiagonal system of M-1 equations and M-1 unknowns ($\theta_{2,n}$, $\theta_{3,n}$, ..., $\theta_{M,n}$), and may be written as follows:

$$-\overset{\theta_{sc}}{\cancel{\theta_{1,n}}} + (\beta+2)\,\theta_{2,n} - \theta_{3,n} = C_{2,n-1} + \gamma_2 = D_2$$

$$\vdots$$

$$-\theta_{m-1,n} + (\beta+2)\,\theta_{m,n} - \theta_{m+1,n} = C_{m,n-1} + \gamma_m = D_m \tag{6.76}$$

$$\vdots$$

$$-\theta_{M-1,n} + (\beta+2)\,\theta_{M,n} - \overset{\theta_b}{\cancel{\theta_{M+1,n}}} = C_{M,n-1} + \gamma_M = D_M$$

where $C_{m,n} = \delta\,\theta_{m-1,n-1} + (\beta - 2\delta)\,\theta_{m,n-1} + \delta\,\theta_{m+1,n-1}$

As in the case of parallel plates, the above tridiagonal system of equations is solved for the temperature profile at column n by Gaussian elimination rising Thomas' method (see Refs. (1, 55) for details of algorithm).

Bulk Temperature

To describe the development of temperature in the downstream direction of the screw channel, the average temperature is calculated at each column in the finite difference grid from the temperature profile obtained in either Eq. 6.70 or 6.76. A common representation of the average temperature is the flow-average (bulk) temperature which is defined as:

$$T_{bulk} = \frac{\int_0^H v_z(y,z)\, T(y,z)\, dy}{\int_0^H v_z(y,z)\, dy} \tag{6.76}$$

or in dimensionless form:

$$\theta_{bulk} = \frac{\int_0^1 Vz(Y,Z)\, \theta(Y,Z)\, dY}{\int_0^1 Vz(Y,Z)\, dY} \tag{6.77}$$

Equation 6.77 may be written in finite difference form for column n, using Simpson's Rule as follows:

$$\theta_{bulk,n} = \frac{Vz_1\ \theta_1 + 4\ Vz_2\ \theta_2 + 2\ Vz_3\ \theta_3 + \ldots + 4\ Vz_M\ \theta_M + Vz_{M+1}\ \theta_{M+1}}{Vz_1 + 4\ Vz_2 + 2\ Vz_3 + \ldots + 4\ Vz_M + Vz_{M+1}} \tag{6.78}$$

Earlier it was indicated that the down channel velocity may be negative in some regions of the screw channel. For this reason, absolute values of velocity have been used in Eq. 6.77, and as a result the bulk temperature is written as:

$$\theta_{bulk,n} = \frac{|Vz_1|\ \theta_1 + 4|Vz_2|\ \theta_2 + \ldots + 4|Vz_M|\ \theta_M + |Vz_{m+1}|\ \theta_{m+1}}{|Vz_1| + 4|Vz_2| + 2|Vz_3| + \ldots + 4|Vz_M| + |Vz_{m+1}|} \tag{6.79}$$

Other forms of average temperature, for example area-average temperature, could be used to avoid the complication caused by negative velocities. Such an alternative is examined further in App. B, and it is concluded that the flow-average (bulk) representation of developing temperature is the most appropriate choice.

Results of Simulations

Plots of bulk templerature versus down channel distance are shown in Figs. 6.11 to 6.13 for melt flow in the feed, compression and metering sections of an extruder screw channel. A constant temperature boundary condition at the screw and barrel surface ($T_{sc} = T_b = 180^{\circ}C$) was used in all three sections. For each section, results are presented for three screw speeds: 40, 60 and 80 rpm. Even though the heat generated by viscous dissipation increases with increasing screw speed, in the regions where the temperatures are still developing the bulk temperatures are lower at higher screw speeds. This trend is reversed as fully developed temperature conditions are approached (i.e. in longer flow channels).

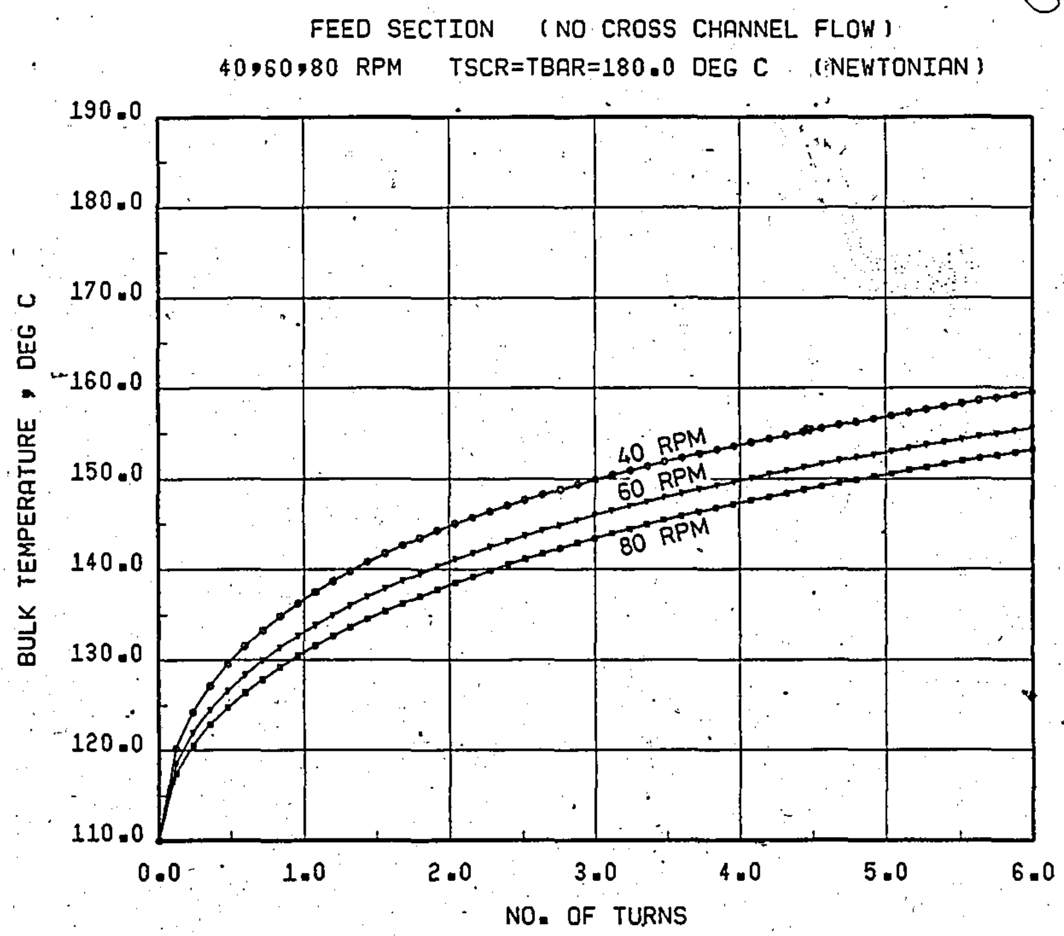

Fig. 6.11 Down channel bulk temperature profiles in the feed section of the extruder screw channel for Newtonian flow. Data for the polymer properties, screw channel dimensions and extruder operating conditions are given in App. G.4

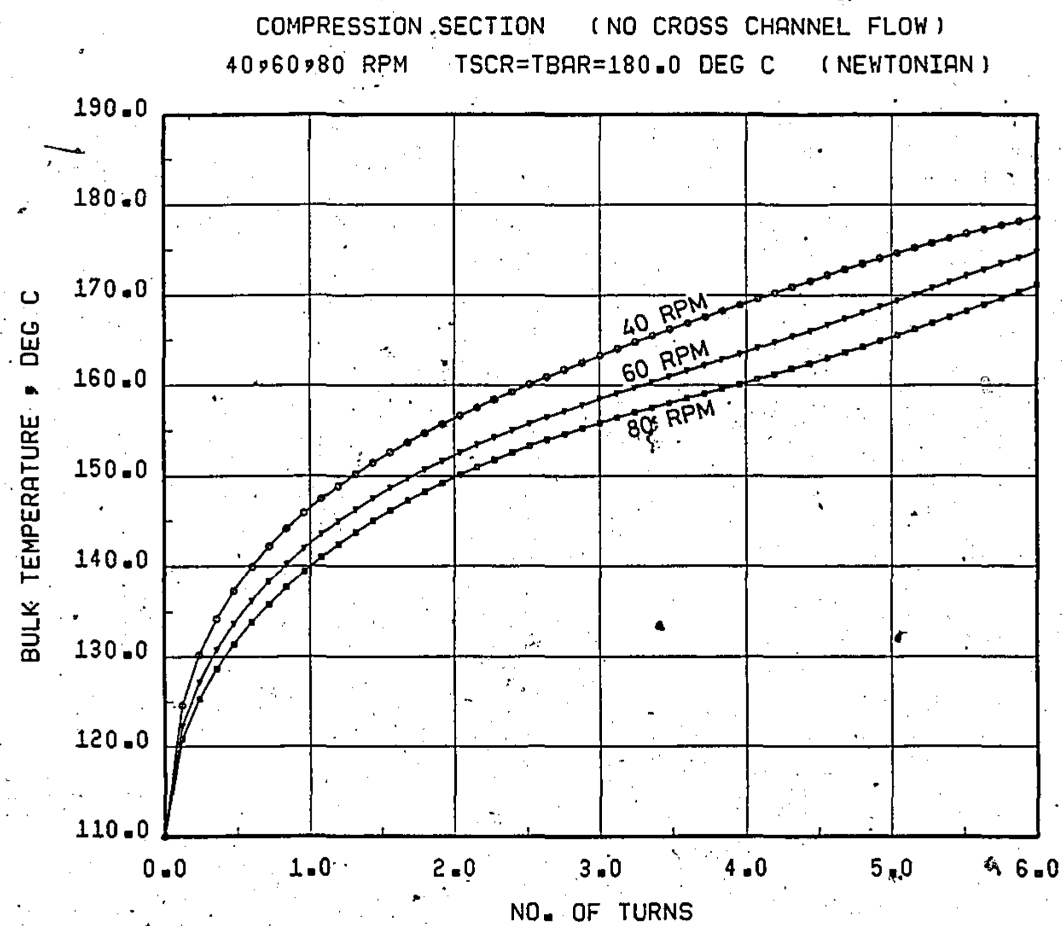

Fig. 6.12 Down channel bulk temperature profiles in the compression section of the extruder screw channel for Newtonian flow. Data for the polymer properties, screw channel dimensions and extruder operating conditions are given in App. G.4

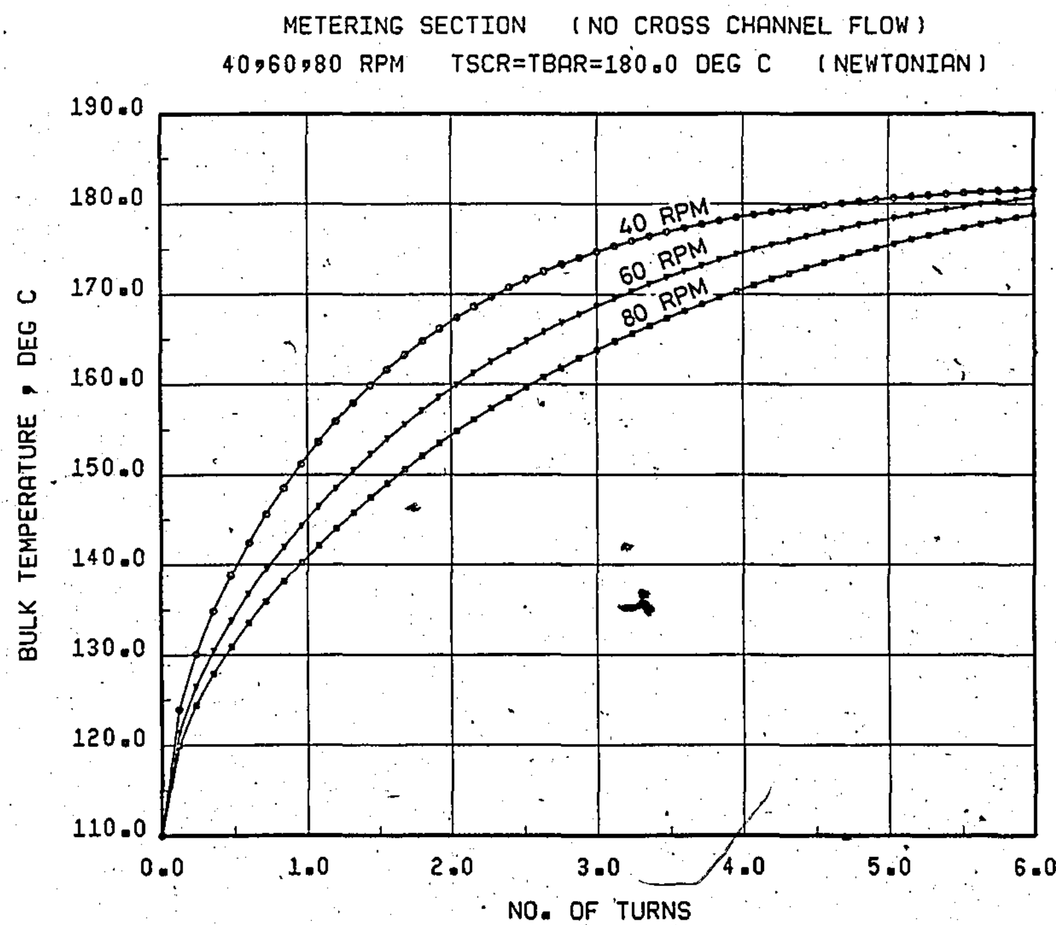

Fig. 6.13 Down channel bulk temperature profiles in the metering section of the extruder screw channel for Newtonian flow. Data for the polymer properties, screw channel dimensions and extruder operating conditions are given in App. G.4

6.2.4 Nonisothermal Newtonian Developing Flow - including Transverse Flow

In Sec. 6.2.1 (isothermal Newtonian flow), only down channel velocity profiles were calculated since the down channel pressure gradient is not influenced by transverse (cross channel) flow. Transverse flow does, however, affect the development of temperature profiles via the viscous dissipation term in the energy equation (6.58). In this section, the cross channel velocity equations are developed and presented in finite difference form. The energy equation is also given with the cross channel velocity gradient included in the viscous dissipation term. Since the down channel velocity equations are the same as before, they are not rewritten here.

Continuity and Momentum Equations in x-direction

The calculation of the cross channel velocity profiles is similar to that for the down channel flow. Assuming no leakage of melt across the screw flights, the continuity and momentum equations maybe written as:

Continuity equation (integral form) in x-direction:

$$\int_{o}^{H} v_x \, dy = 0 \qquad (6.80)$$

Momentum equation in x-direction:

$$-\frac{\partial p}{\partial x} + \mu \frac{\partial^2 v_x}{\partial y^2} = 0 \qquad (6.81)$$

Boundary conditions:

$$\begin{aligned} y &= 0 \qquad v_x = 0 \\ y &= H \qquad v_x = V_{bx} \end{aligned} \qquad (6.82)$$

To represent the continuity and momentum equations in dimensionless form, let:

$$\begin{aligned} Vx &= \frac{v_x}{V_{bx}} \\ X &= \frac{k_m\, x}{\rho_m Cp_m V_b\, H_o^2} \end{aligned} \qquad (6.83)$$

Substituting the above into Eqs. 6.80 and 6.81 along with the other dimensionless parameters given in Eq. 6.21, we obtain:

Continuity equation (integral form) in X-direction:

$$\int_o^1 Vx\, dY = 0 \qquad (6.84)$$

Momentum equation in X-direction:

$$-\frac{k_m}{\mu\, Cp_m\, H_o^2} \frac{\partial P}{\partial X} + \frac{1}{H^2} \frac{\partial^2 Vz}{\partial Y^2} = 0 \qquad (6.85)$$

Boundary conditions:

$$Y = 0 \qquad Vx = 0$$
$$Y = 1 \qquad Vx = \frac{V_{bx}}{V_b} \tag{6.86}$$

Finite Difference Solution - Parallel Channel

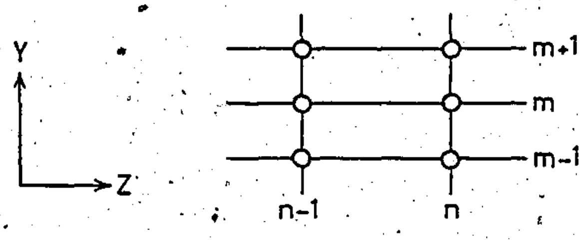

Fig. 6.14 Finite difference grid for parallel channel.

The same implicit finite difference method is used to solve the continuity and momentum equations (6.84 and 6.85) in the X-direction as in Sec 6.2.1 for down channel flow (see Eqs. 6.25 to 6.30). At column n in the finite difference grid (see Fig. 6.14) the continuity and momentum equations for cross channel flow in a parallel channel may be written in finite difference form as follows:

$$\overset{0}{\cancel{Vx_{1,n}}} - 2Vx_{2,n} + Vx_{3,n} - \alpha\left(\frac{\partial P}{\partial X}\right)_n = 0$$

$$\vdots$$

$$Vx_{m-1,n} - 2\,Vx_{m,n} + Vx_{m+1,n} - \alpha\left(\frac{\partial P}{\partial X}\right)_n = 0$$

$$\vdots$$

$$Vx_{M-1,n} - 2\,Vx_{M,n} + \overset{V_{bx}/V_b}{\cancel{Vx_{M+1,n}}} - \alpha\left(\frac{\partial P}{\partial X}\right)_n = 0 \qquad (6.87)$$

$$\overset{0}{\cancel{Vx_{1,n}}} + 4\,Vx_{2,n} + 2\,Vx_{3,n} + \ldots + 4\,Vx_{M,n} + \overset{V_{bx}/V_b}{\cancel{Vx_{M+1,n}}} = 0$$

where $$\alpha = \frac{k_m}{\mu\, Cp_m}\left(\frac{H_n}{H_o}\right)^2 (\Delta Y)^2$$

The above modified tridagonal system of equations is solved for the cross channel velocity profile and velocity gradient by Gaussian elimination (see Ref. (1) for the algorithm).

<u>Finite Difference Solution - Converging Channel</u>

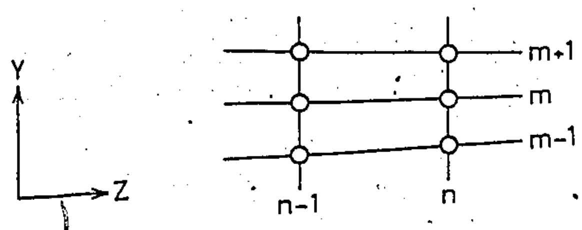

Fig. 6.15 Finite difference grid for a converging channel.

For cross channel flow in a converging channel, the continuity and momentum equations (6.84 and 6.85) may be written in finite difference form for column n in the finite difference grid (see Fig. 6.15) as follows:

$$
\begin{aligned}
&\cancelto{0}{Vx_{1,n}} - 2\,Vx_{2,n} + Vx_{3,n} - \alpha\left(\frac{\partial P}{\partial X}\right)_{n*} = A_{2,n-1} \\
&\qquad\vdots \\
&Vx_{m-1,n} - 2\,Vx_{m,n} + Vx_{m+1,n} - \alpha\left(\frac{\partial P}{\partial X}\right)_{n*} = A_{m,n-1} \\
&\qquad\vdots \\
&Vx_{M-1,n} - 2\,Vx_{M,n} + \cancelto{V_{bx}/V_b}{Vx_{M+1,n}} - \alpha\left(\frac{\partial P}{\partial X}\right)_{n*} = A_{M,n-1} \\
&\cancelto{0}{Vx_{1,n}} + 4\,Vx_{2,n} + 2\,Vx_{3,n} + \ldots + 4\,Vx_{M,n} + \cancelto{V_{bx}/V_b}{Vx_{M+1,n}} = 0
\end{aligned}
\qquad (6.88)
$$

where $n*$ = midpoint between columns n and n–1

$$A_{m,n-1} = -\left(\frac{H_n}{H_{n-1}}\right)^2 \left[Vx_{m-1,n-1} - 2\,Vx_{m,n-1} + Vx_{m,n+1}\right]$$

$$\alpha = 2\,\frac{k_m}{\mu\, Cp_m}\left(\frac{H_n}{H_o}\right)^2 (\Delta Y)^2$$

The above modified tridiagonal system of equations is solved for the cross channel velocity profile and pressure gradient at column n by Gaussian elimination (see Ref. (1) for the algorithm).

Energy Equation

The energy equation may be written in dimensionless terms as follows:

$$\frac{1}{H_o^2} Vz \frac{\partial \theta}{\partial Z} = \frac{1}{H^2} \frac{\partial^2 \theta}{\partial Y^2} + \frac{\mu V_b^2}{k_m T_{melt}} \frac{1}{H^2} \left[\left(\frac{\partial Vx}{\partial Y}\right)^2 + \left(\frac{\partial Vz}{\partial Y}\right)^2 \right] \tag{6.89}$$

where

$$\begin{aligned} Z = 0 \qquad & \theta = \theta_o = \frac{T_o}{T_{melt}} \\ Y = 0 \qquad & \theta = \theta_{sc} = \frac{T_b}{T_{melt}} \\ Y = 1 \qquad & \theta = \theta_b = \frac{T_b}{T_{melt}} \end{aligned} \tag{6.90}$$

Finite Difference Solution - Parallel Channel

Following the method described in Sec. 6.2.3 (see Eqs. 6.66 to 6.70), the energy equation for flow in a parallel channel may be expressed in finite difference form for column n in the finite difference grid (see Fig. 6.14) as follows:

$$\begin{aligned} -\overset{\theta_{sc}}{\cancel{\theta_{1,n}}} + (\beta+2)\, \theta_{2,n} - \theta_{3,n} &= B_{2,n-1} + \gamma_2 \\ &\vdots \\ -\theta_{m-1,n} + (\beta+2)\, \theta_{m,n} - \theta_{m+1,n} &= B_{m,n-1} + \gamma_m \\ &\vdots \\ -\theta_{M-1,n} + (\beta+2)\, \theta_{M,n} - \overset{\theta_b}{\cancel{\theta_{M+1,n}}} &= B_{M,n-1} + \gamma_M \end{aligned} \tag{6.91}$$

where $B_{m,n-1} = \theta_{m-1,n-1} + (\beta-2)\,\theta_{m,n-1} + \theta_{m+1,n-1}$

$$\beta = \frac{2(\Delta Y)^2}{\Delta Z}\left(\frac{H_n}{H_o}\right)^2 Vz_{avg,n}$$

$$\gamma_m = 2(\Delta Y)^2 \frac{\mu V_b^2}{k_m T_{melt}}\left[\left(\frac{\partial Vx}{\partial Y}\right)^2_{m,n} + \left(\frac{\partial Vz}{\partial Y}\right)^2_{m,n}\right]$$

The above tridiagonal system of equations is solved for the temperature profile at column n by Gaussian elimination using Thomas' method (see Refs. (1), (55) for the algorithm).

Finite Difference Solution – Converging Channel

For flow in a converging channel, the energy equation (6.89) may be written in finite difference form for column n in the finite difference grid (see Fig. 6.15) as follows:

$$
\begin{aligned}
-\overset{\theta_{sc}}{\cancel{\theta_{1,n}}} + (\beta+2)\,\theta_{2,n} - \theta_{3,n} &= C_{2,n-1} + \gamma_2 \\
&\vdots \\
-\theta_{m-1,n} + (\beta+2)\,\theta_{m,n} - \theta_{m+1,n} &= C_{m,n-1} + \gamma_m \\
&\vdots \\
-\theta_{M-1,n} + (\beta+2)\,\theta_{M,n} - \overset{\theta_b}{\cancel{\theta_{M+1,n}}} &= C_{M,n-1} + \gamma_M
\end{aligned}
\qquad (6.92)
$$

where $C_{m,n-1} = \delta\,\theta_{m-1,n-1} + (\beta-2\delta)\,\theta_{m,n-1} + \delta\,\theta_{m+1,n-1}$

$$\beta = \frac{(\Delta Y)^2}{\Delta Z}\left(\frac{H_n}{H_o}\right)^2 (Vz_{avg,n} + Vz_{avg,n-1})$$

$$\delta = \left(\frac{H_n}{H_{n-1}}\right)^2$$

$$\gamma_m = (\Delta Y)^2 \frac{\mu V_b}{k_m T_{melt}} \left[\left(\frac{\partial Vx}{\partial Y}\right)^2_{m,n} + \left(\frac{\partial Vz}{\partial Y}\right)^2_{m,n} + \delta \left(\frac{\partial Vx}{\partial Y}\right)^2_{m,n-1} + \delta \left(\frac{\partial Vz}{\partial Y}\right)^2_{m,n-1} \right]$$

The above tridiagonal system of equations is solved for the temperature profile at column n by Gaussian elimination using Thomas' method (see Refs. (1), (55) for the algorithm)

Simulation Results

The development of temperature in the down channel direction with and without cross channel flow in the viscous dissipation term in the energy equation (6.89) is compared in Figs. 6.16 to 6.18 for the feed, compression and metering sections. As expected the bulk temperature is slightly higher when cross channel flow is included.

6.2.5 The Nonisothermal Newtonian Plasticating Extruder Model

In Sec. 6.2.1 to 6.2.4, melt flow models have been developed ranging from the simplest case of isothermal Newtonian down channel flow to the more complex situation of developing nonisothermal Newtonian flow including transverse flow for parallel and converging screw channels. The flow channels were considered to be completely melt filled and shape factors were utilized to account for the effect of screw flights on the

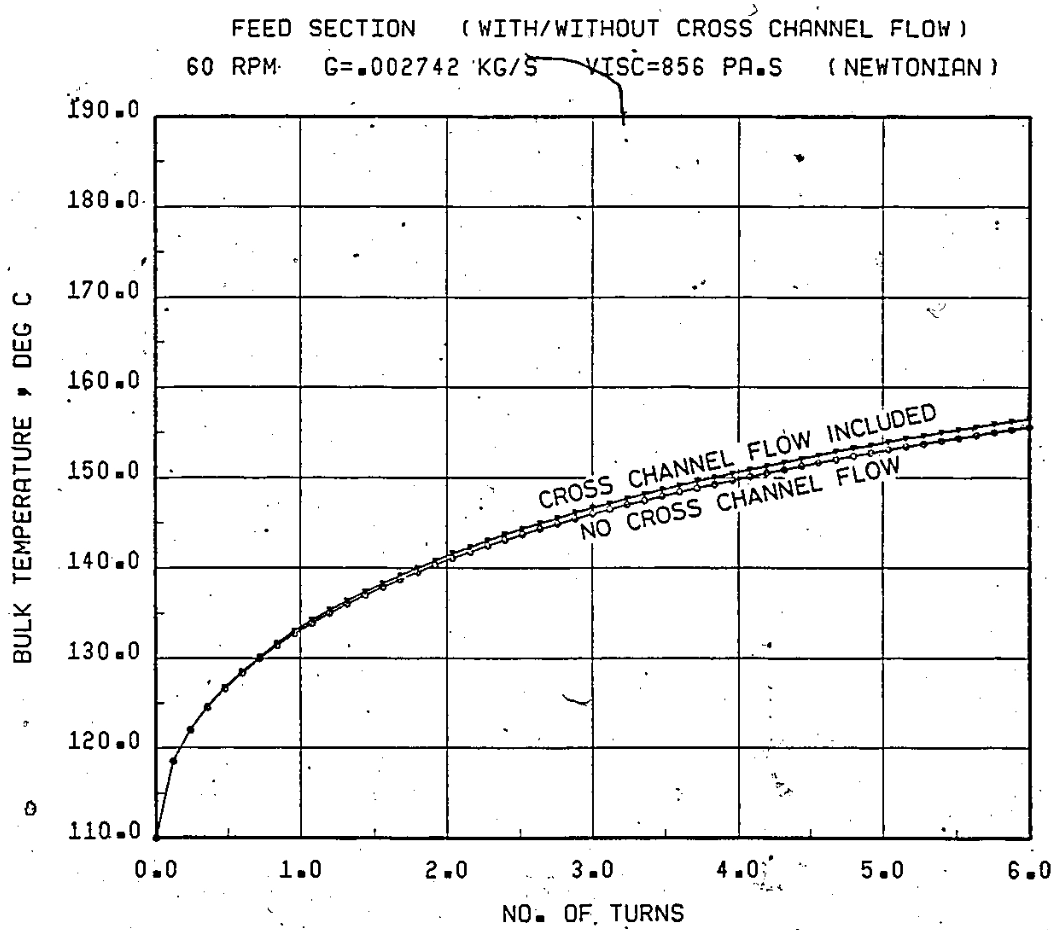

Fig. 6.16 Comparison of down channel bulk temperature profiles in the feed section of the extruder screw channel with and without cross channel flow. Data for the polymer properties, screw channel dimensions and extruder operating conditions are given in App. G.4.

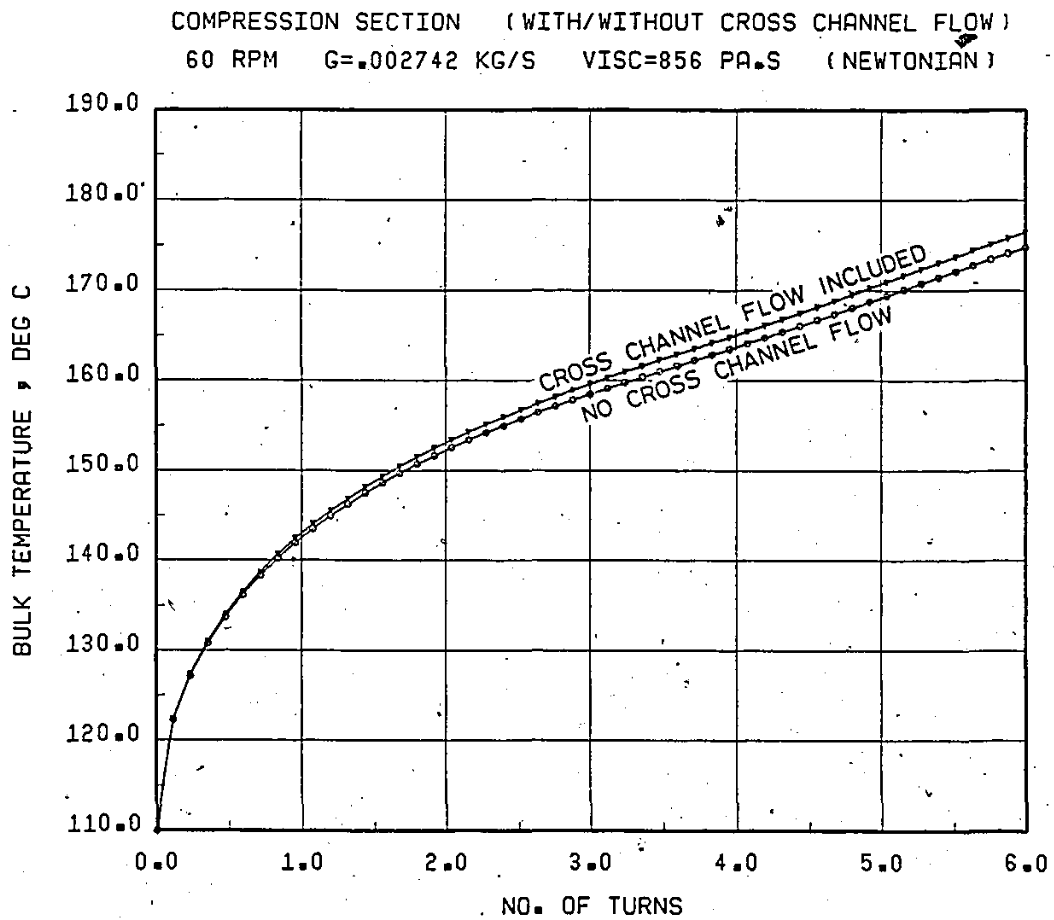

Fig. 6.17 Comparison of down channel bulk temperature profiles in the compression section of the extruder screw channel with and without cross channel flow. Data for the polymer properties, screw channel dimensions and extruder operating conditions are given in App. G.4.

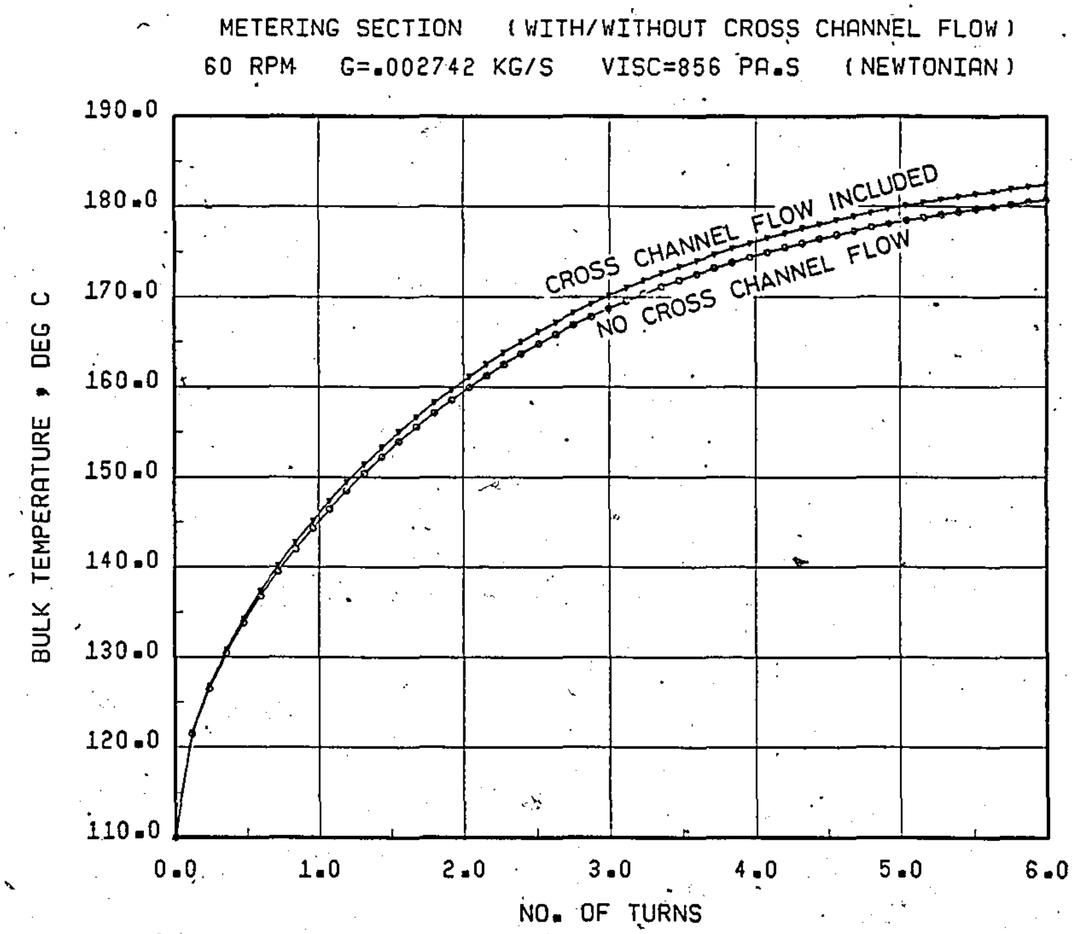

Fig. 6.18 Comparison of down channel bulk temperature profiles in the metering section of the extruder screw channel with and without cross channel flow. Data for the polymer properties, screw channel dimensions and extruder operating conditions are given in App. G.4.

development of pressure in the down channel direction (see Eq. 6.45 in Sec. 6.2.2). Results were presented for the development of pressure and temperature in each of the feed, compression and metering sections of the screw extruder from the Newtonian flow models developed up to this point.

At this stage of model development, the three geometrical sections are joined together. Also, the screw channel is assumed to be fed with solid polymer, as in a plasticating extruder. The solids conveying model (see Chap. 4) is used to calculate the location in the screw channel where melt flow starts, and also the pressure at this location. To determine the width of the melt pool in the melting zone, the solid bed profile is calculated using the Tadmor Newtonian melting model (see Sec. 5.2.1). Shape factors for flow in the melt pool are used to correct the pressure developed in this region (see Eq. 6.50 in Sec. 6.2.2). At the completion of melting, shape factors for the melt filled channel are utilized as before.

The conservation equations and corresponding finite difference equations for the feed, compression and metering sections are summarized below.

1. Feed Section

Continuity Equation (integrated form) in X-direction:

$$\int_0^1 Vx \, dY = 0 \tag{6.93}$$

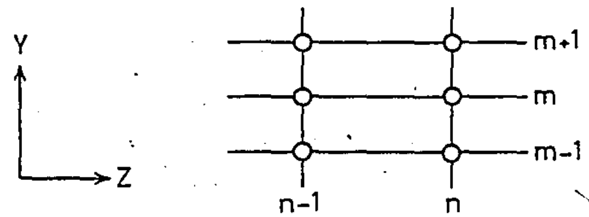

Fig. 6.19 Finite difference grid for the feed section.

<u>Momentum Equation in X-direction</u>:

$$-\frac{k_m}{\mu\, Cp_m}\frac{\partial P}{\partial X}+\frac{\partial^2 Vx}{\partial Y^2}=0 \tag{6.94}$$

Finite difference equations:

$$\begin{aligned}
&\overset{0}{\cancel{Vx_{1,n}}} - 2\, Vx_{2,n} + Vx_{3,n} - \alpha \left(\frac{\partial P}{\partial X}\right)_n = 0\\
&\quad\vdots\\
&Vx_{m-1,n} - 2\, Vx_{m,n} + Vx_{m+1,n} - \alpha \left(\frac{\partial P}{\partial X}\right)_n = 0\\
&\quad\vdots\\
&Vx_{M-1,n} - 2\, Vx_{M,n} + \overset{V_{bx}/V_b}{\cancel{Vx_{M+1,n}}} - \alpha \left(\frac{\partial P}{\partial X}\right)_n = 0
\end{aligned} \tag{6.95}$$

$$\overset{0}{\cancel{Vx_{1,n}}} + 4\, Vx_{2,n} + 2\, Vx_{3,n} + \ldots + 4\, Vx_{M,n} + \overset{V_{bx}/V_b}{\cancel{Vx_{M+1,n}}} = 0$$

where $\alpha = \frac{k_m}{\mu\, Cp_m}(\Delta Y)^2$

<u>Continuity Equation (integrated form) in Z-direction</u>

$$\int_0^1 Vz \, dY = \frac{Q}{W_f \, H_o \, V_b} \tag{6.96}$$

where W_f and H_o are respectively the channel width and depth in the feed section.

<u>Momentum Equation in Z-direction</u>:

$$- \frac{k_m}{\mu \, Cp_m} \frac{\partial P}{\partial Z} + \frac{\partial^2 Vz}{\partial Y^2} = 0 \tag{6.97}$$

Finite difference equations:

$$\begin{aligned}
&\cancelto{0}{Vz_{1,n}} - 2\,Vz_{2,n} + Vz_{3,n} - \alpha \left(\frac{\partial P}{\partial Z}\right)_n = 0 \\
&\qquad\vdots \\
&Vz_{m-1,n} - 2\,Vz_{m,n} + Vz_{m+1,n} - \alpha \left(\frac{\partial P}{\partial Z}\right)_n = 0 \\
&\qquad\vdots \\
&Vz_{M-1,n} - 2\,Vz_{M,n} + \cancelto{V_{bz}/V_b}{Vz_{M+1,n}} - \alpha \left(\frac{\partial P}{\partial Z}\right)_n = 0 \\
&\cancelto{0}{Vz_{1,n}} + 4\,Vz_{2,n} + 2\,Vz_{3,n} + \ldots + 4\,Vz_{M,n} + \cancelto{V_{bz}/V_b}{Vz_{M+1,n}} = 3M \frac{Q}{W_f H_o V_b}
\end{aligned} \tag{6.98}$$

where $\alpha = \dfrac{k_m}{\mu \, Cp_m} (\Delta Y)^2$

<u>Energy Equation</u>:

$$Vz \frac{\partial\theta}{\partial Z} = \frac{\partial^2\theta}{\partial Y^2} + \frac{\mu V_b^{\,2}}{k_m T_{melt}} \left[\left(\frac{\partial Vx}{\partial Y}\right)^2 + \left(\frac{\partial Vz}{\partial Y}\right)^2 \right] \tag{6.99}$$

Finite difference equations:

$$\begin{aligned}
-\cancelto{\theta_{sc}}{\theta_{1,n}} + (\beta+2)\,\theta_{2,n} - \theta_{3,n} &= A_{2,n-1} + \gamma_2 \\
&\vdots \\
-\theta_{m-1,n} + (\beta+2)\,\theta_{m,n} - \theta_{m+1,n} &= A_{m,n} + \gamma_m \\
&\vdots \\
-\theta_{M-1,n} + (\beta+2)\,\theta_{M,n} - \cancelto{\theta_{b}}{\theta_{M+1,n}} &= A_{M,n} + \gamma_M
\end{aligned} \tag{6.100}$$

where $A_{m,n-1} = \theta_{m-1,n-1} + (\beta-2)\,\theta_{m,n-1} + \theta_{m+1,n-1}$

$$\beta = \frac{2(\Delta Y)^2}{\Delta Z}\, Vz_{avg,n}$$

$$\gamma_m = 2(\Delta Y)^2 \frac{\mu V_b^{\,2}}{k_m T_{melt}} \left[\left(\frac{\partial Vx}{\partial Y}\right)^2_{m,n} + \left(\frac{\partial Vz}{\partial Y}\right)^2_{m,n} \right]$$

2. Compression Section

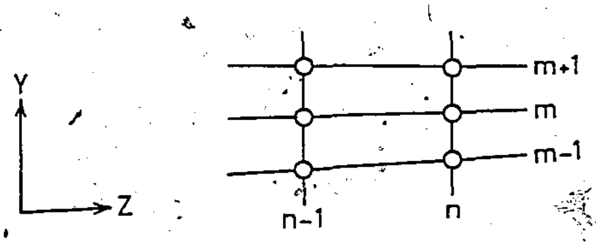

Fig. 6.20 Finite difference grid for the compression section.

Continuity Equation (integrated form) in X-direction

$$\int_0^1 Vx \, dY = 0 \tag{6.101}$$

Momentum Equation in X-direction:

$$-\frac{k_m}{\mu \cdot Cp_m H_o^2}\frac{\partial P}{\partial X} + \frac{1}{H^2}\frac{\partial^2 Vx}{\partial Y^2} = 0 \tag{6.102}$$

Finite difference equations:

$$\begin{aligned}
&\cancelto{0}{Vx_{1,n}} - 2\,Vx_{2,n} + Vx_{3,n} - \alpha\left(\frac{\partial P}{\partial X}\right)_{n*} = A_{2,n-1} \\
&\quad\vdots \\
&Vx_{M-1,n} - 2\,Vx_{M,n} + \cancelto{V_{bx}/V_b}{Vx_{M+1,n}} - \alpha\left(\frac{\partial P}{\partial X}\right)_{n*} = A_{M,n-1}
\end{aligned} \tag{6.103}$$

$$\cancelto{0}{Vx_{1,n}} + 4\,Vx_{2,n} + 2\,Vx_{3,n} + \ldots + 4\,Vx_{M,n} + \cancelto{V_{bx}/V_b}{Vx_{M+1,n}} = 0$$

where n^* = midpoint between columns n and n-1

$$A_{m,n-1} = -\left(\frac{H_n}{H_{n-1}}\right)^2 [Vx_{m-1,n-1} - 2\,Vx_{m,n-1} + Vx_{m+1,n-1}]$$

$$\alpha = 2\,\frac{k_m}{\mu\, Cp_m}\left(\frac{H_n}{H_o}\right)^2 (\Delta Y)^2$$

<u>Continuity Equation (integrated form) in Z-direction:</u>

$$\int_0^1 Vz\, dY = \frac{Q}{W_c\, H \cdot V_b} \qquad (6.104)$$

where W_c is the average channel width in the compression section.

<u>Momentum Equation in Z-direction:</u>

$$-\frac{k_m}{\mu\, Cp_m\, H_o^2}\,\frac{\partial P}{\partial Z} + \frac{1}{H^2}\,\frac{\partial^2 Vz}{\partial Y^2} = 0 \qquad (6.105)$$

Finite difference equations:

$$\overset{0}{\cancel{Vz_{1,n}}} - 2\,Vz_{2,n} + Vz_{3,n} - \alpha\left(\frac{\partial P}{\partial Z}\right)_{n^*} = B_{2,n-1}$$

$$\vdots$$

$$Vz_{m-1,n} - 2\,Vz_{m,n} + Vz_{m+1,n} - \alpha\left(\frac{\partial P}{\partial Z}\right)_{n^*} = B_{m,n-1} \qquad (6.106)$$

$$\vdots$$

$$Vz_{M-1,n} - 2\,Vz_{M,n} + \overset{V_{bz}/V_b}{\cancel{Vz_{M+1,n}}} - \alpha\left(\frac{\partial P}{\partial Z}\right)_{n^*} = B_{M,n-1}$$

$$\overset{0}{\cancel{Vz_{1,n}}} + 4\,Vz_{2,n} + 2\,Vz_{3,n} + \dots + 4\,Vz_{M,n} + \overset{V_{bz}/V_b}{\cancel{Vz_{M+1,n}}} = 3M\,\frac{Q}{W_c H_n V_b}$$

$$\text{where } B_{m,n-1} = -\left(\frac{H_n}{H_{n-1}}\right)^2 [Vz_{m-1,n-1} - 2\, Vz_{m,n-1} + Vz_{m+1,n-1}]$$

$$\alpha = \frac{2\, k_m}{\mu\, Cp_m} \left(\frac{H_n}{H_o}\right)^2 (\Delta Y)^2$$

<u>Energy Equation</u>:

$$\frac{1}{H_o^2} Vz \frac{\partial \theta}{\partial Z} = \frac{1}{H^2} \frac{\partial^2 \theta}{\partial Y^2} + \frac{1}{H^2} \left[\left(\frac{\partial Vx}{\partial Y}\right)^2 + \left(\frac{\partial Vz}{\partial Y}\right)^2\right] \tag{6.107}$$

Finite difference equations:

$$-\cancelto{\theta_{sc}}{\theta_{1,n}} + (\beta+2)\, \theta_{2,n} - \theta_{3,n} = C_{2,n-1} + \gamma_2$$

$$\vdots$$

$$-\theta_{m-1,n} + (\beta+2)\, \theta_{m,n} - \theta_{m+1,n} = C_{m,n-1} + \gamma_m \tag{6.108}$$

$$\vdots$$

$$-\theta_{M-1,n} + (\beta+2)\, \theta_{M,n} - \cancelto{\theta_b}{\theta_{M+1,n}} = C_{M,n-1} + \gamma_M$$

$$\text{where } C_{m,n-1} = \delta\, \theta_{m-1,n-1} + (\beta-2\delta)\, \theta_{m,n-1} + \delta\, \theta_{m+1,n-1}$$

$$\beta = \frac{(\Delta Y)^2}{\Delta Z} \left(\frac{H_n}{H_o}\right)^2 (Vz_{avg,n} + Vz_{avg,n-1})$$

$$\delta = \left(\frac{H_n}{H_{n-1}}\right)^2$$

$$\gamma_m = (\Delta Y)^2 \frac{\mu\, V_b}{k_m T_{melt}} \left[\left(\frac{\partial Vx}{\partial Y}\right)^2_{m,n} + \left(\frac{\partial Vz}{\partial Y}\right)^2_{m,n} + \delta \left(\frac{\partial Vx}{\partial Y}\right)^2_{m,n-1} + \delta \left(\frac{\partial Vz}{\partial Y}\right)^2_{m,n-1}\right]$$

3. Metering Section

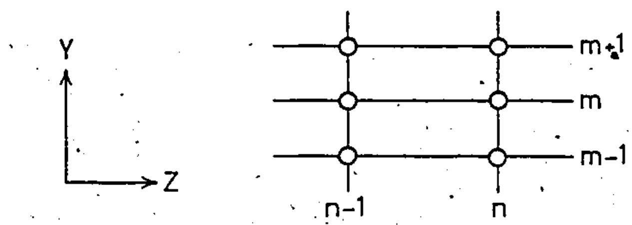

Fig. 6.21 Finite difference grid for the metering section.

Continuity Equation (integrated form) in X-direction:

$$\int_0^1 Vx \, dY = 0 \tag{6.109}$$

Momentum Equation in X-direction:

$$-\frac{k_m}{\mu \, Cp_m} \left(\frac{H_{ex}}{H_o}\right)^2 \frac{\partial P}{\partial X} + \frac{\partial^2 Vx}{\partial Y^2} = 0 \tag{6.110}$$

where H_{ex} is the channel depth in the metering zone.

Finite difference equations:

$$\overset{0}{\cancel{Vx_{1,n}}} - 2\,Vx_{2,n} + Vx_{3,n} - \alpha \left(\frac{\partial P}{\partial X}\right)_n = 0$$

$$\vdots$$

$$Vx_{m-1,n} - 2\,Vx_{m,n} + Vx_{m+1,n} - \alpha \left(\frac{\partial P}{\partial X}\right)_n = 0 \qquad (6.111)$$

$$\vdots$$

$$Vx_{M-1,n} - 2\,Vx_{M,n} + \overset{V_{bx}/V_b}{\cancel{Vx_{M+1,n}}} - \alpha \left(\frac{\partial P}{\partial X}\right)_n = 0$$

$$\overset{0}{\cancel{Vx_{1,n}}} + 4\,Vx_{2,n} + 2\,Vx_{3,n} + \ldots + 4\,Vx_{M,n} + \overset{V_{bx}/V_b}{\cancel{Vx_{M+1,n}}} = 0$$

where $\alpha = \dfrac{k_m}{\mu\, Cp_m} \left(\dfrac{H_{ex}}{H_o}\right)^2 (\Delta Y)^2$

<u>Continuity Equation (integrated form) in Z-direction:</u>

$$\int_0^1 Vz\, dY = \frac{Q}{W_m H_{ex} V_b} \qquad (6.112)$$

where W_m is the channel width in the metering section.

<u>Momentum Equation in Z-direction:</u>

$$-\frac{k_m}{\mu\, Cp_m} \left(\frac{H_{ex}}{H_o}\right)^2 \frac{\partial P}{\partial Z} + \frac{\partial^2 Vz}{\partial Y^2} = 0 \qquad (6.113)$$

Finite difference equations:

$$
\begin{aligned}
&\cancelto{o}{Vz_{1,n}} - 2\,Vz_{2,n} + Vz_{3,n} - \alpha \left(\frac{\partial P}{\partial Z}\right)_n = 0 \\
&\quad\vdots \\
&Vz_{m-1,n} - 2\,Vz_{m,n} + Vz_{m+1,n} - \alpha \left(\frac{\partial P}{\partial Z}\right)_n = 0 \\
&\quad\vdots \\
&Vz_{M-1,n} - 2\,Vz_{M,n} + \cancelto{V_{bz}/V_b}{Vz_{M+1,n}} - \alpha \left(\frac{\partial P}{\partial Z}\right)_n = 0 \\
&\cancelto{o}{Vz_{1,n}} + 4\,Vz_{2,n} + 2\,Vz_{3,n} + \ldots + 4\,Vz_{M,n} + \cancelto{V_{bz}/V_b}{Vz_{M+1,n}} = 3M\,\frac{Q}{W_m H_{ex} V_b}
\end{aligned}
\tag{6.114}
$$

where $\alpha = \dfrac{k_m}{\mu\, Cp_m} \left(\dfrac{H_{ex}}{H_o}\right)^2 (\Delta Y)^2$

<u>Energy Equation</u>:

$$
\left(\frac{H_{ex}}{H_o}\right)^2 Vz\,\frac{\partial \theta}{\partial Z} = \frac{\partial^2 \theta}{\partial Y^2} + \frac{\mu\, V_b^2}{k_m T_{melt}} \left[\left(\frac{\partial Vx}{\partial Y}\right)^2 + \left(\frac{\partial Vz}{\partial Y}\right)^2 \right]
\tag{6.115}
$$

Finite difference equations:

$$
\begin{aligned}
&-\cancelto{\theta_{sc}}{\theta_{1,n}} + (\beta+2)\,\theta_{2,n} - \theta_{3,n} = A_{2,n-1} + \gamma_2 \\
&\quad\vdots \\
&-\theta_{m-1,n} + (\beta+2)\,\theta_{m,n} - \theta_{m+1,n} = A_{m,n-1} + \gamma_m \\
&\quad\vdots \\
&-\theta_{M-1,n} + (\beta+2)\,\theta_{M,n} - \cancelto{\theta_b}{\theta_{M+1,n}} = A_{M,n-1} + \gamma_M
\end{aligned}
\tag{6.116}
$$

where $A_{m,n-1} = \theta_{m-1,n-1} + (\beta-2)\,\theta_{m,n-1} + \theta_{m+1,n-1}$

$$\beta = 2\,\frac{(\Delta Y)^2}{\Delta Z}\left(\frac{H_{ex}}{H_o}\right)^2 Vz_{avg,n}$$

$$\gamma_m = 2(\Delta Y)^2\,\frac{\mu V_b^2}{k_m T_{melt}}\left[\left(\frac{\partial Vx}{\partial Y}\right)^2_{m,n} + \left(\frac{\partial Vz}{\partial Y}\right)^2_{m,n}\right]$$

Results of Simulations

Some typical results using the nonisothermal developing Newtonian model for the melt flow region of a plasticating screw extruder are shown in Figs. 6.22 to 6.24. The pressure, bulk temperature and solid bed profiles along the down channel direction are shown for three screw speeds: 40, 60 and 80 rpm. In Fig. 6.25 the pressure profiles have been calculated with and without the use of shape factors. It can be seen that shape factors alter the pressure profiles quite significantly.

Newtonian models represent a quick (i.e. with respect to computation time) and relatively simple means to obtain results that can be quite realistic as seen in Figs. 6.22 to 6.24. The major drawback of Newtonian models in the necessity to choose a representative Newtonian viscosity which often may be difficult to do. Since polymer melt viscosities are strongly dependent on shear rate and temperature, Newtonian models are not suitable when more precise results are required as in the case of extruder and die design.

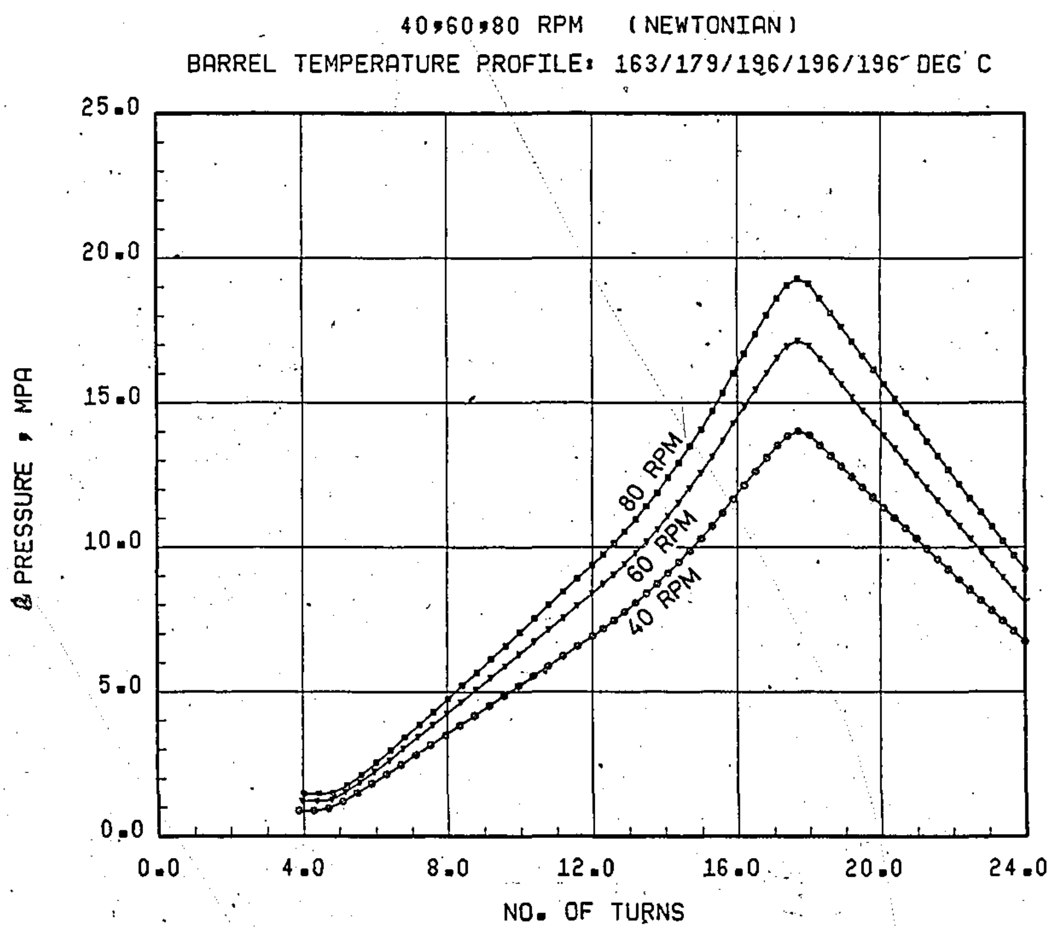

Fig. 6.22 Down channel pressure profiles in the extruder screw channel for Newtonian flow. Data for the polymer properties, screw channel dimensions and extruder operating conditions are given in App. G.5.

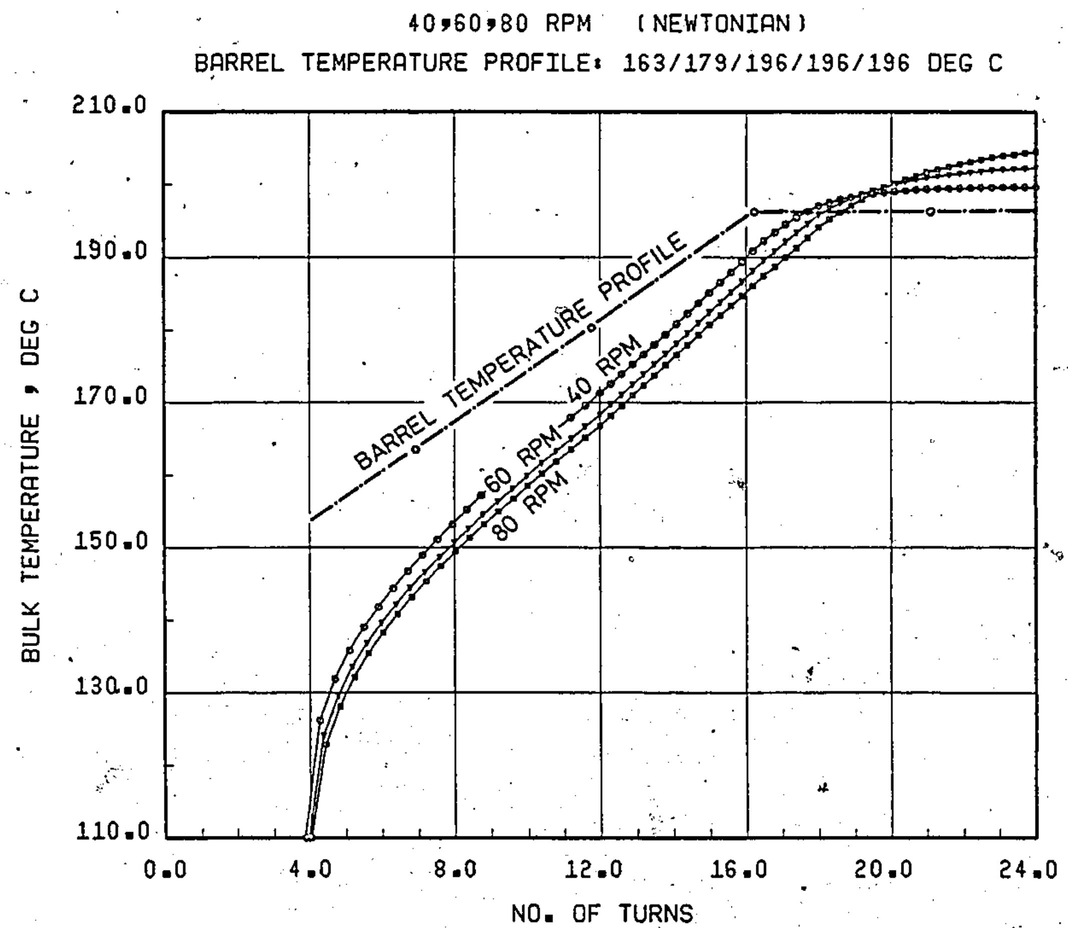

Fig. 6.23 Down channel bulk temperature profiles in the extruder screw channel for Newtonian flow. Data for the polymer properties, screw channel dimensions and extruder operating conditions are given in App. G.5.

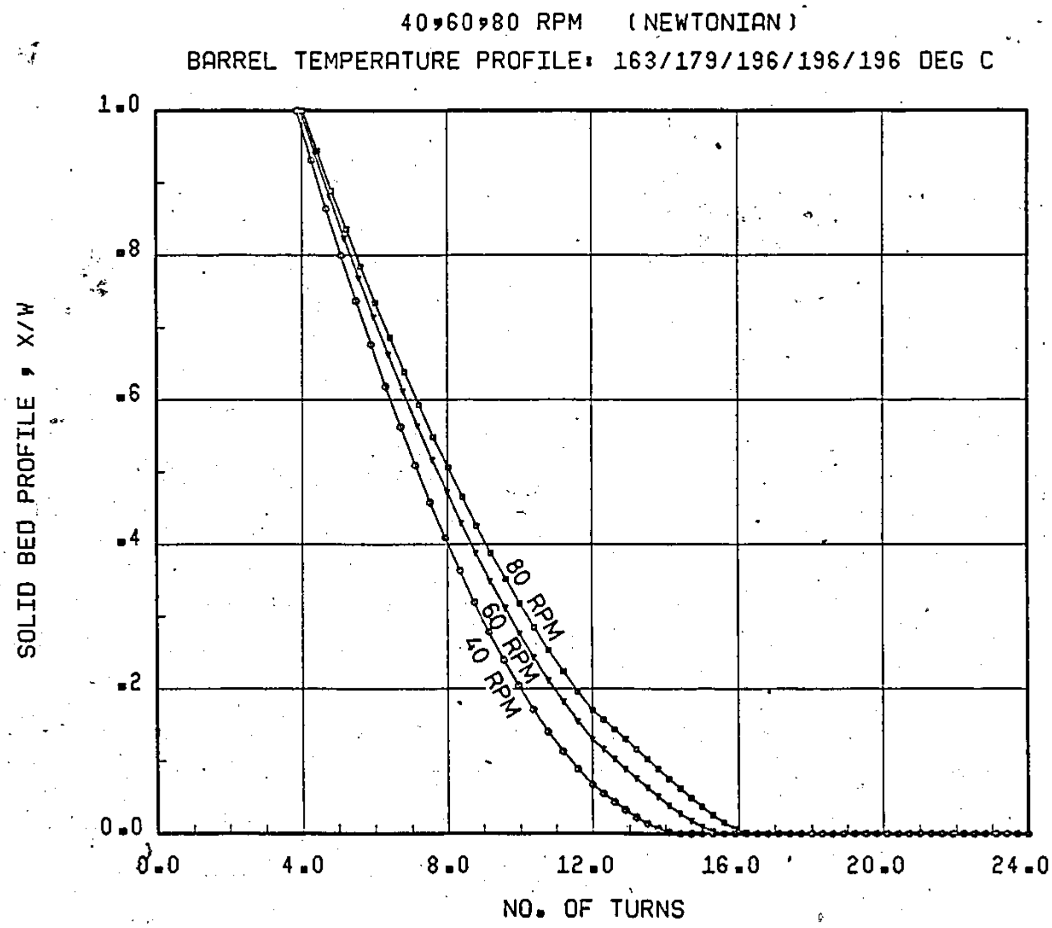

Fig. 6.24 Down channel solid bed profiles in the extruder screw channel for Newtonian flow. Data for the polymer properties, screw channel dimensions and extruder operating conditions are given in App. G.5.

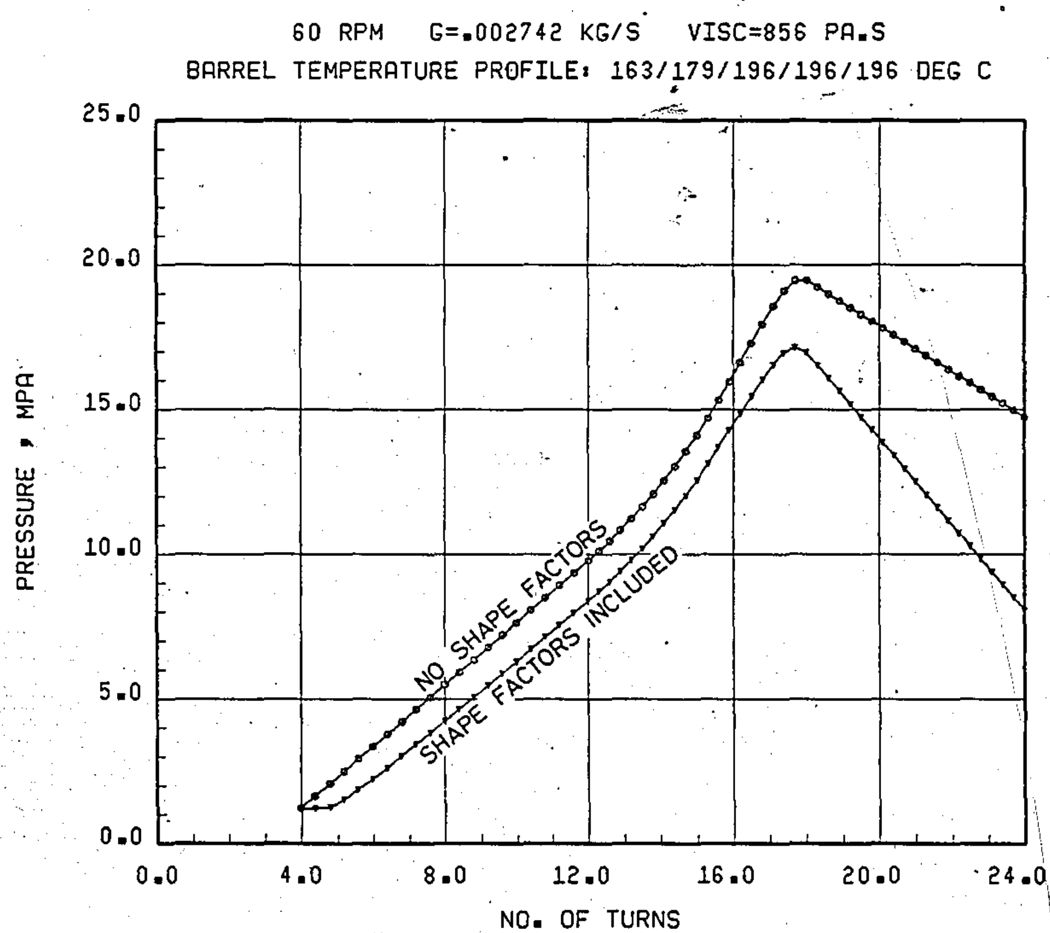

Fig. 6.25 Comparison of down channel pressure profiles in the extruder screw channel for Newtonian flow obtained with and without the use of shape factors. Data for the polymer properties, screw channel dimensions and extruder operating conditions are given in App. G.5.

6.2.6 Nonisothermal Non-Newtonian Developing Flow

In the last stage of the development of the present melt flow model, the non-Newtonian behaviour of the polymer melt is considered. With a temperature and shear rate dependent viscosity, the mass, momentum and energy equations can no longer be solved independently. Instead they have to be solved simultaneously, which means that at a given column in the finite difference grid, the momentum equations in the X- and Z- directions and the energy equation have to be solved iteratively. This added requirement increases computation time significantly as compared with the Newtonian model where no iterations are needed.

Flow Equations

The simplified conservation equations for combined drag and pressure flow of a non-Newtonian fluid in a screw channel are:

Continuity (integral form):

$$\int_0^H v_x \, dy = 0 \tag{6.117}$$

$$\int_0^H v_z \, dy = \frac{Q}{W} \tag{6.118}$$

Momentum:

$$-\frac{\partial p}{\partial x} + \frac{\partial \tau_{yx}}{\partial y} = 0 \tag{6.119}$$

$$-\frac{\partial p}{\partial z} + \frac{\partial \tau_{yz}}{\partial y} = 0 \tag{6.120}$$

Energy: $$\rho_m \, Cp_m \, v_z \frac{\partial T}{\partial z} = k_m \frac{\partial^2 T}{\partial y^2} + \tau_{yx} \frac{\partial v_x}{\partial y} + \tau_{yz} \frac{\partial v_z}{\partial y} \qquad (6.121)$$

The shear rate and temperature dependent constitutive relation (see Eqs. 2.33, 2.34, and 2.36) is written as:

$$\tau_{yx} = \eta \frac{\partial v_x}{\partial y} \qquad (6.122)$$

$$\tau_{yz} = \eta \frac{\partial v_z}{\partial y} \qquad (6.123)$$

$$\log \eta = a_o + a_1 \log \dot{\gamma} + a_2 (\log \dot{\gamma})^2 + a_3 T + a_4 T^2 + a_5 T \log \dot{\gamma} \qquad (6.124)$$

where $$\dot{\gamma} = \sqrt{\left(\frac{\partial v_x}{\partial y}\right)^2 + \left(\frac{\partial v_z}{\partial y}\right)^2}$$

Substituting Eqs. 6.122 to 6.124 into the above momentum and energy equations (6.119 to 6.121), we obtain:

Momentum: $$-\frac{\partial p}{\partial x} + \eta \frac{\partial^2 v_x}{\partial y^2} + \frac{\partial \eta}{\partial y} \frac{\partial v_x}{\partial y} = 0 \qquad (6.125)$$

$$-\frac{\partial p}{\partial z} + \eta \frac{\partial^2 v_z}{\partial y^2} + \frac{\partial \eta}{\partial y} \frac{\partial v_z}{\partial y} = 0 \qquad (6.126)$$

Energy: $$\rho_m \, Cp_m \, v_z \frac{\partial T}{\partial z} = k_m \frac{\partial^2 T}{\partial y^2} + \eta \left[\left(\frac{\partial v_x}{\partial y}\right)^2 + \left(\frac{\partial v_z}{\partial y}\right)^2 \right] \qquad (6.127)$$

The boundary conditions for the above equations are:

$$z = 0 \qquad p = p_o \qquad T = T(y) = T_o$$

$$y = 0 \qquad v_x = v_z = 0 \qquad T = T_{sc} = T_b \qquad (6.128)$$

$$y = H \qquad v_x = V_{bx} \quad v_z = V_{bz} \quad T = T_b$$

A constant temperature profile is chosen at z = 0 (as was the case for the Newtonian flow model).

Let

$$Vx = \frac{v_x}{V_b}$$

$$Vz = \frac{v_z}{V_b}$$

$$P = \frac{p}{\rho_m V_b^2}$$

$$\theta = \frac{T}{T_{melt}} \qquad (6.129)$$

$$Y = \frac{y}{H}$$

$$X = \frac{k_m x}{\rho_m Cp_m V_b H_o^2}$$

$$Z = \frac{k_m z}{\rho_m Cp_m V_b H_o^2}$$

where H is the local channel depth and H_o is the channel depth in the feed section. Substituting the above into Eqs. 6.117, 6.118, and Eqs.

6.125 to 6.127, we obtain in terms of dimensionless parameters:

Continuity (integral form):

$$\int_0^1 Vx\, dY = 0 \qquad (6.130)$$

$$\int_0^1 Vz\, dY = \frac{Q}{WH\, V_b} \qquad (6.131)$$

Momentum:

$$-\frac{k_m}{Cp_m\, H_o^{\,2}} \frac{\partial P}{\partial X} + \frac{1}{H^2} \left[\eta \frac{\partial^2 Vx}{\partial Y^2} + \frac{\partial \eta}{\partial Y} \frac{\partial Vx}{\partial Y} \right] = 0 \qquad (6.132)$$

$$-\frac{k_m}{Cp_m\, H_o^{\,2}} \frac{\partial P}{\partial Z} + \frac{1}{H^2} \left[\eta \frac{\partial^2 Vz}{\partial Y^2} + \frac{\partial \eta}{\partial Y} \frac{\partial Vz}{\partial Y} \right] = 0 \qquad (6.133)$$

Energy:

$$\frac{1}{H_o^{\,2}} Vz \frac{\partial \theta}{\partial Z} = \frac{1}{H^2} \frac{\partial^2 \theta}{\partial Y^2} + \frac{\eta\, V_b^{\,2}}{k_m T_{melt}} \frac{1}{H^2} \left[\left(\frac{\partial Vx}{\partial Y}\right)^2 + \left(\frac{\partial Vz}{\partial Y}\right)^2 \right] \qquad (6.134)$$

The accompanying boundary conditions are:

$$\begin{array}{llll} Z = 0 & P = P_o & & \theta = \theta_o(Y) = \dfrac{T_o}{T_{melt}} \\ Y = 0 & Vx = Vz = 0 & & \theta = \theta_{sc} = \dfrac{T_b}{T_{melt}} \\ Y = 1 & Vx = \dfrac{V_{bx}}{V_b} & Vz = \dfrac{V_{bz}}{V_b} & \theta = \theta_b = \dfrac{T_b}{T_{melt}} \end{array} \qquad (6.135)$$

Finite Difference Equations - Parallel Plates

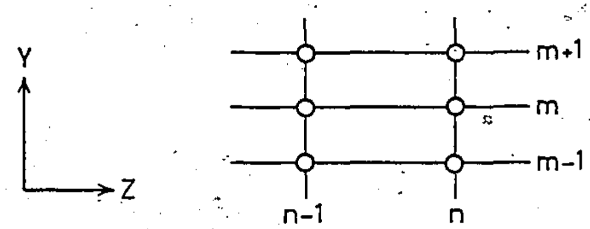

Fig. 6.26 Finite difference grid for flow in a parallel channel.

The Crank-Nicolson implicit finite difference method is used to solve Eqs. 6.130 to 6.134 along with the accompanying boundary conditions (6.135) for non-Newtonian flow in a parallel channel. The finite difference grid is illustrated in Fig. 6.26.

Continuity Equation in X-direction:

Using Simpsons' rule, the continuity equation (6.130) is given in the following finite difference form:

$$\int_0^1 Vx\, dY = \frac{\Delta Y}{3}\left[Vx_{1,n} + 4Vx_{2,n} + 2Vx_{3,n} + \ldots + 4Vx_{M,n} + Vx_{M+1,n}\right] = 0 \tag{6.136}$$

or

$$Vx_{1,n} + 4Vx_{2,n} + 2Vx_{3,n} + \ldots + 4Vx_{M,n} + Vx_{M+1,n} = 0 \tag{6.137}$$

Momentum Equation in X-direction:

For the momentum equation, the following finite difference approximations are used:

$$\frac{\partial^2 Vx}{\partial Y^2} \simeq \frac{Vx_{m+1,n} - 2Vx_{m,n} + Vx_{m-1,n}}{(\Delta Y)^2} \qquad (6.138)$$

$$\frac{\partial Vx}{\partial Y} \simeq \frac{Vx_{m+1,n} - Vx_{m-1,n}}{2\ \Delta Y} \qquad (6.139)$$

Substituting Eqs. 6.138 and 6.139 into Eq. 6.132, we obtain for column n:

$$(-\beta_m+1)\ Vx_{m-1,n} - 2Vx_{m,n} + (\beta_m+1)\ Vx_{m+1,n} - \alpha_m\left(\frac{\partial P}{\partial X}\right)_n = 0 \qquad (6.140)$$

where $m = 2, 3, \ldots, M$

$$\alpha_m = \frac{k_m}{\eta_{m,n} Cp_m} \left(\frac{H_n}{H_o}\right)^2 (\Delta Y)^2$$

$$\beta_m = \frac{\Delta Y}{2\eta_{m,n}} \left(\frac{\partial \eta}{\partial Y}\right)_{m,n}$$

Combining Eqs. 6.137 and 6.140, we have a modified tridiagonal system of M algebraic equations and M unknowns ($Vx_{2,n}$ to $Vx_{M,n}$ and $(\partial P/\partial X)_n$). The equations may be written as:

$$
\begin{aligned}
(-\beta_2+1)\,\cancelto{0}{Vx_{1,n}} - 2Vx_{2,n} + (\beta_2+1)\,Vx_{3,n} - \alpha_2\left(\frac{\partial P}{\partial X}\right)_n &= 0 \\
&\vdots \\
(-\beta_m+1)\,Vx_{m-1,n} - 2Vx_{m,n} + (\beta_m+1)\,Vx_{m+1,n} - \alpha_m\left(\frac{\partial P}{\partial X}\right)_n &= 0 \\
&\vdots \\
(-\beta_M+1)\,Vx_{M-1,n} - 2Vx_{M,n} + (\beta_M+1)\,\cancelto{V_{bx}/V_b}{Vx_{M+1,n}} - \alpha_M\left(\frac{\partial P}{\partial X}\right)_n &= 0
\end{aligned}
\tag{6.141}
$$

$$
\cancelto{0}{Vx_{1,n}} + 4Vx_{2,n} + 2Vx_{3,n} + \ldots + 4Vx_{M,n} + \cancelto{V_{bx}/V_b}{Vx_{M+1,n}} = 0
$$

or in matrix form:

$$
\begin{bmatrix}
B_2 & C_2 & & & & & & -\alpha_2 \\
A_3 & B_3 & C_3 & & & & & -\alpha_3 \\
 & & \ddots & & & & & \vdots \\
 & & A_m & B_m & C_m & & & -\alpha_m \\
 & & & & \ddots & & & \vdots \\
 & & & & & A_M & B_M & -\alpha_M \\
4 & 2 & 4 & \cdots & 2 & 4 & & 0
\end{bmatrix}
\begin{bmatrix}
Vx_{2,n} \\ Vx_{3,n} \\ \vdots \\ Vx_{m,n} \\ \vdots \\ Vx_{M,n} \\ \left(\frac{\partial P}{\partial X}\right)_n
\end{bmatrix}
=
\begin{bmatrix}
0 \\ 0 \\ \vdots \\ 0 \\ \vdots \\ 0 \\ -V_{bx}/V_b \\ -V_{bx}/V_b
\end{bmatrix}
\tag{6.142}
$$

where
$$
\begin{aligned}
A_m &= -\beta_m + 1 \\
B_m &= -2 \\
C_m &= \beta_m + 1
\end{aligned}
$$

This modified tridiagonal system of equations is solved for the velocity profile and pressure gradient in the X-direction using Gaussian elimination (see Ref. (1) for the algorithm).

Continuity and Momentum Equations in Z-direction:

The finite difference representation of the continuity and momentum equations in the Z-direction is very similar to that in the X-direction. For the Z-direction the equations may be written as:

$$(-\beta_2+1)\,\overset{0}{\cancel{Vz_{1,n}}} - 2Vz_{2,n} + (\beta_2+1)\,Vz_{3,n} - \alpha_2 \left(\frac{\partial P}{\partial Z}\right)_n = 0$$

$$\vdots$$

$$(-\beta_m+1)\,Vz_{m-1,n} - 2Vz_{m,n} + (\beta_m+1)\,Vz_{m+1,n} - \alpha_m \left(\frac{\partial P}{\partial Z}\right)_n = 0$$

$$\vdots \qquad\qquad (6.143)$$

$$(-\beta_M+1)\,Vz_{M-1,n} - 2Vz_{M,n} + (\beta_M+1)\,\overset{V_{bz}/V_b}{\cancel{Vz_{M+1,n}}} - \alpha_M \left(\frac{\partial P}{\partial Z}\right)_n = 0$$

$$\overset{0}{\cancel{Vz_{1,n}}} + 4Vz_{2,n} + 2Vz_{3,n} + \ldots + 4Vz_{M,n} + \overset{V_{bz}/V_b}{\cancel{Vz_{M+1,n}}} = 3M\,\frac{Q}{WH_nV_b}$$

where $$\alpha_m = \frac{k_m}{\eta_{m,n}Cp_m}\left(\frac{H_n}{H_o}\right)^2 (\Delta Y)^2$$

$$\beta_m = \frac{\Delta Y}{2\,\eta_{m,n}}\left(\frac{\partial \eta}{\partial Y}\right)_{m,n}$$

Energy Equation

For the energy equation (6.134), the following finite difference approximations are used:

$$\frac{\partial \theta}{\partial Z} \approx \frac{\theta_{m,n} - \theta_{m-1,n}}{\Delta Z} \tag{6.144}$$

$$\frac{\partial^2 \theta}{\partial Y^2} \approx \frac{1}{2} \left[\frac{\theta_{m+1,n} - 2\theta_{m,n} + \theta_{m-1,n}}{(\Delta Y)^2}\right]$$

$$+ \frac{1}{2} \left[\frac{\theta_{m+1,n-1} - 2\theta_{m,n-1} + \theta_{m-1,n-1}}{(\Delta Y)^2}\right] \tag{6.145}$$

Substituting Eqs. 6.144 and 6.145 into Eq. 6.134, we obtain for column n in the finite difference grid:

$$-\theta_{m-1,n} + (\beta+2)\, \theta_{m,n} - \theta_{m+1,n}$$

$$= \theta_{m-1,n-1} + (\beta-2)\, \theta_{m,n-1} + \theta_{m+1,n-1} + \gamma_m \tag{6.146}$$

where $m = 2, 3, \ldots M$

$$\beta = \frac{2(\Delta Y)^2}{\Delta Z} \left(\frac{H_n}{H_o}\right)^2 Vz_{avg,n}$$

$$\gamma_m = 2(\Delta Y)^2 \frac{\eta_{m,n} V_b^2}{k_m T_{melt}} \left[\left(\frac{\partial Vx}{\partial Y}\right)^2_{m,n} + \left(\frac{\partial Vz}{\partial Y}\right)^2_{m,n}\right]$$

As is the case of the Newtonian model, the average down channel velocity Vz_{avg} is used in the convective term since negative values of Vz will cause instabilities in the finite difference solution.

Equation 6.146 represents a tridiagonal system of M-1 equations and M-1 unknowns ($\theta_{2,n}$ to $\theta_{M,n}$) and may be written as follows:

$$
\begin{aligned}
-\overset{\theta_{sc}}{\cancel{\theta_{1,n}}} + (\beta+2)\,\theta_{2,n} - \theta_{3,n} &= D_{2,n-1} + \gamma_2 = E_2 \\
&\vdots \\
-\theta_{m-1,n} + (\beta+2)\,\theta_{m,n} - \theta_{m+1,n} &= D_{m,n-1} + \gamma_m = E_m \\
&\vdots \\
-\theta_{M-1,n} + (\beta+2)\,\theta_{M,n} - \overset{\theta_b}{\cancel{\theta_{M+1,n}}} &= D_{M,n-1} + \gamma_M = E_M
\end{aligned}
\qquad (6.147)
$$

where $\quad D_{m,n-1} = \theta_{m-1,n-1} + (\beta-2)\,\theta_{m,n-1} + \theta_{m+1,n-1}$

or in matrix form:

$$
\begin{bmatrix}
B_2 & C_2 & & & & & \\
A_3 & B_3 & C_3 & & & & \\
 & & \ddots & & & & \\
 & & A_m & B_m & C_m & & \\
 & & & & \ddots & & \\
 & & & & & A_M & B_M
\end{bmatrix}
\begin{bmatrix}
\theta_{2,n} \\ \theta_{3,n} \\ \vdots \\ \theta_{m,n} \\ \vdots \\ \theta_{M,n}
\end{bmatrix}
=
\begin{bmatrix}
E_2 + \theta_{sc} \\ E_3 \\ \vdots \\ E_m \\ \vdots \\ E_M + \theta_b
\end{bmatrix}
\qquad (6.148)
$$

where

$$A_m = -1$$

$$B_m = \beta + 2$$

$$C_m = -1$$

$$E_m = \theta_{m-1,n-1} + (\beta-2)\,\theta_{m,n-1} + \theta_{m+1,n-1} + \gamma_{m,n}$$

This tridiagonal system of equations is solved for the temperature profile at column n by Gaussian elimination using Thomas' method (see Refs. (1), (55) for the algorithm).

Finite Difference Equations - Converging Channel

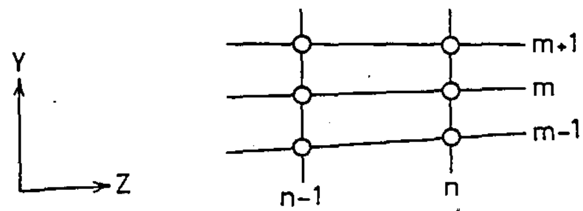

Fig. 6.27 Finite difference grid for flow in a converging channel.

For the analysis of non-Newtonian flow in a converging channel, slightly different finite difference equations are utilized to account for the change in velocity profiles as the cross-sectional area of the flow channel decreases in the down channel direction. Better estimates of pressure and temperature development are obtained when the viscosity and pressure gradient are calculated at the midpoint between columns n and n-1, instead of at column n in the finite difference grid as shown in Fig. 6.27. In doing so, however, the finite difference approximations and the resulting finite difference equations become slightly more complex than in the case of flow in a parallel channel.

As before, the Crank-Nicolson implicit finite difference method is used to solve the conservation equations (6.130 to 6.134) and boundary conditions (6.135).

Continuity Equation in X-direction:

The continuity equation (6.130) in finite difference form is the same as in the case of the parallel channel. For column n, the continuity equation is:

$$Vx_{1,n} + 4Vx_{2,n} + 2Vx_{3,n} + \ldots + 4Vx_{M,n} + Vx_{M+1,n} = 0 \qquad (6.149)$$

Momentum Equation in X-direction

For the momentum equation (6.132), the following finite difference approximations are used:

$$\frac{1}{H^2}\frac{\partial^2 Vx}{\partial Y^2} \simeq \frac{1}{2H_n^2}\left[\frac{Vx_{m+1,n} - 2Vx_{m,n} + Vx_{m-1,n}}{(\Delta Y)^2}\right] + \frac{1}{2H_{n-1}^2}\left[\frac{Vx_{m+1,n-1} - 2Vx_{m,n-1} + Vx_{m-1,n-1}}{(\Delta Y)^2}\right] \qquad (6.150)$$

$$\frac{1}{H}\frac{\partial Vx}{\partial Y} \simeq \frac{1}{2H_n}\left[\frac{Vx_{m+1,n} - Vx_{m-1,n}}{2\,\Delta Y}\right] + \frac{1}{2H_{n-1}}\left[\frac{Vx_{m+1,n-1} - Vx_{m-1,n-1}}{2\Delta Y}\right] \qquad (6.151)$$

The viscosity and viscosity gradient are calculated at the midpoint between columns n and n-1, thus:

$$\eta \simeq \eta(\dot{\gamma}_{m,n*}, T) \qquad (6.152)$$

where

$$\dot{\gamma}_{m,n*} = \sqrt{\frac{1}{2}\left[\left(\frac{\partial v_x}{\partial y}\right)^2_{m,n} + \left(\frac{\partial v_x}{\partial y}\right)^2_{m,n-1}\right] + \frac{1}{2}\left[\left(\frac{\partial v_z}{\partial y}\right)^2_{m,n} + \left(\frac{\partial v_z}{\partial y}\right)^2_{m,n-1}\right]}$$

n* = midpoint between columns n and n-1

$$\frac{1}{H}\frac{\partial \eta}{\partial Y} \approx \frac{1}{\left(\frac{H_n + H_{n-1}}{2}\right)} \left(\frac{\partial \eta}{\partial Y}\right)_{m,n^*}$$

$$= \frac{2}{H_n + H_{n-1}} \left(\frac{\partial \eta}{\partial Y}\right)_{m,n^*} \tag{6.153}$$

Substituting Eqs. 6.150 to 6.153 into Eq. 6.132, we obtain for column n:

$$(-\beta_m + 1)\, Vx_{m-1,n} - 2Vx_{m,n} + (\beta_m + 1)\, Vx_{m+1,n} - \alpha_m \left(\frac{\partial P}{\partial X}\right)_{n^*}$$

$$= (\varepsilon\beta_m - \delta)\, Vx_{m-1,n-1} + 2\delta\, Vx_{m,n-1} - (\varepsilon\beta_m + \delta)\, Vx_{m+1,n-1} \tag{6.154}$$

where $m = 2, 3, \ldots, M$

$$\alpha_m = 2(\Delta Y)^2 \frac{k_m}{Cp_m\, \eta_{m,n^*}} \left(\frac{H_n}{H_o}\right)^2$$

$$\beta_m = \frac{\Delta Y}{\eta_{m,n^*}} \left(\frac{\partial \eta}{\partial Y}\right)_{m,n^*} \left(\frac{\varepsilon}{\varepsilon + 1}\right)$$

$$\delta = \left(\frac{H_n}{H_{n-1}}\right)^2$$

$$\varepsilon = \frac{H_n}{H_{n-1}}$$

Combining Eqs. 6.149 and 6.154, we have a modified tridiagonal system of M algebraic equations and M unknown ($Vx_{2,n}$ to $Vx_{M,n}$ and $(\partial P/\partial X)_{n^*}$). The equations may be written as:

$$(-\beta_2+1)\cancelto{0}{Vx_{1,n}} - 2Vx_{2,n} + (\beta_2+1)\, Vx_{3,n} - \alpha_2 \left(\frac{\partial P}{\partial X}\right)_{n*} = A_{2,n-1}$$

$$\vdots$$

$$(-\beta_m+1)\, Vx_{m-1,n} - 2Vx_{m,n} + (\beta_m+1)\, Vx_{m+1,n} - \alpha_m \left(\frac{\partial P}{\partial X}\right)_{n*} = A_{m,n-1}$$

$$\vdots$$

$$(-\beta_M+1)\, Vx_{M-1,n} - 2Vx_{M,n} + (\beta_M+1)\cancelto{V_{bx}/V_b}{Vx_{M+1,n}} - \alpha_M \left(\frac{\partial P}{\partial X}\right)_{n*} = A_{M,n-1} \qquad (6.155)$$

$$\cancelto{0}{Vx_{1,n}} + 4Vx_{2,n} + 2Vx_{3,n} + \ldots + 4Vx_{M,n} + \cancelto{V_{bx}/V_b}{Vx_{M+1,n}} = 0$$

where $$A_{m,n-1} = (\varepsilon\beta_m-\delta)\, Vx_{m-1,n-1} + 2\delta Vx_{m,n-1} - (\varepsilon\beta_m+\delta)\, Vx_{m+1,n-1}$$

Using Gaussian elimination the above system of equations is solved for the velocity profile at column n and the pressure gradient at the midpoint between columns n and n-1 (see Ref. (1) for the algorithm).

Continuity and Momentum Equations in Z-direction:

The continuity and momentum equations (6.131 and 6.133) in the Z-direction may be solved by the finite difference method in a similar manner as in the X-direction. The modified tridiagonal system of equations for the Z-direction is given by:

$$(-\beta_2+1)\,\overset{0}{\cancel{Vz_{1,n}}} - 2Vz_{2,n} + (\beta_2+1)\,Vz_{3,n} - \alpha_2\left(\frac{\partial P}{\partial Z}\right)_{n*} = B_{2,n-1}$$

$$\vdots$$

$$(-\beta_m+1)\,Vz_{m-1,n} - 2Vz_{m,n} + (\beta_m+1)\,Vz_{m+1,n} - \alpha_m\left(\frac{\partial P}{\partial Z}\right)_{n*} = B_{m,n-1}$$

$$\vdots \qquad (6.156)$$

$$(-\beta_M+1)\,Vz_{M-1,n} - 2Vz_{M,n} + (\beta_M+1)\,\overset{V_{bz}/V_b}{\cancel{Vz_{M+1,n}}} - \alpha_M\left(\frac{\partial P}{\partial Z}\right)_{n*} = B_{M,n-1}$$

$$\overset{0}{\cancel{Vz_{1,n}}} + 4Vz_{2,n} + 2Vz_{3,n} + \ldots + 4Vz_{M,n} + \overset{V_{bz}/V_b}{\cancel{Vz_{M+1,n}}} = 3M\,\frac{Q}{WH_n V_b}$$

where $B_{m,n-1} = (\varepsilon\beta_m-\delta)\,Vz_{m-1,n-1} + 2\delta Vz_{m,n-1} - (\varepsilon\beta_m+\delta)\,Vz_{m+1,n-1}$

The above system of equations is solved for the down channel velocity profile at column n and the pressure gradient at n*, the midpoint between columns n and n-1. The pressure at column n may be calculated as follows:

$$P_n = P_{n-1} + \left(\frac{\partial P}{\partial Z}\right)_{n*}\Delta Z \qquad (6.157)$$

It should be noted that if the pressure gradient at n* is corrected using shape factors, then these shape factors should be calculated using the channel width at n* and not at column n.

Energy Equation

For the energy equation (6.134), the following finite difference equations are used:

$$\frac{\partial\theta}{\partial Z} \simeq \frac{\theta_{m,n} - \theta_{m,n-1}}{\Delta Z} \tag{6.158}$$

$$\frac{1}{H^2}\frac{\partial^2\theta}{\partial Y^2} \simeq \frac{1}{2H_n^2}\left[\frac{\theta_{m+1,n} - 2\theta_{m,n} + \theta_{m-1,n}}{(\Delta Y)^2}\right]$$

$$+ \frac{1}{2H_{n-1}^2}\left[\frac{\theta_{m+1,n-1} - 2\theta_{m,n-1} + \theta_{m-1,n-1}}{(\Delta Y)^2}\right] \tag{6.159}$$

Substituting Eqs. 6.158 and 6.159 into Eq. 6.134, we obtain for column n:

$$-\theta_{m-1,n} + (\beta+2)\,\theta_{m,n} - \theta_{m+1,n}$$

$$= \delta\,\theta_{m-1,n-1} + (\beta-2\delta)\,\theta_{m,n-1} + \delta\,\theta_{m+1,n} + \gamma_m \tag{6.160}$$

where $m = 2, 3, \ldots, M$

$$\beta = \frac{(\Delta Y)^2}{\Delta Z}\left(\frac{H_n}{H_o}\right)^2 (Vz_{avg,n} + Vz_{avg,n-1})$$

$$\delta = \left(\frac{H_n}{H_{n-1}}\right)^2$$

$$\gamma_m = \frac{(\Delta Y)^2\,\eta_{m,n^*}}{k_m T_{melt}}\left[\left(\frac{\partial Vx}{\partial Y}\right)^2_{m,n} + \left(\frac{\partial Vz}{\partial Y}\right)^2_{m,n} + \delta\left(\frac{\partial Vx}{\partial Y}\right)^2_{m,n-1} + \delta\left(\frac{\partial Vz}{\partial Y}\right)^2_{m,n-1}\right]$$

Eq. 6.160 represents a tridiagonal system of M-1 equations and M-1 unknowns ($\theta_{2,n}$ to $\theta_{M,n}$). The equations may be written as:

$$-\overset{\theta_{sc}}{\cancel{\theta_{1,n}}} + (\beta+2)\,\theta_{2,n} - \theta_{3,n} = A_{2,n-1} + \gamma_2$$

$$\vdots$$

$$-\theta_{m-1,n} + (\beta+2)\,\theta_{m,n} - \theta_{m+1,n} = A_{m,n-1} + \gamma_m \qquad (6.161)$$

$$\vdots$$

$$-\theta_{M-1,n} + (\beta+2)\,\theta_{M,n} - \overset{\theta_b}{\cancel{\theta_{M+1,n}}} = A_{M,n-1} + \gamma_M$$

where $A_{m,n-1} = \delta\theta_{m-1,n-1} + (\beta-2\delta)\,\theta_{m,n-1} + \delta\theta_{m+1,n-1}$

Using Gaussian elimination the above tridiagonal system of equations is solved for the temperature profile at column n (see Refs. (1), (55) for the algorithm).

Shape Factors

The finite difference equations developed in this section are for non-Newtonian fluids flowing through infinitely wide parallel or converging channels. Screw channels, however, have a finite width. In the case of Newtonian flow in a screw channel, shape factors were introduced to account for the effect of the screw flights on down channel flow. Analytical expressions for pure drag flow and pure pressure flow shape factors are available (see Eqs. 6.51 and 6.52). Using these shape factors, a correction factor was derived in Sec. 6.2.2 (for the down channel pressure gradient) for combined drag and pressure flow (see Eqs. 6.45 and 6.50).

For the flow of non-Newtonian fluids in a screw channel, the problem is much more complex. Even if analytical expressions for pure drag flow and pure pressure flow shape factors were available for non-Newtonian fluids (but they are not), they would not be useful for combined flow because non-Newtonian drag and pressure flows cannot be superimposed. If the superposition error was to be neglected and if the non-Newtonian shape factors were replaced with the corresponding Newtonian shape factors, the end results would still be unpredictable. In regions of the screw channel where the drag flow and the pressure backflow terms are nearly equal, serious errors can result if Newtonian shape factors are used to correct the down channel pressure gradient. Consequently, no shape factors are used in the present non-Newtonian nonisothermal developing flow model.

Summary of Finite Difference Equations

The conservation equations and corresponding finite difference equations for the non-Newtonian nonisothermal developing flow model are summarized in App. C for the feed, compression and metering sections of the extruder screw channel.

Results of Simulations

Typical results of predicted pressure, bulk temperature and solid bed profiles for low-density polyethylene are presented in Fig. 6.28 to 6.30 as obtained by the use of the non-Newtonian, nonisothermal developing flow model and the non-Newtonian melting model (see Sec.

5.2.2. The solids flow models for the feed hopper and screw channel (see Chaps. 3 and 4) were utilized to calculate the pressure at the beginning of the melt flow region. The simulation results are shown for three screw speeds: 40, 60 and 80 rpm. The polymer properties, screw dimensions and remaining extruder operating conditions are given in App. G.6.

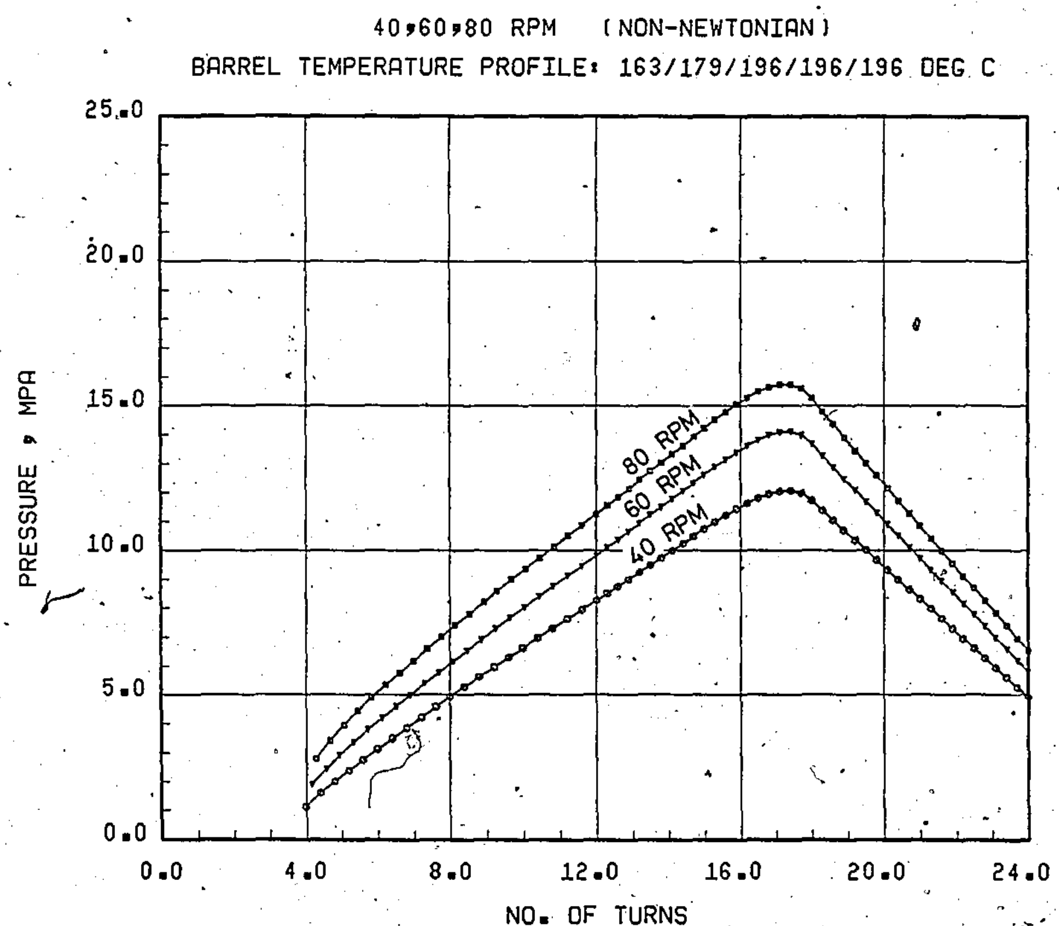

Fig. 6.28 Down channel pressure profiles in the extruder screw channel for non-Newtonian flow. Data for the polymer properties, screw channel dimensions and extruder operating conditions are given in App. G.6.

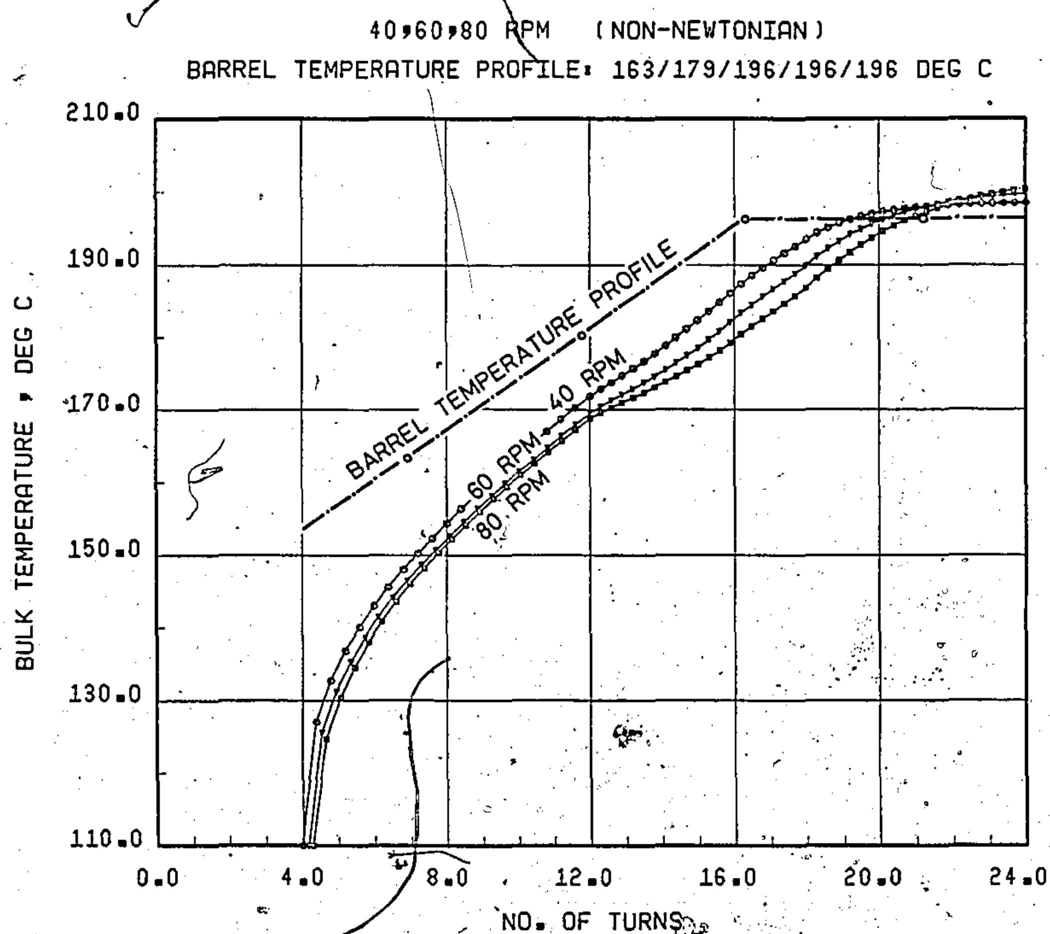

Fig. 6.29 Down channel bulk temperature profiles in the extruder screw channel for non-Newtonian flow. Data for the polymer properties, screw channel dimensions and extruder operating conditions are given in App. G.6.

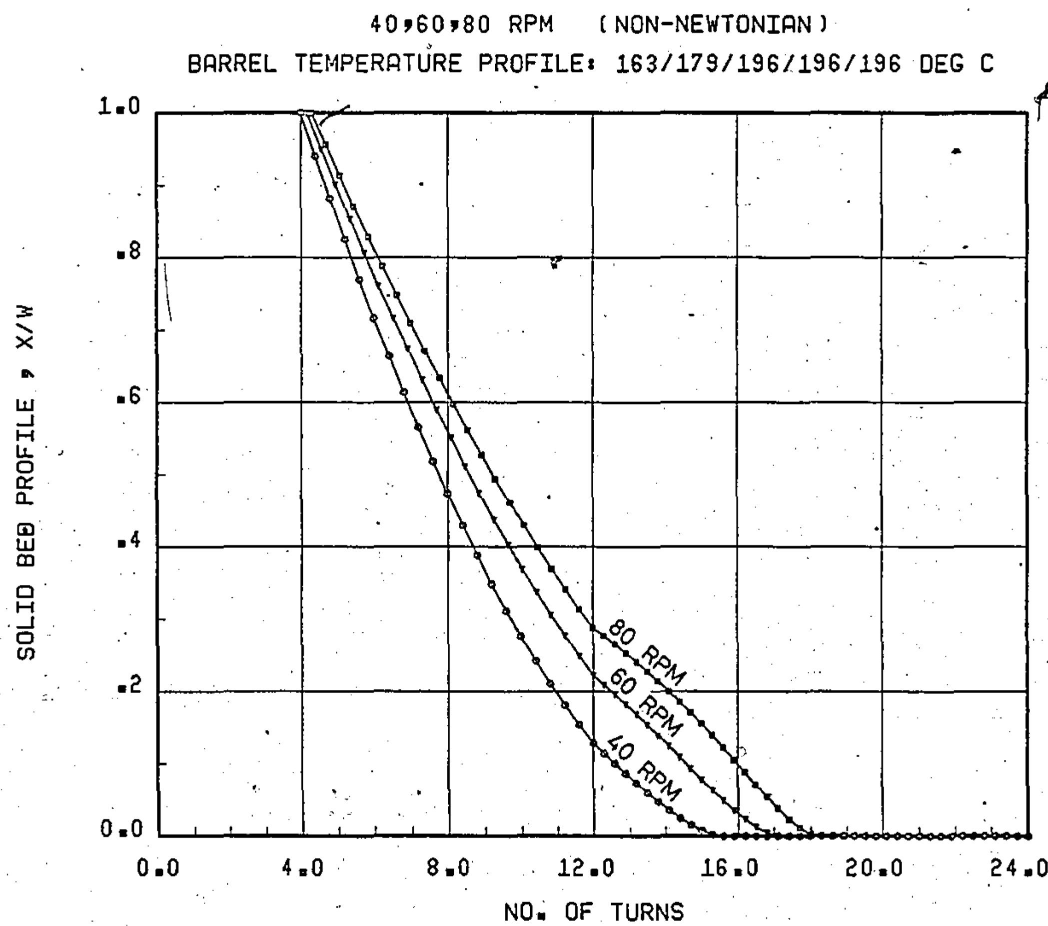

Fig. 6.30 Solid bed profiles in the extruder screw channel for non-Newtonian flow. Data for the polymer properties, screw channel dimensions and extruder operating conditions are given in App. G.6.

CHAPTER 7

MELT FLOW IN THE DIE SECTION

Polymer melt is pumped through a die to give the material a desired shape, for example a rod or tube. After the polymer leaves the extruder screw channel, but before it enters the die, it passes through an adapter which connects the die to the extruder barrel. Placed between the barrel and adapter, there is quite often a breaker plate. The breaker plate is a thick circular plate drilled with several holes spaced closely together. The purpose of the breaker plate is to align the rotating motion of the extrudate as it is pumped from the screw channel into the die channel. It can also be used to support screens to filter out contamination in the polymer and to increase the diehead pressure. Often a higher diehead pressure is desirable in that it results in improved mixing in the extruder screw channel.

Schematic diagrams of the breaker plate, adapter and die used in the flow model are shown in Fig. 7.1 and 7.2. In most cases, the adapter that connects the extruder barrel and die is quite simple in geometry, usually circular in cross-section. In this study a slightly more complex adapter with rectangular flow geometry is used (see Chap. 10 for more details). Attached to the adapter is a cylindrical rod die. For the purpose of melt flow analysis, the tapers in the adapter and die are neglected, for they are very short as compared to the lengths of the adapter and die. The pressure drops across the tapered sections are

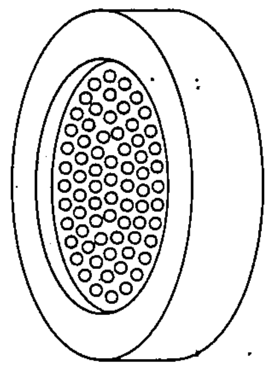

Fig. 7.1 Breaker plate.

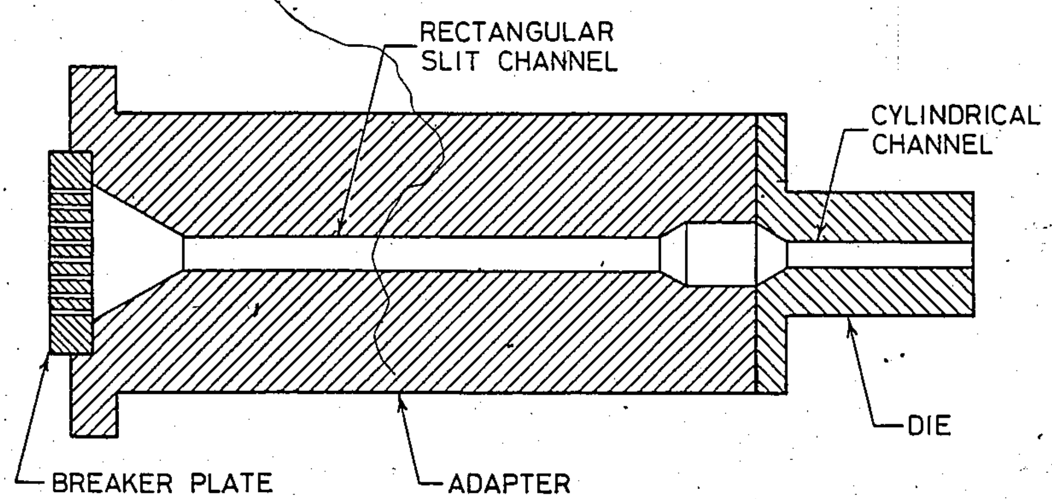

Fig. 7.2 Schematic diagram of the die section (breaker plate/adapter/ die).

negligible as compared to the straight sections.

The purpose of modelling the flow through the breaker plate, adapter and die is to calculate the velocity, temperature and pressure profiles in the flow channel given the extruder operating conditions, flow channel dimensions, and the physical and rheological properties of the polymer melt. The computer model developed here is largely based on work presented in the author's M.Eng. thesis (1). The analysis of melt flow in circular tubes is also presented in a paper by Agur and Vlachopoulos (3). Finally, due to differences in the melt flow analysis in the breaker plate, adaptor and die, each of these three sections will be treated separately.

7.1 Breaker Plate

The physical system for pressure flow through one of the drilled holes in the breaker plate is illustrated in Fig. 7.3. It consists of flow through a tube with inside radius R_B and length z_B. Due to the large number of holes in the breaker plate, the adiabatic temperature boundary condition is assumed at the tube wall.

Flow Equations

The simplified conservation equations for pressure flow through a circular channel are:

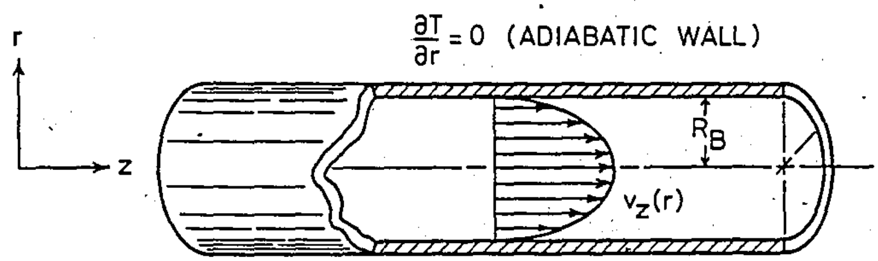

Fig. 7.3 Pressure flow through one of the breaker plate flow channels.

Continuity equation (integral form):

$$\int_{o}^{R_B} v_z \, r \, dr = \frac{Q}{2\pi N_B} \tag{7.1}$$

where N_B is the number of holes in the breaker plate.

Momentum equation:

$$-\frac{dp}{dz} + \frac{1}{r}\frac{d}{dr}(r \; \tau_{rz}) = 0 \tag{7.2}$$

Energy equation:

$$\rho_m \, Cp_m \, v_z \frac{\partial T}{\partial z} = \frac{k_m}{r}\frac{\partial}{\partial r}\left(r \frac{\partial T}{\partial r}\right) + \tau_{rz} \frac{dv_z}{dr} \tag{7.3}$$

The temperature and shear rate dependent constitutive relation (see Eqs. 2.34, and 2.36) may be written as:

$$\tau_{rz} = \eta \frac{dv_z}{dr} \tag{7.4}$$

$$\log \eta = a_o + a_1 \log \dot{\gamma} + a_2 (\log \dot{\gamma})^2 + a_3 T + a_4 T^2 + a_5 T \log \dot{\gamma} \tag{7.5}$$

where $\dot{\gamma} = \left| \frac{dv_z}{dr} \right|$

Substituting Eqs. 7.4 and 7.5 into the above momentum and energy equations (7.2 and 7.3), we obtain:

Momentum:
$$-\frac{dp}{dz} + \eta \frac{d^2 v_z}{dr^2} + \left(\frac{\eta}{r} + \frac{d\eta}{dr}\right) \frac{dv_z}{dr} = 0 \tag{7.6}$$

Energy: $$\rho_m \, Cp_m \, v_z \frac{\partial T}{\partial z} = k_m \left(\frac{\partial^2 T}{\partial r^2} + \frac{1}{r}\frac{\partial T}{\partial r}\right) + \eta \left(\frac{dv_z}{dr}\right)^2 \tag{7.7}$$

The boundary conditions for the above equations are:

$$\begin{array}{lll} z = 0 & p = p_o & T = T(r) = T_o \\ r = 0 & \dfrac{dv_z}{dr} = 0 & \dfrac{\partial T}{\partial r} = 0 \\ r = R_B & v_z = 0 & \dfrac{\partial T}{\partial r} = 0 \end{array} \tag{7.8}$$

A constant temperature profile at the channel entrance equal to the bulk temperature of the polymer at the screw channel exit is utilized.

To represent the above conservation equations (7.1, 7.6 and 7.7) and boundary conditions (7.8) in dimensionless form, let:

$$\begin{aligned} Vz &= \frac{v_z}{V_b} \\ P &= \frac{p}{\rho_m V_b^2} \\ \theta &= \frac{T}{T_{melt}} \\ R &= \frac{r}{R_B} \\ Z &= \frac{k_m z}{\rho_m Cp_m V_b H_o^2} \end{aligned} \tag{7.9}$$

where V_b is the tangential barrel velocity and H_o the screw channel depth in the feed section of the extruder. Substituting the above into Eqs. 7.1, 7.6, 7.7 and 7.8, we obtain in terms of dimensionless parameters:

Continuity equation (integral form):

$$\int_0^1 Vz\ R\ dR = \frac{Q}{2\pi\ N_B\ R_B^2\ V_b} \qquad (7.10)$$

Momentum equation:

$$-\left(\frac{R_B}{H_o}\right)^2 \frac{k_m}{Cp_m}\frac{dP}{dZ} + \eta\frac{d^2Vz}{dR^2} + \left(\frac{\eta}{R} + \frac{d\eta}{dR}\right)\frac{dVz}{dR} = 0 \qquad (7.11)$$

Energy equation:

$$\left(\frac{R_B}{H_o}\right)^2 Vz\frac{\partial\theta}{\partial Z} = \frac{\partial^2\theta}{\partial R^2} + \frac{1}{R}\frac{\partial\theta}{\partial R} + \frac{\eta\ V_b^2}{k_m T_{melt}}\left(\frac{dVz}{dR}\right)^2 \qquad (7.12)$$

Boundary Conditions:

$$\begin{array}{llll} Z = 0 & P = P_o & \theta = \theta_o & \\ R = 0 & \frac{dVz}{dR} = 0 & \frac{\partial\theta}{\partial R} = 0 & (7.13) \\ R = 1 & Vz = 0 & \frac{\partial\theta}{\partial R} = 0 & \end{array}$$

In Eqs. 7.11 and 7.12, when R=0 (at the centre of the channel), $\frac{1}{R}\frac{dVz}{dR}$ and $\frac{1}{R}\frac{\partial\theta}{\partial R}$ are represented by the indeterminate form, $\frac{0}{0}$. According to

L'Hospital's Rule[1]:

$$\lim_{R\to 0}\left(\frac{1}{R}\frac{dVz}{dR}\right) = \frac{d^2Vz}{dR^2} \qquad (7.14)$$

$$\lim_{R\to 0}\left(\frac{1}{R}\frac{\partial\theta}{\partial R}\right) = \frac{\partial^2\theta}{\partial R^2} \qquad (7.15)$$

Thus, the momentum and energy equations become:

Momentum: $$-\left(\frac{R_B}{H_o}\right)^2 \frac{k_m}{Cp_m}\frac{dP}{dZ} + \frac{d\eta}{dR}\frac{dVz}{dR} + 2\eta\frac{d^2Vz}{dR^2} = 0 \quad \text{for } R = 0 \qquad (7.16a)$$

$$-\left(\frac{R_B}{H_o}\right)^2 \frac{k_m}{Cp_m}\frac{dP}{dZ} + \eta\frac{d^2Vz}{dR^2} + \left(\frac{\eta}{R} + \frac{d\eta}{dR}\right)\frac{dVz}{dR} = 0 \text{ for } R>0 \qquad (7.16b)$$

Energy: $$\left(\frac{R_B}{H_o}\right)^2 Vz\frac{\partial\theta}{\partial Z} = 2\frac{\partial^2\theta}{\partial R^2} + \frac{\eta V_b^2}{k_m T_{melt}}\left(\frac{dVz}{dR}\right)^2 \quad \text{for } R = 0 \qquad (7.17a)$$

$$\left(\frac{R_B}{H_o}\right)^2 Vz\frac{\partial\theta}{\partial Z} = \frac{\partial^2\theta}{\partial R^2} + \frac{1}{R}\frac{\partial\theta}{\partial R} + \frac{\eta V_b}{k_m T_{melt}}\left(\frac{dVz}{dR}\right)^2 \text{ for } R>0 \qquad (7.17b)$$

Finite Difference Solution

The Crank-Nicolson implicit finite difference method is used to solve the conservation equations (7.10, 7.16a,b and 7.17a,b) along with the accompanying boundary conditions (7.13). The finite difference grid is shown in Fig. 7.4.

---

[1]L'Hospital's Rule: If $\lim_{x\to a}\frac{f(x)}{g(x)} = \frac{0}{0}$, then $\lim_{x\to a}\left(\frac{f(x)}{g(x)}\right) = \lim_{x\to a}\left(\frac{f'(x)}{g'(x)}\right)$.

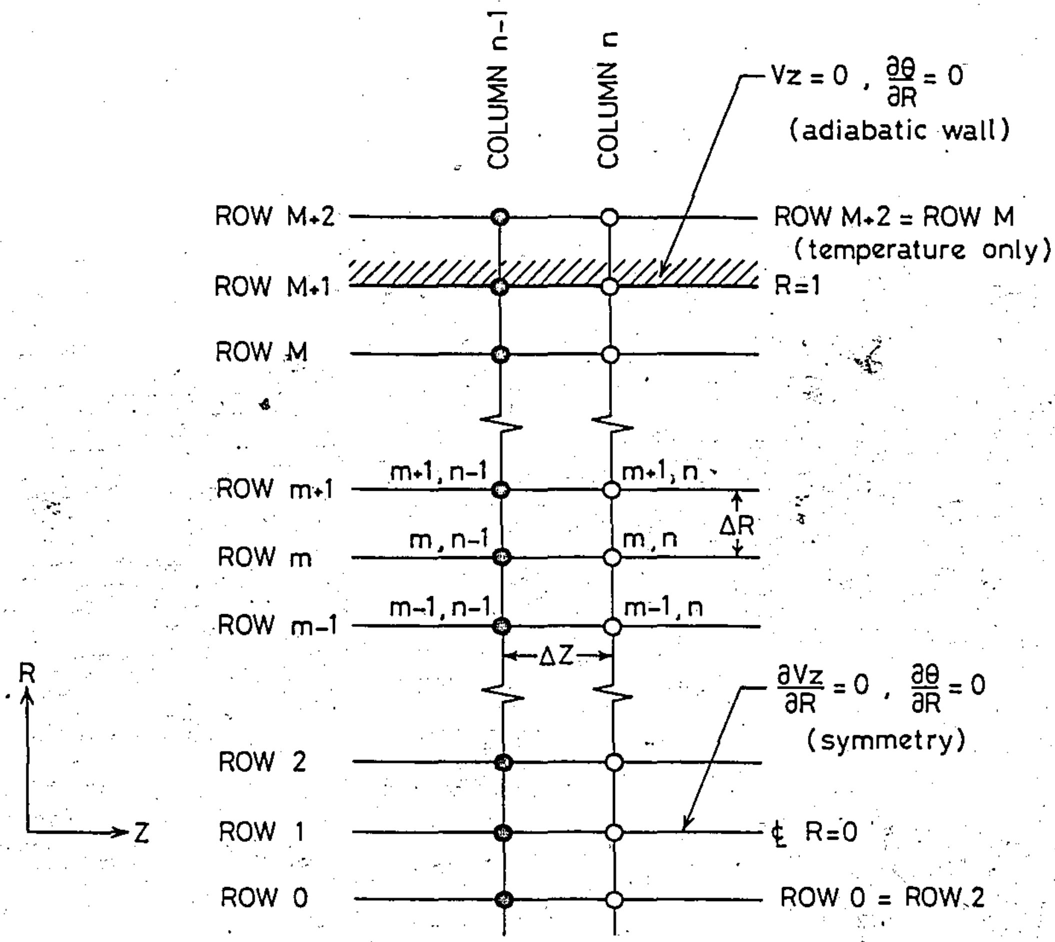

Fig. 7.4 Finite difference grid for a breaker plate flow channel. Dark nodes denote known values and blank nodes denote values to be calculated.

Continuity and Momentum Equations

Simpson's Rule is used to represent the continuity equation (7.10) in finite difference form, and is written as follows for column n in the finite difference grid:

$$\int_0^1 Vz\, R\, dR \simeq \frac{\Delta R}{3}\left[Vz_{1,n} R_1 + 4Vz_{2,n} R_2 + 2Vz_{3,n} R_3 + \ldots + 4Vz_{M,n} R_M + Vz_{M+1,n} R_{M+1}\right] \qquad (7.18)$$

Substituting the above equation into Eq. 7.10, we obtain:

$$\cancel{Vz_{1,n}} \cancelto{0}{R_1} + 4Vz_{2,n} R_2 + 2Vz_{3,n} R_3 + \ldots + 4Vz_{M,n} R_M \cancelto{0}{+ Vz_{M+1,n} R_{M+1}}$$

$$= \frac{3}{\Delta R}\,\frac{Q}{2\pi N_B R_B^2 V_b} = 1.5\, M\, \frac{Q}{\pi N_B R_B^2 V_b} \qquad (7.19)$$

For the momentum equations (7.16a,b) the following finite difference approximations are used:

$$\frac{dVz}{dR} \simeq \frac{Vz_{m+1,n} - Vz_{m-1,n}}{2\,\Delta R} \qquad (7.20)$$

$$\frac{d^2Vz}{dR^2} \simeq \frac{Vz_{m+1,n} - 2Vz_{m,n} + Vz_{m-1,n}}{(\Delta R)^2} \qquad (7.21)$$

Substituting the above equations into Eqs. 7.16a and 7.16b, we obtain for column n:

$Vz_{2,n}$ by symmetry

$$\cancelto{Vz_{2,n}}{Vz_{0,n}} - 2Vz_{1,n} + Vz_{2,n} - \frac{\alpha_1}{2}\left(\frac{dP}{dZ}\right)_n = 0 \quad \text{for } R = 0 \qquad (7.22a)$$

$$(-\beta_m+1)\ Vz_{m-1,n} - 2Vz_{m,n} + (\beta_m+1)\ Vz_{m+1,n} - \alpha_m \left(\frac{dP}{dZ}\right)_n = 0$$

for $R > 0$ (7.22b)

where $m = 2, 3, \ldots, M$

$$\alpha_m = \frac{k_m}{Cp_m\ \eta_{m,n}} \left(\frac{R_B}{H_o}\right)^2 (\Delta R)^2$$

$$\beta_m = \frac{\Delta R}{2} \left[\frac{1}{R_m} + \frac{1}{\eta_{m,n}} \left(\frac{d\eta}{dR}\right)_{m,n} \right]$$

Combining Eqs. 7.19, 7.22a and 7.22b, we have a modified tridiagonal system of M+1 algebraic equations and M+1 unknowns ($Vz_{1,n}$ to $Vz_{M,n}$ and $(dP.dZ)_n$. The equations may be written as follows:

$$- 2Vz_{1,n} + 2Vz_{2,n} - \frac{\alpha_1}{2} \left(\frac{dP}{dZ}\right)_n = 0$$

$$(-\beta_2+1)\ Vz_{1,n} - 2Vz_{2,n} + (\beta_2+1)\ Vz_{3,n} - \alpha_2 \left(\frac{dP}{dZ}\right)_n = 0$$

$$\vdots$$

$$(-\beta_m+1)\ Vz_{m-1,n} - 2Vz_{m,n} + (\beta_m+1)\ Vz_{m+1,n} - \alpha_m \left(\frac{dP}{dZ}\right)_n = 0 \qquad (7.23)$$

$$\vdots$$

$$(-\beta_M+1)\ Vz_{M-1,n} - 2Vz_{M,n} + (\beta_M+1)\ \cancel{Vz_{M+1,n}}^{\,0} - \alpha_M \left(\frac{dP}{dZ}\right)_n = 0$$

$$4Vz_{2,n} R_2 + 2Vz_{3,n} R_3 + \ldots + 4Vz_{M,n} R_M = 1.5\ M \frac{Q}{\pi N_B R_B^2 V_b}$$

or in matrix form:

$$
\begin{bmatrix}
-2 & 2 & & & & -\alpha_1/2 \\
A_2 & B_2 & C_2 & & & -\alpha_2 \\
 & \ddots & & & & \vdots \\
 & A_m & B_m & C_m & & -\alpha_m \\
 & & \ddots & & & \vdots \\
 & & & A_M & B_M & -\alpha_M \\
0 & 4R_2 & 2R_3 & \cdots & 4R_M & 0
\end{bmatrix}
\begin{bmatrix}
Vz_{1,n} \\ Vz_{2,n} \\ \vdots \\ Vz_{m,n} \\ \vdots \\ Vz_{M,n} \\ (\frac{dP}{dZ})_n
\end{bmatrix}
=
\begin{bmatrix}
0 \\ 0 \\ \vdots \\ 0 \\ \vdots \\ 0 \\ 1.5\, M \frac{Q}{\pi N_B R_B{}^2 V_b}
\end{bmatrix}
\qquad (7.24)
$$

where $A_m = -\beta_m + 1$

$B_m = -2$

$C_m = \beta_m + 1$

Using Gaussian elimination, this system of equations is solved for the down channel velocity profile and pressure gradient at column n in the finite difference grid. The algorithm used for solving the above modified tridiagonal system is described in Ref. (1). The pressure at column n may be calculated as follows:

$$P_n = P_{n-1} + (\frac{dP}{dZ})_n \Delta Z \qquad (7.25)$$

Energy Equation

For the energy equations (7.17a,b), the following finite difference approximations are used:

$$\frac{\partial\theta}{\partial Z} \approx \frac{\theta_{m,n} - \theta_{m,n-1}}{\Delta Z} \qquad (7.26)$$

$$\frac{\partial\theta}{\partial R} \approx \frac{1}{2}\left[\frac{\theta_{m+1,n} - \theta_{m-1,n}}{2\Delta R}\right] + \frac{1}{2}\left[\frac{\theta_{m+1,n-1} - \theta_{m-1,n-1}}{2\Delta R}\right] \qquad (7.27)$$

$$\frac{\partial^2\theta}{\partial R^2} \approx \frac{1}{2}\left[\frac{\theta_{m+1,n} - 2\theta_{m,n} + \theta_{m-1,n}}{(\Delta R)^2}\right]$$

$$+ \frac{1}{2}\left[\frac{\theta_{m+1,n-1} - 2\theta_{m,n-1} + \theta_{m-1,n-1}}{(\Delta R)^2}\right] \qquad (7.28)$$

Substituting the above equations into Eqs. 7.17a and 7.17b, we obtain for column n:

$$-\overset{\theta_{2,n}\text{ by symmetry}}{\cancel{\theta_{0,n}}} + \left(\frac{\alpha_1}{2} + 2\right)\theta_{1,n} - \theta_{2,n}$$

$$= \overset{\theta_{2,n-1}}{\cancel{\theta_{0,n-1}}} + \left(\frac{\alpha_1}{2} - 2\right)\theta_{1,n-1} + \theta_{2,n-1} \qquad \text{for } R = 0 \qquad (7.29a)$$

$$(\beta_m-1)\,\theta_{m-1,n} + (\alpha_m+2)\,\theta_{m,n} - (\beta_m+1)\,\theta_{m+1,n}$$

$$= (-\beta_m+1)\,\theta_{m-1,n-1} + (\alpha_m-2)\,\theta_{m,n-1} + (\beta_m+1)\,\theta_{m+1,n-1} + \gamma_m$$

$$\text{for } 0 < R < 1 \qquad (7.29b)$$

$$(\beta_{M+1}-1)\,\theta_{M,n} + (\overset{0}{\cancel{\alpha_{M+1}}}+2)\,\theta_{M+1,n} - (\beta_{M+1}+1)\,\overset{\theta_{M,n}}{\cancel{\theta_{M+2,n}}}$$

$$= (-\beta_{M+1}+1)\,\theta_{M,n-1} + (\overset{0}{\cancel{\alpha_{M+1}}}-2)\,\theta_{M+1,n-1} + (\beta_{M+1}+1)\,\overset{\theta_{M,n-1}}{\cancel{\theta_{M+2,n-1}}} + \gamma_{M+1}$$

$$\text{for } R = 1 \qquad (7.29c)$$

where $m = 2, 3, \ldots, M$

$$\alpha_m = \frac{2(\Delta R)^2}{\Delta Z} \left(\frac{R_B}{H_o}\right)^2 Vz_{m,n}$$

$$\beta_m = \frac{\Delta R}{2R_m}$$

$$\gamma_m = 2(\Delta R)^2 \; \eta_{m,n} \frac{V_b^2}{k_m T_{melt}} \left(\frac{dVz}{dR}\right)^2_{m,n}$$

Equations 7.29a, 7.29b and 7.29c represent a tridiagonal system of M+1 equations and M+1 unknowns ($\theta_{1,n}$ to $\theta_{M+1,n}$) and may be written as follows:

$$\left(\frac{\alpha_1}{2} + 2\right) \theta_{1,n} - 2\theta_{2,n} = D_{1,n-1}$$

$$(\beta_2 - 1)\,\theta_{1,n} + (\alpha_2 + 2)\,\theta_{2,n} - (\beta_2 + 1)\,\theta_{3,n} = D_{2,n-1} + \gamma_2$$

$$\vdots$$

$$(\beta_m - 1)\,\theta_{m-1,n} + (\alpha_m + 2)\,\theta_{m,n} - (\beta_m + 1)\,\theta_{m+1,n} = D_{m,n-1} + \gamma_m \qquad (7.30)$$

$$\vdots$$

$$(\beta_M - 1)\,\theta_{M-1,n} + (\alpha_M + 2)\,\theta_{M,n} - (\beta_M + 1)\,\theta_{M+1,n} = D_{M,n-1} + \gamma_M$$

$$-2\,\theta_{M,n} + 2\theta_{M+1,n} = D_{M+1,n-1} + \gamma_{M+1}$$

where $D_{1,n-1} = \left(\frac{\alpha_1}{2} - 2\right) \theta_{1,n-1} + 2\theta_{2,n-1}$

$$D_{m,n-1} = (-\beta_m + 1)\,\theta_{m-1,n-1} + (\alpha_m - 2)\,\theta_{m,n-1} + (\beta_m + 1)\,\theta_{m+1,n-1}$$

$$D_{M+1,n-1} = 2\,\theta_{M,n-1} - 2\,\theta_{M+1,n-1}$$

or in matrix form:

$$\begin{bmatrix} B_1 & C_1 & & & & & & \\ A_2 & B_2 & C_2 & & & & & \\ & \ddots & & & & & & \\ & & A_m & B_m & C_m & & & \\ & & & \ddots & & & & \\ & & & & A_M & B_M & C_M \\ & & & & & -2 & 2 \end{bmatrix} \begin{bmatrix} \theta_{1,n} \\ \theta_{2,n} \\ \vdots \\ \theta_{m,n} \\ \vdots \\ \theta_{M,n} \\ \theta_{M+1,n} \end{bmatrix} = \begin{bmatrix} D_{1,n-1} \\ D_{2,n-1} + \gamma_2 \\ \vdots \\ D_{m,n-1} + \gamma_m \\ \vdots \\ D_{M,n-1} + \gamma_M \\ D_{M+1,n-1} + \gamma_{M+1} \end{bmatrix} \quad (7.31)$$

where $B_1 = \frac{\alpha_1}{2} + 2$, $C_1 = -2$

$A_m = \beta_m - 1$

$B_m = \alpha_m + 2$

$C_m = -(\beta_m+1)$

This tridiagonal system of equations is solved for the temperature profile at column n by Gaussian elimination using Thomas' method (for details of the algorithm, see Refs. (1), (55)).

Bulk Temperature

The flow-average (bulk) temperature at a given downstream position in the flow channel is defined as:

$$T_{bulk} = \frac{\int_o^{R_B} v_z(r,z)\ T(r,z)\ r\ dr}{\int_o^{R_B} v_z(r,z)\ r\ dr} \tag{7.32}$$

or in dimensionless form:

$$\theta_{bulk} = \frac{\int_o^{1} Vz(R,Z)\ \theta(R,Z)\ R\ dR}{\int_o^{1} Vz(R,Z)\ R\ dR} \tag{7.33}$$

Equation 7.33 may be written in finite difference form for column n in the finite difference grid, using Simpson's Rule as follows:

$$\theta_{bulk,n} = \frac{Vz_1\ \theta_1\ R_1 + 4Vz_2\ \theta_2\ R_2 + 2Vz_3\ \theta_3\ R_3 + \ldots + 4Vz_M\ \theta_M\ R_M + Vz_{M+1}\ \theta_{M+1}\ R_{M+1}}{Vz_1\ R_1 + 4Vz_2\ R_2 + 2Vz_3\ R_3 + \ldots + 4Vz_M\ R_M + Vz_{M+1}\ R_{M+1}} \tag{7.34}$$

7.2 Adapter

The physical system for pressure flow through the rectangular slit channel of the adapter is illustrated in Fig. 7.5. The channel has height H_A, width W_A and length z_A, and it is assumed that the channel walls are at a constant temperature T_A.

Flow Equations

The simplified conservation equations for pressure flow through a rectangular slit channel having infinite width are shown below in Eqs. 7.35, 7.36 and 7.37. The effect of the channel side walls on the flow is accounted for using shape factors as discussed later in this section.

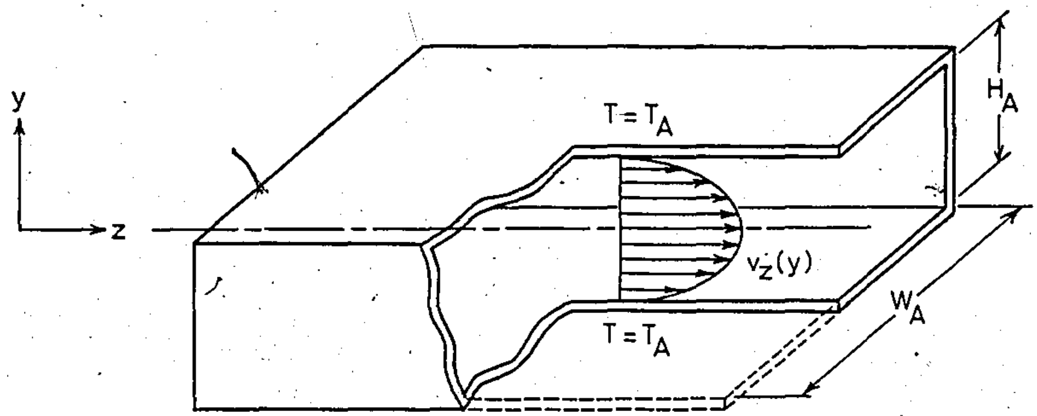

Fig. 7.5 Pressure flow through the adapter flow channel.

Continuity equation (integrated form):

$$\int_{o}^{H_A/2} v_z \, dy = \frac{Q}{2W_A} \tag{7.35}$$

Momentum equation:

$$-\frac{dp}{dz} + \frac{d\tau_{yz}}{dy} = 0 \tag{7.36}$$

Energy equation:

$$\rho_m \, Cp_m \, v_z \frac{\partial T}{\partial z} = k_m \frac{\partial^2 T}{\partial y^2} + \tau_{yz} \frac{dv_z}{dy} \tag{7.37}$$

The temperature and shear rate dependent constitutive relation (see Eqs. 2.34 and 2.36) may be written as:

$$\tau_{yz} = \eta \frac{dv_z}{dy} \tag{7.38}$$

$$\log \eta = a_o + a_1 \log \dot{\gamma} + a_2(\log \dot{\gamma})^2 + a_3 T + a_4 T^2 + a_5 T \log \dot{\gamma} \tag{7.39}$$

where $\dot{\gamma} = \left| \frac{dv_z}{dy} \right|$

Substituting Eqs. 7.38 and 7.39 into the above momentum and energy equations (7.36 and 7.37), we obtain:

$$\text{Momentum:} \quad -\frac{dp}{dz} + \eta \frac{d^2 v_z}{dy^2} + \frac{d\eta}{dy} \frac{dv_z}{dy} = 0 \tag{7.40}$$

$$\text{Energy:} \quad \rho_m \, Cp_m \, v_z \frac{\partial T}{\partial z} = k_m \frac{\partial^2 T}{\partial y^2} + \eta \left(\frac{dv_z}{dy}\right)^2 \tag{7.41}$$

The boundary conditions for the above equations are:

$$z = 0 \qquad p = p_o \qquad T = T(y) = T_o$$

$$y = 0 \qquad \frac{dv_z}{dy} = 0 \qquad \frac{\partial T}{\partial y} = 0 \tag{7.42}$$

$$y = H_A/2 \qquad v_z = 0 \qquad T = T_A$$

The pressure and temperature, p_o and T_o, at the channel entrance are assumed to be equal to the exit pressure and bulk temperature respectively in the breaker plate. Also, it is assumed that the velocity and temperature profiles are symmetric about the central axis of the rectangular channel.

To represent the above conservation equations (7.35, 7.40 and 7.41) and boundary conditions (7.42) in dimensionless form, let:

$$\begin{aligned}
Vz &= \frac{v_z}{V_b} \\
P &= \frac{p}{\rho_m V_b^2} \\
\theta &= \frac{T}{T_{melt}} \\
Y &= \frac{y}{H_A/2} \\
Z &= \frac{k_m\, z}{\rho_m\, Cp_m^*\, V_b\, H_o^2}
\end{aligned} \tag{7.43}$$

where V_b is the tangential barrel velocity and H_o is the screw channel depth in the feed section of the extruder. Substituting the above into Eqs. 7.35, 7.40, 7.41 and 7.42, we obtain in terms of dimensionless parameters:

Continuity equation (integral form):

$$\int_0^1 Vz \; dY = \frac{Q}{W_A H_A V_b} \tag{7.44}$$

Momentum equation:

$$-\left(\frac{H_A}{2\,H_o}\right)^2 \frac{k_m}{Cp_m} \frac{dP}{dZ} + \eta \frac{d^2Vz}{dY^2} + \frac{d\eta}{dY} \frac{dVz}{dY} = 0 \tag{7.45}$$

Energy equation:

$$\left(\frac{H_A}{2\,H_o}\right)^2 Vz \frac{\partial\theta}{\partial Z} = \frac{\partial^2\theta}{\partial Y^2} + \frac{\eta\, V_b^2}{k_m T_{melt}} \left(\frac{dVz}{dY}\right)^2 \tag{7.46}$$

Boundary conditions:

$$\begin{array}{llll} Z = 0 & P = P_o & \theta = \theta_o & \\ Y = 0 & \dfrac{dVz}{dY} = 0 & \dfrac{\partial\theta}{\partial Y} = 0 & \qquad (7.47) \\ Y = 1 & Vz = 0 & \theta = \theta_A = \dfrac{T_A}{T_{melt}} & \end{array}$$

<u>Finite Difference Solution</u>

The Crank-Nicolson implicit finite difference method is used to solve the conservation equations (7.44, 7.45 and 7.46) along with the accompanying boundary conditions (7.47). The finite difference grid is shown in Fig. 7.6.

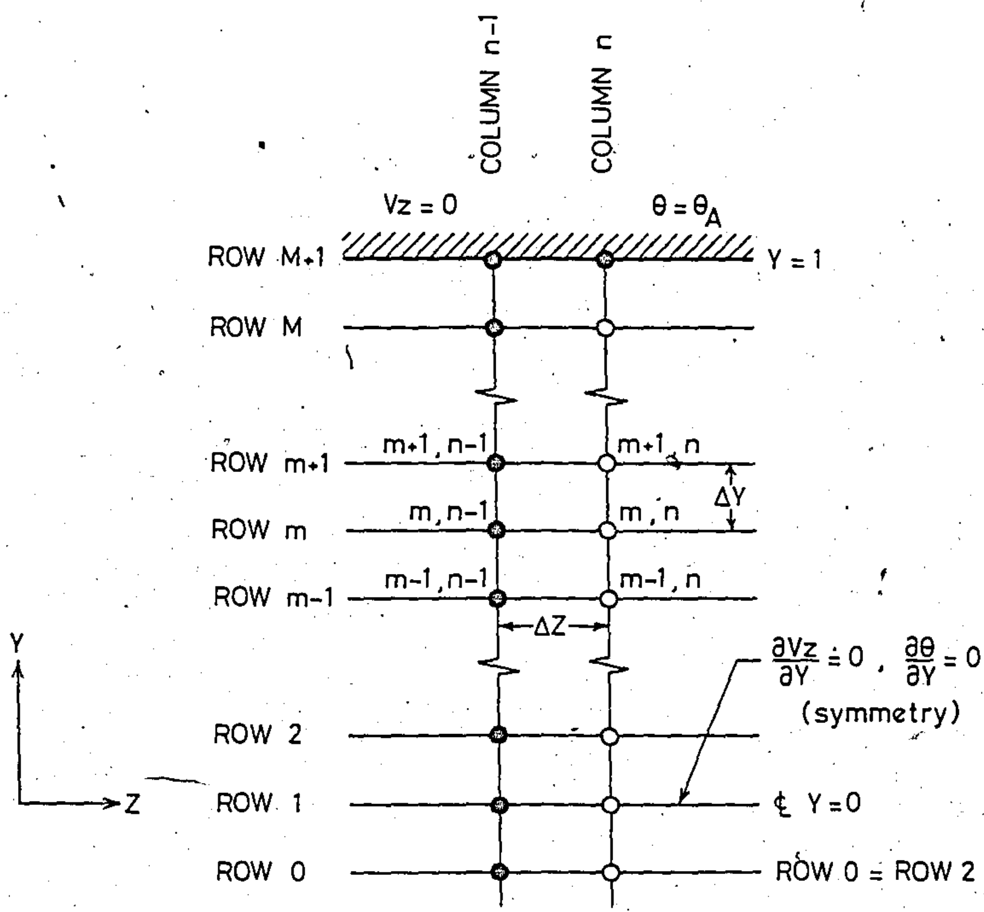

Fig. 7.6 Finite difference grid for the adapter flow channel. Dark nodes denote known values (either calculated or boundary values) and blank nodes denote values to be calculated.

Continuity and Momentum Equations

Simpson's Rule is used to represent the continuity equation (7.44) in finite difference form, and is written for column n in the finite difference grid as follows:

$$\int_0^1 Vz\, dY \approx \frac{\Delta Y}{3} [Vz_{1,n} + 4Vz_{2,n} + 2Vz_{3,n} + \dots + 4Vz_{M,n} + Vz_{M+1,n}] \qquad (7.48)$$

Substituting the above equation into Eq. 7.44, we obtain:

$$Vz_{1,n} + 4Vz_{2,n} + 2Vz_{3,n} + \dots + 4Vz_{M,n} + \cancelto{0}{Vz_{M+1,n}} = \frac{3}{\Delta Y} \frac{Q}{W_A H_A V_b}$$

$$= 3M \frac{Q}{W_A H_A V_b} \qquad (7.49)$$

For the momentum equation (7.45), the following finite difference approximations are used;

$$\frac{dVz}{dY} \approx \frac{Vz_{m+1,n} - Vz_{m-1,n}}{2\ \Delta Y} \qquad (7.50)$$

$$\frac{d^2Vz}{dY^2} \approx \frac{Vz_{m+1,n} - 2Vz_{m,n} + Vz_{m-1,n}}{(\Delta Y)^2} \qquad (7.51)$$

Substituting the above equations into Eq. 7.45, we obtain for column n:

$$(-\beta_m+1)\ Vz_{m-1,n} - 2Vz_{m,n} + (\beta_m+1)\ Vz_{m+1,n} - \alpha_m \left(\frac{dP}{dZ}\right)_n = 0 \qquad (7.52)$$

where $\quad m = 2, 3, \ldots, M$

$$\alpha_m = (\Delta Y)^2 \frac{k_m}{\eta_{m,n}\, Cp_m} \left(\frac{H_A}{2\, H_o}\right)^2$$

$$\beta_m = \frac{\Delta Y}{2\, \eta_{m,n}} \left(\frac{d\eta}{dY}\right)_{m,n}$$

Combining Eqs. 7.49 and 7.52, we have a modified tridiagonal system of M+1 algebraic equations and M+1 unknowns ($Vz_{1,n}$ to $Vz_{M,n}$ and $(dP/dZ)_n$). The equations may be written as follows:

by symmetry

$$\begin{aligned}
&(-\beta_1+1)\, \cancelto{Vz_{2,n}}{Vz_{o,n}} - 2Vz_{1,n} + (\beta_1+1)\, Vz_{2,n} - \alpha_1 \left(\frac{dP}{dZ}\right)_n = 0 \\
&(-\beta_2+1)\, Vz_{1,n} - 2Vz_{2,n} + (\beta_2+1)\, Vz_{3,n} - \alpha_2 \left(\frac{dP}{dZ}\right)_n = 0 \\
&\qquad \vdots \\
&(-\beta_m+1)\, Vz_{m-1,n} - 2Vz_{m,n} + (\beta_m+1)\, Vz_{m+1,n} - \alpha_m \left(\frac{dP}{dZ}\right)_n = 0 \qquad (7.53) \\
&\qquad \vdots \\
&(-\beta_M+1)\, Vz_{M-1,n} - 2Vz_{M,n} + (\beta_M+1)\, \cancelto{0}{Vz_{M+1,n}} - \alpha_M \left(\frac{dP}{dZ}\right)_n = 0 \\
&Vz_{1,n} + 4Vz_{2,n} + 2Vz_{3,n} + \ldots + 4Vz_{M,n} + \cancelto{0}{Vz_{M+1,n}} = 3M \frac{Q}{W_A H_A V_b}
\end{aligned}$$

This system of equations is solved for the downstream velocity profile and pressure gradient at column n by Gaussian elemination (see Ref. (1) for the algorithm). The pressure at column n may be calculated as follows:

$$P_n = P_{n-1} + \frac{1}{F_p} \left(\frac{dP}{dZ}\right)_n \Delta Z \qquad (7.54)$$

where F_p is the Newtonian shape factor for pressure flow in rectangular channels (see Eqs. 6.52 and 6.57b). Of course, a non-Newtonian shape factor would be more suitable. As an approximation, however, the Newtonian shape factor is sufficiently accurate. In Chap. 6 it was stated that difficulties arise when Newtonian shape factors are utilized in combined non-Newtonian drag and pressure flow problems. Such is not the case here, since we are dealing with pure pressure flow.

Energy Equation

For the energy equation (7.46), the following finite difference approximations are used:

$$\frac{\partial \theta}{\partial Z} \approx \frac{\theta_{m,n} - \theta_{m,n-1}}{\Delta Z} \tag{7.55}$$

$$\frac{\partial^2 \theta}{\partial Y^2} \approx \frac{1}{2}\left[\frac{\theta_{m+1,n} - 2\theta_{m,n} + \theta_{m-1,n}}{(\Delta Y)^2}\right] + \frac{1}{2}\left[\frac{\theta_{m+1,n-1} - 2\theta_{m,n-1} + \theta_{m-1,n-1}}{(\Delta Y)^2}\right] \tag{7.56}$$

Substituting the above equations into Eq. 7.46, we obtain for column n:

$$-\theta_{m-1,n} + (\beta_m+2)\,\theta_{m,n} - \theta_{m+1,n}$$
$$= \theta_{m-1,n-1} + (\beta_m-2)\,\theta_{m,n-1} + \theta_{m+1,n-1} + \gamma_m \tag{7.57}$$

where $m = 1, 2, \ldots, M$

$$\beta_m = \frac{2(\Delta Y)^2}{\Delta Z}\left(\frac{H_A}{2H_o}\right)^2 Vz_{m,n}$$

$$\gamma_m = 2(\Delta Y)^2 \, \eta_{m,n} \frac{V_b}{k_m T_{melt}} \left(\frac{dVz}{dY}\right)^2_{m,n}$$

Equation 7.57 represents a tridiagonal system of M equations and M unknowns ($\theta_{1,n}$ to $\theta_{M,n}$) and may be written as follows:

$$-\overset{\theta_{2,n}\text{ by symmetry}}{\cancel{\theta_{o,n}}} + (\beta_1+2)\ \theta_{1,n} - \theta_{2,n} = A_{1,n-1} + \overset{o}{\cancel{\gamma_1}}$$

$$-\theta_{1,n} + (\beta_2+2)\ \theta_{2,n} - \theta_{3,n} = A_{2,n-1} + \gamma_2$$

$$\vdots$$

$$-\theta_{m-1,n} + (\beta_m+2)\ \theta_{m,n} - \theta_{m+1,n} = A_{m,n-1} + \gamma_m \qquad (7.58)$$

$$\vdots$$

$$-\theta_{M-1,n} + (\beta_M+2)\ \theta_{M,n} - \overset{\theta_A}{\cancel{\theta_{M+1,n}}} = A_{M,n-1} + \gamma_M$$

where $A_{m,n-1} = \theta_{m-1,n-1} + (\beta_m-2)\ \theta_{m,n-1} + \theta_{m+1,n-1}$

This system of equations is solved for the temperature profile at column n by Gaussian elimination using Thomas' method (see Refs. (1), (55) for details of the algorithm).

Bulk Temperature

The flow-average (bulk) temperature at a given downstream position in the adapter flow channel may be defined as:

$$T_{bulk} = \frac{\int_0^{H_A/2} v_z(y,z)\ T(y,z)\ dy}{\int_0^{H_A/2} v_z\ (y,z)\ dy} \tag{7.59}$$

or in dimensionless form:

$$\theta_{bulk} = \frac{\int_0^{1} Vz(Y,Z)\ \theta(Y,Z)\ dY}{\int_0^{1} Vz\ (Y,Z)\ dY} \tag{7.60}$$

Using Simpson's Rule, Eq. 7.60 may be written in finite difference form for column n in the finite difference grid as follows:

$$\theta_{bulk,n} = \frac{Vz_{1,n}\ \theta_{1,n} + 4Vz_{2,n}\ \theta_{2,n} + 2Vz_{3,n}\ \theta_{3,n} + \ldots + 4Vz_{M,n}\ \theta_{M,n} + Vz_{M+1,n}\ \theta_{M+1,n}}{Vz_{1,n} + 4Vz_{2,n} + 2Vz_{3,n} + \ldots + 4Vz_{M,n} + Vz_{M+1,n}} \tag{7.61}$$

7.3 Die

The physical system for pressure flow through the cylindrical rod die is illustrated in Fig. 7.7. The die flow channel has a radius R_D and length z_D, and the die walls are at a constant temperature T_D.

Flow Equations

The simplified conservation equations for pressure flow through the die channel are very similar to the breaker plate equations. In dimensionless form, they may be written as:

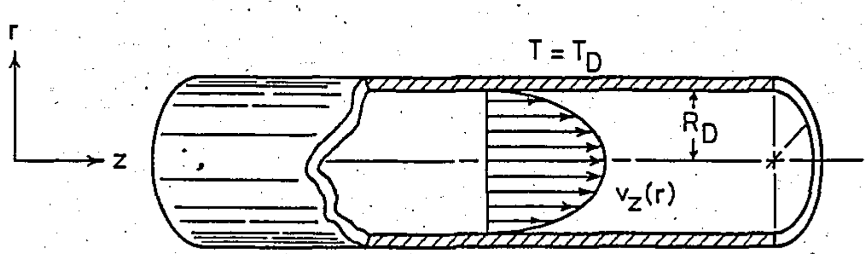

Fig. 7.7 Pressure flow through the die flow channel.

Continuity equation (integrated form):

$$\int_0^1 Vz\ R\ dR = \frac{Q}{2\pi\ R_D^2\ V_b} \tag{7.62}$$

Momentum equation:

$$-\left(\frac{R_D}{H_o}\right)^2 \frac{k_m}{Cp_m} \frac{dP}{dZ} + 2\eta \frac{d^2Vz}{dR^2} = 0 \quad \text{for } R = 0 \tag{7.63a}$$

$$-\left(\frac{R_D}{H_o}\right)^2 \frac{k_m}{Cp_m} \frac{dP}{dZ} + \eta \frac{d^2Vz}{dR^2} + \left(\frac{\eta}{R} + \frac{d\eta}{dR}\right) \frac{dVz}{dR} = 0 \quad \text{for } R > 0 \tag{7.63b}$$

Energy equation:

$$\left(\frac{R_D}{H_o}\right)^2 Vz \frac{\partial\theta}{\partial Z} = 2 \frac{\partial^2\theta}{\partial R^2} + \frac{\eta\ V_b^2}{k_m T_{melt}} \left(\frac{dVz}{dR}\right)^2 \quad \text{for } R = 0 \tag{7.64a}$$

$$\left(\frac{R_D}{H_o}\right)^2 Vz \frac{\partial\theta}{\partial Z} = \frac{\partial^2\theta}{\partial R^2} + \frac{1}{R}\frac{\partial\theta}{\partial R} + \frac{\eta\ V_b^2}{k_m T_{melt}} \cdot \left(\frac{dVz}{dR}\right)^2 \quad \text{for } R > 0 \tag{7.64b}$$

Constitutive equation:

$$\log \eta = a_o + a_1 \log \dot{\gamma} + a_2(\log \dot{\gamma})^2 + a_3\ T + a_4\ T^2 + a_5\ T \log \dot{\gamma} \tag{7.65}$$

where $\dot{\gamma} = \left|\frac{dv_z}{dr}\right|$

Boundary conditions:

$$Z = 0 \qquad P = P_o \qquad \theta = \theta_o(R)$$

$$R = 0 \qquad \frac{dVz}{dR} = 0 \qquad \frac{\partial\theta}{\partial R} = 0 \tag{7.66}$$

$$R = 1 \qquad Vz = 0 \qquad \theta = \theta_D = \frac{T_D}{T_{melt}}$$

In the above equations, V_b is the tangential barrel velocity and H_o is the channel depth in the feed section of the extruder. The temperature profile and pressure at the beginning of the die channel are assumed to be equal to the exit values from the adapter.

Finite Difference Solution

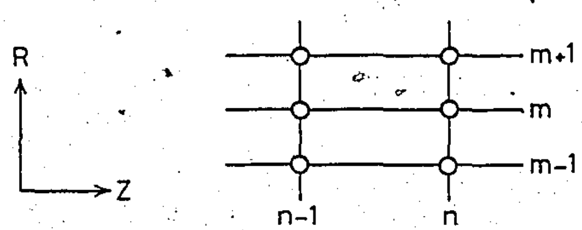

Fig. 7.8 Finite difference grid for the die flow channel.

The Crank-Nicolson implicit finite difference method is used to solve the conservation equations (7.62 to 7.65) along with the accompanying boundary conditions (7.66). An abbreviated version of the finite difference grid is shown in Fig. 7.8. The grid used for the die channel is essentially the same as the one for the adapter (see Fig. 7.6).

Continuity and Momentum Equations

The continuity and momentum equations in finite-difference form are identical to those for the breaker plate (except that R_D replaces R_B) and may be written for column n in the finite difference grid as:

$$- 2Vz_{1,n} + 2Vz_{2,n} - \frac{\alpha_1}{2} \left(\frac{dP}{dZ}\right)_n = 0$$

$$(-\beta_2+1)\ Vz_{1,n} - 2Vz_{2,n} + (\beta_2+1)\ Vz_{3,n} - \alpha_2 \left(\frac{dP}{dZ}\right)_n = 0$$

$$\vdots$$

$$(-\beta_m+1)\ Vz_{m-1,n} - 2Vz_{m,n} + (\beta_m+1)\ Vz_{m+1,n} - \alpha_m \left(\frac{dP}{dZ}\right)_n = 0 \qquad (7.67)$$

$$\vdots$$

$$(-\beta_M+1)\ Vz_{M-1,n} - 2Vz_{M,n} + \cancel{(\beta_M+1)\ Vz_{M+1,n}}^{\,0} - \alpha_M \left(\frac{dP}{dZ}\right)_n = 0$$

$$4Vz_{2,n}\ R_2 + 2Vz_{3,n}\ R_3 + \ldots + 4Vz_{M,n}\ R_M = 1.5\ M \frac{Q}{\pi R_D^2 V_b}$$

where $\alpha_m = \dfrac{k_m}{Cp_m\ \eta_{m,n}} \left(\dfrac{R_D}{H_o}\right)^2 (\Delta R)^2$

$$\beta_m = \frac{\Delta R}{2} \left[\frac{1}{R_m} + \frac{1}{\eta_{m,n}} \left(\frac{d\eta}{dR}\right)_{m,n}\right]$$

The above modified tridiagonal system of equations may be solved for the down channel velocity profile and pressure gradient at column n by Gaussian elimination (see Ref. (1) for details of the algorithm). The pressure at column n may be calcualted as follows:

$$P_n = P_{n-1} + \left(\frac{dP}{dZ}\right)_n \Delta Z \tag{7.68}$$

Energy Equation

The energy equation in finite difference form is similar to that for the breaker plate, except that a constant wall temperature boundary condition instead of the adiabatic condition is used. For column n in the finite difference grid, the energy equation may be written as:

$$\begin{aligned}
&\left(\frac{\alpha_1}{2} + 2\right) \theta_{1,n} - 2\theta_{2,n} = D_{1,n-1} \\
&(\beta_2-1)\ \theta_{1,n} + (\alpha_2+2)\ \theta_{2,n} - (\beta_2+1)\ \theta_{3,n} = D_{2,n-1} + \gamma_2 \\
&\qquad\vdots \\
&(\beta_m-1)\ \theta_{m-1,n} + (\alpha_m+2)\ \theta_{m,n} - (\beta_m+1)\ \theta_{m+1,n} = D_{m,n-1} + \gamma_m \\
&\qquad\vdots \\
&(\beta_M-1)\ \theta_{M-1,n} + (\alpha_M+2)\ \theta_{M,n} - (\beta_M+1)\ \overset{\theta_D}{\cancel{\theta_{M+1,n}}} = D_{M,n-1} + \gamma_M
\end{aligned} \tag{7.69}$$

where $D_{1,n-1} = \left(\frac{\alpha_1}{2} - 2\right) \theta_{1,n-1} + 2\theta_{2,n-1}$

$$D_{m,n-1} = (-\beta_m+1)\ \theta_{m-1,n-1} + (\alpha_m - 2)\ \theta_{m,n-1} + (\beta_m+1)\ \theta_{m+1,n-1}$$

$$\alpha_m = \frac{2(\Delta R)^2}{\Delta Z} \left(\frac{R_D}{H_o}\right)^2 Vz_{m,n}$$

$$\beta_m = \frac{\Delta R}{2R_m}$$

$$\gamma_m = 2(\Delta R)^2 \, \eta_{m,n} \frac{V_b^2}{k_m T_{melt}} \left(\frac{dVz}{dR}\right)^2_{m,n}$$

The above tridiagonal system of equations may be solved for the temperature profile at column n by Gaussian elimination using Thomas' method (see Refs. (1), (55) for details of the algorithm).

Bulk Temperature

The flow-average (bulk) temperature in a tube was defined in Eqs. 7.32 and 7.33. For column n in the finite difference grid, we can write the bulk temperature in finite difference form as:

$$\theta_{bulk,n} = \frac{Vz_1 \theta_1 R_1 + 4Vz_2 \theta_2 R_2 + 2Vz_3 \theta_3 R_3 + \ldots + 4Vz_M \theta_M R_M + Vz_{M+1} \theta_{M+1} R_{M+1}}{Vz_1 R_1 + 4Vz_2 R_2 + 2Vz_3 R_3 + \ldots + 4Vz_M R_M + Vz_{M+1} R_{M+1}} \quad (7.70)$$

7.4 Results of Simultations

Typical pressure profiles in the down channel direction in the die section (breaker plate/adapter/die) are shown in Fig. 7.9. The processing conditions for these results are given in App. G.7. It can be seen that although the pressure drops in the breaker plate and adapter are significant, the greatest drop in pressure occurs in the die channel. Bulk temperature profiles are not shown here because the increase in temperature in the die section is quite small (1 or 2°C).

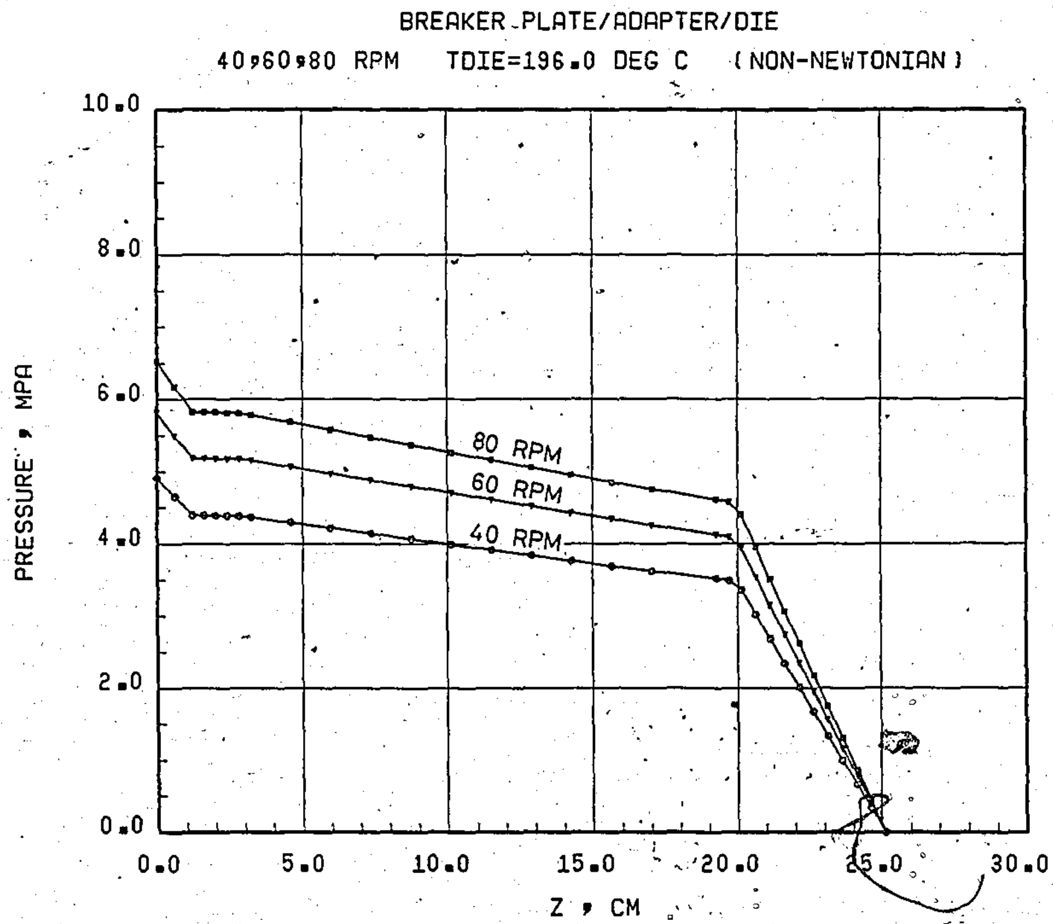

Fig. 7.9 Down channel pressure profiles in the die section (breaker plate/adapter/die) for non-Newtonian flow. Data for the polymer properties, channel dimensions and extruder operating conditions are given in App. G.7.

CHAPTER 8

EXTRUDATE SWELL

Polymer melts undergo an increase in cross-sectional area when they emerge from a die. As was stated in Sec. 2.5, this phenomenon is known as extrudate swell and is primarily due to the viscoelastic behaviour of the material. More specifically, the mechanisms responsible for the swelling of polymer extrudates from long dies are: a Newtonian swell, a sudden elastic recovery, an inelastic swell and finally stress relaxation. For short dies the swelling of the extrudate is also affected by the entrance memory effect.

Various models and theories have appeared in the literature along with experimental results obtained from capillary viscometers. These include finite element calculations, formulas based on the theory of rubber elasticity and Tanner's elastic and inelastic recovery theories. In a recent review by Vlachopoulos (121), many of these theories and models have been summarized including experimental results up to 1980. Despite the large number of investigations performed on the extrudate swelling of polymers, the existing models still do not provide a clear picture of the importance of various rheological parameters and their effects on the mechanism of extrudate swell. A fully predictive theory is still lacking.

Development of a Predictive Model for Extrudate Swell

In this chapter, a predictive model for extrudate swell is developed for cylindrical rod dies based on Tanner's elastic recovery theory (115), studies by White et al. (42,125,126) and Racin and Bogue (96), and measurements of extrudate swell performed on an Instron capillary rheometer. Such a model is then used to predict the swell ratio of polymer melts at the die exit of an extruder.

At the present time, the most widely accepted theory on extrudate swell is by Tanner (115), who made use of unconstrained elastic recovery calculations by Lodge (57) for a KBKZ fluid (50). Variations of Tanner's elastic theory have also been presented by White et al. (42, 125,126) and Pearson and Trottnow (91). A detailed derivation of Tanner's equation has been included in App. D. In its most general form it is written as follows for a cylindrical rod die:

$$\frac{d}{D} = \left[\frac{\int_o^R (N_1 + G - \tau^2/G)\ r\ dr}{\int_o^R G\ r\ dr}\right]^{1/6} \tag{8.1}$$

where d and D are the diameters of the extrudate and die respectively, $N_1 = \tau_{11} - \tau_{22}$ is the first normal stress difference, τ is the shear stress (also written as τ_{12}), G is an elastic modulus, and R is the radius of the die. To express Eq. 8.1 in its more usual form, assume that:

$$N_1 = \frac{2\ \tau_{12}^2}{G} \quad \text{with G constant} \tag{8.2}$$

$$\frac{\tau}{\tau_w} = \frac{r}{R} \tag{8.3}$$

Substituting the above into Eq. 8.1 and integrating, we obtain:

$$\frac{d}{D} = \left[1 + \frac{1}{2}\left(\frac{N_{1,w}}{2\tau_w}\right)^2\right]^{1/6} \tag{8.4}$$

where $N_{1,w}$ and τ_w are the first normal stress difference and shear stress respectively at the die wall.

Equation 8.4 can be used to predict swell ratios of polymer melts in dies provided that values of shear stress and first normal stress difference at the die wall can be obtained. For typical processing conditions, it is a routine procedure to obtain values of shear stress. Such is not the case, however, for normal stresses. The first normal stress difference can be measured with a cone and plate viscometer (for example, the Weissenberg Rheogoniometer), but only at very low shear rates (usually up to 5 or 10 s^{-1}). Since typical processing shear rates are of the order 100 - 1000 s^{-1}, it is usual practice to extrapolate the low shear rate cone and plate viscometer results to the conditions encountered in the extrusion die. However, large errors in the prediction of extrudate swell may result when using this method. A better technique is needed to handle normal stresses for the purposes of extrudate swell prediction.

Studies by Oda et al. (86) suggest that for commercial polystyrene melts the first normal stress difference is a unique function of shear rate, independent of temperature and molecular weight, and may be written as follows:

$$N_1 = A\tau^b \tag{8.5}$$

where A and b are empirical parameters. Racin and Bogue (96) used the above relation to obtain a modified form of Tanner's equation (8.1). Using $\tau/\tau_w = r/R$, Eq. (8.1) is rewritten in the form:

$$\frac{d}{D} = \left[\frac{\int_0^{\tau_w} [N(\tau) + G(\tau) - \frac{\tau^2}{G(\tau)}] \, \tau \, d\tau}{\int_0^{\tau_w} G(\tau) \, d\tau} \right]^{1/6} + 0.12 \tag{8.6}$$

where the term 0.12 is added to account for the effect of Newtonian swell. Assuming that:

$$G = \frac{2\tau^2}{N_1} \tag{8.7}$$

we may write the elastic modulus function with the introduction of Eq. 8.5 into Eq. 8.7 as:

$$G(\tau) = \frac{2}{A} \tau^{2-b} \tag{8.8}$$

In Eq. 8.7 or 8.8, G is not constant except in the special case where b = 2. Substituting Eqs. 8.5 and 8.8 into Eq. 8.6, we obtain:

$$\frac{d}{D} = [\frac{A^2}{4} \left(\frac{4-b}{2+b}\right) \tau_w^{2b-2} + 1]^{1/6} + 0.12 \tag{8.9}$$

Thus, a predictive equation for extrudate swell is obtained in terms of only the wall shear stress τ_w and the two empirical parameters A and b.

In this study, the parameters A and b were obtained by curve fitting Eq. 8.9 to extrudate swell data obtained on an Instron capillary rheometer. The swell measurements were performed at different extrusion temperatures and shear rates and the resulting data points were then plotted against shear stress as shown in Fig. 8.1. Regarding the temperature dependence of extrudate swell, it has been shown in the literature (40) that plots of extrudate swell versus shear rate depend on temperature, whereas plots of extrudate swell versus shear stress do not. The range of shear stress in Fig. 8.1 should encompass the operating range in extrusion dies. Finally, the parameters A and b in Eq. 8.9 were estimated by using non-linear regression analysis. Thus the correlation given by Eq. 8.9 is used to predict the extrudate swell in an extrusion die given the wall shear stress at the die exit and the parameters A and b obtained from measurements of extrudate swell on an Instron capillary rheometer.

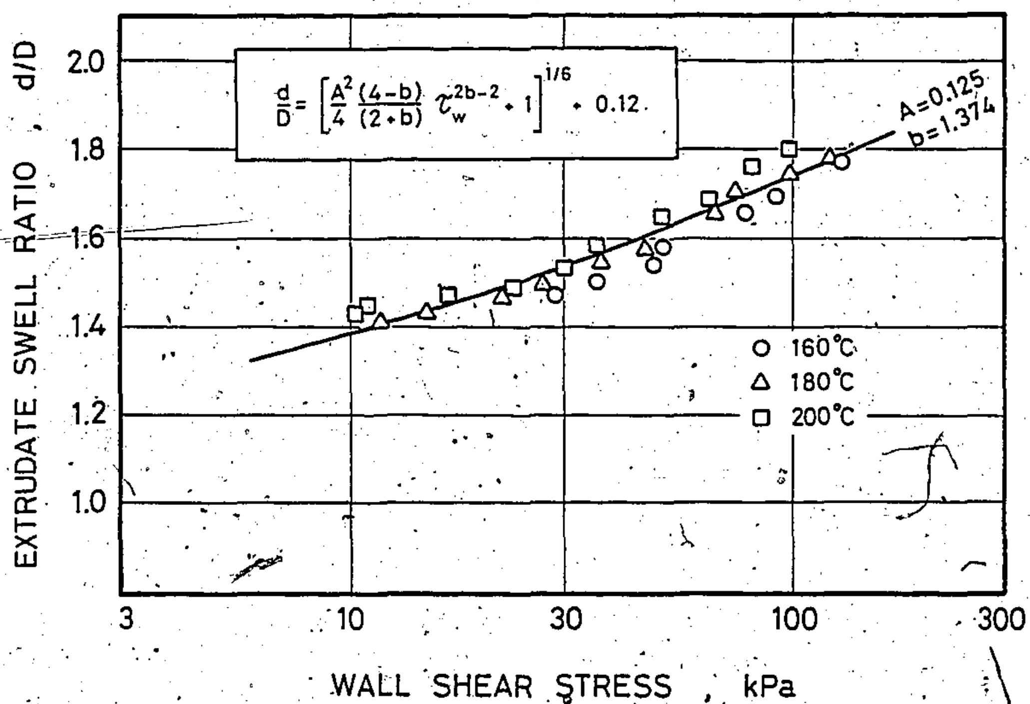

Fig. 8.1. Extrudate swell correlation for a low-density polyethylene resin. Data points represent Instron extrudate swells. Solid curve denote the extrudate swell equation (8.9) where the parameters A and b have been obtained by non-linear regression.

CHAPTER 9

THE OVERALL EXTRUDER MODEL

In Chaps. 3 through 8, individual submodels were developed and described for the various sections of the single screw extruder and die. In this chapter the final version of these submodels are presented together as an overall computer model of the extrusion process. To reiterate, the overall model consists of six interdependent sections as shown in Fig. 9.1. Each of these sections is described briefly below. The method used to predict the mass flow rate of the polymer in the extruder is also presented. The listings of the computer program are not included in this thesis, but are given in fully documented form in Ref. (2).

9.1 <u>Feed Hopper</u>

Solid polymer pellets are fed into the extruder screw channel through the feed hopper usually by gravity. The base pressure in the feed hopper may be determined by analyzing the pressure distribution in the solids as discussed in Chap. 3. Walker (123) has derived relationships for the pressure distribution in both vertical and convergent bins, assuming stress equilibrium in the solid particles. Equations 9.1 and 9.2 are used in combination to calculate the pressure at the base of a hopper with square cross-section as illustrated in Fig. 9.2.

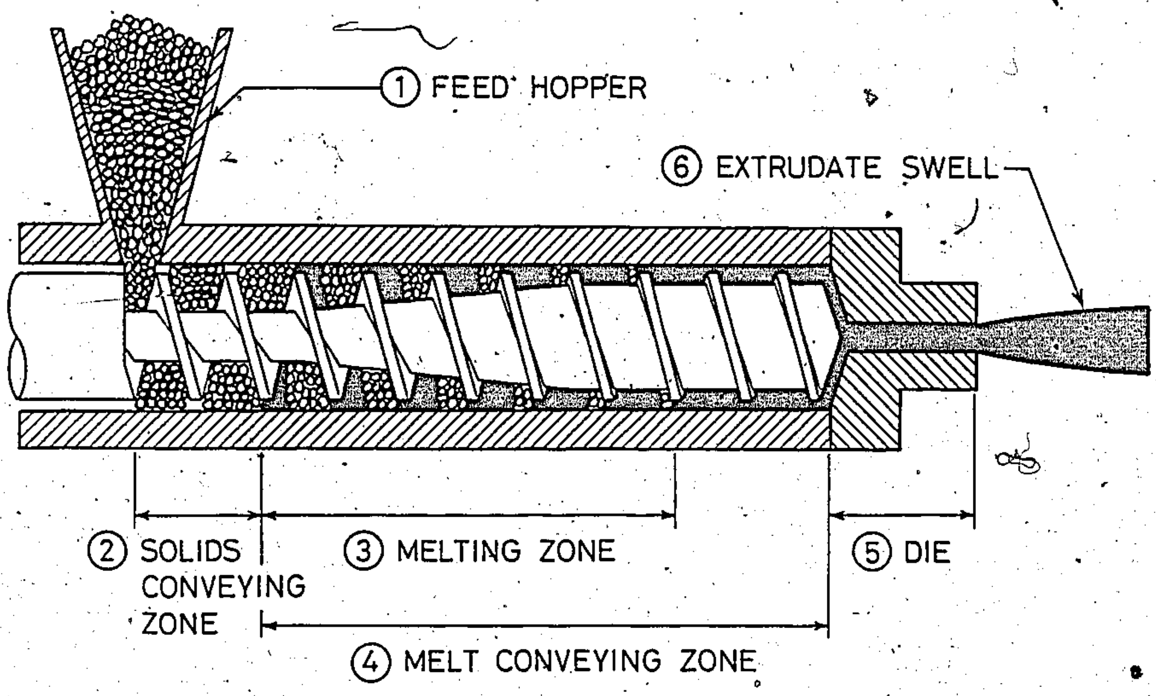

Fig. 9.1 Schematic diagram of a plasticating extruder showing the components of the present computer model.

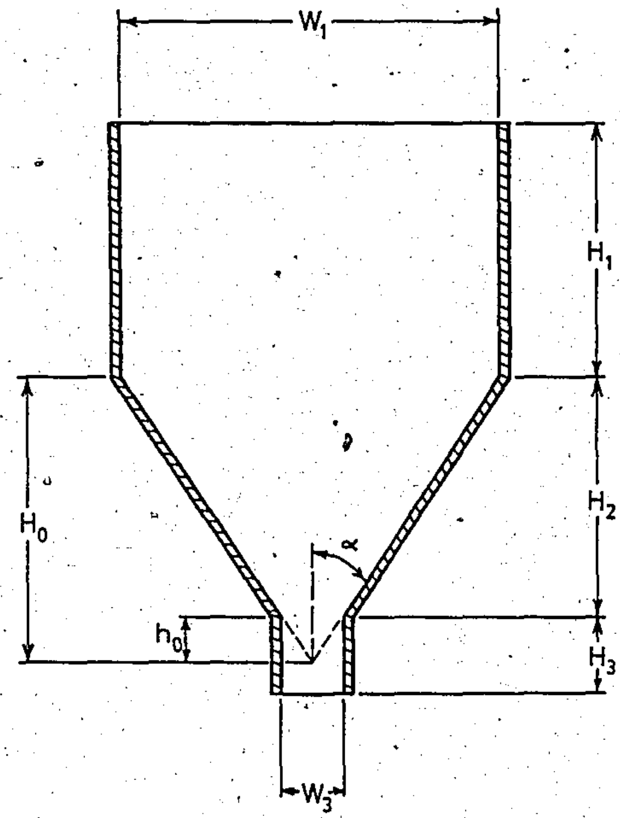

Fig. 9.2 Geometry of a feed hopper with square cross-section.

Vertical Sections:

$$p = p_o \exp(-\frac{4BD^*H}{W}) + \frac{\rho_{bulk}\, gW}{4BD^*g_c}[1 - \exp(-\frac{4BD^*H}{W})] \qquad (9.1)$$

where

$$B = \frac{\sin\delta \sin\kappa_o}{1 - \sin\delta \cos\kappa_o}$$

$$\kappa_o = \beta_w + \arcsin\left(\frac{\sin\beta_w}{\sin\delta}\right) \quad , \quad \arcsin > \frac{\pi}{2}$$

$$\beta_w = \arctan(f_w')$$

and where p and p_o are the pressures at the base and at height H in the vertical section, W the hopper width, ρ_{bulk} the bulk density of the solid polymer particles, g the gravitational acceleration, D* the distribution factor relating the average vertical stress with the vertical stress near the wall and assumed to be unity as a first approximation, δ the effective angle of friction of the solid particles, and f_w' the static coefficient of friction at the hopper wall.

Convergent Section:

$$p = (\frac{h_o}{H_o})^{\psi} p_o + \frac{\rho_{bulk}\, g\, h_o}{(\psi-1)g_c} + [1 - (\frac{h_o}{H_o})^{\psi-1}] \qquad (9.2)$$

where

$$\psi = \frac{2B'D^*}{\tan\alpha}$$

$$B' = \frac{\sin \delta \sin (2\alpha + \kappa_o)}{1 - \sin \delta \cos (2\alpha + \kappa_o)}$$

$$\kappa_o = \beta_w + \arcsin \left(\frac{\sin \beta_w}{\sin \delta}\right) \quad , \quad \arcsin < \frac{\pi}{2}$$

$$\beta_w = \arctan (f'_w)$$

and where p and p_o are the pressures at the base and top of the convergent section, h_o and H_o are the heights in the convergent section as shown in Fig. 4.2, and 2α is the hopper angle. For more details concerning the feed hopper equations, see Chap. 3.

9.2 Solids Conveying Zone

As discussed in Chap. 4, the solids flow mechanism in screw extruders channels is one of drag induced flow, that is, flow due to the frictional drag of the barrel and screw surfaces on the solid polymer granules. Darnell and Mol (20) were the first to obtain solutions for the solids conveying zone ~~in screw~~ extruders. More recently, there have been various refinements applied to their one-dimensional plug flow model by Schneider (100), Tadmor and Broyer (10,110), and Lovegrove and Williams (58,59,60).

In the flow model described here, we assume that the solid bed is isothermal and travels as a solid plug with constant velocity. The stress distribution is assumed to be isotropic, that is, the pressure varies only in the downstream direction. In Sec. 4.2 it was shown that the down channel pressure profile could be obtained by applying a force and torque balance on a differential element of the solid bed in the down channel direction. The pressure at the end of the solids conveying zone may be expressed in the form:

$$p = p_o \, e^{-\lambda z_{b,t}} \tag{9.3}$$

where

$$\lambda = \frac{A_1 K - B_1}{A_2 K + B_2}$$

$$A_1 = f_b W_b \sin \phi + 2H f_s \sin \theta_b + W_s f_s \sin \theta_b$$

$$A_2 = H\overline{W} \sin \overline{\theta}$$

$$B_1 = f_b W_b \cos\phi - 2H f_s \frac{\overline{D}}{D_b} \sin \theta_b \cot \overline{\theta}$$

$$- W_s f_s \frac{D_s}{D_b} \sin \theta_b \cot \theta_s$$

$$B_2 = H\overline{W} \frac{\overline{D}}{D_b} \cos \overline{\theta}$$

$$K = \frac{\overline{D}}{D_b} \frac{\sin \overline{\theta} + f_s \cos \overline{\theta}}{\cos \overline{\theta} - f_s \sin \overline{\theta}}$$

and where p_o is the base pressure in the feed hopper, $z_{t,b}$ is the length of the solids conveying zone in the down channel direction, f_b and f_s

are the dynamic coefficients of friction between the solid polymer particles and the barrel and screw surfaces, H is the screw channel depth, W_b and W_s are the channel widths at the barrel surface and screw root, θ_b and θ_s are the helix angles at the barrel surface and screw root, D_b is the inside barrel diameter, D_s is the diameter of the root of the screw, and W, D and θ are respectively the average channel width, diameter and helix angle measured at the midpoint between the barrel and screw root surfaces. The angle ϕ formed between the tangential velocity of the barrel surface and the down channel velocity of the solid particles is given by:

$$\tan \phi = \frac{\tan \theta_b}{\frac{\pi^2 N}{G} \rho_{bulk} H D_b (D_b - H) \tan \theta_b \left(\frac{W}{W - e}\right) - 1} \qquad (9.4)$$

where N is the frequency of screw rotation, G the mass flow rate of the polymer solids, and e the screw flight width.

The length of the solids conveying zone $z_{t,b}$ is the sum of the distance between the base of the feed hopper and the start of the barrel heaters, and the delay in melting distance. As described in Sec. 4.3 the delay in melting is the down channel distance between the start of barrel heating and the appearance of a melt pool in the screw channel, and may be determined by using the following empirical correlation based on experimental data (114g):

$$N_{delay} = \frac{0.008}{\psi} \qquad (9.5)$$

where N_{delay} is the number of screw turns in the delay zone, and ψ is a dimensionless group related to the rate of melting at the beginning of the melting zone and given by:

$$\psi = \frac{V_{bx}\ \rho_m\ \delta\ H_o}{2G} \tag{9.6}$$

where V_{bx} is the cross channel velocity component of the barrel, ρ_m the polymer melt density, δ the thickness of the melt film (see Sec. 9.3), and H_o the screw channel depth at the beginning of the melting zone.

9.3. Melting Zone

As explained in Chap. 5, the melting mechanism in screw extruders was first formulated by Tadmor (107) on the basis of visual observations. More sophisticated models have since been reported by Edmondson and Fenner (27) and Shapiro et al. (37,103). In the melting zone the solid and melt phases coexist in the screw channel as shown in Fig. 9.3. The two phases are clearly segregated from each other, with the melt phase accumulating in a melt pool at the rear flight and the solids segregated as a solid bed at the front flight. In addition there exists a thin film of melt between the barrel surface and the solid bed. Due to the proximity of the heated barrel and the intense shear, much of the melting occurs in this melt film. The motion of the barrel relative to the solid bed drags the melt in this film into the melt pool. The width of the melt pool gradually increases in the down channel direction.

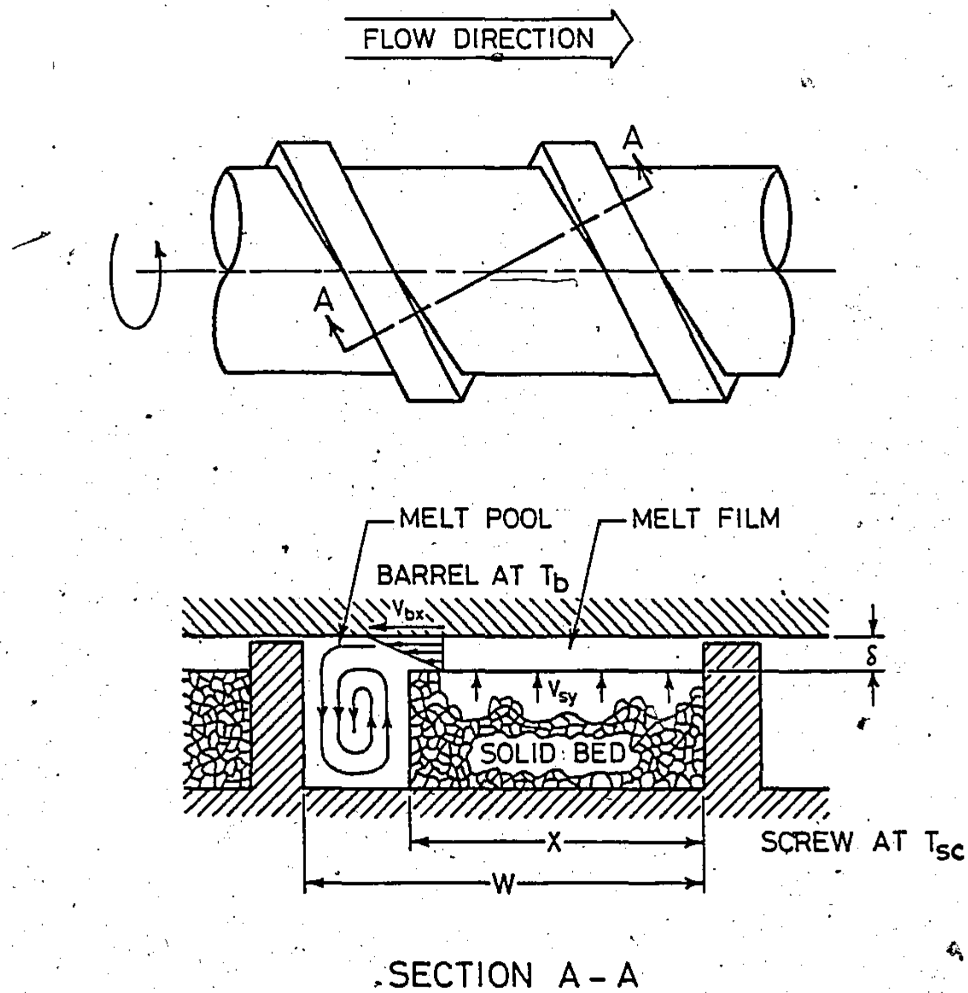

Fig. 9.3 Idealized cross-section in the melting zone (Tadmor's melting model). V_{bx} is the x component of the tangential barrel velocity V_b.

Tadmor's melting model has been used as a basis for the present melting model as stated earlier in Sec. 5.2. Calculations for the melting zone commence at the end of the solids conveying zone, that is, where the melt pool first occurs in the screw channel. It is assumed that the downstream bed velocity is constant and that the thickness of the upper melt film is independent of cross channel position. A temperature and shear rate dependent viscosity relation is used to calculate the temperature profile in the melt film. Mass and energy balances on the melt film and solid bed are carried out to obtain the following equations for the rate of melting and the solid bed profile:

Rate of melting:

$$\omega = \Psi \left(\frac{dT}{dy}\right)_{y=0} X \qquad (9.7a)$$

$$= \frac{V_{bx}}{2} \rho_m \delta \qquad (9.7b)$$

where

$$\Psi = \frac{k_m}{Cp_s (T_{melt} - T_s) + \lambda + Cp_m (T_{bulk} - T_{melt})}$$

$\left(\frac{dT}{dy}\right)_{y=0}$ = temperature gradient in the melt film at the solid-melt interface (and a function of the melt film thickness δ)

and where X is the width of the solid bed, V_{bx} the cross channel component of the barrel velocity, T_{bulk} the flow-average (bulk) temperature of the melt film, T_{melt} the melting temperature of the polymer, T_s the temperature of the solid bed far away from the interface, ρ_m the melt density, Cp_m and Cp_s the heat capacities of the polymer melt and solid, k_m the thermal conductivity of the melt, and λ the heat of fusion of the polymer.

Solid bed profile:

$$\frac{d(H^*X)}{dz} = \frac{-\omega}{\rho_s V_{sz}} = \frac{-\Psi}{\rho_s V_{sz}} \left(\frac{dT}{dy}\right)_{y=0} X \tag{9.8}$$

where $H^* = H-\delta$, ρ_s is the solid polymer density and V_{sz} is the down channel velocity of the solid bed. Equations 9.7a,b and 9.8 are solved simultaneously using a fourth-order Runge-Kutta method to obtain the solid bed profile X/W as a function of the down channel direction in the screw channel. For more details concerning Tadmor's melting model and the present modified version, see Secs. 4.2.1 and 4.2.2.

9.4. Melt Conveying Zone

Two distinct melt conveying regions may be found in plasticating extruders as described in Chap. 6. One is downstream of the melting zone after completion of melting and occupies the entire width of the screw channel. The other occurs in the melt pool extending side by side with the solid bed in the melting zone. Here the width of the melt pool changes in the down channel direction. The mass flow rate of the melt also changes as a result of the influx from the melt film.

Due to the helical geometry of the extruder screw and the relative motions of the barrel and screw, the flow pattern of the polymer melt in the screw channel is quite complex and may be described as a "helix within a helix". In order to solve this complex flow problem, several simplifying assumptions are made as outlined in Secs. 2.1 and 2.4. It is convenient to pick a coordinate system relative to the screw. Also, one may treat the barrel as rotating about a stationary screw, a valid procedure because gravity and centrifugal inertia forces are negligible in comparison with viscous and pressure forces in the screw channel. Another standard assumption is to consider the helical screw channel as "unwound" and rectilinear as shown in Fig. 9.4. This is a valid assumption because in most single screw extruders the screw channel is relatively shallow in the melt flow regions. In the analysis of melt flow it is also standard procedure to introduce the lubrication approximation (89a). This involves the local replacement of the actual flow in the parallel or nearly parallel gap between smooth surfaces by uniform flow between plane parallel surfaces.

As stated in Sec. 6.1, by far the majority of studies on extrusion theory in the literature have dealt with the analysis of melt flow. Griffith (36), Zamodits and Pearson (130) and Fenner (28b) obtained numerical solutions for fully developed, two-dimensional, nonisothermal and non-Newtonian flow of melts in infinitely wide rectangular screw channels. For a similar type of flow, Martin (68) presented a solution which allows for the finite width of the channel. Yates (128) and Fenner (29) have developed two-dimensional, nonisothermal and non-Newtonian solutions for infinitely wide rectangular screw channels

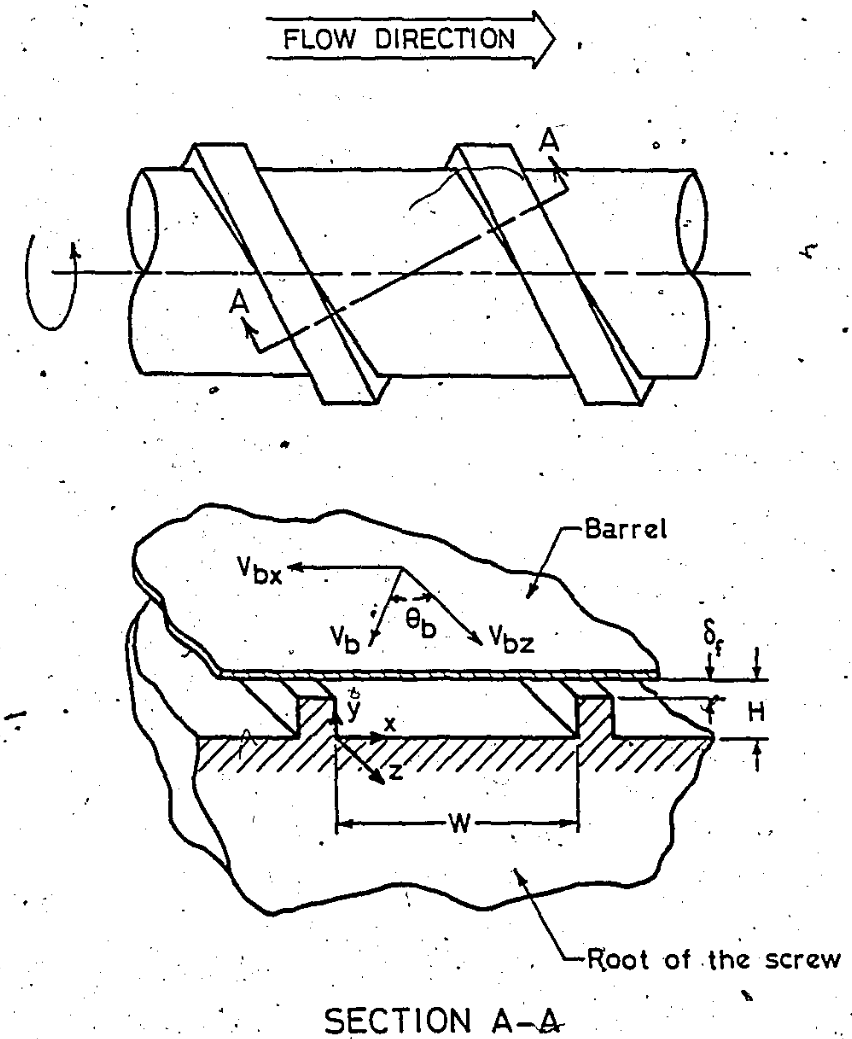

Fig. 9.4 Schematic diagram of a rectangular flow channel in the screw extruder. V_b is the tangential barrel velocity, and V_{bx} and V_{bz} are the x and z barrel velocity components.

in which the temperature profiles are developing along the channel.

In the present melt conveying model, the following equations of conservation of mass, momentum and energy in simplified form together with the accompanying boundary conditions are solved simultaneously (see also Sec. 6.2.6):

Mass (integrated form): $$\int_0^H v_x \, dy = 0 \tag{9.9}$$

$$\int_0^H v_z \, dy = \frac{Q}{W} \tag{9.10}$$

Momentum: $$-\frac{\partial p}{\partial x} + \frac{\partial \tau_{yx}}{\partial y} = 0 \tag{9.11}$$

$$-\frac{\partial p}{\partial z} + \frac{\partial \tau_{yz}}{\partial y} = 0 \tag{9.12}$$

Energy: $$\rho_m \, Cp_m \, v_z \frac{\partial T}{\partial z} = k_m \frac{\partial^2 T}{\partial y^2} + \tau_{yx} \frac{\partial v_x}{\partial y} + \tau_{yz} \frac{\partial v_z}{\partial y} \tag{9.13}$$

Boundary conditions:
$$\begin{array}{llll} z = 0 & p = p_o & & T = T_o \\ y = 0 & v_x = v_z = 0 & & T = T_b \\ y = H & v_x = V_{bx} & v_z = V_{bz} & T = T_b \end{array} \tag{9.14}$$

where Q/W is the flow rate of the melt per unit width of the flow channel, p_o and T_o are the pressure and temperature respectively at the beginning of the melt flow region, T_b is the barrel temperature which may also be specified as a function of the down channel direction, and V_{bx} and V_{bz} are the cross and down channel components of the barrel velocity. The following temperature and shear rate dependent constitutive relation is used:

$$\tau_{yx} = \eta \frac{\partial v_x}{\partial y} \quad (9.15)$$

$$\tau_{yz} = \eta \frac{\partial v_z}{\partial y} \quad (9.16)$$

$$\log \eta = a_o + a_1 \log \dot{\gamma} + a_2 (\log \dot{\gamma})^2 + a_3 T + a_4 T^2 + a_5 T \log \dot{\gamma} \quad (9.17)$$

where $$\dot{\gamma} = \sqrt{\left(\frac{\partial v_x}{\partial y}\right)^2 + \left(\frac{\partial v_z}{\partial y}\right)^2}$$

The parameters a_o to a_5 in Eq. 9.17 are obtained by curve-fitting Instron capillary rheometer data using linear regression analysis as shown in Fig. 9.5. It should be noted that by retaining the convective term in the energy equation, developing temperature profiles are calculated along the screw channel.

The conservation equations (9.9 to 9.13) shown above along with the accompanying boundary conditions (9.14) are solved by an implicit finite difference technique to obtain cross and down channel velocity profiles, temperature profiles and the down channel pressure and bulk temperature profiles in the screw channel. The finite difference equations for melt flow in the feed compression and metering sections have been developed in Sec. 6.2.6 and are also summarized in App. C. In addition to viscosity, the polymer properties required for the model are thermal conductivity, density and heat capacity of the melt. The bulk (flow-average) temperature at a given position in the screw channel is given by:

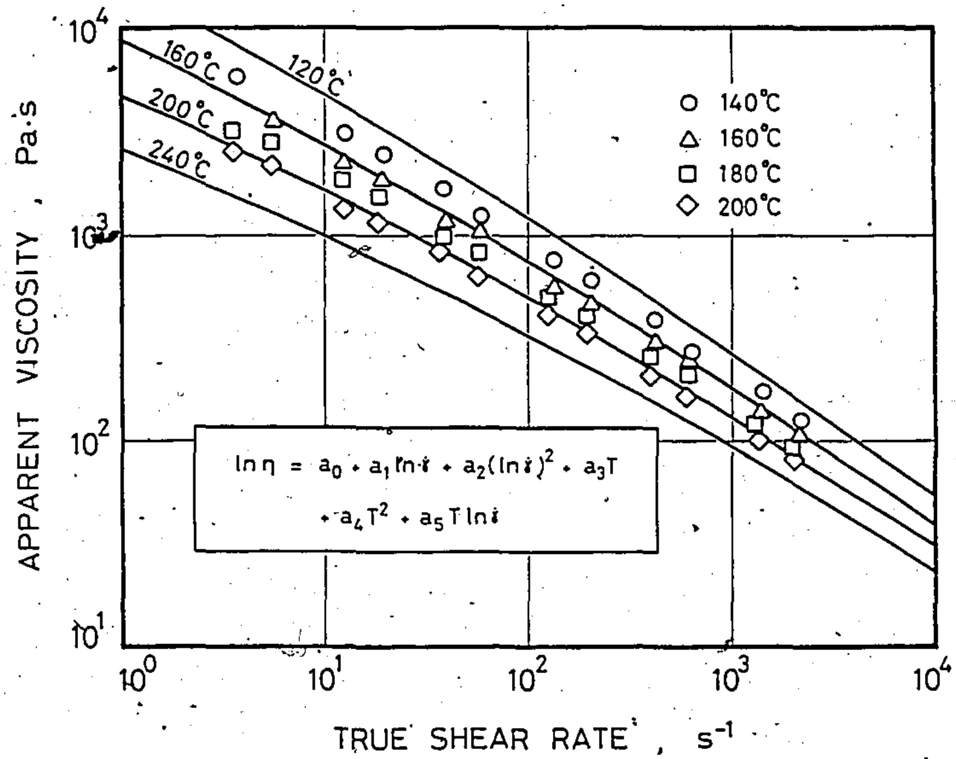

Fig. 9.5 Viscosity curves for a low-density polyethylene resin. Data points represent viscosities measured with an Instron capillary rheometer. Solid curves denote the general viscosity equation (see inset) - parameters a_0 to a_5 are obtained by linear regression.

$$T_{bulk} = \frac{\int_0^H v_z(y,z)\, T(y,z)\, dy}{\int_0^H v_z(y,z)\, dy} \tag{9.18}$$

where $v_z(y,z)$ and $T(y,z)$ are the local down channel velocity and temperature profiles.

9.5 Breaker Plate, Adapter and Die

The adapter and die used in the present extruder model are illustrated in Fig. 9.6. The adapter contains a 3/4" x 3/8" (19.1 mm x 9.5 mm) rectangular slit channel whereas the die has a 3/16" (4.76 mm) diameter channel of circular cross-section. As described in Chap. 7 the melt flow analyses for the breaker plate, adapter and die are essentially the same as for the melt conveying section of the extruder, with the exception that only the down channnel components of velocity are considered and that there are no moving boundaries. The following conservation equations in simplified form for the breaker plate, adapter and die are solved simultaneously:

Breaker Plate

Mass (integrated form): $$\int_0^{R_{Br}} v_z\, r\, dr = \frac{Q}{2\pi\, N_{Br}} \tag{9.19}$$

Momentum: $$-\frac{\partial p}{\partial z} + \frac{1}{r}\frac{\partial}{\partial r}(r\tau_{rz}) = 0 \tag{9.20}$$

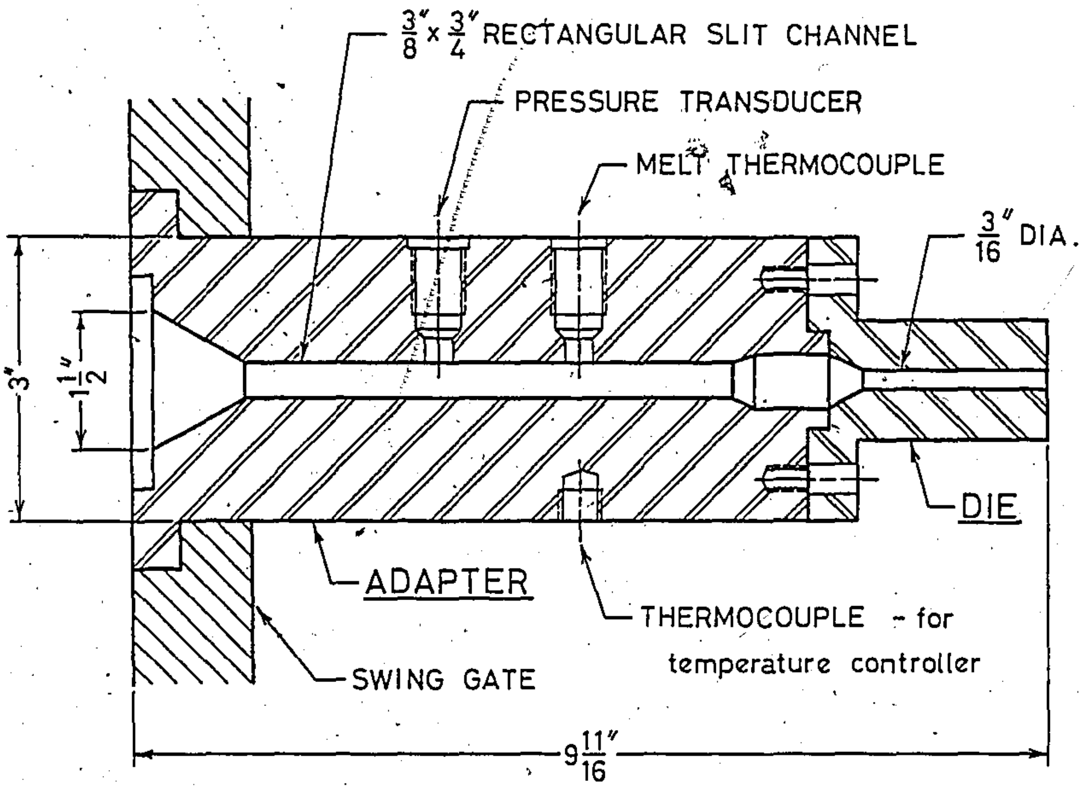

Fig. 9.6 Schematic diagram of adapter and die.

Energy: $$\rho_m Cp_m v_z \frac{\partial T}{\partial z} = \frac{k_m}{r} \frac{\partial}{\partial r}(r \frac{\partial T}{\partial r}) + \tau_{rz} \frac{\partial v_z}{\partial r} \quad (9.21)$$

Boundary conditions:
$$z = 0 \qquad p = p_o \qquad T = T_o$$
$$r = 0 \qquad \frac{\partial v_z}{\partial r} = 0 \qquad \frac{\partial T}{\partial r} = 0 \quad (9.22)$$
$$r = R_{Br} \qquad v_z = 0 \qquad \frac{\partial T}{\partial r} = 0$$

where N_{Br} is the number of flow channels in the breaker plate, R_{Br} is the radius of each channel, and p_o and T_o are the pressure and bulk temperature of the polymer melt at the end of the extruder screw channel.

Adapter

Mass (integrated form): $$\int_0^{H_A/2} v_z \, dy = \frac{Q}{2W_A} \quad (9.23)$$

Momentum: $$-\frac{\partial p}{\partial z} + \frac{\partial \tau_{yz}}{\partial y} = 0 \quad (9.24)$$

Energy: $$\rho_m Cp_m v_z \frac{\partial T}{\partial z} = k_m \frac{\partial^2 T}{\partial y^2} + \tau_{yz} \frac{\partial v_z}{\partial y} \quad (9.25)$$

Boundary conditions:
$$z = 0 \qquad p = p_o \qquad T = T_o$$
$$y = 0 \qquad \frac{\partial v_z}{\partial y} = 0 \qquad \frac{\partial T}{\partial y} = 0 \quad (9.26)$$
$$y = \frac{H_A}{2} \qquad v_z = 0 \qquad T = T_A$$

where H_A and W_A are respectively the height and width of the rectangular flow channel, p_o and T_o are the pressure and bulk temperature of the melt at the end of the breaker plate, and T_A is the temperature of the adapter.

Die

Mass (integrated form): $$\int_0^{R_D} v_z \, r \, dr = \frac{Q}{2\pi} \quad (9.27)$$

Momentum: $$-\frac{\partial p}{\partial z} + \frac{1}{r}\frac{\partial}{\partial r}(r\,\tau_{rz}) = 0 \quad (9.28)$$

Energy: $$\rho_m \, Cp_m \, v_z \frac{\partial T}{\partial z} = \frac{k_m}{r}\frac{\partial}{\partial r}\left(r\frac{\partial T}{\partial r}\right) + \tau_{rz}\frac{\partial v_z}{\partial r} \quad (9.29)$$

Boundary conditions: $$r = 0 \qquad \frac{\partial v_z}{\partial r} = 0 \qquad \frac{\partial T}{\partial r} = 0 \quad (9.30)$$

$$r = R_D \qquad v_z = 0 \qquad T = T_D.$$

where R_D is the radius of the circular flow channel in the die, and T_D is the die temperature.

An implicit finite difference method is used to solve the conservation equations shown above along with the accompanying boundary conditions to obtain velocity, temperature, and pressure profiles in the die section (breaker plate/adapter/die). The finite difference equations for melt flow in the breaker plate, adapter and die are given in the Secs. 7.1, 7.2 and 7.3 respectively. As in the extruder screw channel, the polymer properties required for the calculations are viscosity, thermal conductivity, density and heat capacity of the melt.

9.6 Extrudate Swell

Polymer melts, due to their viscoelastic behavior, exhibit an increase in cross-sectional area whenever they emerge from a die provided there is no subsequent drawing. As stated in Sec. 2.5 this phenomenon is usually called extrudate swell. Depending on the extrusion conditions, the die geometry and dimensions, and the rheological properties of the polymer, the extrudate swell ratio (ratio of extrudate diameter to die diameter in the case of a circular die) may range from 1.5 to 4.

There seems to be general agreement that extrudate swell from long dies is mainly due to a sudden elastic stress release and subsequent relaxation (see also Sec. 2.5). However, no single theory of extrudate swell seems to be generally accepted. A review paper by Vlachopoulos (121) has recently been published on extrudate swell of polymers. It is concluded that despite the large number of investigations on extrudate swell, the existing models do not provide a clear picture as to the importance of the various rheological parameters. There is still disagreement regarding the molecular structure effects for many polymers. The interrelations between molecular, rheological and geometrical parameters and their effect on extrudate swell are not well understood. A fully predictive theory has yet to be developed.

In the present extruder model, the prediction of extrudate swell for the circular die is based on Tanner's elastic recovery theory (115), studies by White et al. (42,125,126) and Racin and Bogue (96), and measurements of extrudate swell performed on an Instron capillary rheometer as described in Chap. 8. For an extrudate emerging from an extruder die with circular cross-section, the prediction of extrudate swell is given by:

$$\frac{d}{D} = \left[\frac{A^2}{4}\frac{(4-b)}{(2+b)}\tau_w^{2b-2} + 1\right]^{1/6} + 0.12 \qquad (9.31)$$

where d and D are the extrudate and die diameters respectively, τ_w is the shear stress at the die wall, and A and b are parameters obtained by curve-fitting Eq. 9.31 to Instron extrudate swell data using non-linear regression. The extrudate swell correlation (Eq. 9.31) along with Instron extrudate swell data are shown in Fig. 9.7 for a typical low-density polyethylene resin.

9.7 Prediction of Mass Flow Rate

In the solids conveying, melting and melt flow submodels described in Chaps. 4 to 7 and summarized in this chapter, it is necessary to specify a mass flow rate of the polymer in the extruder. However, one of the objectives of the overall extruder model is to predict the mass flow rate of the polymer. This can be done only when all of the submodels have been linked together to form an overall extruder model.

The basis for predicting the mass flow rate is that the melt pressure at the die exit should equal zero. When an arbitrary value of mass flow rate G is selected, the predicted die exit pressure P_{exit} will in most cases be either greater or less than zero. Thus the procedure for determining G is an iterative one, and may be described as follows:

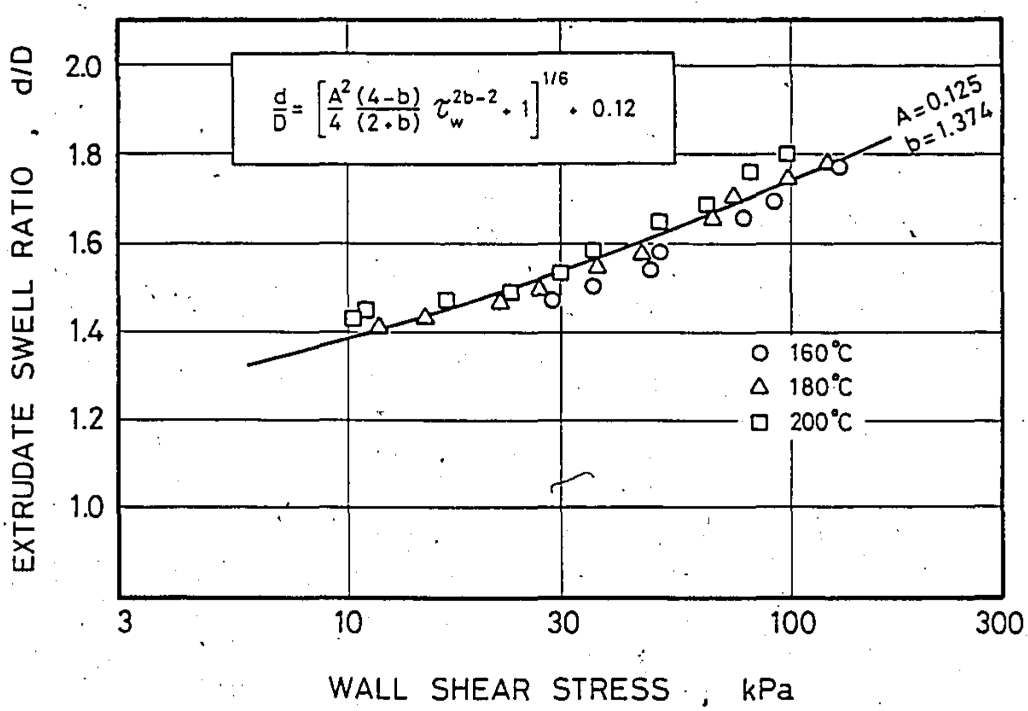

Fig. 9.7 Extrudate swell correlation for a low-density polyethylene resin. Data points represent Instron extrudate swells. Solid curve denotes the extrudate swell equation (see inset) - parameters A and b are obtained by non-linear regression.

(1) Pick an arbitrary value of $G^{(1)}$, and using the overall extruder model obtain a value of $P_{exit}^{(1)}$. (As stated above, $P_{exit}^{(1)}$ will probably be greater or less than zero)

(2) If $P_{exit}^{(1)} > 0$, choose a new $G^{(2)}$ such that $G^{(2)} > G^{(1)}$, or vice versa if $P_{exit}^{(1)} < 0$. Using the overall model obtain a new value of $P_{exit}^{(2)}$. (Again $P_{exit}^{(2)}$ will probably be nonzero.)

(3) Using $G^{(1)}$, $G^{(2)}$ and $P_{exit}^{(1)}$, $P_{exit}^{(2)}$ obtain a new $G^{(3)}$ by linear interpolation (or extrapolation) such that $P_{exit} = 0$. The choice of $G^{(3)}$ in the overall model should give a value of $P_{exit}^{(3)}$ close to zero. (A fourth iteration may be required if $P_{exit}^{(3)}$ is still significantly nonzero.)

The above-described procedure for predicting the mass flow rate of the polymer may be regarded as a "shooting" technique. Different values of mass flow rate are chosen until the predicted die exit pressure equals zero. To illustrate this method, pressure profiles in the extruder channel and die section are shown in Fig. 9.8 for various values of mass flow rate G. Depending on the choice of G, it can be seen that the die exit pressure is either positive, negative or zero.

9.8 Concluding Remarks

The present computer model as described in this chapter is fully predictive. Given the material and rheological properties of the

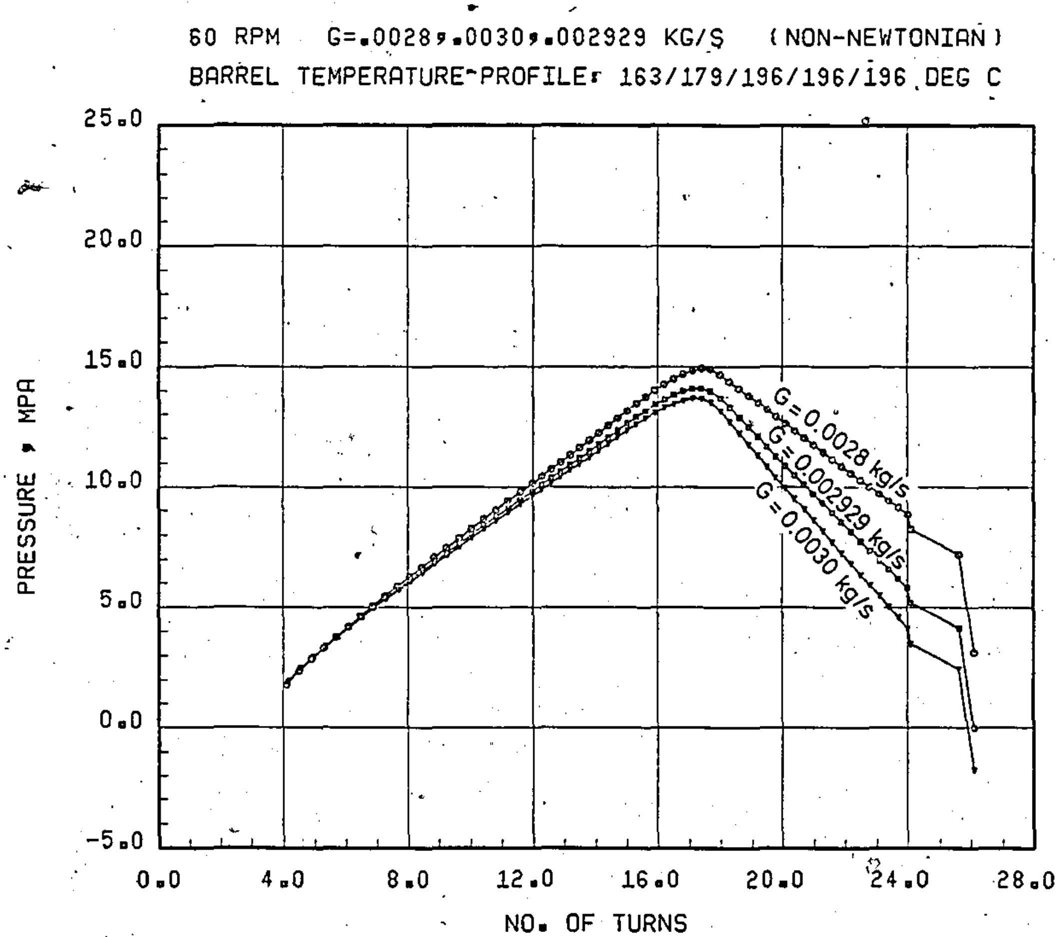

Fig. 9.8 The effect of mass flow rate G on the pressure profiles in the extruder screw channel and die section. Data for the polymer properties and processing conditions are given in Chap. 11, Table 11.2.

polymer, the screw geometry and dimensions, and the extruder operating conditions (screw speed and barrel temperature profile), the model is used to predict:

(i) mass flow rate of the polymer,

(ii) developing pressure and temperature profiles along the extruder screw channel and in the die section, and

(iii) extrudate swell at the die exit.

No adjustments are made to these predictions on the basis of measurements performed during experimental runs on an extruder.

CHAPTER 10

EXPERIMENTAL PROCEDURE

The experiments and measurements carried out in this study can be divided into two parts: (i) experimental runs on an extruder using high-and low-density polyethylene resins to verify the computer model, and (ii) viscosity and extrudate swell measurements on an Instron capillary rheometer for these materials as required in the computer model. In this chapter, the equipment and experimental procedure are described for both the extruder and the rheometer.

10.1 Extruder Experiments

10.1.1 Description of Extruder

A 1 1/2 inch (38 mm) diameter single screw Killion[1] extruder with a 24:1 length to diameter ratio was used for the experimental runs in this study. This machine is representative of the smaller scale extruders used in industry, much more so than the 1 inch (25 mm) or smaller extruders usually found in laboratories. A photograph of the extruder is shown in Fig. 10.1.

The extruder is equipped with a conventional, three section, polyethylene metering screw with square-pitched flights. The geometry and dimensions of the screw are shown in Fig. 10.2. The screw is driven

[1]Killion Extruders, Inc., Verona, N.J., U.S.A.

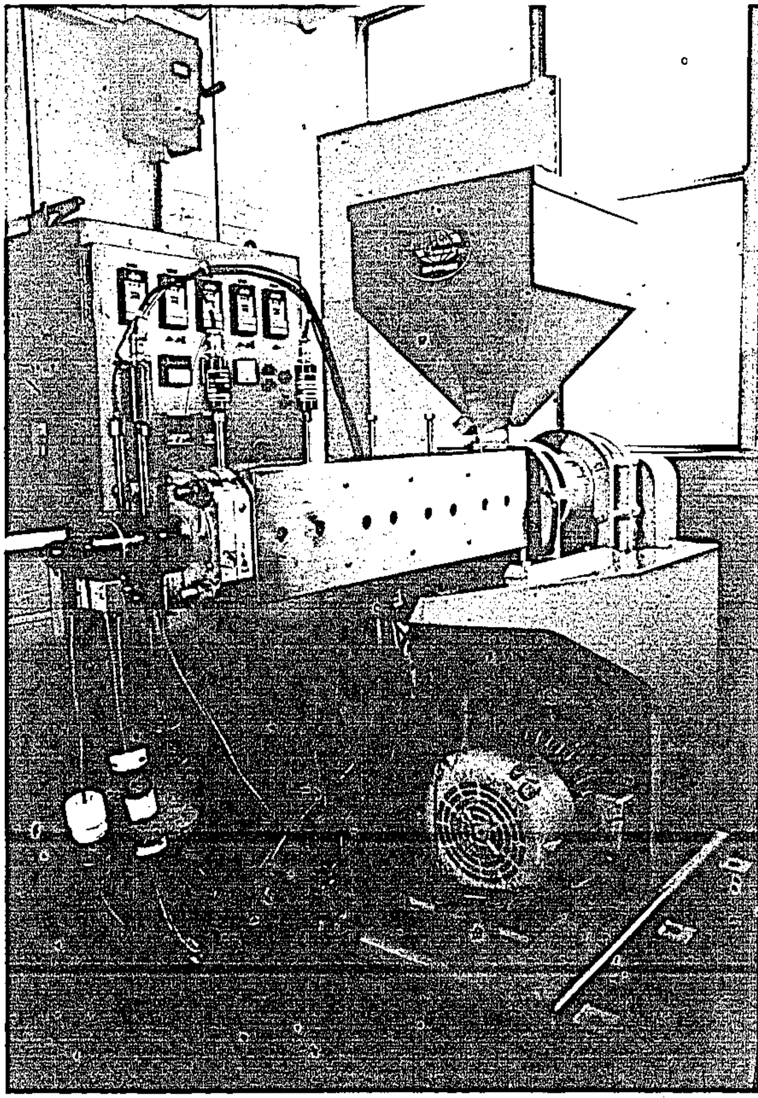

Fig. 10.1 Photograph of the 1 1/2 inch diameter single screw extruder in the Department of Chemical Engineering, McMaster University.

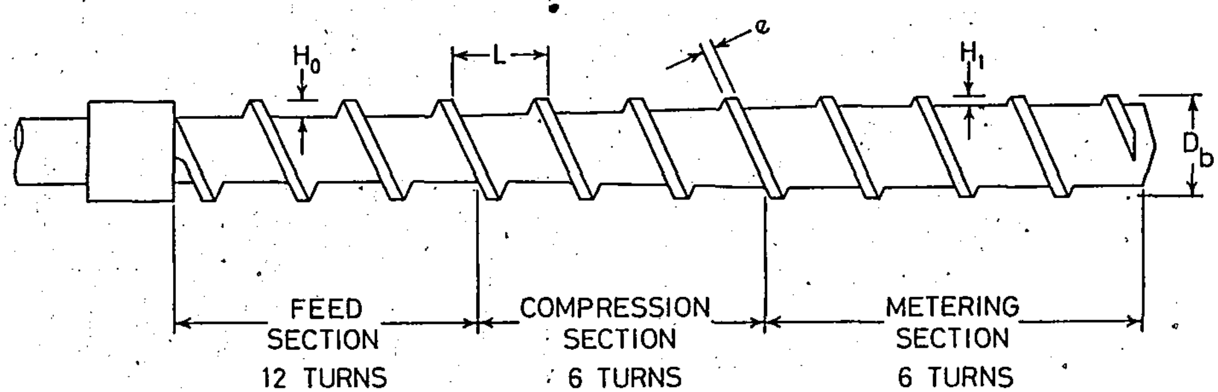

D_b = 1.500 in (38.10 mm)
L = 1.500 in (38.10 mm)
H_o = 0.024 in (0.61 mm)
H_1 = 0.008 in (0.20 mm)
é = 0.25 in (6.35 mm)

Fig. 10.2 Geometry and dimensions of metering screw.

10–282

with a 10 hp. d.c. motor. The extruder barrel is heated in four zones with electrical heater bands. In each zone, the barrel temperature is controlled with a Barber-Colman PI controller. Also, fans are used to provide air cooling to each of the four zones. The inside of the extruder barrel is lined with Xaloy. Finally, the polymer is fed to the extruder screw channel through a feed hopper. The geometry and dimensions of the feed hopper are given in Fig. 10.3

10.1.2 Adapter and Die

A photograph and a schematic diagram of the adapter and cylindrical rod die used in this study are shown in Figs. 10.4 and 10.5 respectively. The die has a 3/16 inch (4.76 mm) diameter channel of circular cross-section and with a 10:1 length to diameter ratio. Connecting the die to the extruder barrel is an adapter with a 3/4 inch x 3/8 inch (19.1 mm x 9.5 mm) rectangular slit channel. A rectangular instead of the more conventional circular flow channel was utilized in the adapter so that the diaphragm of the pressure transducer could be seated flush with one of the channel walls (and thus avoiding pressure-hole errors (39) in the pressure measurements). The adapter and die are heated with electrical heater bands. As in the case of the extruder barrel, the temperature is controlled with a Barber-Colman PI controller. No air cooling, however, is provided to the adapter and die by means of a fan.

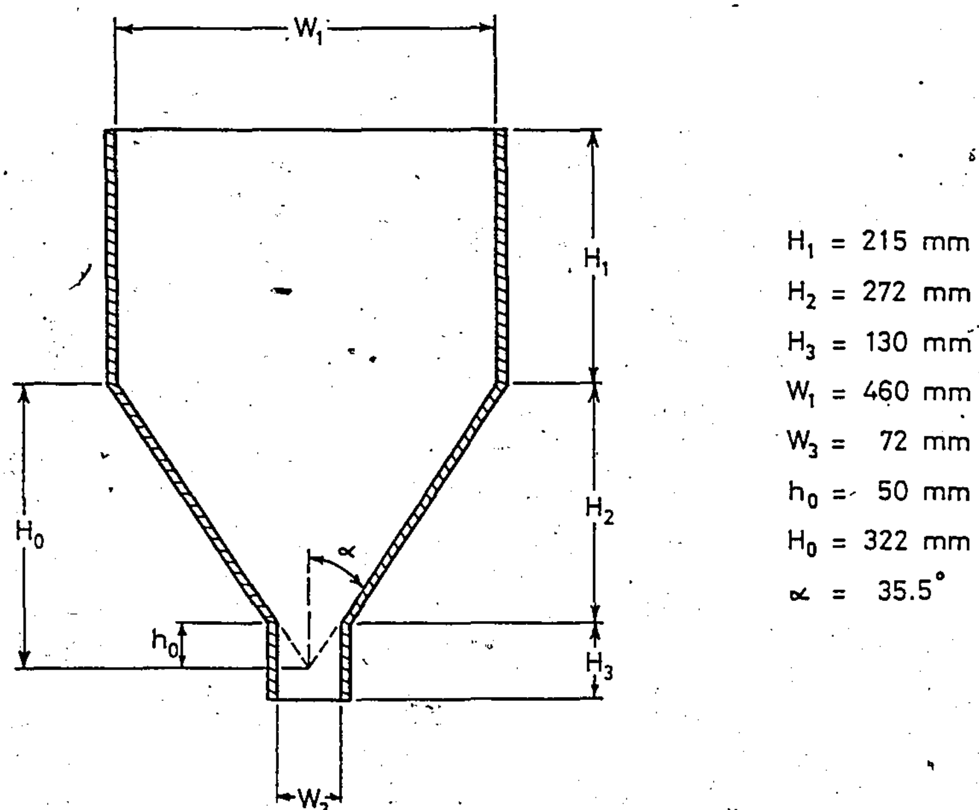

Fig. 10.3 Geometry and dimensions of the feed hopper with square cross-section.

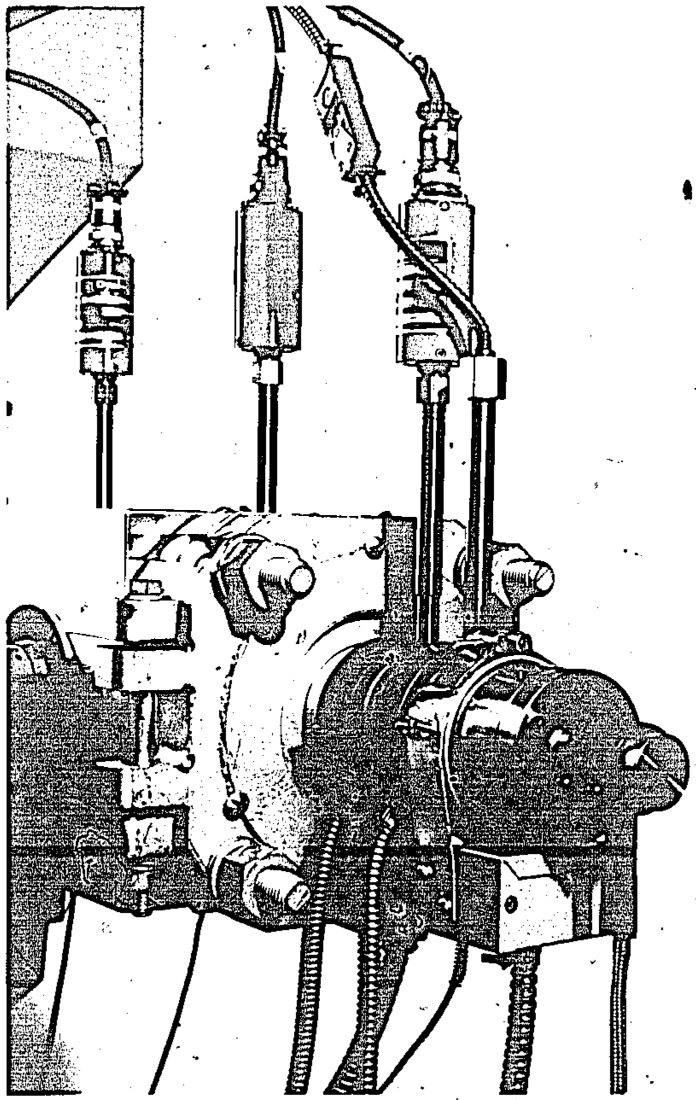

Fig. 10.4 Photograph of adapter and die.

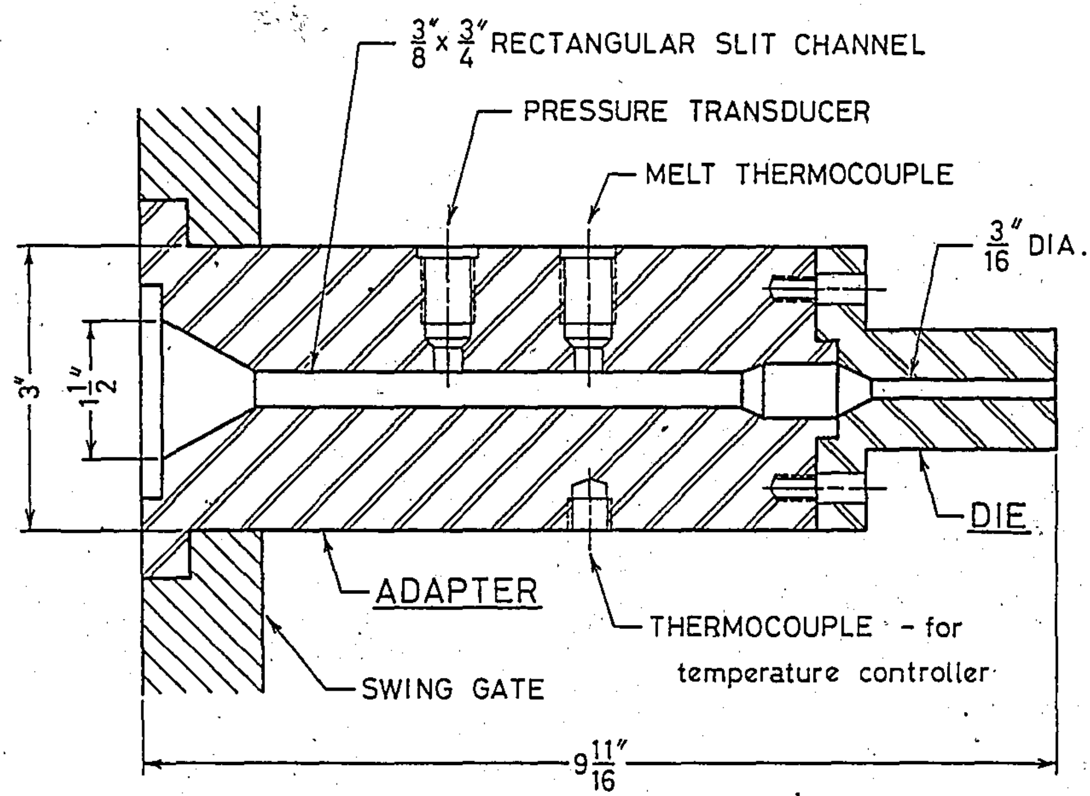

Fig. 10.5 Schematic diagram of adapter and die.

10.1.3 Extruder Instrumentation

Instrumentation on the extruder and die includes the measurement of melt pressure, melt temperature and screw speed. A schematic diagram of the extruder is shown in Fig. 10.6 indicating the instrumentation used on the extruder and die.

The melt pressure is measured at three locations (two in the extruder screw channel and one in the adapter) with Dynisco strain gauge type melt pressure transducers (Model PT 420A). Two of the transducers are connected to Dynisco digital pressure indicators (Model DR482) and one transducer is connected to a Dynisco pressure controller (Model PC201). The controller, however, was not used to control pressure, but to only indicate the melt pressure.

As mentioned above, there are four heating zones along the extruder barrel and one at the die section (adapter/die). The four barrel zones are controlled with Barber-Colman PI time proportioning temperature controllers (Model 523E), each with an on-off auxiliary output for controlling a cooling fan. The adapter/die temperature is controlled with a similar controller (Model 523B) but without the auxiliary output for a cooling fan. The barrel and adapter/die temperatures are measured with iron-constantan (Type J) thermocouples.

The melt temperature in the adapter flow channel is measured with an immersion type iron-constantan (Type J) thermocouple which is connected to a Barber-Colman digital temperature indicator (Model DB11). The thermocouple tip is enclosed in a stainless steel casing which extends 1/4 inch (6.35 mm) into the flow channel. Since the channel is

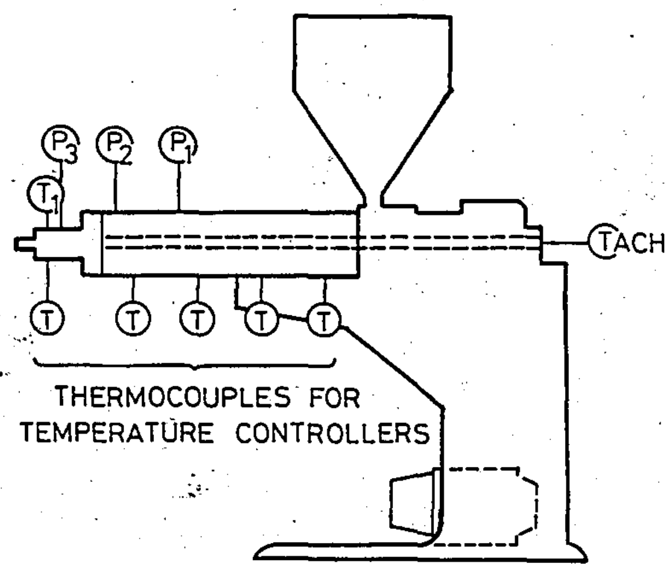

Fig. 10.6 Schematic diagram of the extruder and associated instrumentation. T_1 = melt thermocouple, P_1, P_2, P_3 = pressure transducers, TACH = tachometer.

3/8 inch (9.5 mm) deep, the temperature measurement approximates the bulk (flow-average) temperature of the melt.

Finally the extruder screw speed (i.e., frequency of screw rotation) is measured with a tachometer. A tachometer generator attached to the screw drive transmits a signal to a meter which indicates the screw speed in revolutions per minute.

10.1.4 Description of Extruder Experiments

Extruder experiments were carried out in this study to verify the computer model predictions which are presented in Chap. 12. Each experimental run entailed the measurement of:

(i) screw speed,

(ii) melt pressure at three locations: two in the extruder screw channel and one in the adapter,

(iii) melt temperature in the adapter,

(iv) mass flow rate at the die exit, and

(v) extrudate swell at the die exit.

For each polymer studied, a specific barrel temperature profile was selected and the measurements were performed at several different screw speeds. These processing conditions are listed in Chap. 11.

Experimental Procedure

At the start of each run, the power to the extruder is switched on and the set points on the temperature controllers are set for each of the four barrel heating zones and the adapter/die heater. The polymer in the extruder screw channel is then allowed to heat up for 2 to 3 hours. In actual fact, the polymer requires only 20 to 30 minutes to melt, but the additional heating time is utilized to allow the system to reach steady state. It has been noted that once the screw drive is switched on, the system reaches steady state much faster if a longer warm up period precedes the extrusion run. After the heating period has elapsed, the hopper is filled with the desired polymer and the extruder motor is switched on. The screw speed is then slowly increased to the desired operating level and maintained there for the duration of the experimental run. Approximately 20 to 30 minutes are required for the system to reach steady state conditions. After this period of time has elapsed, the above-listed measurements are performed three times at 20 minute intervals. After all the measurements have been completed for a given run, the screw speed is adjusted to a new level and the system again is allowed to reach steady state conditions. At the end of the day when all desired runs have been performed, the feed port to the extruder screw channel is closed and the extruder is allowed to empty itself of as much polymer as possible. When no more polymer exits from the die, the power to the extruder motor and barrel heaters is switched off.

Measurements of the melt pressure, melt temperature and screw speed were discussed in Sec. 10.1.3. Values for these parameters are obtained from either digital indicators or meters. The mass flow rate of the polymer is measured by weighing the extrudate that has been collected for a specified period of time (usually 1 minute is sufficient). Finally the extrudate swell at the die exit is measured as illustrated in Fig. 10.7. First, as the extrudate emerges from the die, it is cut with scissors (as close to the die exit as possible) and then discarded. After approximately 10 cm of polymer melt has extruded, the extrudate is again cut at the same location while clasping the extrudate near the top with tweezers. The extrudate sample is allowed to cool while suspended in the air, and then the diameter of the strand is measured with a micrometer about 6 mm from the lower end. It is assumed that the elongation of the sample due to gravitational drawdown is negligible at this position. The results of the extruder experiments are given in App. E and are compared with the model predictions in Chap. 12.

10.2 Measurements on Capillary Rheometer

10.2.1 Description of Capillary Rheometer

The Instron[1] capillary rheometer (Model 3211) was used to measure melt viscosities and to obtain extrudate swells of the polymers as required for the extruder model (see Secs. 9.4 and 9.6). Basically the rheometer consists of (i) an extrusion barrel assembly, (ii) a temperature control and distribution assembly, (iii) a drive system, and (iv) an electronic load measuring and readout system.

The extrusion barrel assembly is made up of a hardened steel barrel enclosed in an aluminum jacket to which four cylindrical heating

---

[1] Instron Corporation, Canton, Mass., U.S.A.

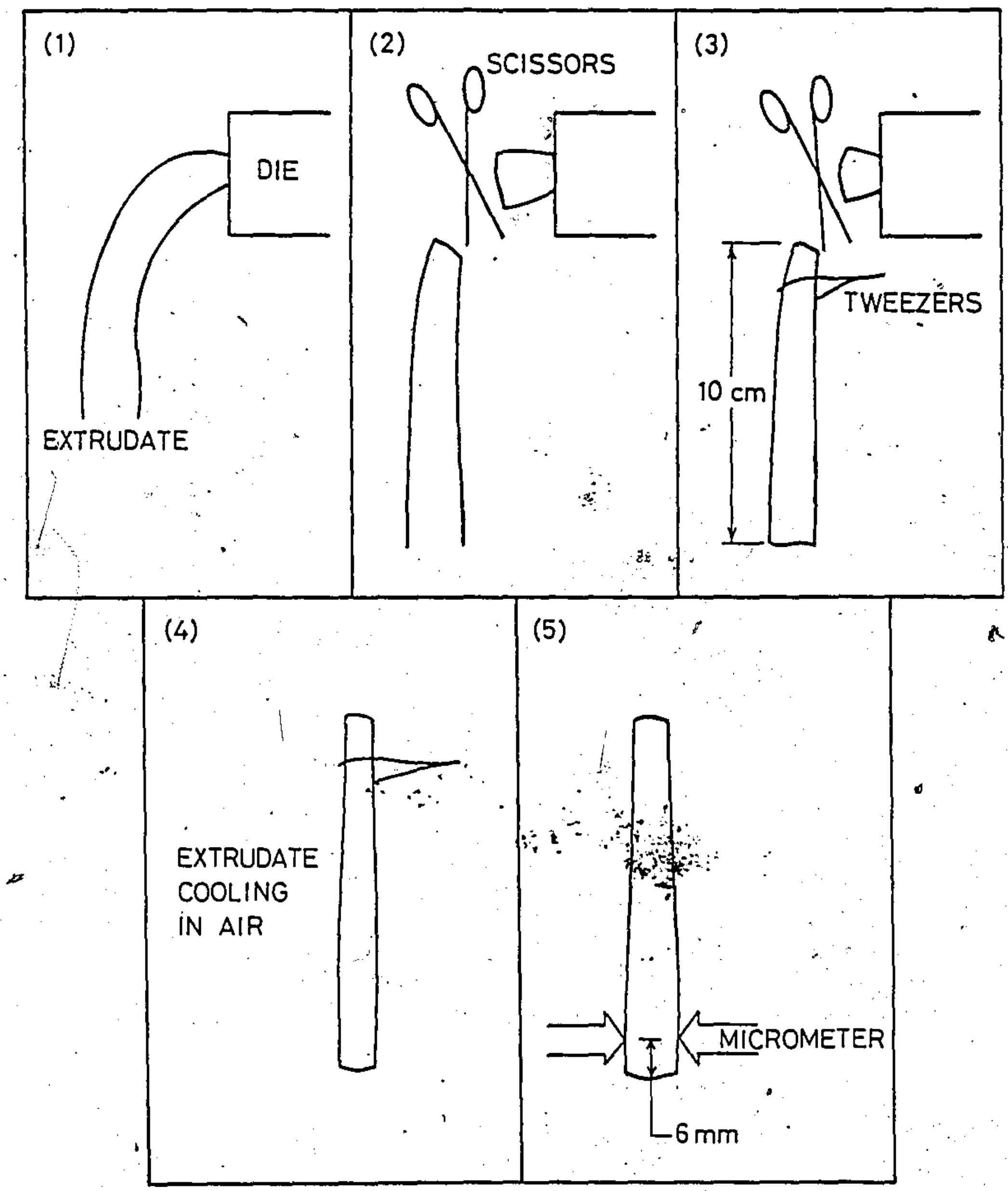

Fig. 10.7 Steps in the measurement of extrudate swell at the die exit of the extruder.

elements are clamped. A capillary die, with a 40:1 length to diameter ratio as shown in Fig. 10.8, is inserted into the bottom of the reservoir and is held there by a clamping nut. Heating of the extrusion barrel assembly is provided by the temperature control and distribution assembly. The barrel temperature may be set between 40°C and 399°C. The drive system consists of a synchronous motor, a gearbox, a lead screw and a plunger. The plunger fits closely into the barrel and is used to force the molten polymer through the capillary at various constant plunger speeds. The load measuring and readout system incorporates a strain gauge load cell which measures the force on the plunger, a solid-state load cell amplifier and a strip chart recorder.

10.2.2 Procedure for Measuring Melt Viscosity

The measurement of the melt (or apparent) viscosity[1] of a material involves determining the wall shear stress and shear rate in the capillary die for different flow rates of the material. The wall shear

[1] The terms "melt viscosity" and "apparent viscosity" are both used in this section, but each has a slightly different meaning. In capillary viscometry, the viscosity of the polymer melt is not "measured", but instead is calculated from the shear stress and true shear rate at the capillary wall as shown in Eq. 10.5 in Sec. 10.2.3. It is common practice to refer to this quantity as "apparent viscosity". The term "apparent viscosity" is most often used when viscometric results are reported (e.g. plots of apparent viscosity versus true shear rate). The term "melt viscosity" simply refers to the viscosity of the polymer melt, irrespective of how it has been determined or calcuated. In this thesis, the "melt viscosity" is simply a given function of shear rate and temperature (see Eq. 2.36 in Sec. 2.4.2, or Eq. 10.1 in Sec. 10.2.3).

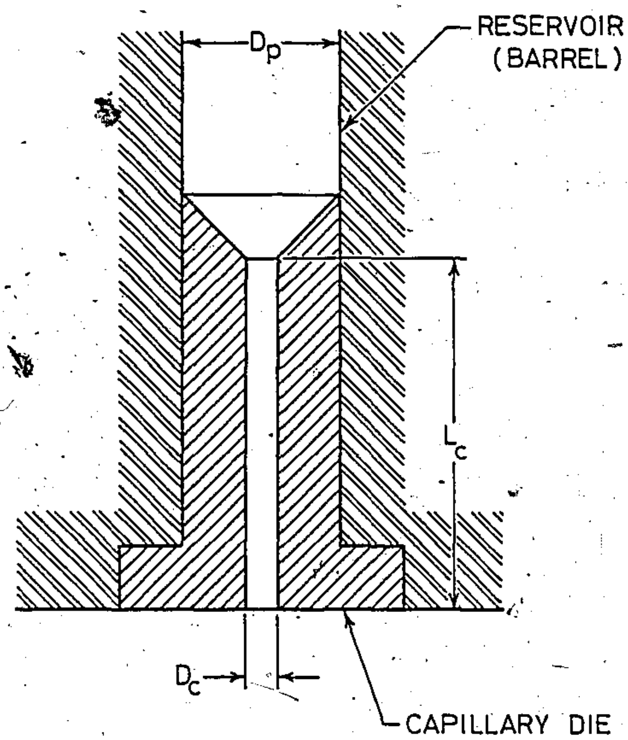

D_c = 0.05025 in (1.2764 mm)
L_c = 2.004 in (50.902 mm)
D_p = 0.375 in (9.525 mm)

Fig. 10.8 Geometry and dimensions of the capillary die and reservoir - Instron capillary rheometer.

stress is obtained by measuring the force required to push the melt through the capillary, and the shear rate by measuring the volumetric flow rate (which can be determined from the plunger speed). Calculation of the melt viscosity from these quantities is discussed in the next section.

To determine the melt viscosity of a given polymer, the rheometer barrel is first preheated to a specified test temperature, and the capillary die is placed into position. Approximately 20 grams of the polymer to be tested is loaded into the reservoir and the plunger is lowered into the barrel until a force is registered by the load cell. The polymer in the reservoir is allowed to heat up for approximately 20 minutes. This amount of time is sufficient for the polymer to melt and reach the temperature of the barrel and die. At selected speeds the plunger is lowered and the force exerted by the plunger on the polymer sample is allowed to reach a steady state value. At low plunger speeds this may take several minutes. In this manner force measurements are obtained for various plunger speeds. Several runs may be needed to accumulate a sufficient number of force-plunger speed readings for a given material at a specified temperature. Between runs it is important to clean the barrel thoroughly.

The Viscosity Curve - Calculation of the Apparent Viscosity

The objective of measuring the viscosity of polymer melts in this study is to represent it as a function of shear rate and temperature so that it may be used in the computer model for the extruder. The following viscosity equation was introduced in Sec. 2.4.2 (see Eq. 2.36):

$$\log \eta = a_o + a_1 \log \dot{\gamma} + a_2(\log \dot{\gamma})^2 + a_3T + a_4T^2 + a_5T \log \dot{\gamma} \qquad (10.1)$$

where η = viscosity (Pa·s)

T = temperature (^oC)

$\dot{\gamma}$ = shear rate (s^{-1})

and where a_o, $a_1,\ldots,$ a_5 are parameters to be determined by curve-fitting viscosity data from the Instron capillary rheometer to the above equation using linear regression.

To calculate the parameters in Eq. 10.1, the force-plunger speed data readings from the rheometer runs must first be converted to values of shear stress τ_w and apparent shear rate $\dot{\gamma}_a$ at the capillary wall using the following equations:

$$\tau_w = \frac{\Delta P\ D_c}{4\ L_c}$$

$$= \frac{(F/A_p)\ D_c}{4\ L_c} \qquad (10.2)$$

where F in the measured force, ΔP is the pressure drop across the capillary, D_c and L_c are the capillary diameter and length, and A_p is the cross-sectional area of the reservoir (see Fig. 10.8).

$$\dot{\gamma}_a = \frac{32Q}{\pi D_c^3}$$

$$= \frac{32\ (V_p\ A_p)}{\pi\ D_c^3} \qquad (10.3)$$

where Q is the volumetric flow rate of the melt and V_p is the plunger speed.

In Eq. 10.2 it is assumed that ΔP represents only the pressure drop across the capillary and that entrance and exit effects are negligible in comparison. Since a very large L/D capillary is used here (L/D = 40), this is a valid assumption. For shorter dies, the Bagley correction (4,112f) would have to be applied to Eq. 10.2 to account for the entrance and exit effects. Equation 10.3 gives the apparent shear rate of the melt at the capillary wall. This would be the true shear rate only if the melt were Newtonian. For non-Newtonian fluids including polymer melts, the Rabinowitch correction (95,112g) is applied to Eq. 10.3 to obtain the true shear rate at the wall as follows:

$$\dot{\gamma}_w = \frac{3}{4}\,\dot{\gamma}_a + \frac{\tau_w}{4}\,\frac{d\dot{\gamma}_a}{d\tau}$$

$$= \frac{3}{4}\,\dot{\gamma}_a + \frac{1}{4}\,\frac{d\dot{\gamma}_a}{d\,\ln\,\tau_w} \qquad (10.4)$$

The apparent viscosity which is function of true shear rate at a given temperature is calculated as follows:

$$\eta = \frac{\tau_w}{\dot{\gamma}_w} \tag{10.5}$$

Thus, given the values of plunger force and speed at various flow rates and temperatures, the apparent viscosity may be calculated using Eqs. 10.2 to 10.5. Apparent viscosity data for a typical low-density polyethylene melt are shown in Fig. 10.9 plotted against true shear rate at various temperatures.

Finally, the viscosity data are curve-fitted to the shear rate and temperature dependent viscosity equation (Eq. 10.1) to obtain values for the parameters a_0 to a_5. Using Eq. 10.1, the melt viscosity can be calculated for any appropriate value of shear rate and temperature in the extruder model. The solid lines in Fig. 10.9, referred to as viscosity curves, have been obtained in this manner.

10.2.3 Procedure for Measuring Instron Extrudate Swell

The objective of measuring the Instron extrudate swell[1] of polymer melts in this study is to represent it as a function of shear stress as required in the computer model for the prediction of extrudate swell at the extruder die exit (see Chap. 8 or Sec. 9.6). The Instron extrudate swell is a measure of the swelling of the melt as it emerges from the capillary die. Thus the viscosity and extrudate swell determinations

---

[1] Instron extrudate swell in this thesis refers to swelling of the polymer melt as measured on the Instron capillary rheometer as opposed to extrudate swell which occurs at the exit of the extruder die.

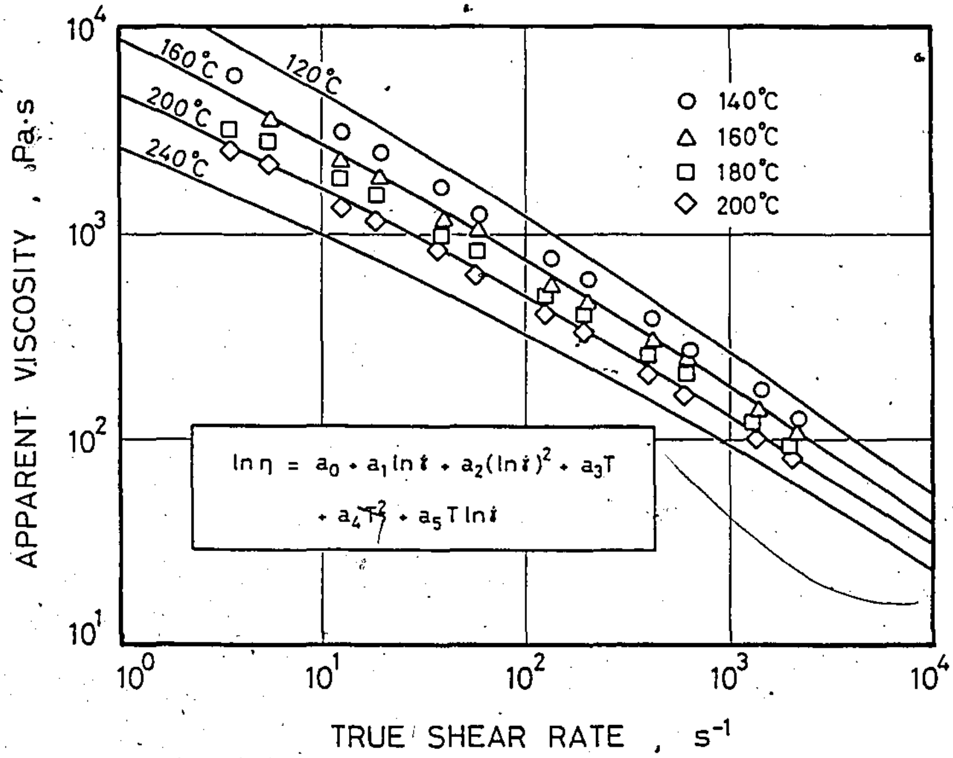

Fig. 10.9 Viscosity curves for a low-density polyethylene resin. Data points represent viscosities measured with an Instron capillary rheometer. Solid curves denote the general viscosity equation (see inset) - parameters a_0 to a_5 are obtained by linear regression.

for a given material can be performed during the same run. Once the plunger force has reached steady state for a given plunger speed, the extrudate is cut with scissors just below the die. When the subsequent extrudate is about 3 inches (75 mm) long, it is clasped with tweezers near the die and again cut. After cooling at ambient temperature, the diameter of the sample is measured with a micrometer approximately 1/4 inch (6 mm) from the lower end where the elongation due to gravitational drawdown is negligible. Samples are collected and the Instron extrudate swell is measured in this manner at various shear rates (or shear stresses) and temperatures.

The following predictive correlation for extrudate swell (d/D) at the extruder die exit was developed in Chap. 8 (see Eq. 8.9):

$$\frac{d}{D} = \left[\frac{A^2}{4}\,\frac{(4-b)}{(2+b)}\,\tau_w^{2b-2} + 1\right]^{1/6} + 0.12 \qquad (10.6)$$

where d and D are the extrudate and die diameters respectively, and τ_w is the shear stress at the die wall. Before calculating the empirical parameters A and b in Eq. 10.6, the extrudate diameter which is measured at ambient temperature should be corrected to the extrusion temperature using the following equation:

$$\frac{d}{d_o} = \left(\frac{\rho_o}{\rho}\right)^{1/3} \qquad (10.7)$$

where d and ρ are the diameter and density of the extrudate sample at the extrusion temperature, and d_o and ρ_o are of the frozen polymer sample at room temperature. Instron extrudate swell data corrected for extrusion temperature are shown in Fig. 10.10 plotted versus wall shear stress. It can be seen that extrudate swell is a very weak function of temperature when plotted against shear stress.

Finally, the Instron extrudate swell data are curve-fitted to Eq. 10.6 using non-linear regression to obtain values of the parameters A and b. Using this equation (shown as a solid curve in Fig. 10.10) the extrudate swell at the extruder die exit may be predicted given a value of the shear stress at the die wall.

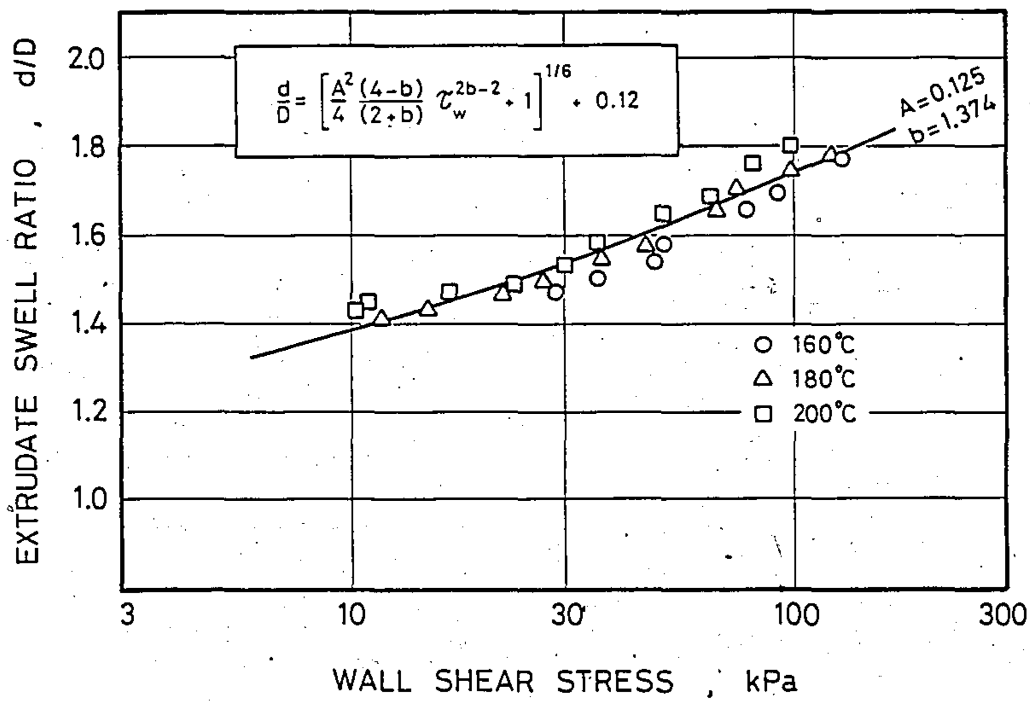

Fig. 10.10 Extrudate swell correlation for a low-density polyethylene resin. Data points represent Instron extrudate swells. Solid curve denotes the extrudate swell equation (see inset) - parameters A and b are obtained by non-linear regression.

CHAPTER 11

POLYMER PROPERTIES AND EXTRUDER PROCESSING CONDITIONS

Polymer property data and extruder operating conditions necessary for the computer model are given in this chapter (see Figs. 11.1 to 11.4 and Tables 11.1 and 11.2 at the end of this chapter). Two polyethylene resins are considered in this study: a low-density polyethylene (Union Carbide Canada Ltd., DFDY 4400) and a high-density polyethylene (DuPont Canada Inc., SCLAIR 19A).

11.1 Material and Rheological Properties

Melt Viscosity

The viscosity data obtained from the Instron capillary rheometer and the resulting viscosity curves for both the LDPE (low-density polyethylene) and HDPE (high-density polyethylene) are shown in Figs. 11.1 and 11.2. For both resins the range of shear rates extends between 4 s^{-1} and 2000 s^{-1}. Viscosity measurements were performed at four temperatures for each material: 140°C, 160°C, 180°C and 200°C for LDPE, and 160°C, 180°C, 200°C and 220°C for HDPE, which adequately covers the extruder temperature processing conditions. It was necessary to extrude the HDPE at a higher temperature than the LDPE because of its higher melting temeprature and higher viscosity. Values for the parameters a_0 to a_5 in the viscosity equation (11.1) are presented in Tables 11.1 and 11.2.

$$\log \eta = a_0 + a_1 \log \dot{\gamma} + a_2 (\log \dot{\gamma})^2 + a_3 T + a_4 T^2 + a_5 T \log \dot{\gamma} \quad (11.1)$$

where η is the viscosity (Pa·s), T is the temperature (°C) and $\dot{\gamma}$ is the shear rate (s^{-1}).

Extrudate Swell

The extrudate swell correlation (Eq. 11.2) shown below was fitted to both the LDPE and HDPE Instron extrudate swell data and is presented in Figs. 11.3 and 11.4 for the two resins. Since the viscosity and extrudate swell measurements were performed at the same time, the shear stress and temperature conditions are the same as for the viscosity results. The parameters A and b in the extrudate swell correlation given below are presented in Tables 11.1 and 11.2.

$$\frac{d}{D} = \left[\frac{A^2}{4} \frac{(4-b)}{(2+b)} \tau_w^{2b-2} + 1\right]^{1/6} + 0.12 \quad (11.2)$$

where τ_w is the wall shear stress (Pa).

Remaining Material Properties

All of the material and rheological properties of the LDPE and HDPE, excluding melt viscosity and extrudate swell, were obtained either from the literature or from the resin manufacturers. The following is a list of polymer properties used in the computer model, values for which are given in Tables 11.1 and 11.2 (the numbers in parentheses indicate the source of data from the literature):

(1) Bulk density ρ_{bulk} (112h)

(2) Density of solid ρ_s and melt ρ_m (114n)

(3) Thermal conductivity of melt k_m (114n)

(4) Heat capacity of the solid Cp_s (114n) and melt Cp_m (114n)

(5) Heat of fusion λ (114n)

(6) Melting temperature T_{melt} (114n)

(7) Dynamic coefficients of friction of solid at barrel and screw surfaces, f_b and f_s (43,112h)

(8) Static coefficient of friction of solid at hopper wall f'_w (112h)

(9) Effective angle of friction of solid in hopper δ (112h)

Resin manufacturers usually supply very little property data with their materials. Normally the only properties given are the solid density ρ_s and the melt index[1]. This is largely due to the fact that polymer properties, especially thermal properties, are difficult to measure. If one does not have access to measurement facilities (which is usually the case), then one is compelled to use literature values even though they may be for slightly different materials.

11.2 Extruder Processing Conditions

There are very few processing variables in the operation of an extruder. Once the screw and die designs have been incorporated, all there remains to choose is the barrel temperature profile and the screw speed. The processing conditions for the LDPE and HDPE are presented in Tables 11.1 and 11.2.

---

[1]The melt index is a crude measure of the viscosity of the polymer melt and has the units of gm/10 min. For polyethylene resins low values of melt index (less than 1.0) indicate a highly viscous melt whereas higher values (greater than 10.0) denote a low viscosity melt.

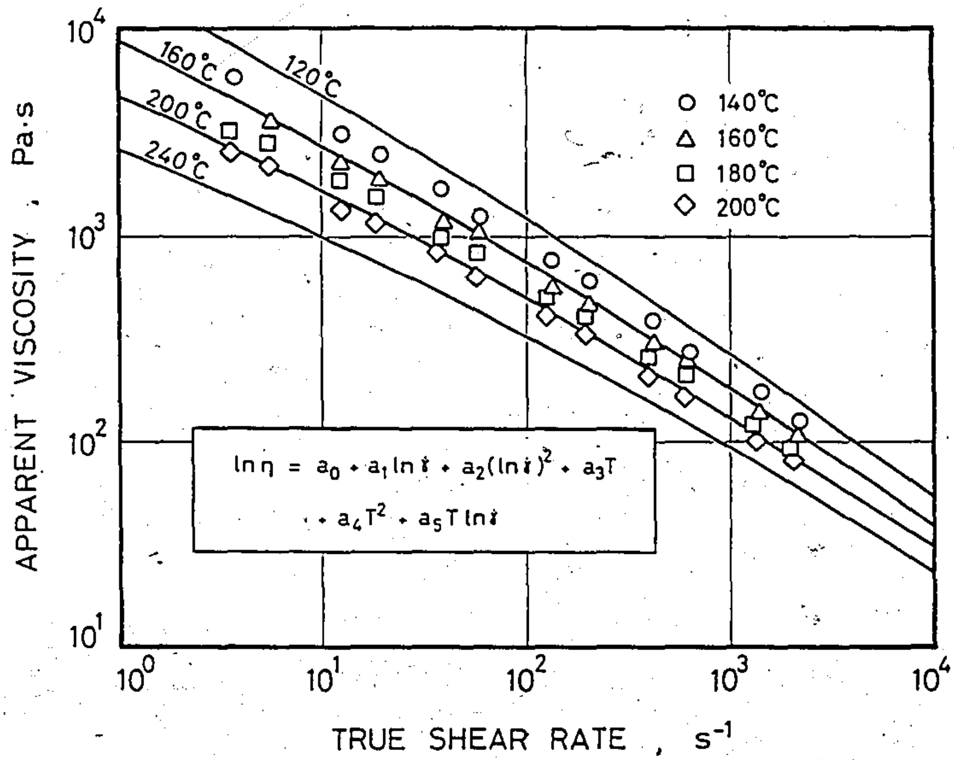

Fig. 11.1 Viscosity curves for LDPE (Union Carbide Canada Ltd., DFDY 4400). Data points represent viscosities measured with an Instron capillary rheometer. Solid curves denote the general viscosity equation (see inset) - parameters a_0 to a_5 are obtained by linear regression.

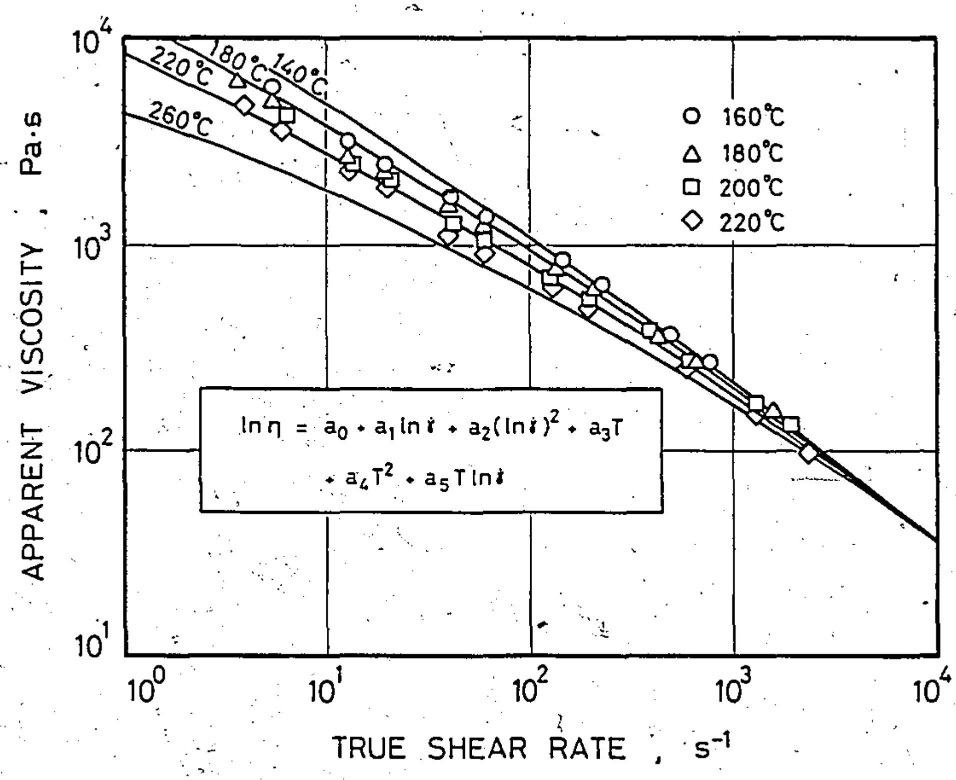

Fig. 11.2 Viscosity curves for HDPE (DuPont Canada Inc., SCLAIR 19A). Data points represent viscosities measured with an Instron capillary rheometer. Solid curves denote the general viscosity equation (see inset) - parameters a_0 to a_5 are obtained by linear regression.

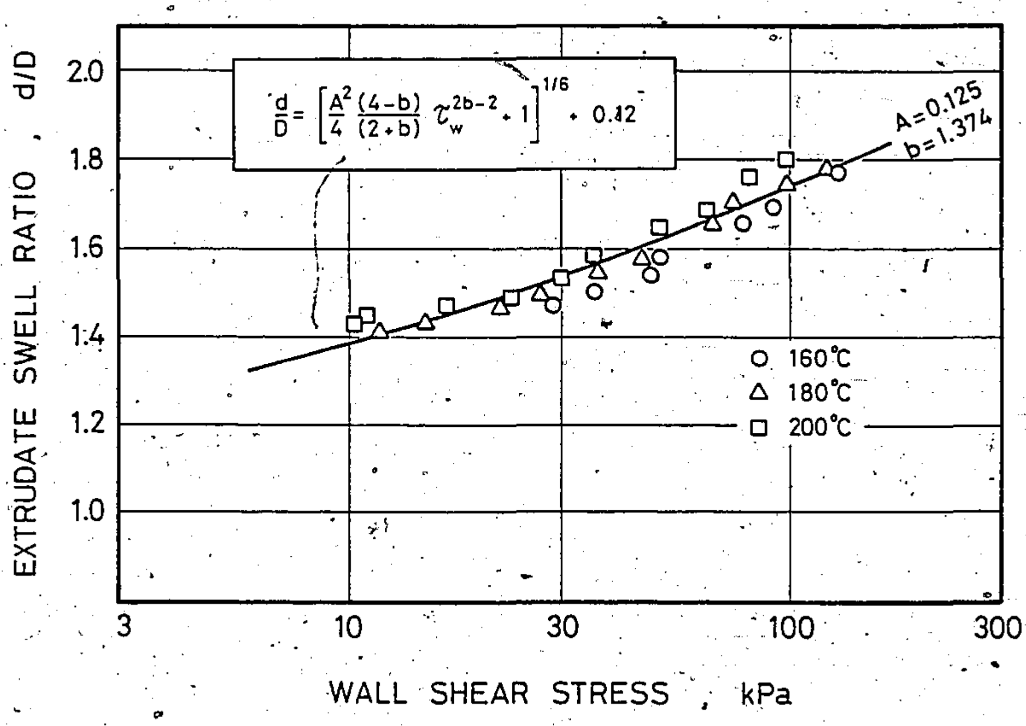

Fig. 11.3 Extrudate swell correlation for LDPE (Union Carbide Canada Ltd., DFDY 4400). Data points represent Instron extrudate swells. Solid curve denotes the extrudate swell equation (see inset) - parameters A and b are obtained by non-linear regression.

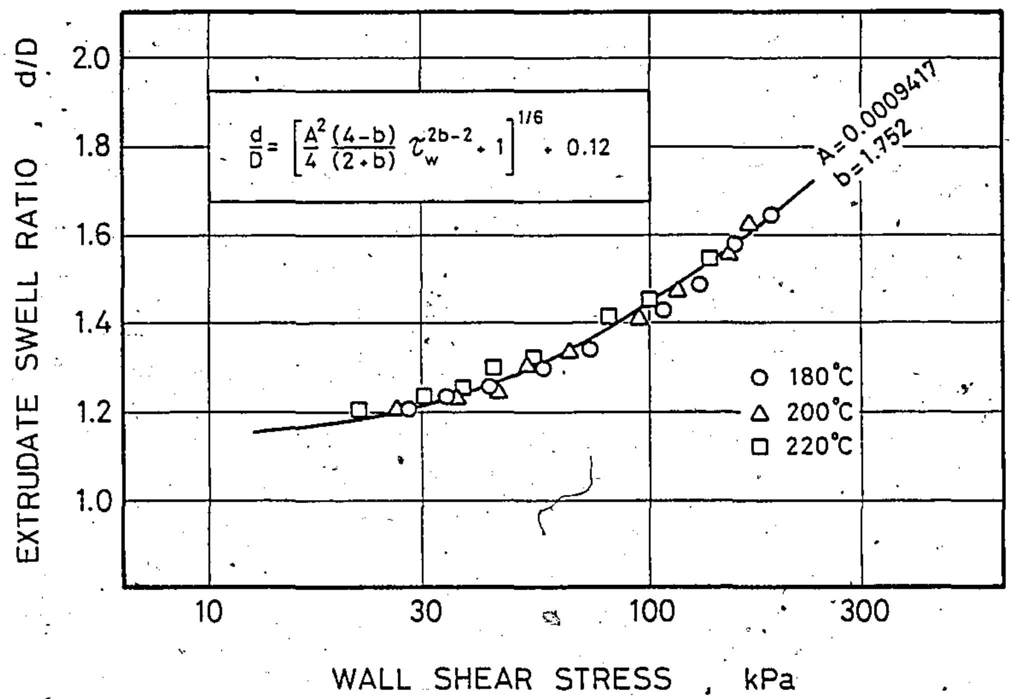

Fig. 11.4 Extrudate swell correlation for HDPE (DuPont Canada Inc., SCLAIR 19A). Data points represent Instron extrudate swells. Solid curve denotes the extrudate swell equation (see inset) - parameters A and b are obtained by non-linear regression.

Table 11.1 Material and rheological properties and processing conditions for LDPE (Union Carbide Canada, Ltd., DFDY 4400).

Material and rheological properties		
Static coefficient of friction, f'_w		0.30
Effective angle of friction, δ		33.7
Dynamic coefficients of friction, f_b		0.40
, f_s		0.25
Heat capacity - melt, Cp_m		2595 J/(kg•K)
- solid, Cp_s		2763 J/(kg•K)
Density - bulk, ρ_{bulk}		595 kg/m^3
- melt, ρ_m		779 kg/m^3
- solid, ρ_s		919 kg/m^3
Thermal conductivity - melt, k_m		0.182 W(m•K)
Heat of fusion, λ		129785 J/kg
Melting temperature, T_{melt}		110°C
Melt index		2.0 g/10 min
Viscosity, η (see Fig. 11.1)	a_0	11.7838
	a_1	-0.639104
	a_2	-0.0112744
	a_3	-0.0183449
	a_4	8.78448×10^{-6}
	a_5	9.66512×10^{-4}
Extrudate swell, $\frac{d}{D}$ (see Fig. 11.3)	A	0.125
	b	1.374
Extruder operating conditions		
Barrel temperature profile		163/179/196/196/196°C
Frequency of screw rotation		40, 60 and 80 rpm (revolutions per minute)

Table 11.2 Material and rheological properties and processing conditions for HDPE (DuPont Canada Inc., SCLAIR 19A).

Material and rheological properties		
Static coefficient of friction, f'_w		0.30
Effective angle of friction, δ		33.7
Dynamic coefficients of friction, f_b		0.40
, f_s		0.25
Heat capacity – melt, Cp_m		2512 J/(kg·K)
– solid, Cp_s		2303 J/(kg·K)
Density – bulk, ρ_{bulk}		595 kg/m^3
– melt, ρ_m		777 kg/m^3
– solid, ρ_s		960 kg/m^3
Thermal conductivity – melt, k_m		0.182 W/(m·K)
Heat of fusion, λ		201189 J/kg
Melting temperature, T_{melt}		130°C
Melt index		0.75 g/10 min
Viscosity, η (see Fig. 11.2)	a_0	9.95345
	a_1	−0.782449
	a_2	−0.0114677
	a_3	4.50087x10^{-3}
	a_4	−3.93029x10^{-5}
	a_5	1.41590x10^{-3}
Extrudate swell, $\frac{d}{D}$ (see Fig. 11.4)	A	9.417x10^{-4}
	b	1.752
Extruder operating conditions		
Barrel temperature profile		188/196/204/204/204°C
Frequency of screw rotation		40, 60 and 80 rpm (revolutions per minute)

CHAPTER 12

VERIFICATION OF THE EXTRUDER MODEL - RESULTS AND DISCUSSION

12.1 Comparison of Experimental and Simulation Results

In this section, the extruder model predictions are compared with the experimental results obtained from a 1 1/2 inch (38 mm) single screw extruder (as described in Sec. 10.1) using two different polyethylene resins: LDPE (Union Carbide Canada Ltd., DFDY 4400) and HDPE (DuPont Canada Inc., SCLAIR 19A). The processing conditions for these experimental runs were presented in Chap. 11, Tables 11.1 and 11.2. Comparisons between the experimental and simulation results are presented in Tables 12.1 to 12.4 and Figs. 12.1 to 12.4 for the following process parameters:

(i) mass flow rate of the polymer,

(ii) melt pressure in the extruder and adapter,

(iii) melt temperature in the adapter, and

(iv) extrudate swell at the die exit.

Experimental results for the above are also given in App. E. In Figs. 12.1 to 12.4 the down channel pressure and bulk temperature profiles are shown only for the melt flow regions in the extruder screw channel and die. No profiles are shown for the solids conveying zone. Predicted solid bed profiles are presented in Figs. 12.5 and 12.6, although no verifications were carried out for this parameter.

The computation time requirements for the extruder model using the

Table 12.1 Predicted versus measured mass flow rate for LDPE.

Screw speed, rpm	Mass flow rate, kg/s	
	Predicted	Measured
40	1.965×10^{-3}	1.911×10^{-3}
60	2.929×10^{-3}	2.948×10^{-3}
80	3.886×10^{-3}	3.968×10^{-3}

Table 12.2 Predicted versus measured mass flow rates for HDPE.

Screw speed, rpm	Mass flow rate, kg/s	
	Predicted	Measured
40	1.881×10^{-3}	1.755×10^{-3}
60	2.812×10^{-3}	2.707×10^{-3}
80	3.748×10^{-3}	3.705×10^{-3}

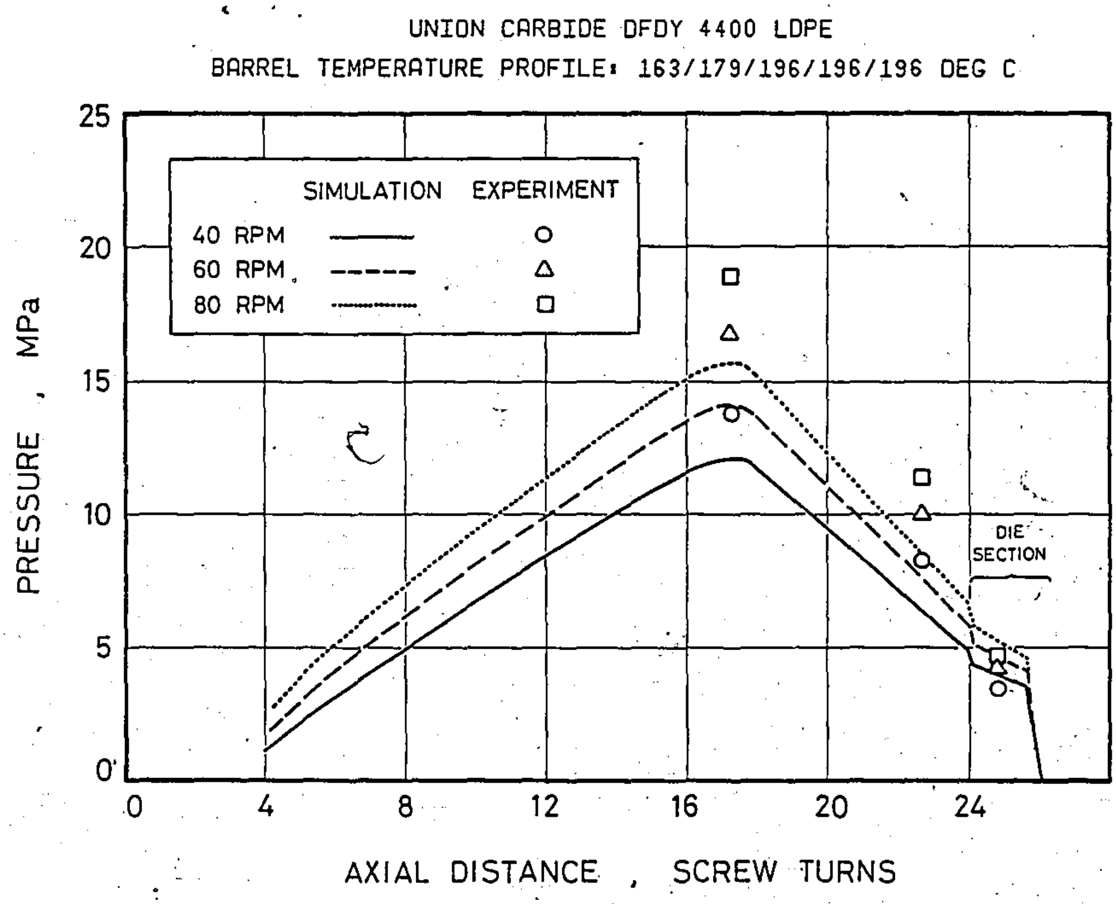

Fig. 12.1 Predicted pressure profiles and pressure measurements in the extruder screw channel and die section for LDPE.

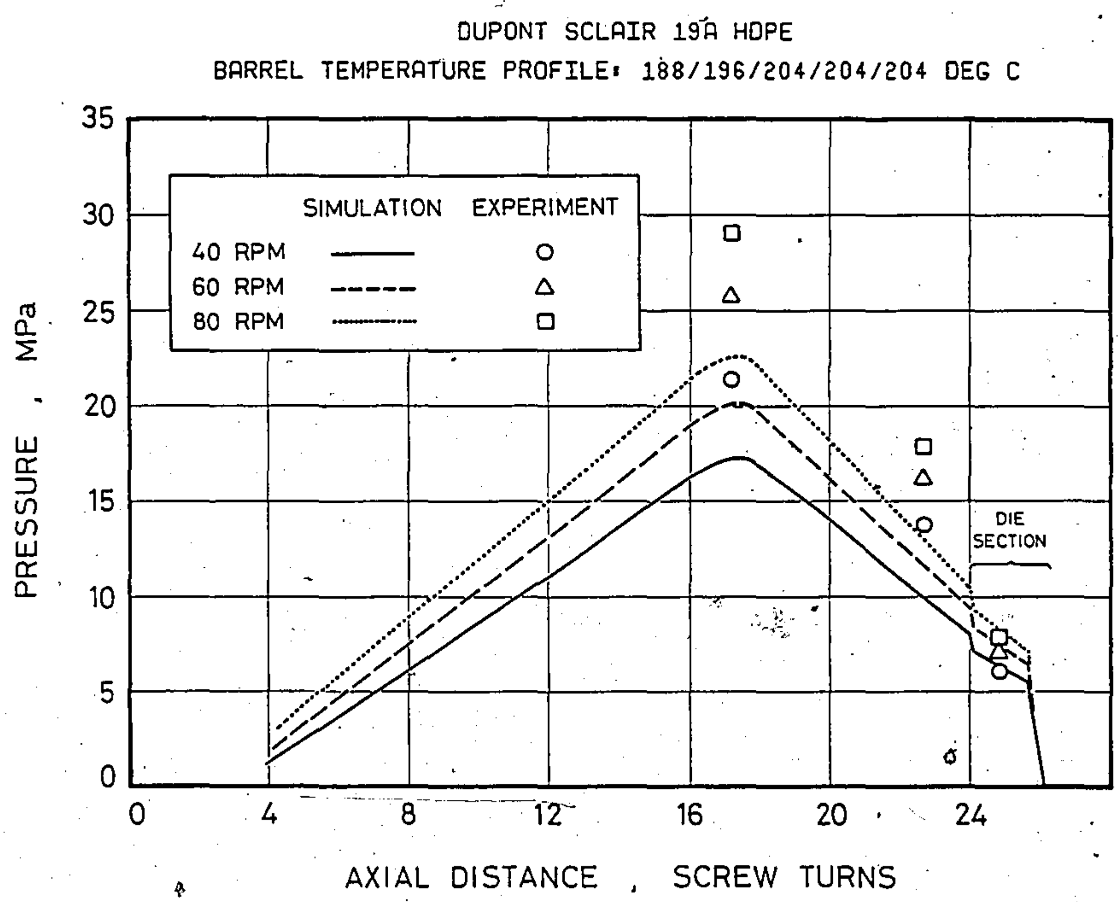

Fig. 12.2 Predicted pressure profiles and pressure measurements in the extruder screw channel and die section for HDPE.

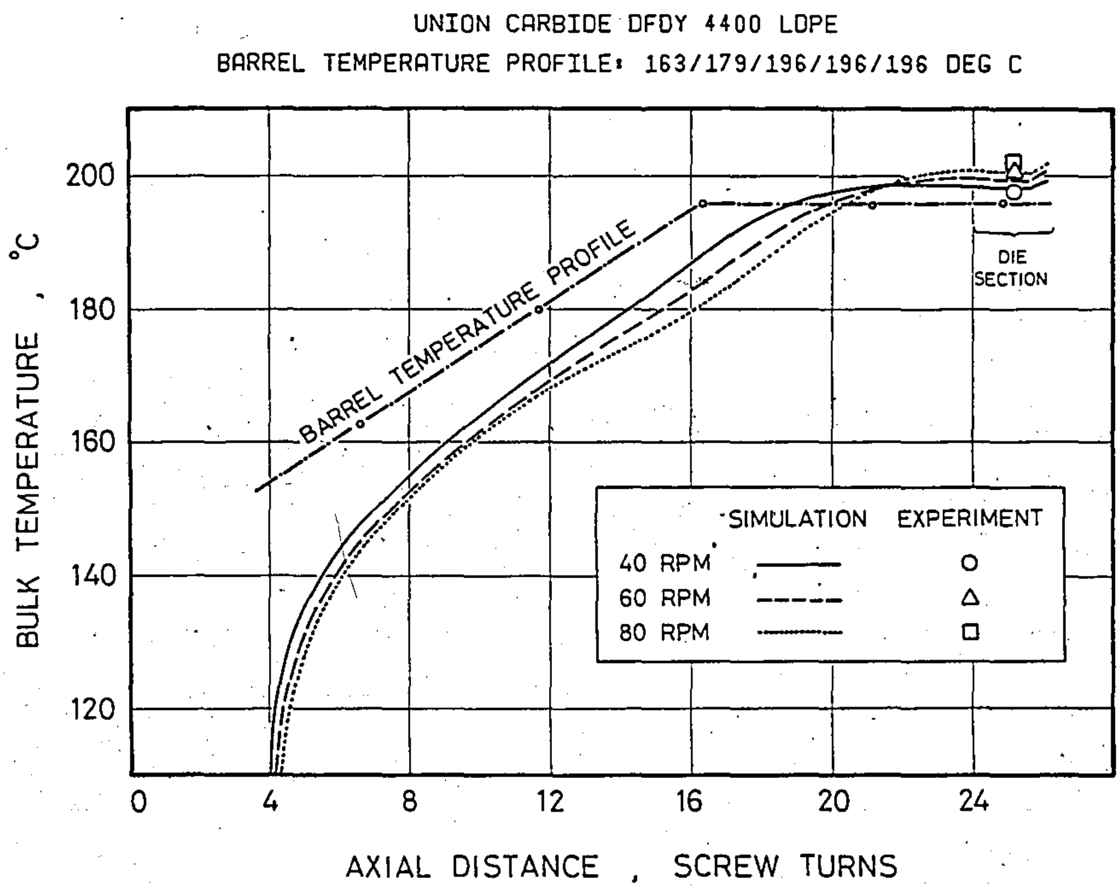

Fig. 12.3 Predicted bulk temperature profiles and melt temperature measurements in the extruder screw channel and die section for LDPE.

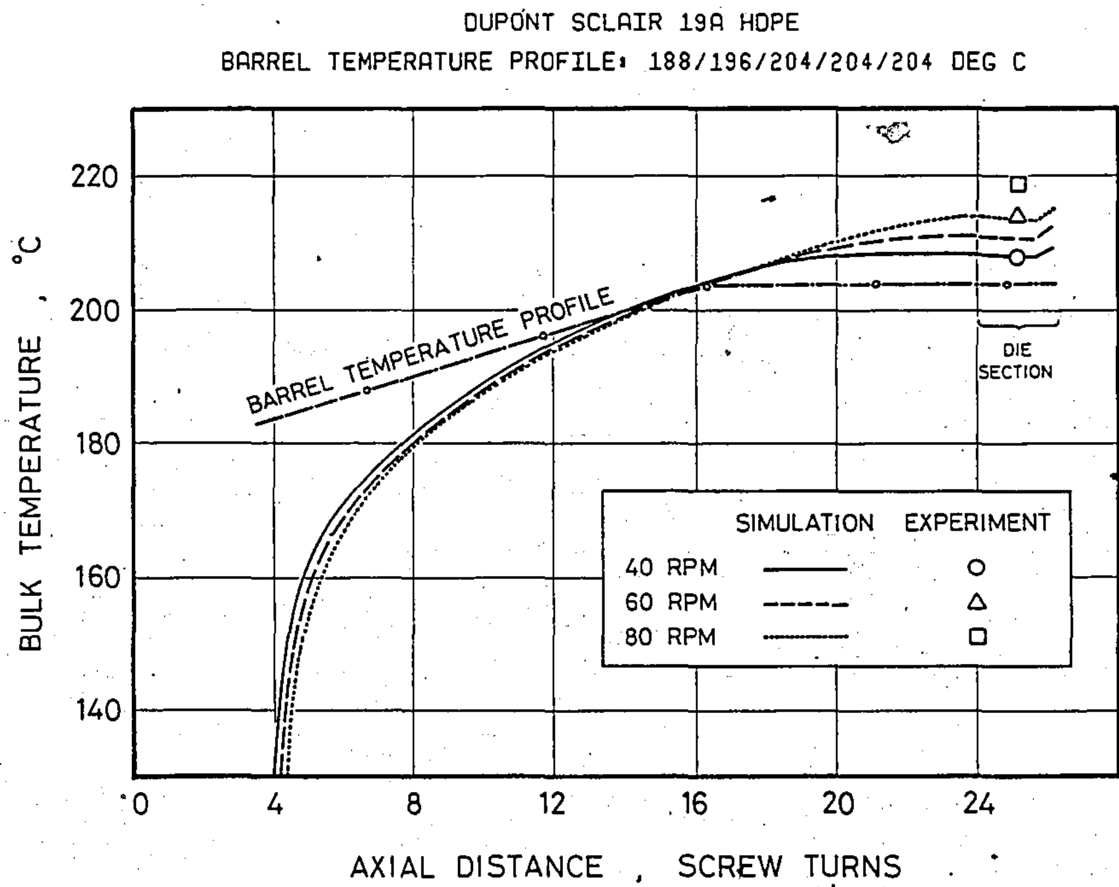

Fig. 12.4 Predicted bulk temperature profiles and melt temperature measurements in the extruder screw channel and die section for HDPE.

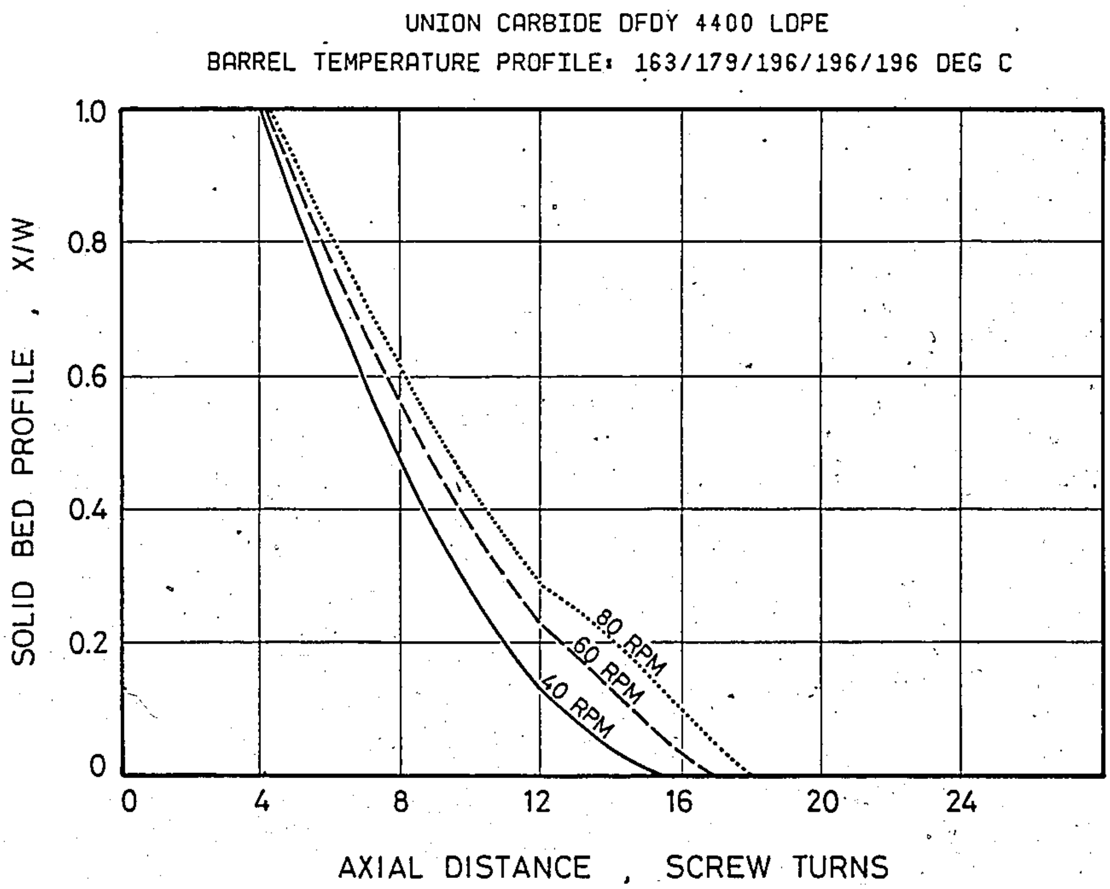

Fig. 12.5 Predicted solid bed profiles in the extruder screw channel for LDPE.

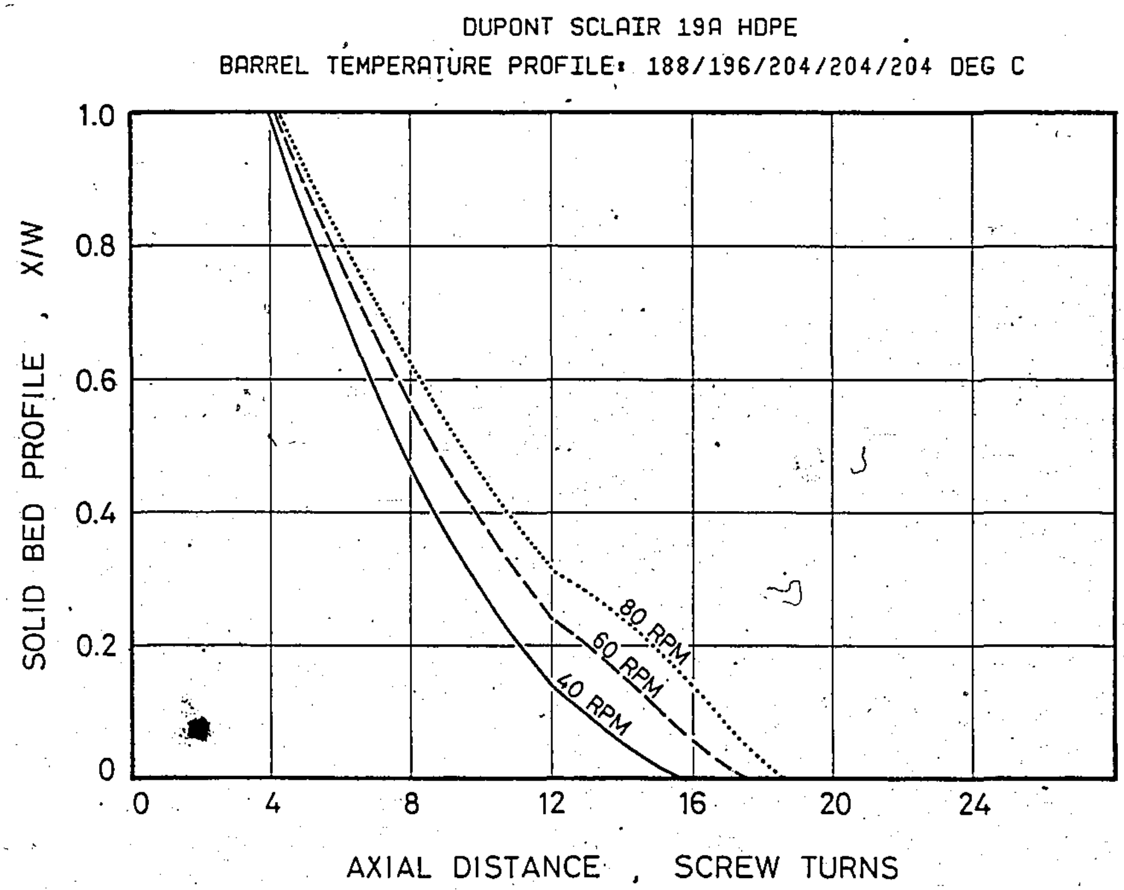

Fig. 12.6 Predicted solid bed profiles in the extruder screw channel for HDPE.

Table 12.3 Predicted versus measured* extrudate swell for LDPE.

Screw speed, rpm	τ_w, kPa	Extrudate swell, d/D	
		Predicted	Measured
40	79.470	1.692	1.646
60	92.979	1.721	1.674
80	103.576	1.742	1.713

Table 12.4 Predicted versus measured* extrudate swell for HDPE.

Screw speed, rpm	τ_w, kPa	Extrudate swell, d/D	
		Predicted	Measured
40	126.236	1.511	1.682
60	146.090	1.556	1.728
80	161.341	1.589	1.767

*Corrected for temperature (see Eq. 10.7)

CYBER 170/730 computer at McMaster University were as follows: 360 to 430 s for the simulations involving LDPE, and 540 to 550 s for the HDPE. The large difference in computation times could be attributed to the difference in viscosity between the two polymers. Since the viscosity of the HDPE is higher than that of the LDPE, more heat is generated by viscous dissipation in the case of the HDPE. In the finite difference method, it is possible that more iterations in the developing temperature regions are required for this reason.

The predicted and measured mass flow rates are compared in Tables 12.1 and 12.2 at three screw speeds (40, 60 and 80 rpm) for the LDPE and HDPE respectively. For the LDPE the predicted and measured values differ by 1 to 3 percent; for the HDPE the difference is significantly larger and ranges between 1 and 7 percent. In both cases it can be seen that the predicted increase in flow rate with increased screw speed is smaller than observed experimentally.

The predicted down channel pressure profiles in the extruder screw channel and die section are shown in Figs. 12.1 and 12.2 for the two resins and are compared with the pressure measurements in the extruder and adapter. In all cases, it can be seen that the predicted pressure profiles in the extruder are significantly lower than the observed values. For the LDPE the difference ranges between 12 and 25 per cent, while for the HDPE the difference is between 19 and 27 percent. Also, with increasing screw speed the predicted pressure profiles do not rise as much as the experimental values. In the adapter the predicted pressures are slightly lower than the measured values. In the case of the LDPE the difference ranges between 14 and 18 percent, while for the HDPE the difference is between 7 and 8 percent.

Next, the down channel bulk temperature profiles in the extruder and die section are shown along with the melt temperature measurements in the adapter in Figs. 12.3 and 12.4 for the LDPE and HDPE respectively. The difference between the experimental values and the predicted profiles is best described here in absolute terms, that is in degrees Celsius, and not as a percentage difference. A difference of 2°C between the predicted and measured temperature is quite tolerable. In the case of the LDPE, the difference ranges between 0.7 and 1.6 °C, whereas for the HDPE the difference is between 0.3 and 5.1°C. As in the case of pressure, the predicted increase in melt temperature with increasing screw speed is smaller than indicated by the melt temperature measurements. Unfortunately, it was not possible to measure the melt temperature in the extruder screw channel.

The final comparison, as presented in Tables 12.3 and 12.4, is between the predicted and experimental values of extrudate swell at the die exit. For the LDPE the predictions are approximately 2 percent higher than the experimental values, whereas the predictions for the HDPE are about 10 percent lower than the experimental values.

Above, comparisons have been made between the predictions from the extruder model and experimental results obtained for two polyethylene resins. Although the prediction error may be significant in certain instances, it should be remembered that the computer model is fully-predictive and the simulation results are not modified on the basis of any measurements performed during the experimental runs on the extruder (for example, pressure measured at the end of the screw). Errors in the simulation results may be due to two factors: (i) incorrect values of polymer properties, and (ii) deficiencies in one or more of the individual submodels used in the overall extruder model. These factors will be discussed in the next sections.

12.2 Polymer Properties

The frictional and thermal properties of polymers are very difficult to measure, especially at elevated temperatures. As a consequence, one must resort to property data reported in the literature. It was stated in Sec. 11.1 that all polymer properties utilized in the extruder model were obtained from the literature except for the melt viscosity and extrudate swell which were measured on the Instron capillary rheometer and the solid density which was supplied by the resin manufacturers. Since the materials used in this study and the materials for which the property data are reported in the literature are not identical, there exists an uncertainty as to how accurate the literature values are for the materials being studied. The difficulty in obtaining accurate property data is a well recognized problem when performing computer simulations on polymer processes. It is not uncommon for two polyethylene resins having approximately the same solid density and molecular weight, but produced by different manufacturers, to have widely differing thermal and frictional properties. Polymer handbooks list various mechanical and electrical properties for different polymers, but not the properties which are needed in process simulation. An ideal situation would be that one could measure each of the properties in the laboratory as is the case for melt viscosity and extrudate swell.

Recognizing the fact that some of the polymer properties may not be very accurate for the polymers utilized in this work, a sensitivity study has been performed on each of the following properties: static coefficient of friction f'_w, effective angle of friction δ, dynamic coefficients of friction at the barrel and screw surfaces f_b and f_s, heat capacity of the melt Cp_m and solid Cp_s, bulk density ρ_{bulk}, melt density ρ_m, thermal conductivity of the melt k_m, heat of fusion λ, and melting temperature T_{melt}. For a given polyethylene resin (LDPE, screw speed = 60 rpm), the values of each of the properties were individually raised by 2 percent in the extruder model and their effects on pressure and bulk temperature at the die exit were then noted. Results of this sensitivity test are given in complete form in App. F. The most significant changes are shown in Table 12.5. It should be noted that maximum pressures in the extruder screw channel range between approximately 10,000 and 30,000 kPa.

Changes in the dynamic coefficients of friction and in the melt density influence the exit pressure the most, and to a lesser extent so does the change in melting temperature of the polymer. For the properties utilized in the feed hopper model, only the bulk density has any significant effect on the hopper base pressure. The remaining properties show negligible effect on the exit pressure when individually

Table 12.5 Effect of changes in some polymer properties on pressure and bulk temperature at the die exit for LDPE. Screw speed = 60 rpm, mass flow rate = 2.929 x 10^{-3} kg/s.

f_b	P_{exit}, kPa	T_{bulk}, °C
0.40	0	200.72
0.408	951	200.72

f_s	P_{exit}, kPa	T_{bulk}, °C
0.25	0	200.72
0.255	-514	200.72

ρ_m, kg/m^3	P_{exit}, kPa	T_{bulk}, °C
779	0	200.72
794.58	1359	200.67

T_{melt}, °C	P_{exit}, kPa	T_{bulk}, °C
110	0	200.72
112.2	206	200.73

increased by 2 percent. It can also be seen that increases in each of the properties have negligible effect on bulk temperature at the die exit.

To carry the sensitivity study one step further, simulations were performed using an increased value of $f_b = 0.408$ such that the pressure at the die exit equalled zero. The resulting values of mass flow rate, extruder and adapter pressures, melt temperature in the adapter and extrudate swell are shown in Table 12.6 and are compared with measured values and predicted values using $f_b = 0.40$. It can be seen that the 2 percent increase in f_b has a significant effect on the resulting mass flow rate and pressures, but that the influence on melt temperature and extrudate swell is negligible.

It would be very useful if frictional coefficients of polymers could be easily measured in the laboratory. However, at elevated temperatures, this measurement is quite difficult. There is no standard and well-accepted method for doing this. It should be noted that frictional coefficients of polymer granules, and not of a solid plug, are needed.

In summary, the sensitivity tests on the polymer properties have shown that small errors in the values of some properties, namely the dynamic coefficients of friction f_b and f_s, the melt density ρ_{bulk}, the bulk density ρ_{bulk} and melting temperature T_{melt}, can significantly influence the predicted mass flow rates and pressure profiles from the extruder model. Thus the difference between the predicted and measured values of mass flow rate and pressure in the extruder may partially be

Table 12.6 Comparison of predicted and measured values of mass flow rate, melt pressures and melt temperature given two values of f_b for LDPE. Screw speed = 60 rpm.

	Mass flow rate, kg/s
Measured	2.948×10^{-3}
Predicted (f_b = 0.40)	2.929×10^{-3}
(f_b = 0.408)	2.969×10^{-3}

	Pressure, kPa		
	P_1	P_2	P_3
Measured	16777	9997	4183
Predicted (f_b = 0.40)	14112	7647	4798
(f_b = 0.408)	14835	7829	4825

	Bulk temperature, °C
Measured	201.1
Predicted (f_b = 0.40)	199.79
(f_b = 0.408)	199.75

	Extrudate swell, d/D
Measured	1.674
Predicted (f_b = 0.40)	1.721
(f_b = 0.408)	1.722

attributed to an uncertainty of the actual properties of the polyethylene resins studied. The sensitivity tests have also shown that the melt temperature in the adapter and the extrudate swell are not influenced to any great extent by changes in polymer properties. The differences between the predicted and measured values for these can only be attributed to deficiencies in the computer model.

12.3 General Critique of the Extruder Model

In Sec. 12.1 the predictions from the extruder model and experimental measurements were compared for two polyethylene resins. It could be seen that in some cases a substantial difference exists between the predicted and experimental results. In the previous section (Sec. 12.2) it was shown that a better knowledge of certain property data could change the predicted mass flow rates, but that the temperature profiles and the extrudate swell are not influenced to any great extent by changes in property data. It was also noted in Sec. 12.1 that the predicted mass flow rates, pressure profiles and melt temperatures did not rise with increasing screw speed to the same extent as did the measured values. Given additional experimental data, it may be possible to improve the overall model results by introducing refinements to the individual submodels. In this section each of the submodels are discussed and the significance and implications of any possible improvements are noted.

The feed hopper model is used to calculate the pressure at the base of the hopper which in turn is the starting point for the pressure profile in the solids conveying zone. Since an exponential rise in the pressure is predicted by the solids conveying model, it is important that the base pressure below the hopper be as accurate as possible. An experiment could be performed to measure the pressure at the base of the hopper and then to compare it with the model prediction. This experiment, however, were not carried out in this study.

In the solids conveying model, it is assumed that the solid polymer granules travel down the ~~screw~~ channel as a solid plug with constant velocity, and that the solid plug is isothermal and isotropic (i.e., the pressure varies only in the down channel direction). More sophisticated models were discussed in Sec. 4.1, for example, the nonisothermal model by Tadmor and Broyer (110) or the model by Lovegrove and Williams (58,59,60) in which the initial pressure is assumed to be entirely due to gravitational and centrifugal forces and not the hopper base pressure. Such modifications may be justified if it can be shown that they significantly affect not only the predictions in the solids conveying zone, but also the predictions for the overall performance of the extruder. In any case, more pressure and temperature measurements are required in this zone, and a better understanding of the actual solids conveying mechanism is needed before substantial improvements can be made to the present model.

In the present model it is also assumed that the delay zone (i.e. the section in the screw channel where melting at the barrel surface has begun but where the steady state melting mechanism has not yet taken over) starts at the location of the first barrel heaters and is included in the solids conveying zone. The calculation of a down channel temperature profile would provide a better estimate of where the delay zone starts, however, one would need temperature measurements along the solid bed in the screw channel to verify and justify this modification. Pressure and temperature measurements in solids flow regions are very difficult to perform. The length of the delay zone, and ultimately that of the solids conveying zone, is determined from a correlation by Tadmor and Klein (114g) based on limited experimental data. Even if a theoretical model which determined the length of the delay zone were available, it would not significantly affect the length of the solids conveying zone because the delay zone is only 1 to 2 screw turns long. In this study it was shown that a decrease in the length of the delay zone by 1 turn had a negligible effect on the predicted performance of the extruder.

A variation of Tadmor's melting model is used in the present extruder model to predict the rate of melting and the solid bed profile in the screw channel. More sophisticated melting models such as the ones discussed in Sec. 5.1 require substantially more computation time to run than the present model. To discriminate among the more refined melting models such as the model by Edmondson and Fenner (27) or the one by Shapiro et al. (37,103) and the present model, one should be able to measure the rate of melting and the solid bed profile in the screw channel for the purposes of comparison. The 1 1/2 inch (38 mm) diameter extruder used in this study does not have the facilities for quick barrel and screw cooling and subsequent rapid screw extraction which would be needed to test the melting models. Thus, the use of a more complex melting model cannot be justified at the present time. It would also have to be shown that the additional model sophistications substantially improve the predictions for the overall performance of the extruder.

One advantage of melting models such as ones by Edmondson and Fenner (27) and Shapiro et al. (37,103) is that they predict an acceleration of the solid bed in the screw channel. Consequently, it is possible to predict solid bed breakup which affects pressure surging in the screw channel. The present melting model cannot predict surging conditions due to its isotropic nature.

The present model for melt pumping in the screw channel is based on non-Newtonian nonisothermal developing flow between infinitely wide parallel or converging plates. It incorporates a temperature and shear rate dependent viscosity relation which is determined by measurements on an Instron capillary rheometer for each polymer studied. In Sec. 6.2.2 shape factors were developed for combined Newtonian drag and pressure flow in rectangular channels. As stated in Sec. 6.2.6, corresponding shape factors for non-Newtonian fluids are much more difficult to obtain, and consequently have not been developed in this study. It was also stated that the inclusion of Newtonian shape factors in non-Newtonian flow only adds difficulties to the numerical solution. This is due to the fact that in combined non-Newtonian drag and pressure flow, the drag and pressure flow contributions cannot be superimposed. For this reason, Newtonian shape factors have not been used in the present model.

For melt flow in the metering section where the melting is complete and the channel aspect ratio (H/W) is small, the infinite channel width approximation does not affect the pressure profile predictions to a great extent. It can be seen in Figs. 12.1 and 12.2 that the slopes of the predicted pressure profiles are comparable with the experimental data points. The infinite width channel approximation does, however, break down in the regions of the screw channel where the melt coexists side by side with the solid bed. Here, the aspect ratio of the melt filled region is simply too high for the melt flow to be not significantly affected by the channel sides. Pressure measurements were not performed in this region on the extruder, so it is difficult to determine the errors in the predicted pressure profiles in this section. It is difficult to measure melt pressures with transducers in regions where melt and solid coexist because of the danger of the solid polymer granules damaging the very sensitive diaphragm at the transducer tip.

The infinite channel width approximation affects not only the predicted pressure profiles in the channel but also the contribution of viscous dissipation to the temperature rise in the melt. When the effects of the channel sides are ignored, it is assumed that the shear rate at the walls are the same as at the centre of the flow channel. Shear rates at the channel sides are, however, much higher than at the centre and consequently the temperature rise due to viscous dissipation is underestimated. This may be the reason why the predicted bulk temperature in the adapter does not rise with increasing screw speed to the same extent as does the measured melt temperature (see Figs. 12.3 and 12.4).

Another factor not considered in the development of temperature in the down channel direction is the contribution of the melt entering the melt pool from the thin film between the solid bed and barrel surface. Due to the high shear rates in this melt film and its close proximity to the heated barrel, the temperature of the melt entering the melt pool is higher than the bulk temperature in the pool. Although this is a significant factor, it was not incorporated into the present model because serious numerical difficulties would have to be overcome.

The above shortcomings in the melt pumping model could be eliminated by solving the melt flow problem in three dimensions. Martin (68) obtained numerical solutions for fully-developed three directional flow in a rectangular channel as discussed in Sec. 6.1.3. To extend this to a developing flow solution in three dimensions, a phenomenal amount of computation time would be needed. Such a method cannot be justified at the present time. Another approach would be to develop non-Newtonian shape factors for both the pressure and bulk temperature profiles. This, however, is a very tedious and time consuming task, since new shape factors would have to be determined each time a different material is to be studied.

The melt flow model for the die section is similar to the model for the extruder screw channel, except that there are no moving boundaries and that the flow is in the down channel direction only. This simplifies the flow problem immensely, since we are now dealing with pure pressure flow. For the circular channels in the breaker plate and die, no shape factors are needed. In the adapter which has a rectangular flow channel, the use of non-Newtonian shape factors would be preferable. However, they are not used for the reasons stated previously. Newtonian shape factors are used instead. Since we are dealing with pure pressure flow and not combined drag and pressure flow, the use of Newtonian shape factors does not create the difficulties which occur in the extruder model for flow in the screw channel. In Figs. 12.1 and 12.2 it can be seen that small differences exist between the predicted and measured values of pressure in the adapter. This is due to the pressure drop which occurs across the screens in the breaker plate, but which has not been included in the extruder model. If the pressure drop across the screens were added to the model for the die section, then the predicted and measured values of pressure would be much closer.

Finally the model for extrudate swelling at the die exit is used to predict the increase in diameter of the extrudate emerging from the die. In Tables 12.3 and 12.4 it can be seen that for the LDPE (Union Carbide Canada Ltd., DFDY 4400) the predicted and measured values of extrudate swell are extremely close, whereas for the HDPE (DuPont Canada Inc., SCLAIR 19A) the agreement is not as good. A possible reason for the later is that when the HDPE emerges from a die it "freezes" much more quickly than does the LDPE, that is, the surface of the extrudate hardens before all of the stresses in the polymer have relaxed and the extrudate swell had reached its asymptotic value. For a thinner extrudate, such as emerging from the Instron capillary rheometer, the freezing will occur more quickly than for an extrudate emerging from the extruder die. Thus the extrudate swell predictions based on measurements on the rheometer for HDPE are lower than observed at the extruder die exit as seen in Table 12.4. A possible solution would be to anneal the extrudate sample from the rheometer or to extrude the sample into a hot silicon bath before measuring its diameter. The extrudate swell correlation (see Eq. 8.9 or 9.31) should also be tested on more polymers to check for its general applicability.

To summarize, a fully-predictive computer model consisting of six interdependent submodels has been developed for a single screw plasticating extruder. The model predictions have been verified with experimental runs on a 1 1/2 inch (38 mm) diameter extruder. It is possible to improve the overall extruder model by introducing refinements to the individual submodels as discussed above. However, these improvements can only be justified when better polymer property data have become available and when more measurements have been performed on the extruder to provide us with a better idea of what exactly is occurring in each of the subsections.

CHAPTER 13

CONCLUSIONS AND RECOMMENDATIONS

A fully-predictive computer model for a single screw plasticating extruder is developed to predict the mass flow rate of the polymer, pressure and temperature profiles along the extruder screw channel and die sections, and the extrudate swell at the die exit. In developing the extruder model a fundamental approach is taken. The simulations depend entirely on the material and rheological properties of the polymer, the screw geometry and dimensions, and the operating conditions of the extruder (i.e. screw speed and barrel temperature profile). The model predictions are not modified on the basis of temperature or pressure measurements performed on the extruder. Any size of extruder or screw design within reasonable limits can be simulated with the present computer model.

The extruder model consists of six distinct and interdependent sections. Included in the overall model are: (i) a model for the feed hopper, (ii) models for the solids conveying, melting and melt conveying zones in the extruder screw channel, (iii) a model for the melt flow in the die section and (iv) a prediction of the extrudate swell at the die exit. For the solids flow in the feed hopper and the extruder screw channel, existing models reported in the literature have been utilized and put to work. For the melting zone, Tadmor's melting model has been modified and a new method of solution has been developed. A finite difference solution has been developed to describe the non-Newtonian nonisothermal developing melt flow in the screw channel and die section. A temperature and shear rate dependent viscosity relation is utilized in the melt flow models. Viscosity measurements were performed on the Instron capillary rheometer for each of the polymers studied. Finally, a correlation developed from extrudate swell theory for capillary viscometers has been used to predict the swelling of the extrudate emerging from the extruder die. The predictive correlation also incorporates extrudate swell measurements from the Instron capillary rheometer.

The extruder model predictions and experimental results are compared for both high- and low-density polyethylene resins processed in a 1 1/2 inch (38 mm) diameter, 24:1 length to diameter ratio, single screw extruder with a 3/16 inch (4.76 mm) diameter cylindrical rod die. Experimental measurements include mass flow rate of the polymer, melt pressures in the extruder screw channel and in the adapter, melt temperature in the adapter, and extrudate swell at the die exit for several frequencies of screw rotation. However, no melt temperatures along the extruder screw channel are measured and no cooling experiments (see Sec. 2.3) are performed to determine the solid bed profile in the screw channel. For each of the polymers studied, it is seen that the model predictions are very representative of the overall extruder performance. Mass flow rate predictions and measurements vary by 1 to 3 percent for LDPE and 1 to 7 percent for HDPE; melt pressure predictions and measurments differ by 12 to 25 percent for LDPE and 19 to 27 percent for HDPE; melt temperature predictions and measurements for the adapter differ by 0.7 to 1.6 ^{O}C for LDPE and 0.3 to 5.1 ^{O}C for HDPE; extrudate swell predictions and measurements differ by 2 percent for LDPE and 10 percent for HDPE. Additional measurements of melt pressure, temperature and solid bed profile would be very useful in further evaluating the extruder model predictions.

Several steps may be taken in the future to reduce the difference between the model predictions and experimental measurements. These include possible improvements to the extruder model and the utilization of more accurate polymer property data. It may be possible in the future to improve the present computer model by introducing improvements to the individual submodels, especially for the solids conveying and melting sections. However, to improve these submodels we need more direct experimental evidence on what exactly happens in these subsections. Such information is not available presently. It should be noted that each time a modification is introduced to an individual submodel, the computation time requirement for the overall model may be increased significantly. The additional computation time required is a key factor to be considered when evaluating possible improvements to the individual submodels. In the present extruder model the best available polymer property data are used. However, it is shown in this study that small changes in the values of some properties such as the dynamic coefficients of friction of the polymer solid have a significant effect on the predicted performance of the extruder. Improved methods in determining these properties are a necessary step to obtaining better predictions from the extruder model.

In the development of the present extruder model an emphasis is placed on the extrusion of low- and high-density polyethylene resins. When the extrusion of other polymers such as polypropylene, polyvinyl chloride, polycarbonate or nylon is considered, it is expected that some adjustments may be necessary in the extruder model, especially with respect to the solids flow and melting mechanisms of the polymer. Due to the modular structure of the present extruder model, such changes to the individual submodels can be easily implemented.

In conclusion, several areas of further study may be considered. It is recognized that the effectiveness of any process simulation depends on the accuracy of the input data to the process model. To ensure an adequate level of polymer property data required in the overall extruder model, measurement techniques for the various polymer material properties should be further investigated and simpler methods developed for determining such properties in the laboratory (as is already done for melt viscosity and extrudate swell). Also, more measurements of pressure, temperature and solid bed profile should be carried out on extruders of varying size and design and for different types of polymers so that the present as well as more sophisticated models for the different subsections can be evaluated. These areas of investigation would form only a small fraction of the ongoing work in polymer research to better understand the mechanisms and processes involved in polymer extrusion.

REFERENCES

1. Agur, E.E., Heat Transfer in Polymer Melt Flows. M.Eng. thesis, McMaster University (1978).

2. Agur, E.E., "A Computer Program for a Single Screw Plasticating Extruder", Department of Chemical Engineering, McMaster University (1982).

3. Agur, E.E. and Vlachopoulos, J., "Heat Transfer to Molten Polymer Flow in Tubes", J. Appl. Polym. Sci., 26, 765 (1981).

4. Bagley, E.B., "End Corrections in the Capillary Flow of Polyethylene", J. Appl. Phys., 28, 624 (1957).

5. Bernhardt, E.C., "Calculating Extruder Performance", Mod. Plast., 32, 127 (1955).

6. Bernhardt, E.C., ed., Processing of Thermoplastic Materials, Chap. 4. Reinhold, New York (1959). (a) pp. 184-186.

7. Bird, R.B., Stewart, W.E. and Lightfoot, E.N., Transport Phenomena. Wiley, New York (1960).

8. Booy, M.L., Influence of Channel Curvature on Flow, Pressure Distribution, and Power Requirements of Screw Pumps and Melt Extruders", SPE Trans., 3, 176 (1963).

9. Boussinesq, M.J., "Sur l'Influence des Frottements dans les Mouvements Reguliers des Fluids", Journal de Mathematique Pures et Appliques, Series 2, 13, 377 (1868).

10. Broyer, E. and Tadmor, Z., "Solids Conveying in Screw Extruders: Part I. A Modified Isothermal Model", Polym. Eng. Sci., 12, 12 (1972).

11. Carley, J.F., Mallouk, R.S. and McKelvey, J.M., "Simplified Flow Theory for Screw Extruders" from the "Symposium on the Theory of Plastics Extrusion", Ind. Eng. Chem., 45, 974 (1953).

12. Carley, J.F. and McKelvey, J.M., "Extruder Scale-up Theory and Experiments", from the "Symposium on the Theory of Plastics Extrusion", Ind. Eng. Chem., 45, 989 (1953).

13. Carley, J.F. and Strub, R.A., "Basic Concepts of Extrusion" from the "Symposium on the Theory of Plastics Extrusion", Ind. Eng. Chem., 45, 970 (1953).

14. Carley, J.F. and Strub, R.A., "Application of Theory to Design of Screw Extruders", from the "Symposium on the Theory of Plastics Extrusion", Ind. Eng. Chem., 45, 978 (1953).

15. Choo, K.P., Hami, M.L. and Pittman, J.F.T., "Deep Channel Operating Characteristics of a Single Screw Extruder: Finite Element Predictions and Experimental Results for Isothermal Non-Newtonian Flow", Polym. Eng. Sci., 21, 100 (1981).

16. Choo, K.P., Neelakantan, N.R. and Pittman, J.F.T., "Experimental Deep-Channel Velocity Profiles and Operating Characteristics for a Single-Screw Extruder", Polym. Eng. Sci., 20, 349 (1980). ibid., 20, 982 (1980).

17. Chung, C.I., "A new theory for single-screw extrusion. Part 1 and Part 2", Mod. Plast., 45, 178 (September 1968); 45, 110 (December 1968).

18. Chung, C.I., "New Ideas About Solids Conveying in Screw Extruders", SPE J., 26, 32 (May 1970).

19. Colwell, R.E. and Nickolls, K.R., "The Screw Extruder", Ind. Eng. Chem., 51, 841 (1959).

20. Darnell, W.H. and Mol, E.A.J., "Solids Conveying in Extruders", SPE J., 12, 20 (April 1956).

21. DeHaven, E.S., "Extruder Design for a Pseudoplastic Fluid", Ind. Eng. Chem., 51, 813 (1959). Also Chemical Engineering Conference, Montreal, April 23, 1958.

22. Denn, M.M., Process Fluid Mechanics. Prentice-Hall, Englewood Cliffs, N.J., (1980). pp. 361-362.

23. Donovan, R.C., "A Theoretical Melting Model for Plasticating Extruders", Polym. Eng. Sci., 11, 247 (1971).

24. Dyer, D.F., "A Numerical Solution for the Single-Screw Extrusion of a Polymer Melt", AIChE J., 15, 823 (1969).

25. Eccher, S. and Valentinotti, A., "Experimental Determination of Velocity Profiles in an Extruder Screw", Ind. Eng. Chem., 50, 829 (1958).

26. Edmondson, I.R., Ph.D. thesis, London University (1973).

27. Edmondson, I.R. and Fenner, R.T., "Melting of thermoplastics in single screw extruders", Polymer, 16, 49 (1975).

28. Fenner, R.T., Extruder Screw Design. Iliffe, London (1970). (a) p.12, (b) pp. 68–71, (c) pp. 42–67, (d) pp.71–73.

29. Fenner, R.T., "The Design of Large Hot Melt Extruders", Polymer, 16, 298 (1975).

30. Fenner, R.T., "Developments in the Analysis of Steady Screw Extrusion of Polymers", Polymer, 18, 617 (1977).

31. Fenner, R.T. and Williams, J.G., "Some Experiments on Polymer Melt Flow in Single Screw Extruders", J. Mech. Eng. Sci., 13, 65 (1971).

32. Ferry, J.D., Viscoelastic Properties of Polymers. Wiley-Interscience, New York, 2nd. ed., (1970).

33. Gerald, C.F., Applied Numerical Analysis. Addison-Wesley, Reading, Mass., 2nd. ed., (1978). (a) pp. 400–406, (b) pp. 406–411.

34. Glyde, B.S. and Holmes-Walker, W.A., "Screw Extrusion of Thermoplastics", Int. Plast. Eng., 2, 338 (1962).

35. Gore, W.L., "Principles of Plastics Screw Extrusion", SPE J., 9, 6 (March 1953).

36. Griffith, R.M., "Fully Developed Flow in Screw Extruders", Ind. Eng. Chem. Fund., 1, 180 (1962).

37. Halmos, A.L., Pearson, J.R.A. and Trottnow, R., "Melting in single screw extruders. III. Solutions for a power law temperature-dependent viscous melt", Polymer, 19, 1199 (1978).

38. Hami, M.L. and Pittman, J.F.T., "Finite Element Solutions for Flow in a Single-Screw Extruder, Including Curvature Effects", Polym. Eng. Sci., 20, 339 (1980). ibid., 20, 983 (1980).

39. Han, C.D., "On Intrinsic Errors in Pressure-Hole Measurments in Flow of Polymer Melts", AIChE J., 18, 116 (1972).

40. Han, C.D., Rheology in Polymer Processing. Academic Press, New York (1976). pp. 117–118.

41. Hinrichs, D.R. and Lilleleht, L.U., "A Modified Melting Model for Plastifying Extruders", Polym. Eng. Sci., 10, 268 (1970).

42. Huang, D.C. and White, J.L., "Extrudate Swell from Slit and Capillary Dies: An Experimental and Theoretical Study", Polym. Eng. Sci., 19, 609 (1979).

43. Huxtable, J., Cogswell, F.N. and Wriggles, J.D. "Polymer-metal friction as relevant to processing", Plast. Rub. Proc. Appl., 1, 87 (1981).

44. Jacobi, H.R., Screw Extrusion of Plastics. Illife, London (1963).

45. Janssen, H.A., "Tests on Grain Pressure Silos", Z. Vereinschr. Dtsch. Ing., 39 (35), 1045 (1895).

46. Jepson, C.H., "Future Extrusion Studies", from the "Symposium on the Theory of Plastics Extrusion", Ind. Eng. Chem., 45, 992 (1953).

47. Kacir, L. and Tadmor, Z., "Solids Conveying in the Screw Extruder. Part III. The Delay Zone", Polym. Eng. Sci., 12, 307 (1972).

48. Kaiser, H. and Smith, C.W., "Prediction of Flow of a Melted Plastic Through a Screw Extruder", J. Basic Eng., Trans. ASME (D), 91, 479 (1969).

49. Kaufman, M., The History of PVC. MacLaren and Sons Ltd., London (1969), pp. 140-155. Also "The birth of the plastics extruder", Plast. Polym., 37, 243 (1969).

50. Kaye, A., "Non-Newtonian Flow in Incompressible Fluids", COA Note No. 134, The College of Aeronautics Cranfield, Bletchley, England (1962), and Bernstein, B., Kearsley, E. and Zapas, L., "A Study of Stress Relaxation with Finite Strain", Trans. Soc. Rheol., 7, 391 (1963).

51. Klein, I. and Marshall, D.I., "Fundamentals of Plasticating Extrusion. III. Development of a Mathematical Model", Polym. Eng. Sci., 6, 198 (1966).

52. Klein, I. and Marshall, D.I., eds. Computer Programs for Plastics Engineers, Chaps. 6.1 and 6.2. Reinhold, New York (1968).

53. Kovarik, Z.V. and Davison, T.M.K. (Department of Mathematical Sciences, McMaster University), private communications (1980).

54. Kroesser, F.W. and Middleman, S., "The Calculation of Screw Characteristics for the Extrusion of non-Newtonian Melts", Polym. Eng. Sci., 5, 230 (1965).

55. Lapidus, L., Digital Computation for Chemical Engineers. cGraw-Hill, New York (1962). pp. 254-255.

56. Lindt, J.T., "A Dynamic Model for Single Screw Extruders", Polym. Eng. Sci., 16, 284 (1976).

57. Lodge, A.S., Elastic Liquids. Academic Press, New York (1964). p. 131.

58. Lovegrove, J.G.A. and Williams, J.G., "Solids Conveying in a Single Screw Extruder; The Role of Gravity Forces", J. Mech. Eng. Sci., 15, 114 (1973).

59. Lovegrove, J.G.A. and Williams, J.G., "Solids Conveying in a Single Screw Extruder; A Comparison of Theory and Experiment", J. Mech. Eng. Sci., 15, 195 (1973).

60. Lovegrove, J.G.A. and Williams, J.G., "Pressure Generation Mechanism in the Feed Section of Screw Extruders", Polym. Eng. Sci., 14, 589 (1974).

61. Maddock, B.H., "Fundamental Mechanisms in Polyethylene Extrusion-Part I", SPE J., 12, 49 (October 1956).

62. Maddock, B.H., "How to Predict Extruder Performance with Polyethylene", Plast. Tech., 3, 385 (1957).

63. Maddock, B.H., "A Visual Analysis of Flow and Mixing in Screw Extruders", SPE J., 15, 383 (1959). Also Soc. Plast. Engs. 15th ANTEC, 5, New York (January 1959).

64. Maillefer, C., "An Analytical Study of the Single Screw Extruder", Brit. Plast., 27, 394 (1954).

65. Mallouk, R.S. and McKelvey, J.M., "Power Requirements of Melt Extruders", from the "Symposium on the Theory of Plastics Extrusion", Ind. Eng. Chem., 45, 987 (1953).

66. Mangulis, V., Handbook of Series for Scientists and Engineers. Academic Press, New York (1965). (a) p.51, (b) p.25.

67. Marshall, D.I. and Klein, I., "Fundamentals of Plasticating Extrusion. II. Experiments", Polym. Eng. Sci., 6, 191 (1966).

68. Martin, B., Numerical Studies of Steady State Extrusion Processes. Ph.D. thesis, Cambridge University (1969).

69. Martin, B., "Theoretical Aspects of Screw Extruder Design", Plast. Polym., 38, 113 (1970).

70. Martin, B., Pearson, J.R.A. and Yates, B., "On Screw Extrusion. Part I. Steady Flow Calculations", Report No. 5, Cambridge University (1969).

71. McKelvey, J.M., "Experimental Studies of Melt Extrusion" from the "Symposium on the Theory of Plastics Extrusion", Ind. Eng. Chem., 45, 982 (1953).

72. McKelvey, J.M., "Theory of Adiabatic Extruder Operation", Ind. Eng. Chem., 46, 660 (1954).

73. McKelvey, J.M., Polymer Processing. Wiley, New York (1962). (a) pp. 265-272.

74. McKelvey, J.M. and Bernhardt, E.C., "Adiabatic Extrusion of Polyethylene", SPE J., 10, 22 (March 1954).

75. Meskat, W., "Theory of the Flow of Materials in Worm Machines, Part I", Kunststoffe, 45, 87 (1955).

76. Metzner, A.B., White, J.L. and Denn, M.M., "Behavior of viscoelastic materials in short time processes", Chem. Eng. Prog., 62, No. 12, 81 (December 1966).

77. Middleman, S., "Flow of Power Law Fluids in Rectangular Ducts", Trans. Soc. Rheol., 9, 83 (1965).

78. Middleman, S., Fundamentals of Polymer Processing. McGraw-Hill, New York (1977). (a) pp. 183-184, (b) pp. 464-465.

79. Middleman, S. and Gavis, J., "Expansion and Contraction of Capillary Jets of Newtonian Liquids", Phys. Fluids, 4, 355 (1961).

80. Mohr, W.D., Clap, J.B. and Starr, F.C., "Flow Patterns in a Non Newtonian Fluid in a Single-Screw Extruder", SPE Trans., 1, 113 (1961).

81. Mohr, W.D., Saxton, R.L. and Jepson, C.H., "Theory of Mixing in the Single-Screw Extruder", Ind. Eng. Chem., 49, 1857 (1957).

82. Mohr, W.D., Squires, P.H. and Starr, F.C., "Flow Patterns in a Single-Screw Extruder", SPE J., 16, 1015 (1960).

83. Mori, Y. and Matsumoto, T.K., "Analytical Study of Plastics Extrusion", Rheol. Acta, 1, 240 (1958).

84. Narkis, M. and Ram, A., "Extrusion Discharge Rate Equations for Non-Newtonian Fluids", Polym. Eng. Sci., 7, 161 (1967).

85. Nebrensky, J., Pittman, J.F.T. and Smith, J.M., "Flow and Heat Transfer in Screw Extruders: I. A Variational Analysis Applied in Helical Coordinates", Polym. Eng. Sci., 13, 209 (1973).

86. Oda, K., White, J.L. and Clark, E.S., "Correlation of Normal Stresses in Polystyrene Melts and Its Implications", Polym. Eng. Sci., 18, 25 (1978).

87. Palit, K. and Fenner, R.T., "Finite Element Analysis of Slow Non-Newtonian Channel Flow", AIChE J., 18, 628 (1972).

88. Palit, K. and Fenner, R.T., "Finite Element Analysis of Two-Dimensional Slow Non-Newtonian Flows", AIChE J., 18, 1163 (1972).

89. Pearson, J.R.A., Mechanical Principles of Polymer Melt Processing. Pergamon Press, Oxford (1966). (a) pp. 60-63.

90. Pearson, J.R.A. (W.R. Schowalter, ed.), "Heat Transfer Effects in Flowing Polymers", Prog. Heat Mass Transfer, Vol. 5, p. 73. Pergamon Press, Oxford (1972).

91. Pearson, J.R.A. and Trottnow, R., "On Die Swell: Some Theoretical Results", J. Non-Newtonian Fluid Mech., 4, 195 (1978).

92. Phuoc, H.B. and Tanner, R.I., "Thermally - induced extrudate swell", J. Fluid Mech., 98, 253 (1980). Also 1st. Nat. Conf. Rheol., Melbourne, Australia (1979).

93. Pigott, W.T., "Pressures Developed by Viscous Materials in the Screw Extrusion Machine", Trans. ASME, 73, 947 (1951).

94. Poon, S.Y., "The Flow of a Power-Law Fluid in a Melt-Fed Single Screw Extruder", J. Fluid. Eng., Trans. ASME, 81 (1973).

95. Rabinowitsch, B., Z. Physik-Chemie, A145, 1 (1929).

96. Racin, R. and Bogue, D.C., "Molecular Weight Effects in Die Swell and in Shear Rheology", J. Rheol., 23, 263 (1979).

97. Rowell, H.S. and Finlayson, D., "Screw Viscosity Pumps", Engineering, 114, 606 (1922); 126, 249 (1928).

98. Sackett, R.D., "Viscosity Data for Extruder Flow Equations", SPE J., 12, 32 (October 1956).

99. Schenkel, G. (L.A.H. Eastman, trans.), Plastics Extrusion Technology and Theory. Iliffe, London (1966). (a) pp. 1-6.

100. Schneider, K., "Technical Report on Plastics Processing - Processes in the Feeding Zone of an Extruder", Institute of Plastics Processing (IKV), Aachen (1969).

101. Semjonow, V., "Pressure Dependence of the Viscosity of Some Polyolefin Melts", Rheol. Acta, 4, No. 2, 133 (1965).

102. Shapiro, J., Melting in Plasticating Extruders. Ph.D. thesis, Cambridge University (1973).

103. Shapiro, J., Halmos, A.L. and Pearson, J.R.A., "Melting in single screw extruders. I. The mathematical model. II. Solution for a Newtonian fluid", Polymer, 17, 905 (1976).

104. Squires, P.H., "Screw-Extruder Pumping Efficiency", SPE J., 14, 24 (May 1958).

105. Street, L.F., "Plastifying Extrusion", Int. Plast. Eng., 1, 289 (1961).

106. Strub, R.A., "The Theory of Screw Extruders", Proc. Second Midwestern Conference on Fluid Mechanics, pp. 481-494. Ohio State University (1952).

107. Tadmor, Z., "Fundamentals of Plasticating Extrusion. I. A Theoretical Model for Melting", Polym. Eng. Sci., 6, 185 (1966).

108. Tadmor, Z., "Non-Newtonian Tangential Flow in Cylindrical Annuli", Polym. Eng. Sci., 6, 203 (1966).

109. Tadmor, Z., Private communication (1981).

110. Tadmor, Z. and Broyer, E., "Solids Conveying in Screw Extruders. Part II. Non Isothermal Model", Polym. Eng. Sci., 12, 378 (1972).

111. Tadmor, Z., Duvdevani, I.J. and Klein, I., "Melting in Plasticating Extruders. Theory and Experiments", Polym. Eng. Sci., 7, 198 (1967).

112. Tadmor, Z. and Gogos, C.G., Principles of Polymer Processing. Wiley-Interscience, New York (1979). (a) pp. 1-3, (b) p. 486, (c) p.154, (d) pp. 253-256, (e) pp. 486-491, (f) pp. 525-527, (g) pp. 176-178, (h) pp. 491-492.

113. Tadmor, Z. and Klein, I., "The Effect of Design and Operating Conditions on Melting in Plasticating Extruders", Polym. Eng. Sci., 9, 1 (1969).

114. Tadmor, Z. and Klein, I., Engineering Principles of Plasticating Extrusion. Reinhold, New York (1970). (a) p.2, (b) pp. 40-41, (c) pp.45-46, (d) pp. 52-54, (e) p. 154, (f) pp. 55-63, (g) pp. 129-130, (h) pp. 146-153, (i) pp.164-182, (j) pp. 107-124, (k) p.132, (l) pp. 133-143, (m) pp 308-329, (n) p. 156.

115. Tanner, R.I., "A Theory of Die-Swell", J. Polym. Sci., A-2, 8, 2067 (1970)

116. Tanner, R.I., "Die-Swell Reconsidered: Some Numerical Solutions Using a Finite Element Program", Appl. Polym. Symp., 20, 201 (1973).

117. Tanner, R.I., "A New Inelastic Theory of Extrudate Swell", J. Non-Newtonian Fluid Mech., 6, 289 (1980).

118. Truesdell, C., The Elements of Continuum Mechanics. p. 18, Springer-Verlag, New York (1966).

119. Tung, T.T. and Laurence, R.L., "A Coordinate Frame for Helical Flows", Polym. Eng. Sci., 15, 401 (1975).

120. Vermeulen, J.R., Scargo, P.G. and Beek, W.G., "The melting of a crystalline polymer in a screw extruder", Chem. Eng. Sci., 26, 1457 (1971).

121. Vlachopoulos, J., "Extrudate Swell in Polymers", Rev. Def. Beh. Mat., 3 (4), 219 (1981).

122. Vlachopoulos, J. and Hrymak, A.N., "Calendering Poly (Vinyl Chloride): Theory and Experiments", Polym. Eng. Sci., 20, 725 (1980).

123. Walker, D.M., "An Approximate Theory for Pressures and Arching in Hoppers", Chem. Eng. Sci., 21, 975 (1966).

124. Weeks, D.J. and Allen, W.J., "Screw Extrusion of Plastics", J. Mech. Eng. Sci., 4, 380 (1962).

125. White, J.L., "Considerations of Unconstrained Elastic Recovery in Viscoelastic Fluids", Trans. Soc. Rheol., 19, 271 (1975).

126. White, J.L. and Roman, J.T., "Extrudate Swell During the Melt Spinning of Fibers - Influence of Rheological Properties and Take-up Force", J. Appl. Polym. Sci., 20, 1005 (1976). ibid., 21, 869 (1977).

127. Winter, H.H., "Temperature-Induced Pressure Gradient in the Clearance Between Screw Flight and Barrel of a Single Screw Extruder", Polym. Eng. Sci., 20, 406 (1980). Also Soc. Plast. Engs. 37th ANTEC, 25, 170, New Orleans, Louisiana (May 1979).

128. Yates, B., Temperature Development in Single - Screw Extruders. Ph.D. thesis, Cambridge University (1968).

129. Zamodits, H.J., Extrusion of Thermoplastics. Ph.D. thesis, University of Cambridge (1964).

130. Zamodits, H.J. and Pearson, J.R.A., "Flow of Polymer Melts in Extruders. Part I. The Effect of Transverse Flow and of a Superposed Steady Temperature Profile", Trans. Soc. Rheol., 13, 357 (1969).

APPENDIX A

SHAPE FACTOR IDENTITIES

The analytical expressions for the Newtonian shape factors F_d and F_p for pure drag and pure pressure flows are given respectively as (104):

$$F_d\left(\frac{H}{W}\right) = \frac{16W}{H\pi^3} \sum_{n=1,3,\ldots}^{\infty} \frac{1}{n^3} \tanh\left(\frac{n\pi H}{2W}\right) \tag{A.1}$$

$$F_p\left(\frac{H}{W}\right) = 1 - 192\,\frac{H}{W\pi^5} \sum_{n=1,3,\ldots}^{\infty} \frac{1}{n^5} \tanh\left(\frac{n\pi W}{2H}\right) \tag{A.2}$$

where H and W are respectively the channel depth and width. Shape factors for various channel espect ratios (H/W) are given in Table A.1 where it can be seen that the following identities hold:

$$F_d\left(\frac{H}{W}\right) = 1 - F_d\left(\frac{W}{H}\right) \tag{A.3}$$

$$F_p\left(\frac{H}{W}\right) = \left(\frac{W}{H}\right)^2 F_p\left(\frac{W}{H}\right) \tag{A.4}$$

These identities have not been realized by anyone else prior to this study. In this appendix proofs for the above identities for drag and pressure flow shape factors are presented.

<u>Drag Flow</u>

The proof given below for the identity in Eq. A.3 is due to Kovarik and Davison (53).

Table A.1 Shape factors for drag and pressure flow in a rectangular channel.

	H/W				
	0.20	0.50	1.0	2.0	5.0
F_d	0.891447	0.729584	0.499999	0.270415	0.108551
F_p	0.873950	0.686045	0.421731	0.171511	0.034958

Theorem

If $f(x) = \frac{16}{\pi^3 x} \sum_{n=1,3,\ldots}^{\infty} \frac{1}{n^3} \tanh\left(\frac{n\pi x}{2}\right)$

$$= \frac{16}{\pi^3 x} \sum_{n=0}^{\infty} \frac{1}{(2n+1)^3} \tanh\left[\frac{(2n+1)\ \pi x}{2}\right]$$

then $f(x) + f\left(\frac{1}{x}\right) = 1$ for $x \in R$

where $x = \frac{H}{W}$

Proof

The series is absolutely convergent for real x since each term is dominated by:

$$\sum_{n=0}^{\infty} \frac{1}{(2n+1)^2} = \frac{\pi^2}{8}$$ (see Ref. (66a), Formula A.b.3)

Since $\tanh z = 2z \sum_{k=0}^{\infty} \frac{1}{\frac{(2k+1)^2\pi^2}{4} + z^2}$ (see Ref. (66b), Formula 7.6)

then $\tanh\left[\frac{(2n+1)\ \pi x}{2}\right] = \frac{4x}{\pi}(2n+1) \sum_{k=0}^{\infty} \frac{1}{(2k+1)^2+(2n+1)^2\ x^2}$

$$f(x) = \frac{16}{\pi^3 x} \sum_{n=0}^{\infty} \frac{1}{(2n+1)^3} \tanh\left[\frac{(2n+1)\ \pi x}{2}\right]$$

$$= \frac{64}{\pi^4} \sum_{n=0}^{\infty} \sum_{k=0}^{\infty} \frac{1}{(2n+1)^2} \frac{1}{(2k+1)^2+(2n+1)^2 x^2}$$

$$f(\tfrac{1}{x}) = \frac{64}{\pi^4} \sum_{n=0}^{\infty} \sum_{k=0}^{\infty} \frac{1}{(2n+1)^2} \frac{1}{(2k+1)^2+(2n+1)^2/x^2}$$

$$= \frac{64}{\pi^4} \sum_{n=0}^{\infty} \sum_{k=0}^{\infty} \frac{1}{(2n+1)^2} \frac{x^2}{(2k+1)^2 x^2+(2n+1)^2}$$

$$= \frac{64}{\pi^4} \sum_{n=0}^{\infty} \sum_{k=0}^{\infty} \frac{1}{(2k+1)^2} \frac{x^2}{(2n+1)^2 x^2+(2k+1)^2}$$

$$f(x) + f(\tfrac{1}{x}) = \frac{64}{\pi^4} \sum_{n=0}^{\infty} \sum_{k=0}^{\infty} [\frac{1}{(2n+1)^2} \frac{1}{(2k+1)^2+(2n+1)^2 x^2}$$

$$+ \frac{1}{(2k+1)^2} \frac{x^2}{(2n+1)^2 x^2+ (2k+1)^2}]$$

$$= \frac{64}{\pi^4} \sum_{n=0}^{\infty} \sum_{k=0}^{\infty} [\frac{1}{(2n+1)^2} + \frac{x^2}{(2k+1)^2}][\frac{1}{(2k+1)^2+(2n+1)^2 x^2}]$$

$$= \frac{64}{\pi^4} \sum_{n=0}^{\infty} \sum_{k=0}^{\infty} \frac{1}{(2n+1)^2 (2k+1)^2}$$

$$= \frac{64}{\pi^4} \cdot \frac{\pi^2}{8} \cdot \frac{\pi^2}{8} = 1 \qquad \text{Q.E.D.}$$

Pressure Flow

The identity given in Eq. A.4 was suggested by Tadmor (109) and the proof given below is similar to the one for drag flow.

Theorem

$$\text{If } f(x) = 1 - \frac{192x}{\pi^5} \sum_{n=1,3,\dots}^{\infty} \frac{1}{n^5} \tanh\left(\frac{n\pi}{2x}\right)$$

$$= 1 - \frac{192x}{\pi^5} \sum_{n=0}^{\infty} \frac{1}{(2n+1)^5} \tanh\left[\frac{(2n+1)\,\pi}{2x}\right]$$

$$\text{then } f(x) = \frac{1}{x^2} f\left(\frac{1}{x}\right) \qquad \text{for } x \in R$$

$$\text{where } x = \frac{H}{W}$$

Proof

The series is absolutely convergent for real x since each term is dominated by:

$$\sum_{n=0}^{\infty} \frac{1}{(2n+1)^2} \doteq \frac{\pi^2}{8} \qquad \text{(see Ref. (66b), Formulas A.b.3 and A.b.5)}$$

and

$$\sum_{n=0}^{\infty} \frac{1}{(2n+1)^4} = \frac{\pi^4}{96}$$

$$\text{Since} \qquad \tanh z = 2z \sum_{k=0}^{\infty} \frac{1}{\frac{(2k+1)^2\pi^2}{4} + z^2}$$

then $$\tanh\left[\frac{(2n+1)\pi}{2x}\right] = \frac{4nx}{\pi}\sum_{k=0}^{\infty}\frac{1}{(2k+1)^2x^2 + (2n+1)^2}$$

$$f(x) = 1 - \frac{192x}{\pi^5}\sum_{n=0}^{\infty}\frac{1}{(2n+1)^5}\tanh\left[\frac{(2n+1)\pi}{2x}\right]$$

$$= 1 - \frac{768x^2}{\pi^6}\sum_{n=0}^{\infty}\sum_{k=0}^{\infty}\frac{1}{(2n+1)^4}\,\frac{1}{(2k+1)^2x^2 + (2n+1)^2}$$

$$f\left(\frac{1}{x}\right) = 1 - \frac{768}{\pi^6 x^2}\sum_{n=0}^{\infty}\sum_{k=0}^{\infty}\frac{1}{(2n+1)^4}\,\frac{1}{(2k+1)^2/x^2 + (2n+1)^2}$$

$$= 1 - \frac{768}{\pi^6}\sum_{n=0}^{\infty}\sum_{k=0}^{\infty}\frac{1}{(2n+1)^4}\,\frac{1}{(2k+1)^2 + (2n+1)^2x^2}$$

$$\frac{1}{x^2}f\left(\frac{1}{x}\right) = \frac{1}{x^2} - \frac{768}{\pi^6 x^2}\sum_{n=0}^{\infty}\sum_{k=0}^{\infty}\frac{1}{(2n+1)^4}\,\frac{1}{(2k+1)^2 + (2n+1)^2x^2}$$

$$= \frac{1}{x^2} - \frac{768}{\pi^6 x^2}\sum_{n=0}^{\infty}\sum_{k=0}^{\infty}\frac{1}{(2k+1)^4}\,\frac{1}{(2n+1)^2 + (2k+1)^2x^2}$$

Write $$f(x) = \frac{1}{x^2}f\left(\frac{1}{x}\right)$$

$$1 - \frac{768x^2}{\pi^6}\sum_{n=0}^{\infty}\sum_{k=0}^{\infty}\frac{1}{(2n+1)^4}\,\frac{1}{(2k+1)^2x^2 + (2n+1)^2}$$

$$= \frac{1}{x^2} - \frac{768}{\pi^6 x^2}\sum_{n=0}^{\infty}\sum_{k=0}^{\infty}\frac{1}{(2k+1)^4}\,\frac{1}{(2k+1)^2x^2 + (2n+1)^2}$$

$$1 - \frac{1}{x^2} = \frac{768}{\pi^6} \sum_{n=0}^{\infty} \sum_{k=0}^{\infty} \left[\frac{x^2}{(2n+1)^4} - \frac{1}{x^2(2k+1)^4}\right]\left[\frac{1}{(2k+1)^2x^2 + (2n+1)^2}\right]$$

$$= \frac{768}{\pi^6} \sum_{n=0}^{\infty} \sum_{k=0}^{\infty} \left[\frac{x^4(2k+1)^4 - (2n+1)^4}{(2n+1)^4(2k+1)^4\ x^2}\right]\left[\frac{1}{(2k+1)^2x^2 + (2n+1)^2}\right]$$

$$= \frac{768}{\pi^6} \sum_{n=0}^{\infty} \sum_{k=0}^{\infty} \frac{x^2(2k+1)^2 - (2n+1)^2}{(2n+1)^4(2k+1)^4\ x^2}$$

$$= \frac{768}{\pi^6} \sum_{n=0}^{\infty} \sum_{k=0}^{\infty} \frac{1}{(2n+1)^4(2k+1)^2}$$

$$- \frac{768}{\pi^6} \sum_{n=0}^{\infty} \sum_{k=0}^{\infty} \frac{1}{(2n+1)^2(2k+1)^4\ x^2}$$

$$= \frac{768}{\pi^6} \sum_{n=0}^{\infty} \sum_{k=0}^{\infty} \frac{1}{(2n+1)^4(2k+1)^2}$$

$$- \frac{768}{\pi^6} \sum_{n=0}^{\infty} \sum_{k=0}^{\infty} \frac{1}{(2k+1)^2(2n+1)^4\ x^2}$$

$$= \frac{768}{\pi^6} \sum_{n=0}^{\infty} \sum_{k=0}^{\infty} \frac{1}{(2n+1)^4(2k+1)^2} \left(1 - \frac{1}{x^2}\right)$$

$$= \frac{768}{\pi^6} \cdot \frac{\pi^4}{96} \cdot \frac{\pi^2}{8} \left(1 - \frac{1}{x^2}\right)$$

$$= 1 - \frac{1}{x^2}$$

Q.E.D.

APPENDIX B

CALCULATION OF THE FLOW-AVERAGE (BULK) TEMPERATURE

In developing flow situations it is common to represent the temperature field at a given distance in the down channel direction by some average temperature. The flow-average (bulk) temperature which represents the temperature of the fluid if it were well mixed is given as follows:

$$T_{bulk,z} = \frac{\int_0^H v_z(y,z)\, T(y,z)\, dy}{\int_0^H v_z(y,z)\, dy} \tag{B.1}$$

where $v_z(y,z)$ and $T(y,z)$ are the down channel velocity and temperature profiles at a given location z in the flow channel and H is the channel depth.

In some regions of melt flow in the screw channel, a fraction of the down channel velocity profile may be negative as shown in Fig. B.1. For such a velocity profile, Eq. B.1 can result in a poor representation of the average temperature especially when the flow rate in the negative direction approaches that in the positive direction. For this situation it is preferable to define the bulk temperature as:

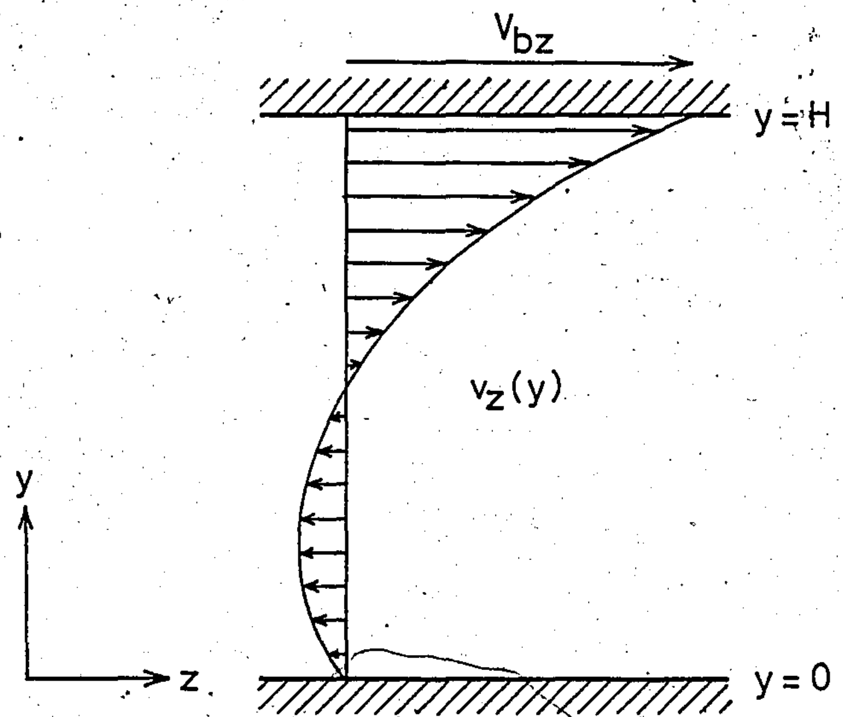

Fig. B.1 Down channel velocity profile showing "backflow". V_{bz} is the down channel component of the barrel velocity and H is the screw channel depth.

$$T_{bulk,z} = \frac{\int_0^H \left| v_z(y,z) \right| T(y,z)\, dy}{\int_0^H \left| v_z(y,z) \right| dy} \qquad (B.2)$$

In Eq. B.2 the bulk temperature depends not on the direction of flow but only on the magnitude of the down channel velocities and temperatures at various points in the y-direction. It is possible to use other forms of average temperature as alternatives to the form given in Eq. B.2. One such representation is the area-average (or volume-average) temperature which is defined as:

$$T_{avg,z} = \frac{1}{H} \int_0^H T(y,z)\, dy \qquad (B.3)$$

The direction (or magnitude, for that matter) of the down channel velocities do not affect the value of T_{avg} in Eq. B.3.

The bulk temperatures (Eq. B.2) and area-average temperatures (Eq. B.3) are compared in Figs. B.2, B.3 and B.4 for typical flow conditions in the feed, compression and metering sections of a screw extruder (see App G.3 for polymer properties and processing conditions). In the feed section where there are some negative velocities (see inset in Fig. B.2), the area-average temperature is considerably lower than the bulk temperature. In the metering section where all the velocities are positive (see inset in Fig. B.4), the area-average and bulk temperatures are almost indentical. However, no conclusions should be drawn from this, since for different temperature boundary conditions the above

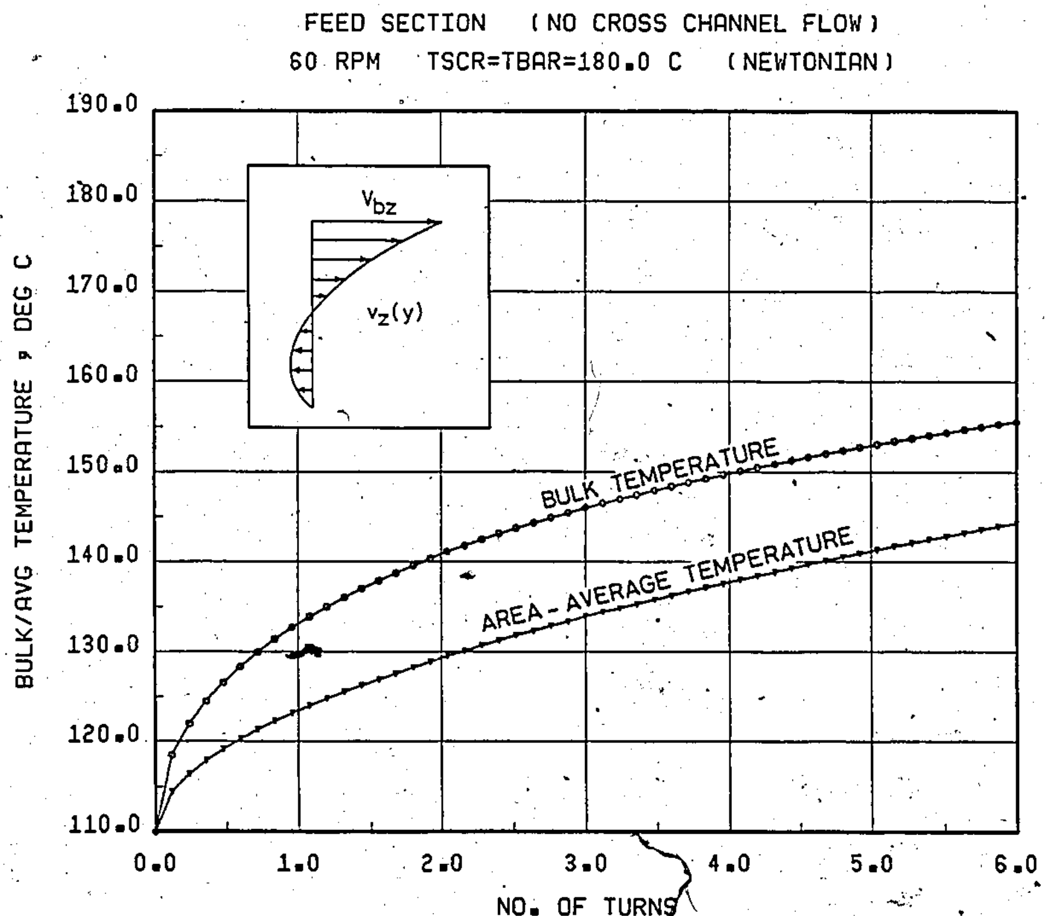

Fig. B.2 Comparison of bulk temperature and area-average temperature profiles for the feed section of an extruder. Polymer properties, screw channel dimensions and extruder operating conditions are given in App. G.4. Velocity profile is shown in inset.

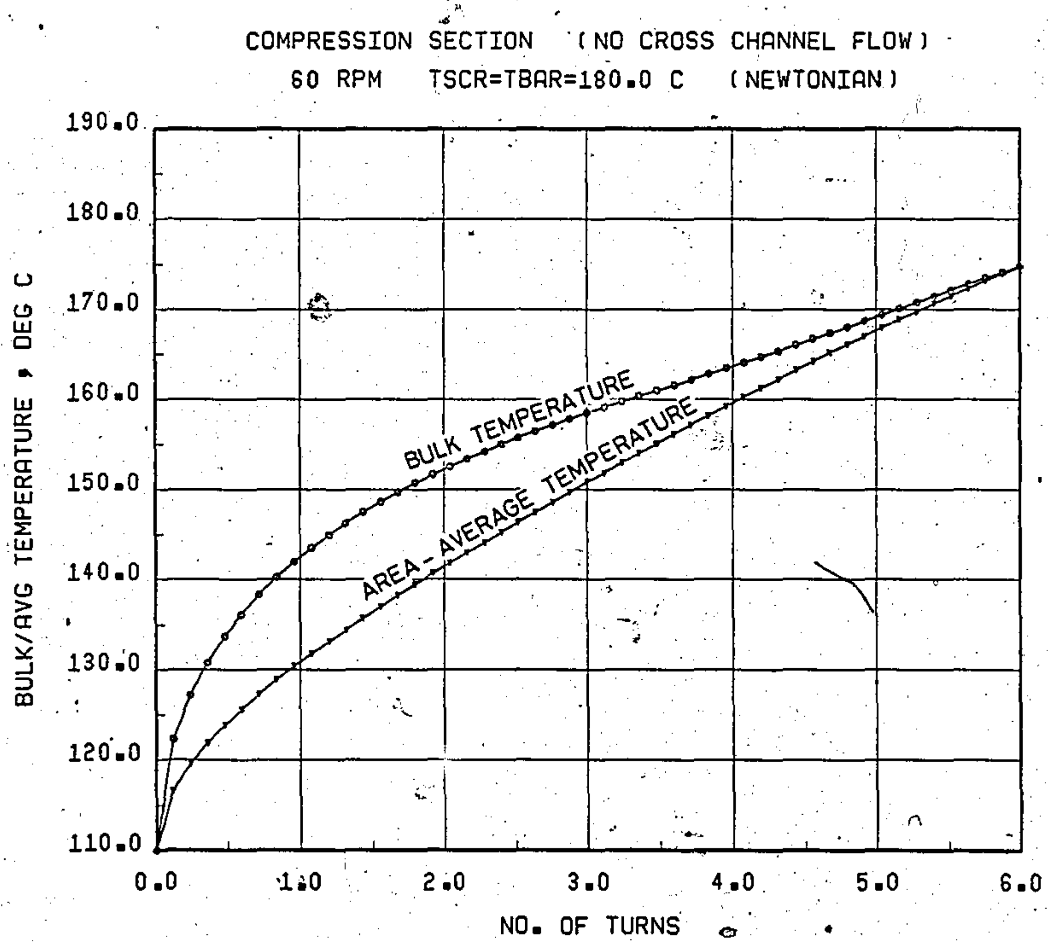

Fig. B.3 Comparison of bulk temperature and area-average temperature profiles for the compression section of an extruder. Polymer properties, screw channel dimensions and extruder operating conditions are given in App. G.4.

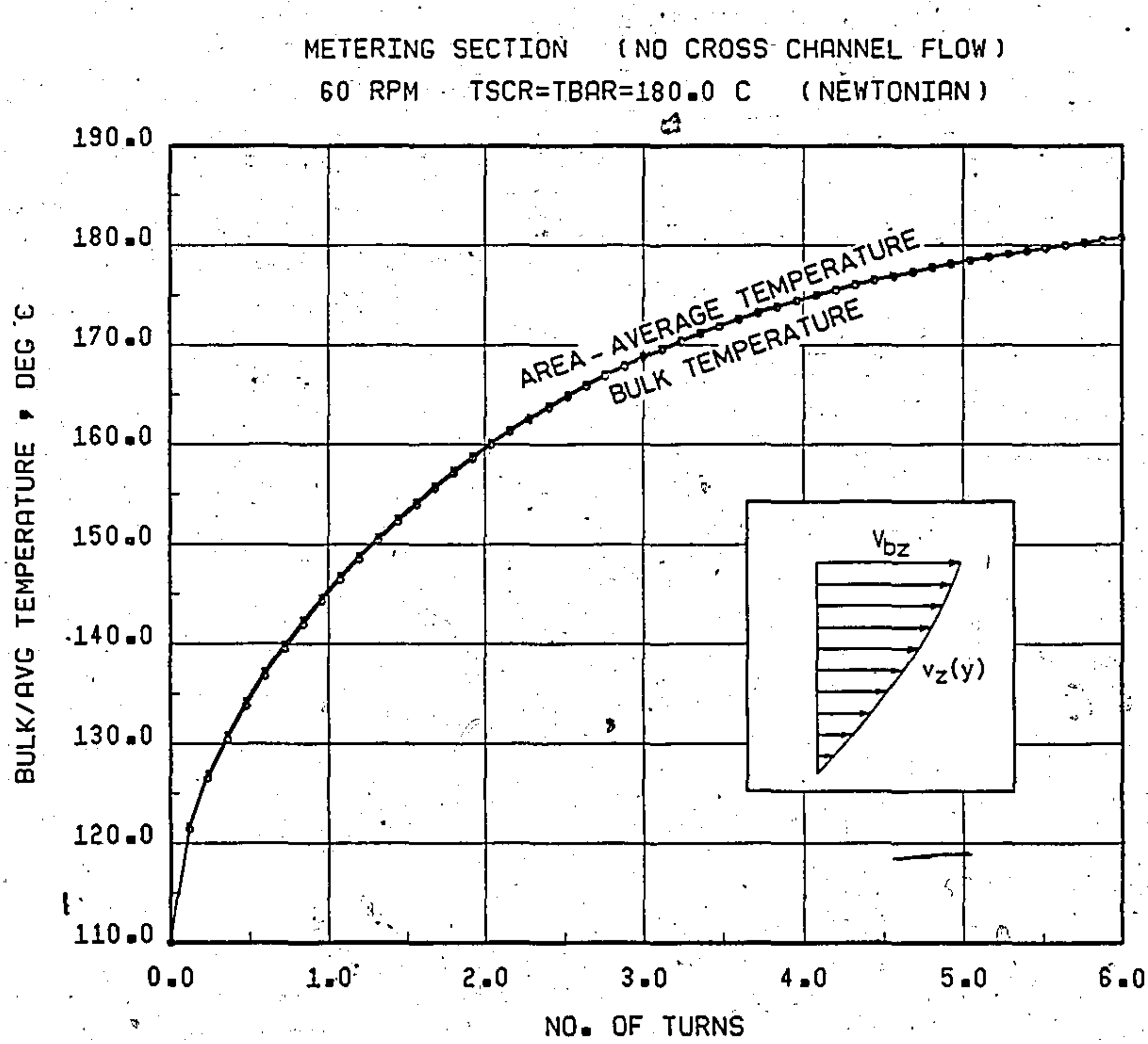

Fig. B.4 Comparison of bulk temperature and area-average temperature profiles for the metering section of an extruder. Polymer properties, screw channel dimensions and extruder operating conditions are given in App. G.4. Velocity profile is shown in inset.

trend is not necessarily the same.

Finally it should be noted that full temperature profiles are calculated in the extruder screw channel, and that these calculations are not affected by any choice of an average temperature. Thus, there is no problem of a fundamental nature in representing the temperature field by an average value. The choice of an appropriate form of average temperature is just a matter of deciding which average value will hopefully be close to the one measured by a thermocouple placed in the flow channel. Using this criterion, it is concluded that the flow-average (bulk) temperature (Eq. B.2) is a better representation of the average temperature in the extruder screw channel than is the area-average (or volume-average) temperature (Eq. B.3).

APPENDIX C

SUMMARY OF FINITE DIFFERENCE EQUATIONS IN THE

NON-NEWTONIAN NONISOTHERMAL DEVELOPING FLOW MODEL

FOR THE EXTRUDER SCREW CHANNEL

C.1 Feed Section

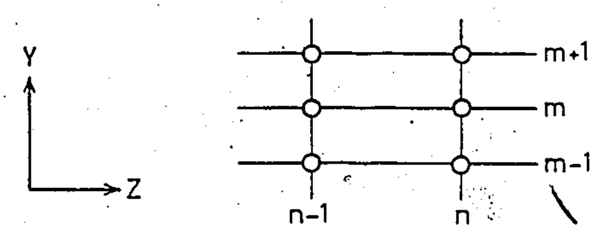

Fig. C.1 Finite difference grid for the feed section

Continuity Equation (integrated form) in X-direction

$$\int_0^1 Vx \, dY = 0 \tag{C.1}$$

Momentum Equation in X-direction

$$-\frac{k_m}{Cp_m}\frac{\partial P}{\partial X} + \eta\frac{\partial^2 Vx}{\partial Y^2} + \frac{\partial \eta}{\partial Y}\frac{\partial Vx}{\partial Y} = 0 \tag{C.2}$$

Finite difference equations:

$$(-\beta_2+1)\,\overset{0}{\cancel{Vx_{1,n}}} - 2Vx_{2,n} + (\beta_2+1)\,Vx_{3,n} - \alpha_2 \left(\frac{\partial P}{\partial X}\right)_n = 0$$

$$\vdots$$

$$(-\beta_m+1)\,Vx_{m-1,n} - 2Vx_{m,n} + (\beta_m+1)\,Vx_{m+1,n} - \alpha_m \left(\frac{\partial P}{\partial X}\right)_n = 0$$

$$\vdots \tag{C.3}$$

$$(-\beta_M+1)\,Vx_{M-1,n} - 2Vx_{M,n} + (\beta_M+1)\,\overset{V_{bx}/V_b}{\cancel{Vx_{M+1,n}}} - \alpha_M \left(\frac{\partial P}{\partial X}\right)_n = 0$$

$$\overset{0}{\cancel{Vx_{1,n}}} + 4Vx_{2,n} + 2Vx_{3,n} + \ldots + 4Vx_{M,n} + \overset{V_{bx}/V_b}{\cancel{Vx_{M+1,n}}} = 0$$

where $\alpha_m = \dfrac{k_m}{\eta_{m,n}\,Cp_m}\,(\Delta Y)^2$

$$\beta_m = \frac{\Delta Y}{2\,\eta_{m,n}} \left(\frac{\partial \eta}{\partial Y}\right)_{m,n}$$

<u>Continuity Equation (integrated form) in Z-direction</u>

$$\int_0^1 Vz\ dY = \frac{Q}{W_f\,H_o\,V_b} \tag{C.4}$$

where W_f and H_o are respectively the channel width and depth in the feed section.

<u>Momentum Equation in Z-direction</u>

$$-\frac{k_m}{Cp_m}\frac{\partial P}{\partial Z} + \eta\,\frac{\partial^2 Vz}{\partial Y^2} + \frac{\partial \eta}{\partial Y}\frac{\partial Vz}{\partial Y} = 0 \tag{C.5}$$

Finite difference quations:

$$
\begin{aligned}
&(-\beta_2+1)\,\overset{0}{\cancel{Vz_{1,n}}} - 2Vz_{2,n} + (\beta_2+1)\,Vz_{3,n} - \alpha_2\left(\frac{\partial P}{\partial Z}\right)_n = 0\\
&\qquad\vdots\\
&(-\beta_m+1)\,Vz_{m-1,n} - 2Vz_{m,n} + (\beta_m+1)\,Vz_{m+1,n} - \alpha_m\left(\frac{\partial P}{\partial Z}\right)_n = 0\\
&\qquad\vdots\\
&(-\beta_M+1)\,Vz_{M-1,n} - 2Vz_{M,n} + (\beta_M+1)\,\overset{V_{bz}/V_b}{\cancel{Vz_{M+1,n}}} - \alpha_M\left(\frac{\partial P}{\partial Z}\right)_n = 0
\end{aligned}
\qquad (C.6)
$$

$$
\overset{0}{\cancel{Vz_{1,n}}} + 4Vz_{2,n} + 2Vz_{3,n} + \ldots + 4Vz_{M,n} + \overset{V_{bz}/V_b}{\cancel{Vz_{M+1,n}}} = 3M\,\frac{Q}{WH_n V_b}
$$

where $\alpha_m = \dfrac{k_m}{\eta_{m,n} Cp_m}\,(\Delta Y)^2$

$\beta_m = \dfrac{\Delta Y}{2\,\eta_{m,n}}\left(\dfrac{\partial \eta}{\partial Y}\right)_{m,n}$

Energy equation

$$
Vz\,\frac{\partial \theta}{\partial Z} = \frac{\partial^2 \theta}{\partial Y^2} + \frac{\eta\, V_b^{\,2}}{k_m\, T_{melt}}\left[\left(\frac{\partial Vx}{\partial Y}\right)^2 + \left(\frac{\partial Vz}{\partial Y}\right)^2\right] \qquad (C.7)
$$

Finite difference equations:

$$-\theta_{1,n} + (\beta+2)\,\theta_{2,n} - \theta_{3,n} = A_{2,n-1} + \gamma_2$$

$$\vdots$$

$$-\theta_{m-1,n} + (\beta+2)\,\theta_{m,n} - \theta_{m+1,n} = A_{m,n-1} + \gamma_m \qquad (C.8)$$

$$\vdots$$

$$-\theta_{M-1,n} + (\beta+2)\,\theta_{M,n} - \theta_{M+1,n} = A_{M,n-1} + \gamma_M$$

where $A_{m,n-1} = \theta_{m-1,n-1} + (\beta-2)\,\theta_{m,n-1} + \theta_{m+1,n-1}$

$$\beta = \frac{2(\Delta Y)^2}{\Delta Z}\, Vz_{avg,n}$$

$$\gamma_m = 2(\Delta Y)^2 \frac{\eta_{m,n} V_b^{\,2}}{k_m T_{melt}} \left[\left(\frac{\partial Vx}{\partial Y}\right)^2_{m,n} + \left(\frac{\partial Vz}{\partial Y}\right)^2_{m,n} \right]$$

C.2 Compression Section

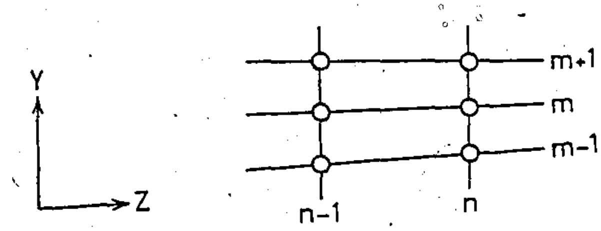

Fig. C.2 Finite difference grid for the compression section.

Continuity Equation (integrated form) in X-direction

$$\int_0^1 Vx \, dY = 0 \qquad \text{(C.9)}$$

Momentum Equation in X-direction

$$-\frac{k_m}{Cp_m \, H_o^{\,2}} \frac{\partial P}{\partial X} + \frac{1}{H^2} \left[\eta \frac{\partial^2 Vx}{\partial Y^2} + \frac{\partial \eta}{\partial Y} \frac{\partial Vx}{\partial Y} \right] = 0 \qquad \text{(C.10)}$$

Finite difference equations:

$$(-\beta_2+1) \cancelto{0}{Vx_{1,n}} - 2Vx_{2,n} + (\beta_2+1)\, Vx_{3,n} - \alpha_2 \left(\frac{\partial P}{\partial X}\right)_{n*} = B_{2,n-1}$$

$$\vdots$$

$$(-\beta_m+1)\, Vx_{m-1,n} - 2Vx_{m,n} + (\beta_m+1)\, Vx_{m+1,n} - \alpha_m \left(\frac{\partial P}{\partial X}\right)_{n*} = B_{m,n-1}$$

$$\vdots \qquad \text{(C.11)}$$

$$(-\beta_M+1)\, Vx_{M-1,n} - 2Vx_{M,n} + (\beta_M+1) \cancelto{V_{bx}/V_b}{Vx_{M+1,n}} - \alpha_M \left(\frac{\partial P}{\partial X}\right)_{n*} = B_{M,n-1}$$

$$\cancelto{0}{Vx_{1,n}} + 4Vx_{2,n} + 2Vx_{3,n} + \ldots + 4Vx_{M,n} + \cancelto{V_{bx}/V_b}{Vx_{M+1,n}} = 0$$

where $B_{m,n-1} = (\varepsilon\beta_m-\delta)\, Vx_{m-1,n-1} + 2\delta Vx_{m,n-1} - (\varepsilon\beta_m+\delta)\, Vx_{m+1,n-1}$

$$\alpha_m = 2(\Delta Y)^2 \frac{k_m}{Cp_m \, \eta_{m,n*}} \left(\frac{H_n}{H_o}\right)^2$$

$$\beta_m = \frac{\Delta Y}{\eta_{m,n*}} \left(\frac{\partial \eta}{\partial Y}\right)_{m,n*} \left(\frac{\varepsilon}{\varepsilon+1}\right)$$

$$\delta = \left(\frac{H_n}{H_{n-1}}\right)^2$$

$$\varepsilon = \frac{H_n}{H_{n-1}}$$

The shear rate $\dot{\gamma}_{m,n*}$ used in the calculation of the viscosity $\eta_{m,n*}$ is given by:

$$\dot{\gamma}_{m,n*} = \sqrt{\frac{1}{2}\left[\left(\frac{\partial v_x}{\partial y}\right)^2_{m,n} + \left(\frac{\partial v_x}{\partial y}\right)^2_{m,n-1}\right] + \frac{1}{2}\left[\left(\frac{\partial v_z}{\partial y}\right)^2_{m,n} + \left(\frac{\partial v_z}{\partial y}\right)^2_{m,n-1}\right]} \tag{C.12}$$

Continuity Equation (integrated form) in Z-direction

$$\int_0^1 Vz \, dY = \frac{Q}{W_c \cdot H \; V_b} \tag{C.13}$$

where W_c and H are respectively the local channel width and depth in the compression section.

Momentum Equation in Z-direction

$$-\frac{k_m}{Cp_m \; H_o^2} \frac{\partial P}{\partial Z} + \frac{1}{H^2}\left[\eta \frac{\partial^2 Vz}{\partial Y^2} + \frac{\partial \eta}{\partial Y} \frac{\partial Vz}{\partial Y}\right] = 0 \tag{C.14}$$

Finite difference equations:

$$(-\beta_2+1)\cancelto{0}{Vz_{1,n}} - 2Vz_{2,n} + (\beta_2+1)\,Vz_{3,n} - \alpha_2\left(\frac{\partial P}{\partial Z}\right)_{n*} = C_{2,n-1}$$

$$\vdots$$

$$(-\beta_m+1)\,Vz_{m-1,n} - 2Vz_{m,n} + (\beta_m+1)\,Vz_{m+1,n} - \alpha_m\left(\frac{\partial P}{\partial Z}\right)_{n*} = C_{m,n-1}$$

$$\vdots \tag{C.15}$$

$$(-\beta_M+1)\,Vz_{M-1,n} - 2Vz_{M,n} + (\beta_M+1)\cancelto{V_{bz}/V_b}{Vz_{M+1,n}} - \alpha_M\left(\frac{\partial P}{\partial Z}\right)_{n*} = C_{M,n-1}$$

$$\cancelto{0}{Vz_{1,n}} + 4Vz_{2,n} + 2Vz_{3,n} + \ldots + 4Vz_{M,n} + \cancelto{V_{bz}/V_b}{Vz_{M+1,n}} = 3M\,\frac{Q}{WH_n\,V_b}$$

where $\quad C_{m,n-1} = (\varepsilon\beta_m-\delta)\,Vz_{m-1,n-1} + 2\delta Vz_{m,n-1} - (\varepsilon\beta_m+\delta)\,Vz_{m+1,n-1}$

$$\alpha_m = 2(\Delta Y)^2\,\frac{k_m}{Cp_m\,\eta_{m,n*}}\left(\frac{H_n}{H_o}\right)^2$$

$$\beta_m = \frac{\Delta Y}{\eta_{m,n*}}\left(\frac{\partial\eta}{\partial Y}\right)_{m,n*}\left(\frac{\varepsilon}{\varepsilon+1}\right)$$

$$\delta = \left(\frac{H_n}{H_{n-1}}\right)^2$$

$$\varepsilon = \frac{H_n}{H_{n-1}}$$

Energy Equation

$$\frac{1}{H_o^{\,2}}\,Vz\,\frac{\partial\theta}{\partial Z} = \frac{1}{H^2}\,\frac{\partial^2\theta}{\partial Y^2} + \frac{\eta\,V_b^{\,2}}{k_m T_{melt}}\,\frac{1}{H^2}\left[\left(\frac{\partial Vx}{\partial Y}\right)^2 + \left(\frac{\partial Vz}{\partial Y}\right)^2\right] \tag{C.16}$$

Finite difference equations:

$$\overset{\theta_{sc}}{\cancel{-\theta_{1,n}}} + (\beta+2)\,\theta_{2,n} - \theta_{3,n} = D_{2,n-1} + \gamma_2$$

$$\vdots$$

$$-\theta_{m-1,n} + (\beta+2)\,\theta_{m,n} - \theta_{m+1,n} = D_{m,n-1} + \gamma_m \qquad (C.17)$$

$$\vdots$$

$$-\theta_{M-1,n} + (\beta+2)\,\theta_{M,n} - \overset{\theta_b}{\cancel{\theta_{M+1,n}}} = D_{M,n-1} + \gamma_M$$

where $D_{m,n-1} = \delta\theta_{m-1,n-1} + (\beta-2\delta)\,\theta_{m,n-1} + \delta\theta_{m+1,n-1}$

$$\beta = \frac{(\Delta Y)^2}{\Delta Z}\left(\frac{H_n}{H_o}\right)^2 (Vz_{avg,n} + Vz_{avg,n-1})$$

$$\delta = \left(\frac{H_n}{H_{n-1}}\right)^2$$

$$\gamma_m = \frac{(\Delta Y)^2\,\eta_{m,n*}}{k_m\,T_{melt}}\left[\left(\frac{\partial Vx}{\partial Y}\right)^2_{m,n} + \left(\frac{\partial Vz}{\partial Y}\right)^2_{m,n} + \delta\left(\frac{\partial Vx}{\partial Y}\right)^2_{m,n-1} + \delta\left(\frac{\partial Vz}{\partial Y}\right)^2_{m,n-1}\right]$$

C.3 Metering Section

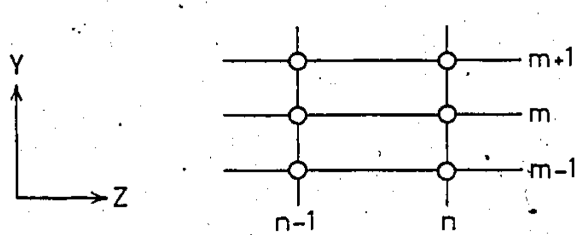

Fig. C.3 Finite difference grid for the metering section.

Continuity Equation (integrated form) in X-direction

$$\int_0^1 Vx \, dY = 0 \tag{C.18}$$

Momentum Equation in X-direction

$$-\frac{k_m}{Cp_m}\left(\frac{H_{ex}}{H_o}\right)^2 \frac{\partial P}{\partial X} + \eta \frac{\partial^2 Vx}{\partial Y^2} + \frac{\partial \eta}{\partial Y}\frac{\partial Vx}{\partial Y} = 0 \tag{C.19}$$

Finite difference equations:

$$\begin{aligned}
&(-\beta_2+1)\,\overset{0}{\cancel{Vx_{1,n}}} - 2Vx_{2,n} + (\beta_2+1)\,Vx_{3,n} - \alpha_2 \left(\frac{\partial P}{\partial X}\right)_n = 0 \\
&\qquad\vdots \\
&(-\beta_m+1)\,Vx_{m-1,n} - 2Vx_{m,n} + (\beta_m+1)\,Vx_{m+1,n} - \alpha_m \left(\frac{\partial P}{\partial X}\right)_n = 0 \\
&\qquad\vdots \\
&(-\beta_M+1)\,Vx_{M-1,n} - 2Vx_{M,n} + (\beta_M+1)\,\overset{V_{bx}/V_b}{\cancel{Vx_{M+1,n}}} - \alpha_M \left(\frac{\partial P}{\partial X}\right)_n = 0
\end{aligned} \tag{C.20}$$

$$\overset{0}{\cancel{Vx_{1,n}}} + 4Vx_{2,n} + 2Vx_{3,n} + \dots + 4Vx_{M,n} + \overset{V_{bx}/V_b}{\cancel{Vx_{M+1,n}}} = 0$$

where $$\alpha_m = \frac{k_m}{Cp_m\,\eta_{m,n}}\left(\frac{H_{ex}}{H_o}\right)^2 (\Delta Y)^2$$

$$\beta_m = \frac{\Delta Y}{2\,\eta_{m,n}}\left(\frac{\partial \eta}{\partial Y}\right)_{m,n}$$

<u>Continuity Equation (integrated form) in Z-direction</u>

$$\int_0^1 Vz \, dY = \frac{Q}{W_m H_{ex} V_b} \tag{C.21}$$

where W_m and H_{ex} are respectively the channel width and depth in the metering section.

<u>Momentum Equation in Z-direction</u>

$$-\frac{k_m}{Cp_m} \left(\frac{H_{ex}}{H_o}\right)^2 \frac{\partial P}{\partial Z} + \eta \frac{\partial^2 Vz}{\partial Y^2} + \frac{\partial \eta}{\partial Y} \frac{\partial Vz}{\partial Y} = 0 \tag{C.22}$$

Finite difference equations:

$$(-\beta_2+1) \overset{0}{\cancel{Vz_{1,n}}} - 2Vz_{2,n} + (\beta_2+1) Vz_{3,n} - \alpha_2 \left(\frac{\partial P}{\partial Z}\right)_n = 0$$

$$\vdots$$

$$(-\beta_m+1) Vz_{m-1,n} - 2Vz_{m,n} + (\beta_m+1) Vz_{m+1,n} - \alpha_m \left(\frac{\partial P}{\partial Z}\right)_n = 0$$

$$\vdots$$

$$(-\beta_M+1) Vz_{M-1,n} - 2Vz_{M,n} + (\beta_M+1) \overset{V_{bz}/V_b}{\cancel{Vz_{M+1,n}}} - \alpha_M \left(\frac{\partial P}{\partial Z}\right)_n = 0 \tag{C.23}$$

$$\overset{0}{\cancel{Vz_{1,n}}} + 4Vz_{2,n} + 2Vz_{3,n} + \dots + 4Vz_{M,n} + \overset{V_{bz}/V_b}{\cancel{Vz_{M+1,n}}} = 3M \frac{Q}{W_m H_{ex} V_b}$$

where $\alpha_m = \dfrac{k_m}{Cp_m \, \eta_{m,n}} \left(\dfrac{H_{ex}}{H_o}\right)^2 (\Delta Y)^2$

$\beta_m = \dfrac{\Delta Y}{2 \, \eta_{m,n}} \left(\dfrac{\partial \eta}{\partial Y}\right)_{m,n}$

Energy Equation

$$\left(\frac{H_{ex}}{H_o}\right)^2 Vz \frac{\partial\theta}{\partial Z} = \frac{\partial^2\theta}{\partial Y^2} + \frac{\eta\, V_b^{\,2}}{K_m\, T_{melt}} \left[\left(\frac{\partial Vx}{\partial Y}\right)^2 + \left(\frac{\partial Vz}{\partial Y}\right)^2\right] \qquad \text{(C.24)}$$

Finite difference equations:

$$-\overset{\theta_{sc}}{\theta_{1,n}} + (\beta+2)\,\theta_{2,n} - \theta_{3,n} = E_{2,n-1} + \gamma_2$$

$$\vdots$$

$$-\theta_{m-1,n} + (\beta+2)\,\theta_{m,n} - \theta_{m+1,n} = E_{m,n-1} + \gamma_m \qquad \text{(C.25)}$$

$$\vdots$$

$$-\theta_{M-1,n} + (\beta+2)\,\theta_{M,n} - \overset{\theta_b}{\theta_{M+1,n}} = E_{M,n-1} + \gamma_M$$

where $\quad E_{m,n-1} = \theta_{m-1,n-1} + (\beta-2)\,\theta_{m,n-1} + \theta_{m+1,n-1}$

$$\beta = \frac{2(\Delta Y)^2}{\Delta Z} \left(\frac{H_{ex}}{H_o}\right)^2 Vz_{avg,n}$$

$$\gamma_m = 2(\Delta Y)^2 \frac{\eta_{m,n} V_b^{\,2}}{k_m T_{melt}} \left[\left(\frac{\partial Vx}{\partial Y}\right)^2_{m,n} + \left(\frac{\partial Vz}{\partial Y}\right)^2_{m,n}\right]$$

APPENDIX D

DERIVATION OF TANNER'S EXTRUDATE SWELL EQUATION

In 1970 Tanner (115) published a paper on extrudate swell and showed that for an extrudate emerging from a capillary of diameter D the extrudate swell d/D is given by:

$$\frac{d}{D} = \left[1 + \frac{1}{2}\left(\frac{N_{1,w}}{2\tau_w}\right)^2\right]^{1/6} \tag{D.1}$$

where $N_{1,w} = (\tau_{11} - \tau_{22})_w$

= first normal stress difference at the wall

τ_w = shear stress at the wall.

Versions of Tanner's theory have been presented by White et al. (42,125,126) and Pearson and Trottnow (91). A recent review by Vlachopoulos (121) summarizes many other works on this subject as well as the experimental results up to 1980.

In this appendix a detailed derivation of Tanner's equation is presented. While Tanner started from the elastic recovery of a KBKZ fluid,[1] a Maxwellian type constitutive equation along with simple assumptions are used here. The results are shown to be identical to those of Tanner.

---

[1] Kaye-Bernstein-Kearsley-Zapas fluid (50).

Basic Assumptions

We have a long capillary as shown in Fig. D.1. The flow is of Poiseuille type (pressure flow) in the capillary. Thus we have simple shear flow. At the exit all constraints are suddenly removed and the stress is brought instantaneously to zero. The swelling due to instantaneous recovery will be determined.

Constitutive Equation

$$\overline{\overline{\sigma}} = -p\overline{\overline{I}} + \int_0^\infty m(s)\, \underline{\underline{C}}^{-1}\, ds \qquad (D.2)$$

where $\overline{\overline{\sigma}}$ = stress tensor

p = pressure

$$\overline{\overline{I}} = \begin{bmatrix} 1 & 0 & 0 \\ 0 & 1 & 0 \\ 0 & 0 & 1 \end{bmatrix}$$

$m(s)$ = suitable memory function

$\overline{\overline{C}}$ = Cauchy strain tensor

$$\left(C_{ij} = \frac{\partial x_i}{\partial x_m^t} \frac{\partial x_j}{\partial x_m^t} \right)$$

$\underline{\underline{C}}^{-1}$ = Finger strain tensor

$$\left(C_{ij}^{-1} = \frac{\partial x_i^t}{\partial x_m} \frac{\partial x_j^t}{\partial x_m} \right)$$

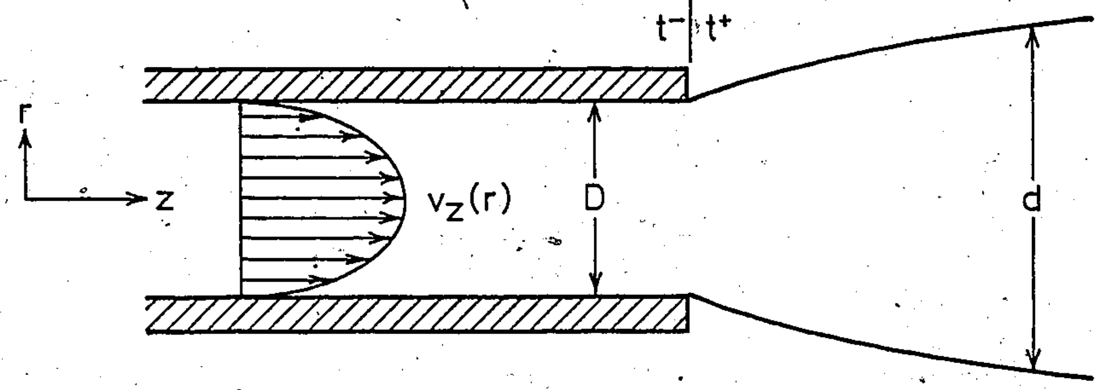

Fig. D.1 Physical system for Poiseuille flow at the exit of a capillary die.

x^t = present configuration (at time $\tau = t$)

x = past configuration

$s = \tau - t$

(Mathematical note: the repeated index m m signifies summation over m = 1,2,3.)

The following Maxwellian memory function is used:

$$m(s) = \frac{G}{\lambda} e^{-s/\lambda} \tag{D.3}$$

where G = modulus of elasticity

λ = relaxation time

Inside the Capillary

Inside the capillary we have simple shear flow. The coordinates of a material particle in axial flow must satisfy:

$$z^t = z + s\, v(r) = z + \dot{\gamma} r s \tag{D.4a}$$

$$r^t = r \tag{D.4b}$$

$$\theta^t = \theta$$

or in rectangular coordinates:

$$x_1^t = x_1 + \dot{\gamma}\, x_2 s \tag{D.5a}$$

$$x_2^t = x_2 \tag{D.5b}$$

$$x_3^t = x_3 \tag{D.5c}$$

Therefore, the components of the Finger strain tensor may be written as:

$$C_{11}^{-1} = \frac{\partial x_1^t}{\partial x_1}\frac{\partial x_1^t}{\partial x_1} + \frac{\partial x_1^t}{\partial x_2}\frac{\partial x_1^t}{\partial x_2} + \frac{\partial x_1^t}{\partial x_3}\frac{\partial x_1^t}{\partial x_3} = 1 + \dot{\gamma}^2 s^2$$

$$C_{12}^{-1} = \frac{\partial x_1^t}{\partial x_1}\frac{\partial x_2^t}{\partial x_1} + \frac{\partial x_1^t}{\partial x_2}\frac{\partial x_2^t}{\partial x_2} + \frac{\partial x_1^t}{\partial x_3}\frac{\partial x_2^t}{\partial x_3} = \dot{\gamma}s$$

$$C_{21}^{-1} = \dot{\gamma}s \tag{D.6}$$

$$C_{22}^{-1} = C_{33}^{-1} = 1$$

$$C_{13}^{-1} = C_{31}^{-1} = C_{23}^{-1} = C_{32}^{-1} = 0$$

Thus:

$$\underline{\underline{C}}^{-1} = \begin{bmatrix} 1 + \dot{\gamma}^2 s^2 & \dot{\gamma}s & 0 \\ \dot{\gamma}s & 1 & 0 \\ 0 & 0 & 1 \end{bmatrix} \tag{D.7}$$

Substitute $\underline{\underline{C}}^{-1}$ in Eq. D.7 into $\int_0^\infty m(s)\, \underline{\underline{C}}^{-1}\, dS$ and expand term-by-term:

$$\int_0^\infty \frac{G}{\lambda} e^{-s/\lambda} (1 + \dot{\gamma}^2 s^2)\, dS = G(1 + 2\, \dot{\gamma}^2 \lambda^2) \tag{D.8a}$$

$$\int_0^\infty \frac{G}{\lambda} e^{-s/\lambda}\, \dot{\gamma}s\, ds = G\, \dot{\gamma}\lambda \tag{D.8b}$$

$$\int_0^\infty \frac{G}{\lambda} e^{-s/\lambda} ds = G \tag{D.8c}$$

Thus:

$$\int_0^\infty m(s) \underline{\underline{C}}^{-1} ds = G \begin{bmatrix} 1 + 2\dot{\gamma}^2\lambda^2 & \dot{\gamma}\lambda & 0 \\ \dot{\gamma}\lambda & 1 & 0 \\ 0 & 0 & 1 \end{bmatrix} \tag{D.9}$$

For the material under consideration it is well known that:

$$\tau_{11} - \tau_{22} = N_1 = \frac{2\tau_{12}^2}{G} = 2\ G\ \lambda^2\ \dot{\gamma}^2 \tag{D.10}$$

Therefore, we may write:

$$\int_0^\infty m(s) \underline{\underline{C}}^{-1} ds = \begin{bmatrix} G + N_1 & \tau_{12} & 0 \\ \tau_{12} & G & 0 \\ 0 & 0 & G \end{bmatrix} \tag{D.11}$$

This means that viscometric stress conditions exist inside the capillary. (It should be noted that for this material the second normal stress difference $\tau_{22} - \tau_{33}$ equals 0.)

Supposition

The fluid has a viscometric history up to time t^-. Then a sudden strain occurs, followed by rigid body motion at time t^+. If we apply the material constitutive equation for the instant just after the jump, then we should have:

$$\overline{\overline{\sigma}} = - p\overline{\overline{I}} + \int_0^\infty m(s)\, \underline{\underline{C}}_o^{-1}\, ds \tag{D.12}$$

where

$$(C_o^{-1})_{ij} = \frac{\partial x_i^o}{\partial x_m} \frac{\partial x_j^o}{\partial x_m}$$

The subscript/superscript o refers to $t^+ = 0$ outside of the capillary. The only stress that might exist here would be σ_{zz} (or σ_{11} in terms of the present notation). Thus we have:

$$\sigma_{ij} + p\, \delta_{ij} = \int_0^\infty m(s)\, (C_o^{-1})_{ij}\, ds$$

$$= \int_0^\infty m(s) \frac{\partial x_i^o}{\partial x_m} \frac{\partial x_j^o}{\partial x_m}\, ds \tag{D.13}$$

Then, using the chain rule of differentiation, we obtain:

$$\sigma_{ij} + \rho\, \delta_{ij} = \int_0^\infty m(s) \frac{\partial x_i^o}{\partial x_k^t} \frac{\partial x_k^t}{\partial x_m} \frac{\partial x_j^o}{\partial x_n^t} \frac{\partial x_n^t}{\partial x_m}\, ds$$

$$= \int_0^\infty \left(\frac{\partial x_i^o}{\partial x_k^t} \frac{\partial x_j^o}{\partial x_n^t}\right) m(s) \frac{\partial x_k^t}{\partial x_m} \frac{\partial x_n^t}{\partial x_m}\, ds \tag{D.14}$$

Since the jump to a new state is sudden, the quantity $(\partial x_i^o/\partial x_k^t \cdot \partial x_j^o/\partial x_n^t)$ should be independent of time and can be taken outside of the integral:

$$\sigma_{ij} + p\ \delta_{ij} = \frac{\partial x_i^o}{\partial x_k^t} \frac{\partial x_j^o}{\partial x_n^t} \int_o^\infty m(s) \frac{\partial x_k^t}{\partial x_m} \frac{\partial x_n^t}{\partial x_m} ds \tag{D.15}$$

or

$$\frac{\partial x_k^t}{\partial x_i^o} (\sigma_{ij} + p\ \delta_{ij}) \frac{\partial x_n^t}{\partial x_j^o} = \int_o^\infty m(s) \frac{\partial x_k^t}{\partial x_m} \frac{\partial x_n^t}{\partial x_m} ds \tag{D.16}$$

Earlier it was stated that, just outside the capillary we have:

$$\bar{\bar{\sigma}} + p\bar{\bar{I}} = \begin{bmatrix} \sigma_{11} + p & 0 & 0 \\ 0 & p & 0 \\ 0 & 0 & p \end{bmatrix} \tag{D.17}$$

Thus

$$\sigma_{11} \frac{\partial x_1^t}{\partial x_1^o} \frac{\partial x_1^t}{\partial x_1^o} + \frac{\partial x_k^t}{\partial x_i^o} (p\ \delta_{ij}) \frac{\partial x_n^t}{\partial x_j^o} = \int_o^\infty m(s) \frac{\partial x_k^t}{\partial x_m} \frac{\partial x_n^t}{\partial x_m} ds \tag{D.18}$$

or

$$\sigma_{11} \frac{\partial x_1^t}{\partial x_1^o} \frac{\partial x_1^t}{\partial x_1^o} + p \frac{\partial x_k^t}{\partial x_j^o} \frac{\partial x_n^t}{\partial x_j^o} = \int_o^\infty m(s) \frac{\partial x_k^t}{\partial x_m} \frac{\partial x_n^t}{\partial x_m} ds \tag{D.19}$$

Here it should be noted that the right-hand side of Eq. D.19 represents the viscometric stress inside the capillary which has been already calculated (see Eqs. D.2 and D.11). Thus we have:

$$\sigma_{11} \frac{\partial x_1^t}{\partial x_1^o} \frac{\partial x_1^t}{\partial x_1^o} + p \frac{\partial x_k^t}{\partial x_j^o} \frac{\partial x_n^t}{\partial x_j^o} \Rightarrow \begin{bmatrix} G + N_1 & \tau_{12} & 0 \\ \tau_{12} & G & 0 \\ 0 & 0 & G \end{bmatrix} \tag{D.20}$$

Next, we must obtain a relationship for the left-hand side of Eq. D.20. According to Truesdell (118), the most general axisymmetrical (non-twisting) deformation possible in an incompressible solid rod is of the form (for volume preservation):

$$z^t = \frac{z^o}{\alpha^2} + g(r) \tag{D.21a}$$

$$r^t = \alpha r^o \tag{D.21b}$$

$$\theta^t = \theta^o \tag{D.21c}$$

where $1/\alpha$ = swell ratio of cylindrical rod

$g(r)$ = shearing deformation.

In Eqs. D.21a to D.21c, the left-hand side represents the solid configuration at time t^- (still inside the capillary whereas the right-hand side represents the solid configuration at time t^+ (just outside of the capillary). Equations D.21a to D.21c may be written in rectangular coordinates as follows:

$$x_1^t = \frac{x_1^o}{\alpha^2} + g(x_2) \tag{D.22a}$$

$$x_2^t = \alpha\, x_2^o \tag{D.22b}$$

$$x_3^t = \alpha\ x_3^o \tag{D.22c}$$

Calculate $\dfrac{\partial x_k^t}{\partial x_j^o}$:

$$\frac{\partial x_1^t}{\partial x_1^o} = \frac{1}{\alpha^2}$$

$$\frac{\partial x_2^t}{\partial x_2^o} = \alpha$$

$$\frac{\partial x_3^t}{\partial x_3^o} = \alpha \tag{D.23}$$

$$\frac{\partial x_1^t}{\partial x_2^o} = g'$$

The remaining terms of $\partial x_k^t/\partial x_j^o$ are equal to zero. Therefore, we may write:

$$\frac{\partial x_k^t}{\partial x_j^o} \Rightarrow \begin{bmatrix} \frac{1}{\alpha^2} & g' & 0 \\ 0 & \alpha & 0 \\ 0 & 0 & \alpha \end{bmatrix} \tag{D.24}$$

$$\frac{\partial x_k^t}{\partial x_j^o}\frac{\partial x_n^t}{\partial x_j^o} \Rightarrow \begin{bmatrix} \frac{1}{\alpha^4} + (g')^2 & \alpha g' & 0 \\ \alpha g' & \alpha^2 & 0 \\ 0 & 0 & \alpha^2 \end{bmatrix} \tag{D.25}$$

Substituting Eq. D.25 into Eq. D.20, we obtain:

$$\begin{bmatrix} \frac{1}{\alpha^4}\sigma_{11} & 0 & 0 \\ 0 & 0 & 0 \\ 0 & 0 & 0 \end{bmatrix} + p \begin{bmatrix} \frac{1}{\alpha^4} + (g')^2 & \alpha g' & 0 \\ \alpha g' & \alpha^2 & 0 \\ 0 & 0 & \alpha^2 \end{bmatrix} = \begin{bmatrix} G + N_1 & \tau_{12} & 0 \\ \tau_{12} & G & 0 \\ 0 & 0 & G \end{bmatrix} \tag{D.26}$$

From Eq. D.26, we may write the following scalar equations:

$$\frac{1}{\alpha^4}\sigma_{11} + p\left(\frac{1}{\alpha^4} + (g')^2\right) = G + N_1 \tag{D.27}$$

$$p\alpha g' = \tau_{12} \tag{D.28}$$

$$p\alpha^2 = G \tag{D.29}$$

From Eqs. D.28 and D.29, we obtain:

$$p = \frac{G}{\alpha^2} \tag{D.30}$$

$$g' = \frac{\tau_{12}}{p\alpha} = \frac{\alpha\,\tau_{12}}{G} \tag{D.31}$$

Substituting Eqs. D.30 and D.31 into Eq. D.27, we may write:

$$\frac{1}{\alpha^4}\sigma_{11} + \frac{G}{\alpha^2}\left(\frac{1}{\alpha^4} + \frac{\alpha^2\,\tau_{12}^2}{G^2}\right) = G + N_1 \tag{D.32a}$$

$$\frac{1}{\alpha^4}\sigma_{11} + \frac{G}{\alpha^6} + \frac{\tau_{12}^2}{G} = G + N_1 \tag{D.32b}$$

$$\frac{1}{\alpha^4}\sigma_{11} + \frac{G}{\alpha^6} = G + N_1 - \frac{\tau_{12}^2}{G} \tag{D.32c}$$

Integrating over the capillary cross-section (from $r = 0$ to $r = R = D/2$), we have:

$$2\pi \int_0^R \sigma_{11}\, r\, dr = 0 \tag{D.33}$$

and

$$\frac{1}{\alpha} = \frac{r^o}{r^t} = \frac{d}{D} = \left[\frac{\int_0^R (N_1 + G - \frac{\tau_{12}^2}{G})\, r\, dr}{\int_0^R G\, r\, dr} \right]^{1/6} \tag{D.34}$$

Note in Eq. D.34, that N_1, G and τ_{12} are variables expressed in terms of the variables inside the capillary. Using:

$$\frac{N_1}{2\tau_{12}} = \frac{\tau_{12}}{G} \tag{D.35}$$

$$\frac{\tau_{12}}{\tau_w} = \frac{r}{R} \tag{D.36}$$

we write Eq. D.34 as follows:

$$\frac{\text{extrudate diameter}}{\text{capillary diameter}} = \frac{d}{D} = [1 + \frac{1}{2} (\frac{N_{1,w}}{2\tau_w})^2]^{1/6} \tag{D.37}$$

Q.E.D.

APPENDIX E

EXPERIMENTAL RESULTS

1. Union Carbide DFDY 4400 LDPE

Barrel temperature profile: 163/179/196/196/196°C

Screw speed, rpm	P_1, kPa	P_2, kPa	P_3, kPa	T, °C
40	13697	8274	3447	197.8
60	16777	9997	4183	201.1
80	18869	11376	4711	202.2

Screw speed, rpm	G, kg/s	d/D	d*/D
40	1.911×10^{-3}	1.558	1.646
60	2.948×10^{-3}	1.584	1.674
80	3.968×10^{-3}	1.621	1.713

(a) Location of pressure and temperature measurements:

(i) P_1 at 17.28 screw turns

(ii) P_2 at 22.59 screw turns

(iii) P_3 at 7.563 cm from adapter entrance

(iv) T at 11.373 cm from adapter entrance

(b) d*/D represents temperature corrected swell ratio (see Sec. 10.2.3, Eq. 10.7).

2. DuPont SCLAIR 19A HDPE

Barrel temperature profile: 188/196/204/204/204°C

Screw speed, rpm	P_1, kPa	P_2, kPa	P_3, kPa	T, °C
40	21374	13789	6136	208.1
60	25809	16203	7136	214.4
80	29142	17926	7963	219.1

Screw speed, rpm	G, kg/s	d/D	d*/D
40	1.755×10^{-3}	1.568	1.682
60	2.707×10^{-3}	1.610	1.728
80	3.705×10^{-3}	1.647	1.767

(a) Location of pressure and temperature measurements

(i) P_1 at 17.26 screw turns

(ii) P_2 at 22.59 screw turns

(iii) P_3 at 7.563 cm from adapter entrance

(iv) T at 11.373 cm from adapter entrance

(b) d*/D represents temperature corrected swell ratio (see Sec. 10.2.3, Eq. 10.7).

APPENDIX F

SENSITIVITY STUDY ON POLYMER MATERIAL PROPERTIES

The results of the sensitivity study on the polymer material properties as they influence the predictions of the extruder model are given in this appendix. For a given polyethylene resin and processing conditions (LDPE, screw speed = 60 rpm, mass flow rate = 2.929×10^{-3} kg/s), each of the properties shown below were increased by 2 per cent in the extruder model. The following are the resulting pressures and bulk temperatures as compared to P_{exit} = 0 kPa and $T_{bulk,exit}$ = 200.72 °C which were obtained using the polymer properties given in Sec. 11.1, Table 11.1 and shown in brackets (maximum pressures in the extruder screw channel are of the order 10,000 to 30,000 kPa):

Polymer property	P_{exit}, kPa	$T_{bulk,exit}$, °C
f'_w = 0.306 (0.30)	-5	200.72
δ = 34.374° (33.7)	5	200.72
f_b = 0.408 (0.40)	951	200.72
f_s = 0.255 (0.25)	-514	200.72
Cp_m = 2646.90 J/(kg·K)(2595)	-13	200.64
Cp_s = 2818.26 J/(kg·K) (2763)	29	200.72
ρ_{bulk} = 606.90 kg/m^3 (595)	123	200.72
ρ_m = 794.58 kg/m^3 (779)	1359	200.67
ρ_s = 937.38 kg/m^3 (919)	-4	200.72
k_m = 0.18564 W(m·K) (0.182)	-12	200.69
λ = 132380.7 J/kg (129785)	17	200.72
T_{melt} = 112.2°C (110)	206	200.73

APPENDIX G

SCREW CHANNEL DIMENSIONS, POLYMER PROPERTIES

AND PROCESSING CONDITIONS

G.1 Feed Hopper

Feed hopper dimensions

H_1 = 215 mm
H_2 = 272 mm
H_3 = 130 mm
W_1 = 460 mm
W_3 = 72 mm
h_o = 50 mm
H_o = 322 mm
α = 35.5°

G.2 Solids Conveying Zone (Figs. 4.5 and 4.6)

Screw channel dimensions

D_b = 38.1 mm
L = 38.1 mm
H = 6.1 mm
e = 6.35 mm

Feed hopper base: 1.59 screw turns

Distance between feed hopper opening and first heater band: 1.41 screw turns.

Polymer properties

$$\rho_{bulk} = 595 \text{ kg/m}^3$$
$$f_b = 0.40$$
$$f_s = 0.25$$

Processing conditions

$$N = 40,\ 60,\ 80 \text{ rpm}$$
$$G = 0.001965,\ 0.002929,\ 0.003886 \text{ kg/s}$$
$$p_o = 1.0 \text{ kPa}$$

G.3 Melting zone (Figs. 5.4, 5.5, 5.6 and 5.7)

Screw channel dimensions

$$D_b = 38.1 \text{ mm}$$
$$L = 38.1 \text{ mm}$$
$$H_1 = 6.1 \text{ mm}$$
$$e = 6.35 \text{ mm}$$

Constant depth channel: $\overline{\theta} = 20.8^{\circ}$

$\overline{W} = 29.3$ mm

Tapered channel: $\overline{\theta} = 19.7^{\circ}$

$\overline{W} = 29.5$ mm

$A = 6.038 \times 10^{-3}$

Polymer properties

ρ_m = 779 kg/m^3

ρ_s = 919 kg/m^3

Cp_m = 2595 J/(kg•K)

Cp_s = 2763 J/(kg•K)

k_m = 0.182 W/(m•K)

λ = 129785 J/kg

T_{melt} = 110^oC

Newtonian viscosity: μ = 1000 Pa•s

Non-Newtonian viscosity:

$$\log \eta = a_o + a_1 \log \dot{\gamma} + a_2(\log \dot{\gamma})^2 + a_3T + a_4T^2 + a_5T \log \dot{\gamma}$$

where
a_o = 11.7838
a_1 = −0.639104
a_2 = −0.0112744
a_3 = −0.0183449
a_4 = 8.78448×10^{-6}
a_5 = 9.66512×10^{-4}

η = [Pa•s], T = [^oC], $\dot{\gamma}$ = [s^{-1}]

Processing conditions

N = 40, 60, 80 rpm
G = 0.001965, 0.002929, 0.003886 kg/s

T_b = 180°C
T_s = 30°C

G.4 Melt Conveying Zone I (Figs. 6.6, 6.7, 6.8, 6.11, 6.12, 6.13, 6.16, 6.17, 6.18, B.2, B.3, B.4)

Screw channel dimensions

D_b = 38.1 mm
L = 38.1 mm
e = 6.35 mm

Feed section: 6 screw turns

H = 6.1 mm
$\bar{\theta}$ = 20.8°
$\bar{W}$ = 29.3 mm

Compression section: 6 screw turns

H = 6.1 to 2.0 mm
$\bar{\theta}$ = 19.7°
$\bar{W}$ = 29.5 mm

Metering section: 6 screw turns

H = 2.0 mm
$\bar{\theta}$ = 18.6°
$\bar{W}$ = 29.8 mm

Polymer properties

ρ_m = 779 kg/m^3

Cp_m = 2595 kg/m^3

k_m = 0.182 W/(m·K)

Newtonian viscosity: μ = 1043, 856, 722 Pa·s

Processing conditions

N = 40, 60, 80 rpm

G = 0.001826, 0.002742, 0.003652 kg/s

T_o = 110^oC

T_b = 180^oC

G.5 Melt Conveying Zone II (Figs. 6.22, 6.23, 6.24, 6.25)

Screw channel dimensions

D_b = 38.1 mm
L = 38.1 mm
e = 6.35 mm

Feed section: 12 screw turns

H = 6.1 mm

$\overline{\theta}$ = 20.8^o

$\overline{W}$ = 29.3 mm

Compression section: 6 screw turns

$H = 6.1$ to 2.0 mm

$\overline{\theta} = 19.7^{\circ}$

$\overline{W} = 29.5$ mm

Metering section: 6 screw turns

$H = 2.0$ mm

$\overline{\theta} = 18.6^{\circ}$

$\overline{W} = 29.8$ mm

Polymer properties

$\rho_{bulk} = 595\ kg/m^3$

$f_b = 0.40$

$f_s = 0.25$

$\rho_m = 779\ kg/m^3$

$\rho_s = 919\ kg/m^3$

$Cp_m = 2595\ J/(kg \cdot K)$

$Cp_s = 2763\ J/(kg \cdot K)$

$k_m = 0.182\ W/(m \cdot K)$

$\lambda = 129785\ J/kg$

$T_{melt} = 110^{\circ}C$

Newtonian viscosity: $\mu = 1043, 856, 722\ Pa \cdot s$

Processing conditions

N	=	40, 60, 80 rpm
G	=	0.001826, 0.002742, 0.003652 kg/s
T_o	=	$110^{o}C$
T_b	=	$163/179/196/196/196^{o}C$
p_o	=	0.890 kPa

G.6 Melt Conveying Zone III (Figs. 6.28, 6.29, 6.30)

Screw channel dimensions

D_b	=	38.1 mm
L	=	38.1 mm
e	=	6.35 mm

Feed section: 12 screw turns

H = 6.1 mm

$\overline{\theta}$ = 20.8^{o}

$\overline{W}$ = 29.3 mm

Compression section: 6 screw turns

H = 6.1 to 2.0 mm

$\overline{\theta}$ = 19.7^{o}

$\overline{W}$ = 29.5 mm

Metering section: 6 screw turns

H = 2.0 mm

$\overline{\theta}$ = 18.6^{o}

$$\overline{W} = 29.8 \text{ mm}$$

Polymer properties

$$\begin{aligned}
\rho_{bulk} &= 595 \text{ kg/m}^3 \\
f_b &= 0.40 \\
f_s &= 0.25 \\
\rho_m &= 779 \text{ kg/m}^3 \\
\rho_s &= 919 \text{ kg/m}^3 \\
Cp_m &= 2595 \text{ J/(kg·K)} \\
Cp_s &= 2763 \text{ J/(kg·K)} \\
k_m &= 0.182 \text{ W/(m·K)} \\
\lambda &= 129785 \text{ J/kg} \\
T_{melt} &= 110^{\circ}\text{C}
\end{aligned}$$

Non-Newtonian viscosity:

$$\log \eta = a_0 + a_1 \log \dot{\gamma} + a_2(\log \dot{\gamma})^2 + a_3 T + a_4 T^2 + a_5 T \log \dot{\gamma}$$

where

$$\begin{aligned}
a_o &= 11.7838 \\
a_1 &= -0.639104 \\
a_2 &= -0.0112744 \\
a_3 &= -0.0183449 \\
a_4 &= 8.78448 \text{x} 10^{-6} \\
a_5 &= 9.66512 \text{x} 10^{-4}
\end{aligned}$$

$$\eta = [\text{Pa·s}],\ T = [^{\circ}\text{C}],\ \dot{\gamma} = [s^{-1}]$$

Processing conditions

$$N = 40,\ 60,\ 80 \text{ rpm}$$

G = 0.001965, 0.002929, 0.003886 kg/s
T_o = 110°C
T_b = 163/179/196/196/196°C
p_o = 0.890 kPa

G.7 <u>Die Section</u> (Fig. 7.9)

<u>Flow channel dimensions</u>

Breaker plate: N_B = 65
R_B = 1.29 mm
z_B = 12.2 mm

Adapter: H_A = 9.53 mm
W_A = 19.05 mm
z_A = 138.03 mm

Die: R_D = 2.39 mm
z_D = 50.07 mm

<u>Polymer properties</u>

ρ_m = 779 kg/m^3
Cp_m = 2595 J/(kg·K)
k_m = 0.182 W/(m·K)

Non-Newtonian viscosity:

$$\log \eta = a_0 + a_1 \log \dot{\gamma} + a_2(\log \dot{\gamma})^2 + a_3 T + a_4 T^2 + a_5 T \log \dot{\gamma}$$

where a_o = 11.7838
a_1 = −0.639104
a_2 = −0.0112744

$$a_3 = -0.0183449$$
$$a_4 = 8.78448\text{x}10^{-6}$$
$$a_5 = 9.66512\text{x}10^{-4}$$

$$\eta = [\text{Pa}\cdot\text{s}],\ T = [^{\circ}\text{C}],\ \dot{\gamma} = [\text{s}^{-1}]$$

Processing conditions

$$G = 0.001965,\ 0.002929,\ 0.003886\ \text{kg/s}$$
$$T_B = T_A = T_D = 196^{\circ}\text{C}$$
$$p_o = 4916,\ 5813,\ 6529\ \text{kPa}$$
$$T_o = 198.4,\ 199.7,\ 200.5\ ^{\circ}\text{C}$$